2006

High growth rate SiC CVD via hot-wall epitaxy

Rachael L. Myers-Ward
University of South Florida

High Growth Rate SiC CVD via Hot-Wall Epitaxy

by

Rachael L. Myers-Ward

A dissertation submitted in partial fulfillment
of the requirements for the degree of
Doctor of Philosophy
Department of Electrical Engineering
College of Engineering
University of South Florida

Major Professor: Stephen E. Saddow, Ph.D.
Andrew M. Hoff, Ph.D.
John T. Wolan, Ph.D.
Grisselle Centeno, Ph.D.
Olle Kordina, Ph.D.
Yevgeniy Shishkin, Ph.D.

Date of Approval:
January 13, 2006

Keywords: silicon carbide, chemical vapor deposition, epitaxial layers, high growth speeds, low-pressure

TABLE OF CONTENTS

LIST OF TABLES

LIST OF FIGURES

HIGH GROWTH RATE SIC CVD VIA HOT-WALL EPITAXY

Rachael L. Myers-Ward

ABSTRACT

This dissertation research focused on the growth of 4H-SiC epitaxial layers in low-pressure horizontal hot-wall chemical vapor deposition (CVD) reactors. The goal of the research was to develop a growth process that maximized the growth rate and produced films of smooth morphology. The epitaxial growth of SiC was carried out in two different reactor sizes, a 75 mm reactor and a 200 mm reactor. The maximum repeatable growth rate achieved was 30-32 μm/h in the 200 mm reactor using the standard chemistry of hydrogen-propane-silane (H_2-C_3H_8-SiH_4) at growth temperatures ≤ 1600 °C, which is the highest growth rate reported to date in a horizontal hot-wall reactor at these temperatures. This growth rate was achieved with a silane flow rate of 30 sccm. The process development and characterization of 4H-SiC epitaxial films grown using the standard chemistry are presented.

There are many ways to increase the growth rate, such as changing the pressure, increasing the reactant flow rates, or increasing the temperature. The method of choice for this dissertation work was to first increase the reactant flow rates, i.e. silane flow rate, and then to alter the growth chemistry by using a growth additive. When the silane flow is increased, while maintaining a specific growth temperature, supersaturation of silicon

may occur. When this happens, particulates may form and deposit onto the sample surface during growth which degrades the film morphology of the epitaxial layers. In order to overcome this severe limitation in the growth of SiC, hydrogen chloride (HCl) was added to the standard chemistry of H_2-C_3H_8-SiH_4 during growth when the SiH_4 flow was increased beyond 30 sccm. With the addition of HCl, the Si supersaturation was suppressed and the growth rate was increased from ~32 μm/h to ~ 49 μm/h by increasing the silane precursor up to 45 sccm, while maintaining the Si/C ratio of the standard chemistry process. The addition of HCl to the standard chemistry for growth of SiC films was pioneering work that has since been duplicated by several research groups.

PREFACE

There are many people whom I would like to acknowledge for their utmost assistance during my dissertation work. Without them, I would not have succeeded. I would like to first and foremost give thanks and gratitude to my advisor Dr. Stephen E. Saddow for his guidance and loyalty to my research. He has been my mentor throughout my post graduate studies by being an inspiration and has encouraged me throughout the years. Without his guidance and constant support, I would not have been able to achieve all that I have. He has taught me a tremendous amount and has given me much support. Dr. Saddow has provided me the opportunity to study abroad and attend many conferences throughout the country and in Europe. For all of these things, I am truly grateful.

I would also like to thank Dr. A. M. Hoff, Dr. J. T. Wolan, and Dr. G. Centeno for being part of my committee. They have supported me and given me guidance throughout my research. I wish to give gratitude to Dr. O. Kordina, who has helped and advised me with my dissertation work. Much appreciation goes to Dr. Y. Shishkin, who has provided me with insight about my research and spent a considerable amount of time helping to refine my dissertation. Next I wish to thank Professor W. J. Choyke for providing LTPL analysis on many of the epitaxial films grown during this dissertation work.

Next, I wish to thank Dr. S. P. Rao, for being my best friend and colleague. She has always been there for me and has always provided help and encouragement. I would also like to thank T. Fawcett for his assistance with simulations. I extend my appreciation to the SiC group, especially I. Haselbarth, C. Frewin, M. Reyes, B. Grayson, C. Coletti, J. Walker and S. Harvey, who have been of great assistance to me during this research. My appreciation also goes to R. Everly and R. Tufts of the NNRC. I would also like to thank Dr. U. Starke of the Max-Planck Institute, Stuttgart, Germany, for allowing me to visit and perform research in his laboratory. My gratitude goes to Dr. C. Wood of the Office of Naval Research (ONR) for his support of this research. This work has been supported under Dr. Wood by the Defense University Research Initiative on Nanotechnology (DURINT) program, Grant N00014-0110715.

Finally, I would like to thank my parents, aunt, sister, brothers and most of all, my husband. They have been very patient with me and have given me support and encouragement throughout my education. Even though I have not been able to see them much over the past few months, they have understood and been there for me when I needed them. They are very loving and caring, and always have wanted the best for me. For this, I am grateful, more than words can express.

CHAPTER 1

INTRODUCTION

1.1 Silicon Carbide Overview

Silicon carbide (SiC) is a semiconductor material which is being developed for high-temperature, microwave and high-power switching device applications. Unlike silicon-based electronics, which can only withstand temperatures up to 250 °C [1], SiC-based devices can endure elevated temperatures up to 650 °C due to its excellent chemical and physical stability [2]. Some of the physical and electrical properties that make this semiconductor superior to Si and GaAs are a large energy bandgap, high critical electric field, high saturated electron drift velocity, and high thermal conductivity [3]. From Table 1.1 it can be seen that the material properties (excluding mobility) of SiC are outstanding compared to those of Si.

High-temperature device applications are not generally possible using Si due to its narrow bandgap of 1.12 eV. At elevated temperatures, the thermal generation of electron-hole pairs exceeds the number of dopant-provided free carriers, causing the device to fail [4]. The thermal generation of electron-hole pairs is much lower in SiC than in Si due to its wider energy bandgap (3.2 eV at room temperature for the 4H-SiC polytype). The difference in the intrinsic carrier concentration, n_i, between Si and SiC, is 19 orders of magnitude (i.e., 10^{19}), which enables higher temperature applications using SiC. As seen

in Table 1.1, the bandgap values for SiC are at least twice that of Si with the resulting values of intrinsic carrier concentration being several orders of magnitude lower. The intrinsic carrier concentration is proportional to minus the exponent of the bandgap value. Since the bandgap of SiC is higher than that of Si, n_i is much lower for SiC than Si.

For high-voltage, high-power devices, the semiconductor material must be able to withstand high electric fields (> 0.3 MV/cm [1]). Since SiC has a wide bandgap, the impact ionization energy, the impact energy which creates additional electrons into the conduction band, is higher for this material than it is for Si [4]. Therefore, the electric field may be higher for SiC before impact-ionization driven breakdown occurs, caused by avalanche multiplication of ionized carriers [5]. SiC devices can be made to have ten times higher breakdown voltage compared to Si with the same depletion width [4], or the depletion region of SiC can be much thinner than that of Si with the same breakdown voltage.

Table 1.1 Properties of commonly used SiC polytypes compared with Si [1,3,6].

Property	4H-SiC	6H-SiC	3C-SiC	Si
Energy bandgap at 300K (eV)	3.20	3.00	2.29	1.12
Intrinsic Carrier Concentration at 300K (cm^{-3})	$5x10^{-9}$	$1.6x10^{-6}$	$1.5x10^{-1}$	$1x10^{10}$
Critical breakdown electric field (MV/cm)	2.2	2.5	2.12	0.25
Saturated electron drift velocity (x 10^7 cm/s)	2.0	2.0	2.5	1.0
Thermal conductivity (W/cm-K)	4.9	4.9	3.2	1.5
Electron mobility (cm^2/V-s)	1000	600	800	1450
Hole mobility (cm^2/V-s)	115	100	40	470

At low electric fields (E < 10 kV/cm), the drift velocity (the velocity a particle reaches due to an electric field) is proportional to the applied electric field. However, at fields greater than 10 kV/cm, the velocity increases sub-linearly with the field. At fields substantially higher than 10 kV/cm, the drift velocity saturates and becomes independent of electric field [7]. The saturated drift velocity in SiC is much higher than that in Si, making SiC a candidate material for high-frequency devices. With similar breakdown voltages for Si and SiC devices, the depletion width can be thinner in SiC, thus the device will be much faster using SiC because the series resistance is lower, thus a faster RC time constant can be realized [4].

The dissipation of heat in a high-power device is critical to the reliability of that device [3]. When the material is heated, the physical properties often change. For example, the carrier mobility decreases with increasing temperature [5] and the intrinsic carrier concentration increases, which may cause the device to fail. Since the thermal conductivity of SiC is greater than three times that of Si, the heat can flow more readily from hot spots in the SiC-based device to the package [1] compared to Si and other semiconductors.

SiC possesses the ability to crystallize into different structures which are called polytypes. There are over 200 different known polytypes of SiC which have been observed to date [1]. The differentiation of these polytypes is based on the stacking sequence of the tetrahedrally bonded Si-C bilayers in the vertical (c-axis) direction. There are three general categories in which the polytypes fall under: cubic (C), hexagonal (H), and rhombohedral (R). There is only one purely cubic structure which is labeled 3C-SiC. The only pure hexagonal structure is 2H-SiC. The rest of the polytypes have a

combination of cubic and hexagonal bonding [6]. The most commonly studied polytypes of SiC are 4H-, 6H-, and 3C-SiC. The designation of each polytype is by a number and a letter. The number represents the number of layers required to complete the unit cell and the letter designates the type of the structure [5]. Figure 1.1 shows the stacking sequence of the three most common polytypes.

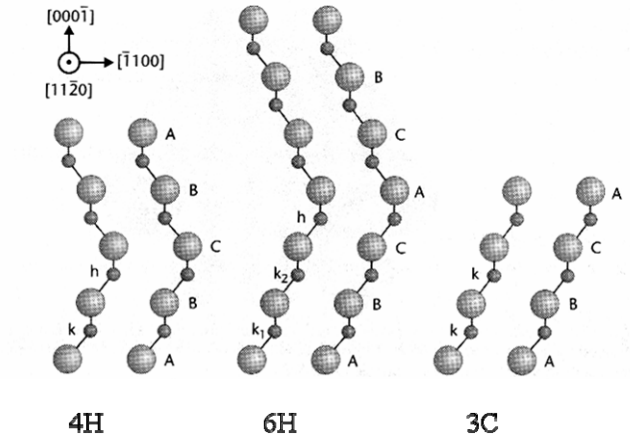

Figure 1.1 Stacking sequences of the three most common SiC polytypes. The larger atoms are Si, while the smaller atoms are C. Symbols 'k' and 'h' denote lattice sites with cubic and hexagonal symmetry, respectively [5].

The 'A', 'B', and 'C' labels in Figure 1.1 denote the position of the carbon atoms within the bilayers of the hexagonal structure [3]. The designation of 'k' and 'h' are the type of crystal symmetry at that point, which is either cubic (k) or hexagonal (h), respectively. As seen in Figure 1.1, 4H-SiC has a stacking sequence of ABCB, or 4 layers, therefore the designation is 4H. This structure has an equal number of cubic and hexagonal lattice sites. The 6H-SiC structure has 6 stacking layers before the sequence repeats ABCACB, and, finally, 3C-SiC is a continuation of the ABC stacking sequence which has purely cubic symmetry. Due to differences in stacking sequence, the electrical, mechanical and optical properties vary for each polytype of SiC, as shown in Table 1.1.

3C-SiC has a high electron mobility which makes it a promising material for high-frequency devices. However, there is still not a commercially available growth process that produces bulk substrates for this polytype [6]. The growth of 3C-SiC typically takes place heteroepitaxially on Si substrates. The lattice and thermal expansion coefficient mismatch between these two materials are ~ 22% and 8%, respectively [8]. This often creates defects at the SiC/Si interface which propagate through the epitaxial layer [9], thus limiting the quality of the films. Therefore, this polytype was not the material chosen for this dissertation research, although a considerable amount of 3C-SiC growth has and is being conducted in the USF SiC group [10,11].

The hexagonal close-packed structure is a main reason for the high stability of the hexagonal SiC polytypes. The 4H-SiC polytype has the highest stability due to the alternating cubic and hexagonal layers [12]. 6H-SiC has a low, anisotropic electron mobility, while 4H-SiC has a much higher electron mobility and is less anisotropic (i.e. less directionally dependent) [6]. Thus 4H-SiC is, at present, the most commonly used polytype for electronic devices [5]. With all these factors outlined, the research for this dissertation was focused on the growth of 4H-SiC epitaxial layers.

1.2 Motivation for Dissertation Research

Growing epitaxial films is one of the key technological steps in the fabrication of SiC device structures [13]. In order to produce the desired electrical specifications for device applications, such as doping, epitaxial layers are grown on bulk SiC substrates. These epitaxial layers are required to have high crystalline quality, low surface

roughness, low point and extended defect density, while exhibiting a high degree of doping and thickness uniformity [13]. A limitation for the success of SiC as a device material is the high extended defect density within the epitaxial films. Defects reduce the minority carrier lifetime, which is important for high voltage device performance. The crystal defects tend to decrease the carrier lifetime of the films, which in turn reduces the performance of the devices [14].

A few SiC-based devices have recently emerged as the leading candidates for power electronic applications [15]. Some of these devices are Schottky diodes and metal semiconductor field effect transistors (MESFET's). The MESFET device requires thin epitaxial layers with different doping concentrations, both n- and p-type, with abrupt doping profiles [15]. Other high power devices, PiN diodes (where a p-type region and an n-type region are separated by an intrinsic 'i' region), require low-doped drift layers that are approximately 40-50 μm thick (or even up to 100 μm thick [16]) with a low n-type doping concentration of 1 x 10^{14} cm^{-3} [15]. It is generally understood that epitaxial layers of SiC greater than 80 μm thick are needed for electrical switching devices in order to outperform Si-based devices [17].

In order to produce thick (> 40 μm) uniform epitaxial films, high growth rates are needed for economical reasons. For example, if the growth rate is only 5 μm/h and a film thickness of 100 μm is desired, it will take approximately 20 hours to grow the film. This results in very high production costs, thereby increasing the cost of the actual device. It would obviously be more advantageous to grow a film for 2 hours at 50 μm/h. The primary goal of growing at such high speeds then becomes maintaining a high quality epitaxial deposition in a shorter amount of time.

The main concern with high growth rates is being able to maintain the electrical and structural quality of the films. Many of the methods developed to date, in attempt to achieve this purpose, take place at elevated temperatures, which limit the life of the reactor parts and can create defects in the grown films. The work conducted during this research was focused on using growth temperatures around 1600 °C with the goal of growing thick, high-quality 4H-SiC films.

1.3 SiC CVD Epitaxy Background

The most common technique used to grow epitaxial SiC is chemical vapor deposition (CVD) [5]. The typical chemistry used to grow SiC CVD films is hydrogen, propane, and silane, or H_2-C_3H_8-SiH_4. In this mixture, hydrogen serves as the carrier gas and silane and propane are the precursors for growth. Growth of SiC to produce device-quality thick films has been the focus of many groups over the years. Nakazawa, *et al*. [18] grew 4H-SiC in a horizontal hot-wall CVD reactor. For reference, a schematic drawing of a horizontal hot-wall reactor is shown in Figure 1.2. A detailed description of this type of reactor is presented in Chapter 2, Section 2.2.1. The growth rate Nakazawa [18] produced was 14 μm/h, and film surfaces grown using this rate displayed growth pits on the surface. The growth rate was then reduced to 6-7 μm/h and the films were smooth without such defects. A 50 μm thick film was grown with this process. An X-ray diffraction (XRD) rocking curve of the sample proved the film to be of very high quality with a full-width at half maximum (FWHM) of the (0004) diffraction peak of 9 arcsec. Low temperature photoluminescence (LTPL) was also performed and no L_1 defect line at

2.902 eV or Ti peak (C_o at 2.790 eV) were observed. The background doping level was 1-2 x 10^{13} cm^{-3}. Clearly, this process produced high quality films, but at such a low growth rate as to render the process economically infeasible to produce thick films. Kimoto, *et al*. [13] also reported growth in a horizontal hot-wall reactor with a growth rate of 5 μm/h. A 50 μm thick 4H-SiC epitaxial film of smooth morphology was grown. The unintentionally doped layers had a low carrier concentration of 2 x 10^{13} cm^{-3}. Again, at a rate of 5 μm/h, the growth rate was too low to economically produce thick films. Zhang, *et al*. [19] recently documented that growth of 4H-SiC epitaxial layers in a horizontal hot-wall reactor could be carried out with a growth rate of 20 μm/h, however, repeatable results were only achievable at 15 μm/h. A 50 μm film was grown at 8.3 μm/h, resulting in a smooth morphological film surface as determined by Nomarski microscopy. At thicknesses of 50 μm and above, the films displayed step-bunching. A film was also grown at 15 μm/h, to produce a thickness of 120 μm. The thickness uniformity was 5.2% with a p-type background doping of 7 x 10^{14} cm^{-3}. Clearly, thick films are attainable with horizontal hot-wall reactors; however, the growth rates need to be improved along with the surface morphology of the thick grown films.

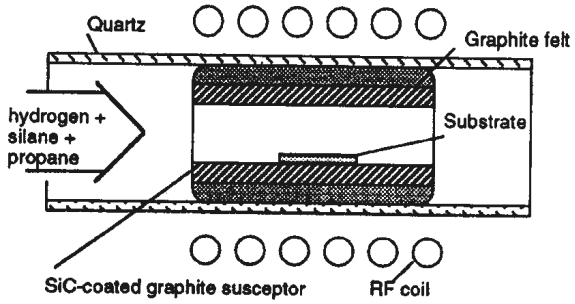

Figure 1.2 Schematic drawing of a horizontal hot-wall CVD reactor growth zone showing gas inlet from the left and exit on the right. Drawing includes RF coil, SiC-coated graphite susceptor, graphite felt insulation, and SiC substrate [20].

A vertical cold-wall reactor has been used to grow 4H-SiC films of 20 – 40 μm thickness at a growth rate of 5-6 μm/h by Rupp, *et al*. [21]. In this stainless steel vertical reactor, the substrate was placed on a holder and the gases were injected from the top and flow down and then laterally over the substrate. The reactor was water cooled. The susceptor was heated using a radio frequency source. A schematic drawing of this type of reactor is shown in Figure 1.3. For the films that were grown beyond a thickness of 30 μm, any substrate surface damage became very pronounced on the surface of the epitaxial layers. To reduce this effect, the substrates were re-polished and dry-etched prior to growth. The resulting thick films did not have any severe surface defects. Again, the produced films were of reasonable surface morphology, but the growth rate was too low to achieve films of >40 μm within a reasonable time frame.

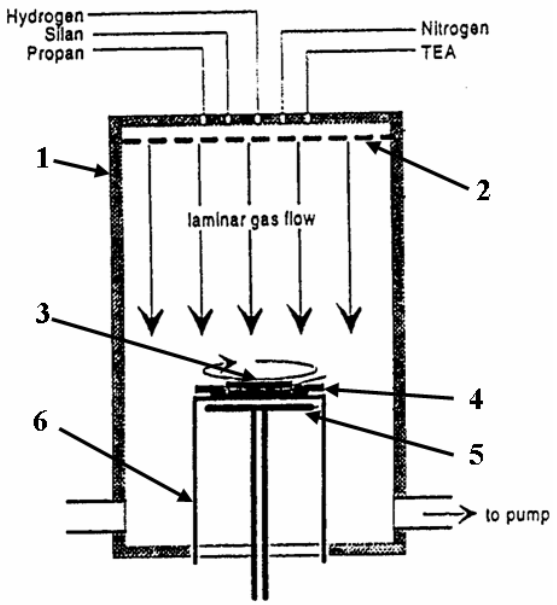

Figure 1.3 Schematic drawing of a vertical cold-wall CVD reactor: (1) double-walled chamber, (2) gas diffuser, (3) SiC- wafer, (4) substrate holder, (5) RF coil, and (6) graphite susceptor. The gases enter from the top and exit out the bottom sides [22].

Another CVD technique used to grow SiC is the vertical hot-wall, or chimney, reactor [23-25]. Figure 1.4 shows a schematic drawing of such a reactor. It is similar to the cold-wall vertical reactor, however, the samples are placed on the side walls of the growth zone and there is no cooling water jacket. The gases flow vertically up the reactor parallel to the sample surface. Growth was carried out in a vertical hot-wall reactor by Zhang, *et al*. [25] to produce 30 – 120 μm thick 4H-SiC epitaxial layers. The temperature at which these films were grown ranged between 1650 and 1850 °C. Growth of a 74 μm film took place at 1710 °C at a rate of 25 μm/h, resulting in a step-bunched surface. In order to reduce or eliminate the macroscopic step-bunching, the temperature was increased to 1850 °C for the growth conditions used. Epitaxial growth in a vertical hot-wall reactor have also been reported by Ellison, *et al*. [26]. N-type 4H-SiC epitaxial

layers with thicknesses of over 100 μm at a growth temperature of ~1750 °C were grown. A thickness uniformity was 5% and a growth rate of 23 μm/h was achieved. The lowest doping concentration for the growth process was 6 x 10^{13} cm^{-3}.

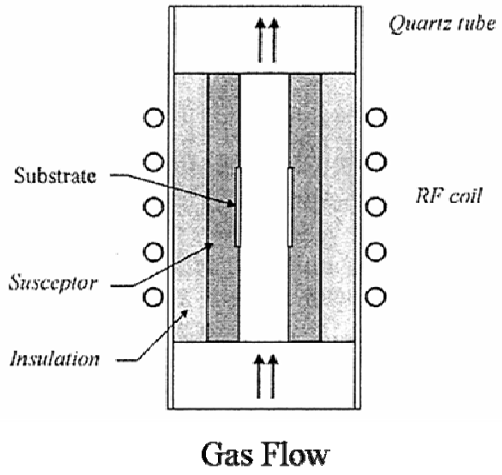

Figure 1.4 Schematic drawing of a vertical hot-wall, or chimney, reactor showing gas inlet from the bottom and exhausts out of the top. Drawing includes quartz tube, RF coils, susceptor, insulation, and SiC substrate [17].

Masahara, *et al*. [23] was able to accomplish 4H-SiC epitaxial growth at rates up to 70 μm/h at a growth temperature of 1800 °C in a vertical-type, quasi-hot-wall, reactor. A schematic drawing of this quasi-hot-wall reactor is shown in Figure 1.5. The gas nozzle and susceptor may be independently heated by RF power. The gas nozzle heats the substrate surface by radiative heating and it also controls the temperature of the reactants. There are radiation reflectors in this reactor instead of graphite foam insulation. The surface morphology and structural quality of films grown at two different speeds (26 μm/h and 70 μm/h) were compared. The thicknesses of the films were 26 μm and 31 μm, respectively. The surface morphology of the 31 μm thick film was rougher than the 26 μm thick. Even so, an X-ray rocking curve of the 31 μm thick film had a FWHM value of

13.5 arcsec indicating good crystallinity. As described in the literature, the vertical hot-wall reactor is a technique that produces thick films much faster than the horizontal hot-wall system. However, the films are grown at high process temperatures which increases the wear and tear on the reactor.

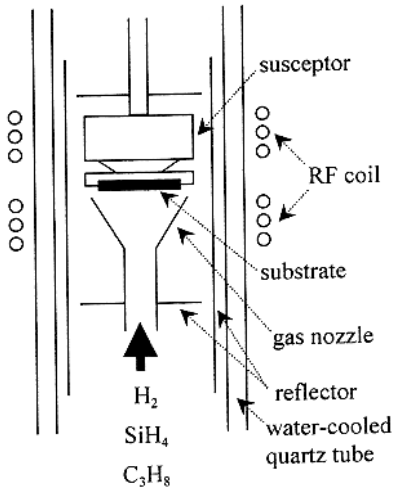

Figure 1.5 Schematic drawing of the quasi-hot-wall reactor. The reactor contains an outer water-cooled quartz tube as shown [23].

Vertical radiant reactors have also been developed to increase the growth rate to permit the production of thick films [16]. This type of reactor is very similar to the vertical, or chimney, reactor except that the susceptor is V-shaped with the samples placed on the side of the V (see Figure 1.6). In this geometry, the gases flow upward over the substrate. Induction heating is applied directly to the hot-wall while the susceptor and substrate are heated by radiation from the hot-wall. The temperature of the substrate is higher than the susceptor for this type of reactor. Tsuchida, *et al*. [16] was able to achieve growth rates up to 18 μm/h in a vertical radiant reactor at growth temperatures between 1530 and 1560 °C. Thick 4H-SiC epitaxial films of 150 μm were grown with smooth surfaces. The net carrier concentration of one of the 150 μm thick films was 1 x 10^{14}

cm^{-3}. A film was also grown by Tsuchida, *et al*. [27] with a growth rate of 15 μm/h, resulting in a thickness of 250 μm. The surface roughness increased slightly for films of higher thicknesses. An X-ray rocking curve measurement of a 110 μm film was taken, and the FWHM was 6.0 arcsec [27]. A 4H-SiC epitaxial layer was grown by Tsuchida at 16 μm/h resulting in a thickness of 246 μm. The Nomarski contrast of the film showed no features except for occasional growth pits. As pointed out, the vertical radiant growth technique shows promising results for epitaxial growth, however, the growth rate is relatively low compared to the vertical reactor.

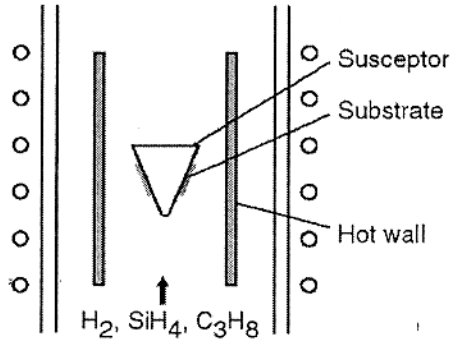

Figure 1.6 Schematic drawing of a vertical radiant reactor showing gas inlet from bottom. Drawing includes RF coils, susceptor, hot-wall, and substrate [27].

Overall, the processes described in this section resulted in epitaxial layers that were thick and of good quality. However, using the horizontal hot-wall reactor or the vertical cold-wall reactor to produce growth rates around 5 – 15 μm/h, the process time would be very long to achieve films up to and beyond 50 μm in thickness, which are needed for power devices. The vertical radiant reactor is able to produce films within reasonable amounts of time, however, the loading of the samples is more difficult than for a horizontal reactor. Finally, the vertical reactors are capable of producing such film

thicknesses, but at high process temperatures. This limits the lifetime of the reactor parts and increases the probability of particulate contamination in the films for long growth times. This dissertation focuses on the fast growth of 4H-SiC epitaxial films in a horizontal hot-wall CVD reactor. This type of reactor allows for easy loading/unloading of samples and, more importantly, operates at a growth temperature lower than those possible in vertical reactors.

1.4 Organization of Thesis

The growth of 4H-SiC at elevated growth rates using a horizontal hot-wall chemical vapor deposition (CVD) reactor will be demonstrated. There are four main chapters. Chapter 2 discusses the general theory of CVD with a look into the kinetics, fluid flow and thermodynamics of SiC CVD. Two CVD reactors were used in the dissertation research and they will be described in this chapter. The development of a standard H_2-C_3H_8-SiH_4 chemistry 4H-SiC epitaxial process to achieve a high growth rate of 32 μm/h will then be discussed in Chapter 3. The addition of chlorine to the process via hydrogen chloride (HCl) will be described in Chapter 4. It will be seen that an increase of growth rate from 32 to 49 μm/h was achieved using HCl as a growth additive. Chapter 5 will provide a summary of the dissertation research as well as suggestions for future work.

1.4.1 Publications and Presentations

The following are a list of publications and presentations resulting from research conducted at USF in the area of SiC CVD technology. The items related to the research presented in this dissertation are annotated with (PhD) afterwards:

Publications (3 Journal, 6 conference papers)

- R. L. Myers, Y. Shishkin, O. Kordina, and S. E. Saddow, "High growth rates (>30μm/h) of 4H-SiC epitaxial layers using a horizontal hot-wall CVD reactor", *Journal of Crystal Growth* 285 (2005) 483-486. (PhD)
- R. L. Myers, Y. Shishkin, O. Kordina, I. Haselbarth, and S. E. Saddow, "High Epitaxial Growth Rate of 4H-SiC using Horizontal Hot-Wall CVD", *Materials Science Forum, in press* (2005). (PhD)
- R. Myers, O. Kordina, Z. Shishkin, S. Rao, R. Everly, and S.E. Saddow, , "Increased growth rate in a SiC CVD reactor using HCl as a growth additive", *Materials Science Forum* 483-485 (2005) 73-76. (PhD)
- S. E. Saddow, R. L. Myers and S. P. Rao, "Use of a CVD Reactor for Advanced SiC Processing," Proc. of International Symposium on Advanced Materials and Processing ISAMAP2K4, Kharagpur, India (2004) 1002-1009. (PhD)
- R. L. Myers, K. D. Hobart, M. Twigg, S. Rao, M. Fatemi, F. J. Kub, and S. E. Saddow, "Structural characterization of 3C-SiC films grown on Si layers wafer bonded to polycrystalline SiC substrates" *Materials Research Society Symposium. Proceedings* 815 (2004) 145-148.

- R. L. Myers, S.E. Saddow, S. Rao, K.D. Hobart, M. Fatemi, F.J. Kub, "Development of 3C-SiC SOI structures using Si on polycrystalline SiC wafer bonded substrates," *Materials Science Forum* Vols. 457-460 (2004) 1511-1514.
- T. Fawcett, J.T. Wolan, R.L. Myers, J. Walker, and S.E. Saddow, "Hydrogen gas sensors using 3C-SiC/Si epitaxial layers," *Materials Science Forum* Vols. 457-460 (2004) 1499-1502.
- T. J. Fawcett, J. T. Wolan, R. L. Myers, J. Walker, and S. E. Saddow, **"**Wide-range (0.33%–100%) 3C–SiC resistive hydrogen gas sensor development," *Applied Physics Letters*, Vol. 85 (3) (2004) 416–418.
- S. Dogan, A. Teke, D. Huang, H. Morkoc, C. B. Roberts, J. Parish, B. Ganguly, M. Smith, R. L. Myers and S. E. Saddow, "4H–SiC photoconductive switching devices for use in high-power applications*," Applied Physics Letters* Vol. 82 (18) (2003) 3107-3109.

Presentations

- R. L. Myers, Y. Shishkin, O. Kordina, I. Haselbarth, and S. E. Saddow, "High Epitaxial Growth Rate of 4H-SiC using Horizontal Hot-Wall CVD," *International Conference on Silicon Carbide and Related Materials,* Pittsburgh, PA, September 2005. (PhD)
- R. Myers, O. Kordina, Z. Shishkin, S. Rao, R. Everly, and S.E. Saddow, "Increased growth rate in a SiC CVD reactor using HCl as a growth additive", *European Conference on Silicon Carbide and Related Materials,* Bologna, Italy, September 2004. (PhD)
- R. L. Myers, K. D. Hobart, M. Twigg, S. Rao, M. Fatemi, F. J. Kub, and S. E. Saddow, "Structural characterization of 3C-SiC films grown on Si layers wafer bonded to polycrystalline SiC substrates", *Materials Research Society spring meeting*, San Francisco, CA April 2004.

- R.L. Myers, S.E. Saddow, S. Rao, K.D. Hobart, M. Fatemi, and F.J. Kub, "Development of 3C-SiC SOI structures using Si on polycrystalline SiC wafer bonded substrates," *International Conference on Silicon Carbide and Related Materials*, Lyon, France, October 2003.

CHAPTER 2

HOT-WALL CHEMICAL VAPOR DEPOSITION

In Chapter 1, SiC was introduced as a candidate semiconductor material for high-frequency, high-temperature, and high-power electronic device applications. One of the key factors in developing devices for such applications is the growth of epitaxial layers on bulk SiC substrates. Epitaxy is the arrangement of atoms on a crystalline substrate, which results in a deposited film with the same crystallographic orientation as that of the substrate [28,29]. There are two different types of epitaxy, namely hetero- and homo-epitaxy. Heteroepitaxy is the term used for the growth of an epitaxial layer on a crystal that is not of the same material (e.g. 3C-SiC on Si). Homoepitaxy is the term used for the growth of an epitaxial layer that is of the same material as the substrate (e.g. 4H-SiC on 4H-SiC). The focus of this dissertation work is the homoepitaxial growth of 4H-SiC. The goal of epitaxial growth is to produce films of desired physical specifications, i.e. film thickness, electrical polarity and conductivity. The doping of the layers may be performed during the growth by the incorporation of dopant atoms provided by reactant gases, or after growth by ion implantation. For the later process, the crystal is bombarded with dopant ions, which damages the crystal structure. Implant annealing is then performed to both activate the implanted ions and repair the crystal damage [30]. However, the highest quality doped films are always realized during film growth.

The focus of this dissertation research is the growth of device-quality homoepitaxial layers with a specific conductivity, normally low-doped n-type.

2.1 Chemical Vapor Deposition

Chemical vapor deposition is the formation of a stable film on a crystal surface due to a chemical reaction from gaseous species [31]. While this is a deposition technique, it is commonly referred to as a 'growth' process. The basic process (i.e. procedure followed to achieve growth) of CVD begins by flowing precursors (or reactants), via a carrier gas, into a reaction chamber. The gases are heated so that chemical reactions can take place above and at the substrate surface, which results in the deposition of a film. The by-products of the reactions, along with any un-reacted species, are exhausted out of the chamber. The gas phase reactions are activated by thermal energy supplied by either resistive heating, a laser source, the creation of a plasma, or radio frequency (RF) induction heating of the reactants [32]. The latter, RF heating, is the source that is most commonly used in SiC CVD and was used during this research.

There are many variables that impact the deposition rate and film properties, such as the reactants selected, the temperature of the reactor, the type of substrate, the ratio of reactants to each other, the gas flow rates, the process pressure, the geometry of the chamber, and, finally, the substrate surface preparation [31]. With elevated process temperatures, the deposition rate (or growth rate) is typically increased. In addition, certain reactions can take place which might not occur at lower temperatures, and in-situ etching of the substrate simultaneously takes place [31]. The CVD reactor may be

operated at atmospheric pressure (AP), or low pressure (LP) and, therefore, are commonly referred to as APCVD and LPCVD, respectively. SiC LPCVD is typically carried out in the pressure range of 10 – 150 Torr. Growth at low pressures results in improved atomic step coverage, with the deposition rate governed by the surface reactions. As a consequence, the defect density is typically reduced [31].

The reactor geometry is an important parameter in the growth of epitaxial films. There are many types of reactors, as described in Chapter 1, and the choice of reactor is governed by the requirements of the epitaxial films. The two main reactor geometries are vertical and horizontal, both of which can be further classified as hot-wall, cold-wall, or intermediate configurations. The cold-wall design has a reaction tube that is surrounded by a water-cooled jacket which sets the temperature of the reaction tube to approximately 100 °C. The hottest component of the cold-wall reactor is the susceptor which is the part that the substrate is placed on and heated during growth. The remaining areas of the reactor are kept cold [33], hence the name "cold-wall reactor". A large temperature gradient from the surface of the susceptor to the walls of the reactor is produced. In this configuration, there is less deposition on the walls of the reaction tube due to the lower temperature of these surfaces. In the hot-wall reactor, there is a much lower temperature gradient because the side-walls, bottom and top of the susceptor are all heated to approximately the same temperature. This design is basically an isothermal furnace. This dissertation research was performed using a horizontal, hot-wall, low-pressure CVD reactor since this combination of parameters is most likely to result in high-quality epitaxial layers grown at fast growth speeds.

During CVD, a carrier gas transports the reactant gases to the surface of the substrate. The carrier gas also aids the reactions to take place. Typical carrier gases are argon (Ar), helium (He), and hydrogen (H_2); however, H_2 is the most commonly used, especially for SiC CVD [4]. There are a number of precursors that have been used to grow SiC epitaxial films [34]. Some of the silicon based precursors include silane (SiH_4), disilane (Si_2H_6), and silicon tetrachloride ($SiCl_4$). Some of the carbon source precursors that have been reported are acetylene (C_2H_2), propane (C_3H_8), methyl chloride (CH_3Cl), methane (CH_4), and carbon tetrachloride (CCl_4). Precursors containing both Si and C have also been investigated such as hexamethyldisilane ($C_6H_{18}Si_2$ or HMDS) methyltrichlorosilane (CH_3SiCl_3 or MTS) and dimethyldichlorosilane ($(CH_3)_2SiCl_2$). Propane and silane, C_3H_8 and SiH_4, are the most commonly used precursors for SiC growth and are the precursors used for the growth of 4H-SiC epitaxial films in this dissertation research.

As stated in the beginning of this chapter, the epitaxial films are grown to have specific doping concentrations depending upon the device application. The desired doping density may be achieved during the growth process by controlling the amount of precursors along with the addition of dopant gases. The dopants for SiC are aluminum (Al) and boron (B) for p-type conductivity and nitrogen (N) and phosphorus (P) for n-type conductivity. Typical dopant precursors are trimethylaluminum ($(CH_3)_3Al$ or TMA), diborane (B_2H_6), nitrogen gas (N_2), and phosphine gas (PH_3) [4]. Al is the most common p-type dopant because it has a low acceptor ionization energy, while N is the preferred n-type dopant over P because it has a higher probability to be incorporated into the lattice [4]. These dopants are incorporated into the Si or C lattice sites as substitutional

impurities. Al typically competes with Si and N competes with C for lattice sites (positions) during growth [35]. An inlet gas Si/C ratio is typically specified when growing SiC films. This ratio is the amount of moles of Si atoms to the amount of moles of C atoms in the gas mixture. For a low Si/C ratio, the incorporation of Al into the lattice is enhanced as its relative concentration in the gas mixture increases, resulting in a p-type layer. Likewise, for a high Si/C ratio, there is an ample supply of Si atoms. This enables N to occupy the C lattice sites which produces an n-type epitaxial layer. With the ability to control the doping of the epitaxial films, CVD is an excellent technique to dope various layers for specific device applications.

For control of the CVD process, knowledge of the gas flow dynamics, equilibrium thermodynamics, mass transport, and chemical kinetics is needed. Thermodynamics may determine the feasibility of the reaction to occur while kinetics determines the rate of the reaction [32]. These will be discussed separately in the following sections.

2.2 CVD Thermodynamics

Thermodynamic calculations are often used to provide insight into the CVD process [31-33]. The analysis can predict the feasibility of a CVD process chemistry and what gaseous species may be produced during the process. In order to obtain this information, data is needed such as the temperature and pressure of the system, as well as the reactant flow rates (which will be denoted as Q_i, where i denotes the i^{th} specie). The thermodynamic equilibrium state of a CVD system can be calculated for the identification of the condensed phases, partial pressures of all the gaseous species,

possible equilibrium deposition rates, and the theoretical reaction efficiency. It must be noted that the thermodynamic calculations are used as a guide for the CVD process as the calculations are performed under equilibrium conditions, while the actual CVD process is clearly not in equilibrium [32].

There are two ways to calculate thermodynamic equilibrium in CVD: the non-linear equations method using partial pressures of the species (see section 2.2.1) and the Gibbs free energy minimization method (see section 2.2.2) [31]. Both methods use the Gibbs free energy to evaluate the thermodynamics of CVD. The Gibbs free energy, G, is a thermodynamic state function which can be used to determine whether a reaction is likely to occur. The change in Gibbs free energy is the maximum amount of work obtainable for a reaction [36], given temperature and pressure remain constant. If the associated change in G, ΔG, is a negative value, the reaction will occur spontaneously. If ΔG is positive, then the reaction is not favorable (non- spontaneous). The system has reached equilibrium when ΔG is zero. If several reactions occur simultaneously, the most prominent reaction would be the one resulting in the lowest Gibbs free energy because it would be the most stable reaction [31]. However, this prediction is not always correct since the equilibrium thermodynamics does not consider the reaction kinetics, so care must be used when drawing conclusions from these calculations only [31].

2.2.1 Non-linear Equation Method

The non-linear equation method uses independent equations to express the partial pressures of each gaseous specie in the system. These may be expressed as the

equilibrium constants of each reaction in terms of partial pressure of each species, or as a function of the partial pressures. The total pressure of the system is found by the addition of all partial pressures [31]. This method uses the law of mass action to find the equilibrium constant of each reaction [33]. As an example, consider the following reaction,

$$v_a A + v_b B \leftrightarrow v_c C + v_d D \tag{2.1}$$

where v_i is the stoichiometric coefficient for each specie. The law of mass action can be described in terms of partial pressures, p_i, by [33]:

$$\frac{(p_c)^{v_c}(p_d)^{v_d}}{(p_a)^{v_a}(p_b)^{v_b}} = K_T \tag{2.2}$$

where K_T is an equilibrium constant of the reaction and is a function of temperature. The Gibbs free energy is related to the equilibrium constant by [37]:

$$\Delta G = -RT \log K_T \tag{2.3}$$

where R is the universal gas constant and T is the temperature.

The standard state free energy of formation, ΔG^o, is the change of free energy in the system obtained at the reactants and products standard states (i.e. when T = 298 K and P = 101 kPa) [38]. This may be used instead of ΔG and is found by adding the ΔG^o of each specie for each reaction [39]. For example, the reaction in equation (2.1) would have a total ΔG^o as follows:

$$\Delta G^\circ = \Delta G^\circ{}_D + \Delta G^\circ{}_C - \left(\Delta G^\circ{}_A + \Delta G^\circ{}_B\right) \tag{2.4}$$

Note the ΔG^o for elements in their reference state is conventionally set equal to zero [39], i.e. $\Delta G^o{}_{H2}$=0. The change in Gibbs free energy of a reaction is given by:

$$\Delta G_R = \Delta H_R - T\Delta S_R \tag{2.5}$$

where the subscript R stands for the reaction, ΔH_R (the change in enthalpy), is the change of energy in the form of heat, ΔS_R (the change in entropy), is disorder in the system and T is the temperature.

Equation (2.5) may also be written in the standard states as [39]:

$$\Delta G_R^\circ = \Delta H_R^\circ - T\Delta S_R^\circ \tag{2.6}$$

The enthalpy of the reaction may be calculated from the enthalpy of formations ΔH_f° [31], which is the heat absorbed or released in a reaction [39]. ΔH_f^o can be expressed by:

$$\Delta H_R^\circ = \sum \Delta H_f^\circ(\text{products}) - \sum \Delta H_f^\circ(\text{reactants}) \tag{2.7}$$

The standard heat of formation (i.e. ΔH_f^o at 25°C) for elements is equal to zero by convention. The standard entropy, ΔS_R°, may be found using a similar equation as equation (2.7), however, one must replace H with S.

Using the non-linear method, the equilibrium constant is found using equation (2.3). The Gibbs free energy may be found using equations (2.4) – (2.7), while the values of enthalpy and entropy are found from data tables [37]. Then, the partial pressures of each specie can be calculated by solving the equilibrium constant equation for all reactions, equation (2.2). This would leave n unknowns, with (n-1) equations. To solve for all the partial pressures in the system, another equation would be needed to make n equations with n unknowns, which is: the total pressure is equal to all the partial pressures of the species.

The equilibrium constant may be used to determine whether or not a reaction is feasible. The higher the equilibrium constant, the more thermodynamically feasible the reaction is [31]. Using this method, one must predict all of the appropriate reactions and

which species are significant and their phase for the reaction [33]. Clearly, it becomes quite tedious to calculate the equilibrium species concentrations when there are numerous reactions to evaluate; such is the case for SiC CVD.

2.2.2 Minimization of Gibbs Free Energy

Another method has been developed to predict the species concentrations at thermodynamic equilibrium during CVD growth. Using the free energy minimization method, equilibrium is reached when the Gibbs free energy reaches a minimum. In order to calculate the equilibrium concentration, the following equation is used [31,33,39]:

$$G = \sum_i n_i \mu_i = \sum_i n_i \left(\mu_i^\circ + RT \ln a_i\right) =$$

$$= \sum_i n_i \left(\mu_i^\circ + RT \ln\left(\frac{n_i}{N_g}\right)\frac{P}{P^\circ}\right) =$$

$$= \sum_{i=1}^{m} \left(n_i^{\,g} \mu_{ig}^\circ + n_i^{\,g} RT \ln\left[\left(\frac{n_i^{\,g}}{N_g}\right)\frac{P}{P^\circ}\right]\right) + \sum_{i=1}^{s} n_i^{\,s} \mu_{is}^\circ$$

or
$$G = \sum_{i=1}^{m} \left(G_{ig}^\circ + n_i^{\,g} RT \ln\left(\frac{P}{P^\circ}\right) + n_i^{\,g} RT \ln\left(\frac{n_i^{\,g}}{N_g}\right)\right) + \sum_{i=1}^{s} G_{is}^\circ \qquad (2.8)$$

where G is the Gibbs free energy of the system, $G_{ig}{}^o$ and $G_{is}{}^o$ are the free energy of formation of gaseous and solid species, n_i^g and n_i^s are the moles of gaseous and solid species, $\mu_{ig}{}^o$ and $\mu_{is}{}^o$ are the chemical potentials of gaseous and solid species which is the contribution of that substance to the total Gibbs energy of a mixture, N_g is the total moles in the gas phase, m is the number of gaseous species, s is the number of solid species, R is the universal gas constant, and P and T are the process pressure and temperature,

respectively and $P°$ is a standard pressure of 750 Torr. Finally a_i is the activity [31], which is the effective mole fraction. This is the partial pressure of specie *i* to the standard pressure of 750 Torr [37]. Activity, a_i, is therefore equal to 1 for pure solids [31].

The values of n_i must be found in order to minimize *G*, which is subject to the mass balance constraint [33]. Taking the mass balance relation where the number of atoms of a particular element are conserved:

$$\sum_{i=1}^{m} a_{ij}{}^{g} n_i{}^{g} + \sum_{i=1}^{s} a_{ij}{}^{s} n_i{}^{s} = b_j \tag{2.9}$$

where the number of atoms of element *j* in a molecule of species *i* is a_{ij}. For example, for the molecule C_3H_8, let *i*=1 and *j*=1 represent carbon, C, and *j*=2 represent hydrogen, H. Therefore, a_{11} = 3 and a_{12}=8. The total number of moles of the element *j* is b_j, *m* is the number of gaseous species, and *s* is the number of solid phase species.

The solution of the equilibrium state is found by minimizing the Gibbs free energy subject to the constraints of equation (2.9) [33]. Using free energy minimization, there is no need to predict the number of reactions which may take place in the reactor. This technique enables one to consider all possible species, without speculating which species are important and without determining the reactions of the system *a priori*.

2.2.3 Thermodynamic Simulations

Thermodynamic numerical calculations, based on the theory of the minimization of the Gibbs free energy just presented, were performed to predict the equilibrium concentrations of the chemical species in the USF CVD reactor. The calculations were performed using the NASA-Lewis Chemical Equilibrium Computations and Applications

(CEA) computer code [40]. This program uses the minimization of Gibbs free energy method to determine the composition of species in the system. An outline of how to use the program is given in Appendix A. Information about the software can be found in the literature [41,42]. Two thermodynamic state functions are required to determine the equilibrium compositions; in this case, temperature and total pressure were supplied. Along with the thermodynamic functions, *T* and *P*, the chemical reactants and their flow rates were input into the program. The species flow rates were to be specified in moles; however, since the pressure and temperature were constant, the volumetric flows were input into the program instead of the mole values. This was valid because the CVD process is assumed to follow the ideal gas law: PV = nRT. With the same system temperature and pressure, the volumetric flow is equal to the molar flow. Given the reactants, temperature and pressure of the system, the program calculated the possible species present for all phases (gas, liquid, and solid). Based on this information, one could predict the dominant chemical species of the process.

The input values for the calculations were based on typical process parameters for 4H-SiC epitaxial growth in the low-pressure horizontal reactor, which will be described in Chapter 3. The input gases were H_2-C_3H_8-SiH_4 and the total pressure was 150 Torr. The temperature range was chosen between 1500 and 2000 K for the reason that the growth of 4H-SiC typically takes place within a temperature range of 1800 - 1900 K. Figure 2.1 shows a simulation of the mole and mass fractions of the dominant computed species as a function of temperature. The input H_2 flow was 30 slm (standard liters per minute), C_3H_8 flow was 10 sccm (standard cubic centimeters per minute) and SiH_4 flow was 30 sccm giving a Si/C precursor flow ratio of 1.0.

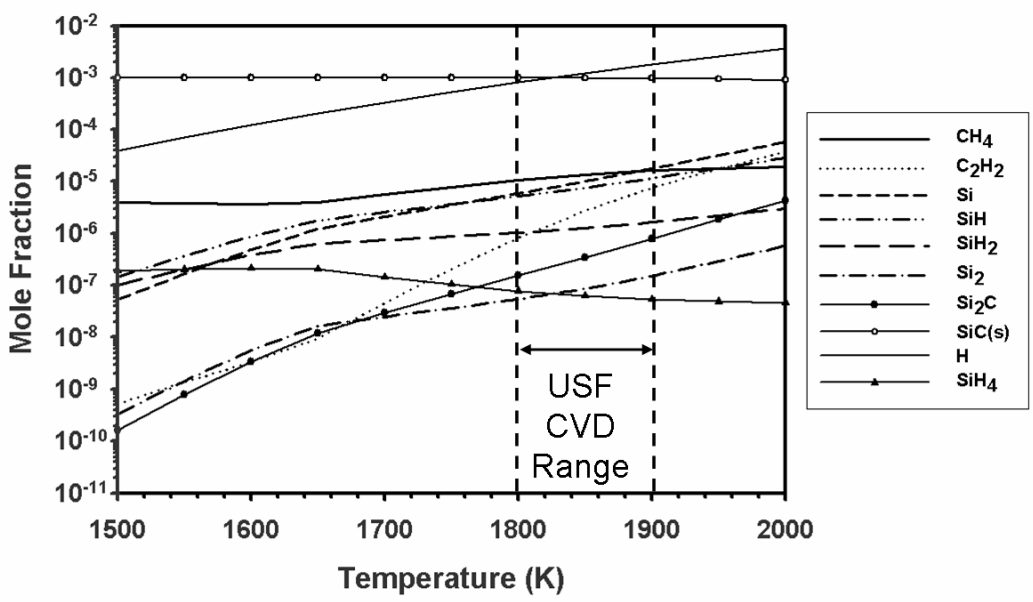

(a)

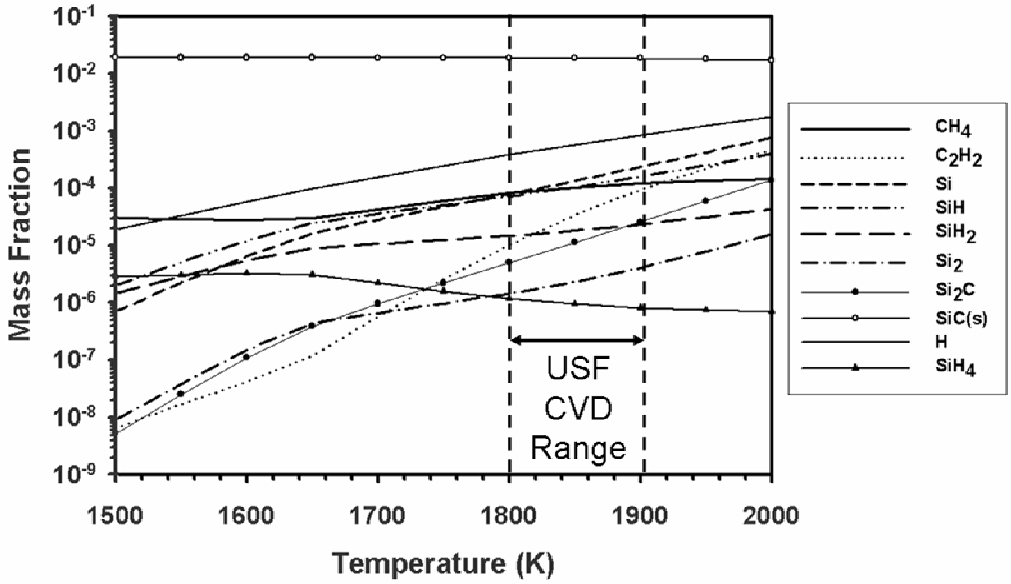

(b)

Figure 2.1 Thermodynamic predictions of chemical specie (a) mole fraction and (b) mass fraction as a function of temperature for the H_2-C_3H_8-SiH_4 system. Input parameters were P = 150 Torr, Q_{H2} = 30 slm, Q_{C3H8} = 10 sccm, and Q_{SiH4} = 30 sccm. The Si/C ratio was 1.0. The NASA CEA code was used to perform these simulations [40].

The mole and mass fraction of H_2 is higher than the other species in Figure 2.1 since it is the dominant chemical specie. However, it was excluded from the figure so that

the range of mole and mass fractions could be seen clearly. Atomic hydrogen has a higher mole fraction for temperatures beyond 1850 K, most likely due to the dissociation of hydrogen-containing molecules. As seen in Figure 2.1, the most dominant specie is solid SiC. The mole fraction of SiH_4 decreases with temperature, as expected, due to the dissociation of SiH_4. The C_3H_8 precursor is not seen on the figure as it has very low mole fractions at these high of temperatures. The mass fractions were computed to compare the thermodynamic simulations with simulations used to predict the mass fraction distribution of species within the 200 mm reactor (which are presented Chapter 5). The mass fractions have similar profiles as that of the mole fractions, as seen in Figure 2.1. The only difference is that there are order of magnitude differences between the mole and mass fractions because the molecular weight is taken into account for the mass fraction, while it is not for the mole fraction. For example the difference between the mass and mole fractions of C_2H_2 at each temperature is approximately 12.7. This difference, however, is not the molecular weight of C_2H_2. The reason the difference between mole and mass fractions is not the actual molecular weight of the specie is that when converting between the two fractions, the molecular weight of all species considered in the simulation is taken into account along with the molecular weight of the specific specie. From the thermodynamic simulations, the dominant species in the system are predicted to be as follows: CH_4, C_2H_2, SiH_2, SiH, Si, Si_2, Si_2C, SiC and H.

2.3 Kinetics

In order to interpret what is occurring in the CVD process, it is also necessary to study the chemically reacting gas flows [33]. It is important to study the reactions occurring at the surface which results in film deposition. In the gas above the substrate, homogeneous, i.e. gas phase, reactions take place, while at the surface, there are heterogeneous surface reactions (reactions occurring at the gas–solid interface) [33]. To accurately describe the CVD process, chemical kinetics is required.

The epitaxial growth of SiC depends on the surface mobility of atoms on the surface (adatoms) and the number of available growth sites [29]. A series of steps must occur for the deposition of epitaxial layers by CVD to take place, which are shown schematically in Figure 2.2. In step (1), gases enter the reaction tube in a bulk flow. In step (2), intermediate reactants are formed from dissociation of reactant gases. In step (3), the reactant gases diffuse through a gaseous boundary layer, of thickness δ, to the substrate. The boundary layer is a stagnant layer above the surface of the substrate. Adsorption of the species onto the surface occurs in step (4). In step (5), a heterogeneous surface reaction takes place, which results in the deposition of the film on the substrate. Finally, the by-products desorb from the substrate surface and then diffuse through the boundary layer back into the main gas stream where they exit the reactor, steps (6) and (7), respectively [31-33].

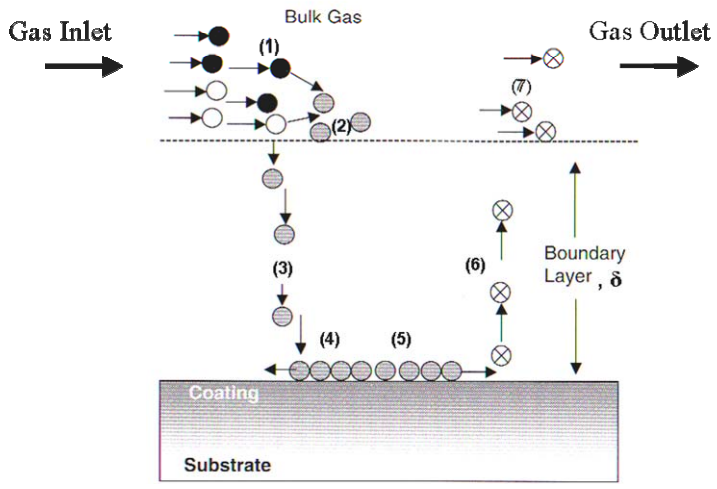

Figure 2.2 Schematic diagram of mechanistic steps which occur during the CVD process which are (1) Gas inlet, (2) dissociation of reactants, (3) diffusion of reactants to the surface, (4) adsorption of reactants to the surface, (5) heterogeneous surface reaction, (6) desorption of by-products, (7) diffusion of by-products back into the bulk gas [32].

2.3.1 Fluid Dynamics

In order to quantify the CVD growth process, the fluid dynamics of the system (which includes gases) must be investigated. For a CVD process, the fluid flow must be of laminar fashion to avoid intermixing of gas concentrations [43]. For example, when switching from a p-type dopant source to an n-type dopant source during growth to produce an abrupt pn-junction, one does not want the two dopant sources to intermix. If they do, then there will not be an abrupt junction [43]. In laminar flow, the fluid moves along straight, parallel paths in layers [44]. For turbulent flow, the particles move in all directions and it becomes difficult to follow the motion of individual particles. In order to provide an indication of the type of fluid flow, the Reynold's number, Re, is introduced, which is a dimensionless number and is shown in equation 2.11. For laminar flow, *Re*

must be below 2000; above this value the flow is turbulent [44]. Typically in a CVD process the *Re* number ~ 200 [43], which falls well inside the laminar flow regime.

When a fluid flows over a solid surface, the velocity at the surface is assumed to be equal to zero. The velocity increases from zero at the surface, to a maximum velocity, which is the bulk gas velocity. The 'boundary layer' is defined as the distance from the surface of the substrate to the maximum velocity of the bulk gas. With high velocities and laminar flow, the boundary layer, δ, can be thin and is proportional to the inverse of the square root of the Reynold's number, R_e [45]:

$$\delta = \frac{x}{\sqrt{\mathrm{Re}}} \tag{2.10}$$

where

$$R_e = \frac{\rho u x}{\eta} \tag{2.11}$$

and ρ is the mass density of the fluid, u is the flow velocity of the fluid, x is the distance along the susceptor in the flow direction, and η is the dynamic viscosity of the fluid. The kinematic viscosity, v, is related to the dynamic velocity by:

$$v = \eta / \rho \tag{2.12}$$

Note that the viscosity and density of the fluid changes with temperature.

The distance along the susceptor, x, may be replaced by the hydraulic diameter, d_h (which is 2 times the radius of the tube), for flow within in a circular tube. However, the flow is assumed to be across a plate since the area of focus is on the susceptor where the sample is placed.

A sketch of the boundary layer is shown in Figure 2.3. The velocity is initially constant, however, when the fluid comes into contact with the surface, a velocity gradient is generated, where the thickness of the gradient is the boundary layer, δ.

An estimation of the Reynold's number for the 200 mm reactor is approximately 300, which is well within the laminar flow regime. This was determined by using equation (2.11) and assuming hydrogen as the dominant gas since it has a much higher flow rate compared to the precursors. The velocity of the gas was found from the flow rate of H_2, 30 slm, divided by the area of the inlet. The distance along the susceptor for the calculation was 100 mm.

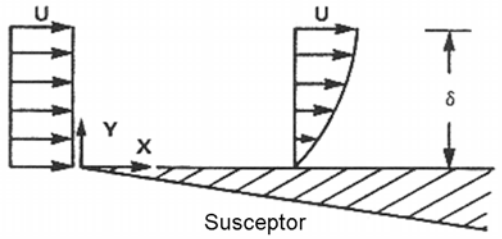

Figure 2.3 Sketch of boundary layer showing an initially uniform gas velocity. Once the fluid comes into contact with the surface, there is a velocity gradient with thickness, δ [33].

There are two types of regimes that CVD processes are typically classified into. One is "surface reaction" controlled and the other "diffusion" controlled CVD process [33]. The surface controlled regime, more commonly referred to as "reaction rate limited," is based on surface kinetics while the diffusion controlled regime, more commonly called "mass transport limited," is based on diffusion of the reacting species through the boundary layer. The determination between the two regimes depends on the slowest step for the deposition to occur, which is the overall rate controlling (or limiting)

step [32]. In the surface controlled regime, reactants easily diffuse to the surface, where an over abundant supply of reactants are available for the reaction. The rate of the surface reaction therefore depends on how fast the reaction can take place and not the availability of reactants. This regime typically occurs when the process pressure is low, producing large diffusion coefficients, and the surface temperature is low [33].

At higher pressures (small diffusion coefficients) and high temperatures, the growth process is governed by the "diffusion" regime. In this regime, if the reactants can diffuse to the surface, the surface reaction will occur quickly. The diffusion through the gas adjacent to the surface governs the rate of deposition. Diffusion is weakly affected by temperature compared to the surface reaction regime, therefore, the surface temperature does not play as strong a role in this regime until the reaction rate slows down and starts to limit the process [33]. Typically it is preferred to have the growth process controlled by diffusion, or mass transport [29], since the growth rate is not highly sensitive to temperature changes. To fully understand the CVD process, the fluid mechanics, chemical kinetics and thermodynamics must all be examined, preferably together. Until recently, this has been a daunting task but commercial software packages are now available for this purpose [46,47]. These will be described later in this chapter.

2.3.2 Mass Transport Limited Versus Surface Reaction Limited CVD

If the process is mass transport limited, it is typically the diffusion of reactants through the boundary layer that is limiting the rate of reaction [32]. Assuming there is a mixture of ideal reacting gases (although in the actual system it is not ideal) and a

concentration boundary layer, the diffusion of the species from the bulk gas to the surface is determined by Fick's Law [48]:

$$J = -\rho_i D_i \frac{d\omega_i}{dy} \tag{2.12}$$

such that J is the mass flux, ρ_i is the density of the species i, D_i is the diffusion coefficient of the specie i in the mixture, ω_i is the mass fraction of specie i and y is the direction perpendicular to the substrate surface. The negative sign shows that the initial substances are consumed.

The mass fraction, ω_i, is:

$$\omega_i = \rho_i \Big/ \rho \tag{2.13}$$

The flux may then be written as [33]:

$$J = D_i \frac{d\rho_i}{dy} \tag{2.14}$$

Since density is mass divided by volume and assuming an ideal gas, because the temperature is high and the pressure is low, the mass flux can be written in terms of pressure:

$$\rho = \frac{PM}{RT} \tag{2.15}$$

where M is the molecular weight of the specie and R is the universal gas constant. So the mass flux becomes

$$J = \frac{DM}{RT}\frac{dP}{dy} \tag{2.16}$$

Assuming pressure varies linearly across the boundary layer because we are assuming steady state conditions, equation (2.16) becomes:

$$J = \frac{DM}{RT}\frac{\Delta P}{\Delta y} = \frac{DM}{RT}\frac{\left(p_{ib} - p_{is}\right)}{\delta} \tag{2.17}$$

where p_{ib} is the partial pressure of specie i in the bulk gas, p_{is} is the partial pressure of specie i at the surface, and δ is the boundary layer thickness.

As seen from equation (2.17), for diffusion controlled deposition, the boundary layer thickness is inversely proportional to the mass flux, thereby affecting the ability for reactants to reach the surface to undergo the surface reaction. Note that when there is a higher velocity, due to constrictions of flow or by lower pressures, the boundary layer thickness decreases as predicted by equations (2.10) and (2.11). When the boundary layer decreases, the ability for the reactants to reach the surface should increase.

When reacting species are diffusing through the boundary layer, reactions may be taking place which are considered homogeneous gas phase reactions. Once the species reach the surface, they may adsorb to the surface, react with the surface, and become a film. This type of reaction is considered a heterogeneous surface reaction which will have a characteristic reaction rate [33]. Figure 2.4 shows a schematic diagram of the concentration gradient of reactants going from the bulk gas, through the boundary layer and approaching the solid film.

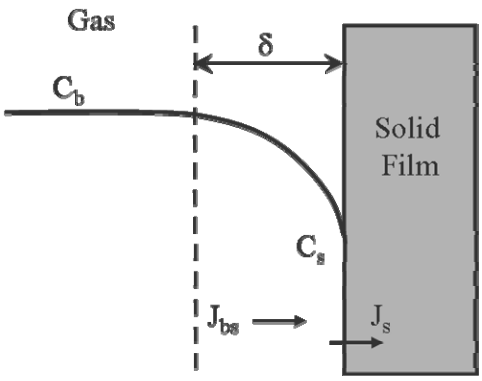

Figure 2.4 Schematic diagram of the growth process for CVD where C_b is the reactant concentration in the bulk gas, C_s is the reactant concentration at the surface, J_{bs} is the flux from the bulk gas to the surface, J_s is the flux at the surface and δ is the boundary layer. The solid line is the concentration gradient.

In Figure 2.4, C_b is the reactant concentration in the gas bulk phase, C_s is the reactant concentration at the surface, δ is the boundary layer, J_{bs} is the flux of reactants from the bulk gas to the surface, and J_s is the flux of reactants at the surface. The phenomena may be described in terms of a "mass transfer" coefficient. The flux of the reactants from the bulk gas to the surface may given by [32]:

$$J_{bs} = h_g\left(C_b - C_s\right) \tag{2.18}$$

where h_g is the mass transfer coefficient, which is used when the diffusion takes place across an interface and increases with increasing pressure and decreasing temperature.

Assuming first order kinetics, where the flux depends on the surface concentration to the first power, the flux at the surface is determined by [32,39]:

$$J_s = k_s C_s \tag{2.19}$$

where k_s is the surface reaction rate constant for the slowest surface reaction. For steady state conditions, the flux from the bulk gas to the substrate, J_{bs}, and the flux at the substrate, J_s, are equal. Therefore:

$$J_s = J_{bs} \tag{2.20}$$

Combining equations (2.18) and (2.19) gives:

$$k_s C_s = h_g \left(C_b - C_s \right) \tag{2.21}$$

which can then be written in terms of concentration at the surface by:

$$C_s = \frac{C_b}{1 + {k_s}/{h_g}} \tag{2.22}$$

From equation (2.22), if $k_s >> h_g$ (which means a low gas transport rate through the boundary layer), then C_s goes to zero and the system is mass transport limited. However, if $k_s << h_g$, then C_s approaches C_b. This indicates the process is surface reaction rate limited because the surface reaction is slow even though reactants are getting to the surface in sufficient time to feed the reaction. There is typically a linear relation between the deposition rate and the concentration of the silicon precursor. From this, the surface reaction rate constant may be found by [31]:

$$k_s = {V_g}/{x} \tag{2.23}$$

where V_g is the growth rate and x is the silane mole fraction in the gas mixture. The growth rate is the thickness of the film divided by the time of growth.

The activation energy, E_A, is the energy needed for a chemical reaction to occur. This energy may be used to determine which type of regime (mass transport limited or surface reaction limited) the process is in and, ideally, to improve the process. It may be found by using the Arrhenius equation [39]:

$$k_s = A e^{-\frac{E_A}{RT}} \tag{2.24}$$

where A is the pre-exponential factor, R is the universal gas constant, T is the temperature and k_s is the rate constant. By plotting log k_s vs. 1/T, the activation energy and pre-exponential factor may be found as the slope and intercept, respectively. When the growth rate increases with increasing temperature (in the low temperature region) according to the Arrhenius equation, the process is deemed to be surface reaction limited. However, when the growth rate varies little with increasing temperature (in the high temperature region) according to the Arrhenius equation, the process is mass transport limited.

2.4 Reactor Hardware

The research for this dissertation was performed using two different horizontal hot-wall reactors which were of two different sizes. The first reactor had an inside tube diameter of 75 mm and it will be referenced as the "75 mm reactor". This reactor was suitable for epitaxial growth, however, there was one drawback to the reactor design. It was only able to accommodate 20 mm diameter samples. In order to grow on larger substrates, the reaction tube was enlarged to 200 mm in diameter. This reactor will also be designated by the inside tube diameter size, i.e. the "200 mm reactor". With the 200 mm reactor, substrates up to 100 mm in diameter are capable of fitting into the reactor. The hardware and components of these reactors are discussed in the following subsections.

2.4.1 75 mm Hot-wall System

Originally, the 75 mm reactor was a horizontal atmospheric-pressure cold-wall reactor. The quartz reaction tube was surrounded by a cooling water jacket. Details of the cold-wall reactor are given in references [9,49]. With the cold-wall design, there was a large temperature gradient between the susceptor and the water-cooled quartz. In order to achieve a more uniform temperature distribution in the direction perpendicular to the susceptor length, the 75 mm reactor was converted from a cold-wall to a hot-wall configuration by redesigning the hot-zone. Figure 2.5 shows a sketch of the USF 75 mm hot-wall SiC CVD reactor configuration.

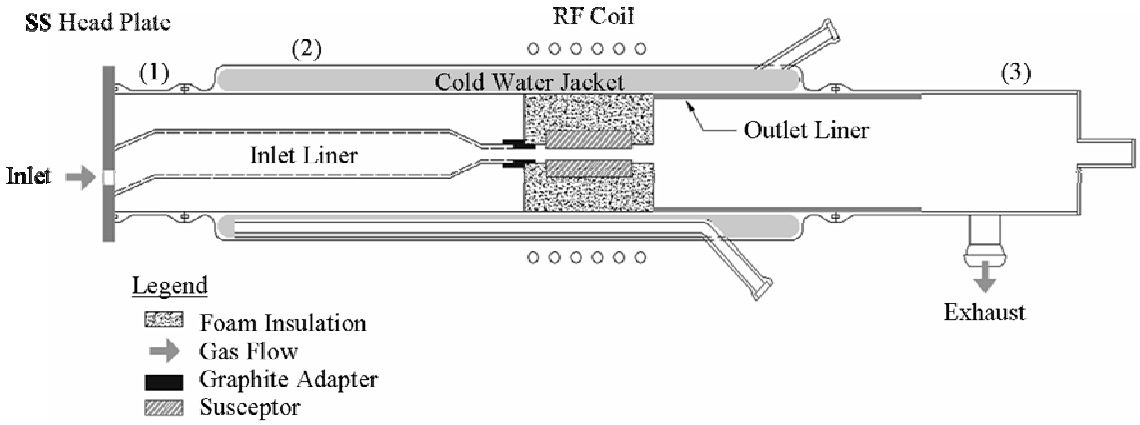

Figure 2.5 Sketch of the 75 mm horizontal hot-wall reactor including graphite foam insulation, susceptor, graphite adapter, RF coil, gas inlet liner, ss head plate and cold-water jacket. (1) Denotes the quartz adapter, (2) denotes water-cooled quartz reaction tube, and (3) denotes the quartz end-cap. Sketch provided by I. Haselbarth, University of South Florida.

The total length of the 75 mm hot-wall reactor was 900 mm. The reactor was separated into three parts, as indicated by numbers in Figure 2.5; (1) a quartz adapter, (2) a water-cooled quartz reaction tube, and (3) a quartz end-cap. The quartz adapter was attached to a stainless steel head plate, using an o-ring (viton) and a clamp. The stainless

steel head plate was fixed to the reactor housing and had a VCR to conflat inlet port from which the gases were injected into the reaction tube. The quartz end-cap was connected to the exhaust by a 50 mm (outer diameter) ball and socket joint. The end-cap had a quartz pyrometer view port which was used to focus the pyrometer onto the susceptor to read the temperature. The view port had an extended shape to prevent parasitic reaction by-product deposition, which would give inaccurate temperature readings. The reaction tube was inserted between the quartz adapter and end-cap, and sealed with viton o-rings using bake-o-lite clamps. The reaction tube and end-cap were supported by bake-o-lite stand-offs to reduce stress at the reaction tube connections caused by the weight of the tube. With this set-up, the reaction tube could be easily removed for cleaning purposes. The samples were loaded by removing the clamps and detaching the end-cap. As seen in Figure 2.5, the gases entered the quartz reaction tube from the left and exited to the right were they were exhausted to a scrubber. A specially designed quartz inlet liner directed the gases from the inlet port into the susceptor slot. A SiC-coated adapter was placed between the quartz liner and the susceptor to provide a temperature transition which reduced thermal wear of the quartz liner. Since the hot-wall reactor was converted from a cold-wall reactor, the cooling-water jacket surrounding the quartz reaction tube was still present and used as an extra safety precaution.

With the hot-wall design, the substrate was surrounded by a graphite susceptor which consisted of a bottom part with integral side-walls, and a top, or ceiling, part. Figure 2.6 shows sketches of the susceptor and foam insulation. The only openings to the susceptor were at the inlet side for gases to enter and at the outlet side for the gases to exit. The top part of the susceptor was SiC coated dense graphite while the bottom was

TaC coated dense graphite. The coatings were used to reduce chemical etching of carbon during growth, impurity out-diffusion and provide a longer life span of the susceptor. The bottom was TaC coated to reduce the nucleation of SiC on its surface. The top portion of the susceptor was not TaC coated, as particles would tend to drop from the ceiling onto the sample since the particles do not adhere well to TaC. With the SiC coating, the particles nucleate on the surface of the ceiling. The particles, however, do not tend to fall onto the substrate surface unless there is too much buildup of particles on the surface. Another reason the top part of the susceptor was SiC coated was that the emissivity of SiC does not vary over time. However, the emissivity of TaC changes because SiC deposits on the surface. The emissivity of SiC is ~ 0.8 [50], while that of TaC is ~ 0.3 [51]. The higher emissivity of SiC provides more accurate pyrometer readings because a higher amount of radiation is emitted from SiC compared to TaC. Also, the smooth surface of the TaC reduces the accuracy of the pyrometer readings. Therefore, the top portion of the susceptor was SiC coated.

The susceptor was enclosed in porous graphite foam which acted as both a support as well as thermal insulation. Ar flow was established outside of the liner to provide additional thermal insulation for the susceptor. The susceptor and foam insulation comprise the 'hot-zone' of the reactor as this is the heated area of the system. The graphite susceptor was heated by radio frequency (RF) radiation by an RF coil that was wrapped around the reaction tube. This design essentially provided an isothermal environment, however, there were still temperature gradients along the flow direction of the susceptor. In the hot wall reactor, the amount of power needed to achieve a specific temperature is lower compared to the cold-wall reactor [43]. In a cold-wall reactor,

radiation losses are higher than in a hot-wall reactor due to the susceptor not being insulated. Lower radiative losses in a hot-wall reactor are achieved by using the porous graphite foam insulation. Not only is there more uniform heating within the hot-wall reactor, there is also a higher cracking efficiency of reactants with this design [43,52].

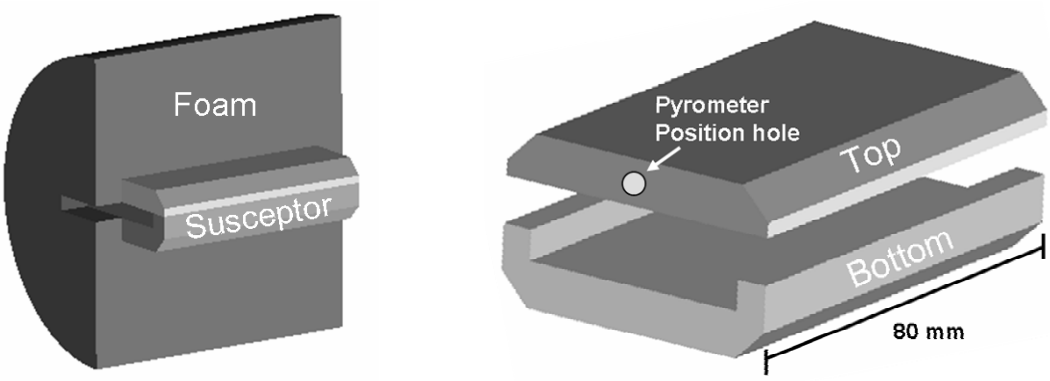

(a) (b)

Figure 2.6 Sketches of the 75 mm hot-wall reactor's (a) susceptor, placed inside graphite half of the foam insulation and (b) susceptor top and bottom portions. The width and length of susceptor were 50 and 80 mm, respectively, and the thickness of the susceptor top and bottom were 15 mm. The pyrometer position hole is where the infrared pyrometer was focused. Sketches provided by I. Haselbarth, University of South Florida.

The temperature of the susceptor was estimated by focusing an infrared pyrometer at a machined recess, denoted as "pyrometer position hole" in Figure 2.6(b), in the top part of the susceptor. The temperature of the substrate was estimated by performing Si melt tests. This was accomplished by placing a piece of Si on top of a SiC substrate, which was itself placed onto the graphite susceptor. The test consisted of heating the susceptor until the Si was observed with the naked eye to melt. This temperature was recorded and compared to the actual melting temperature of Si (1410 °C). The difference between the two temperatures was used to control the growth temperature during all subsequent CVD experiments. This was done using the following equation:

$$T = T_{pyrometer} - \Delta T \quad (2.25)$$

where T is the temperature desired, $T_{pyrometer}$ is the pyrometer temperature reading, and ΔT is the temperature difference between the melt temperature of Si (1410 °C) and the temperature reading of the pyrometer at the time of Si melt during the melt test. For example, if the Si melted at a pyrometer reading of 1310 °C, and since the true melting temperature of Si is 1410 °C, then the ΔT, the temperature error, is -100 °C. Therefore, when performing experiments with a desired growth temperature of, say, 1560 °C, the set point temperature should be 1460 °C due to the temperature difference between the pyrometer reading and the actual temperature. Note that the melt test method is used only as an approximation of the actual temperature. Since the melt temperature varies for different pressures and H_2 flow rates, the temperature error, ΔT, is a function of the pressure and H_2 flow rate. To improve the accuracy of the temperature set point, melt tests were conducted for specific process flows and pressures, for each hot-wall configuration used. In addition, whenever the hot-zone was changed, the melt test was performed to optimize the temperature accuracy.

In order to supply the process gases to the CVD system, a gas handling system was used. The gases (H_2, C_3H_8, SiH_4, N_2, Ar, HCl and CH_3Cl (methyl chloride)) were each fed separately from their respective gas bottles, through welded stainless-steel lines into a gas manifold, where the gases were distributed through individual gas mass flow controllers (MFC's). The gas flows were controlled with the MFC's and dual actuated pneumatic valves. The valves were controlled at the CVD reactor operator control panel. The reactor control system is detailed in M. Smith's Master's thesis [49]. The gases could be directed into the reactor, or they could be directed to a vent. The vent enabled gases to

be purged without entering the reaction tube if necessary. The SiH_4, HCl, and methyl chloride (CH_3Cl) lines each had the option to flow Ar gas through the lines and out to the vent. This option was implemented to purge the lines of any moisture or air that may have seeped into the lines after reactor shutdown. Therefore, the lines were purged at the end of each day and backfilled with Ar. The H_2 was fed into a palladium diffusion cell purifier before entering the gas manifold to purify the gas beyond VLSI grade (< 1ppb of O_2, H_2O, CO, CO_2, N_2 and all hydrocarbons [53]).

Multiple sensors were incorporated within the system for safety purposes. When a sensor was activated, the system would shut down by shutting down all process gases and the heating source and Ar would be purged through the system. The different sensors monitored the presence of H_2 and HCl gas, cooling water flow, and the security of the chamber door lock. In addition, an emergency override button was installed which allowed the operator to shut down the process at any desired moment. The safety sensors were also incorporated into the 200 mm hot-wall system, which is detailed in the next section.

2.4.2 200 mm Hot-wall System

Although modifications were made to the hardware, the 200 mm horizontal hot-wall CVD reactor was similar to the 75 mm reactor in the basic design of the hot-zone. Figure 2.7 shows a sketch of the reaction tube and its components. Like the 75 mm reactor, a gas inlet liner was used to guide the process gases into the slot in this susceptor via a SiC coated graphite adapter which was placed between the liner and the susceptor.

The susceptor was again surrounded by porous graphite foam insulation and was made of two molded parts. The reaction tube was a single wall tube, i.e. no cooling jacket, which was placed between two stainless-steel plates, one at the front (gas inlet) end and one at the back (gas exhaust) end. An exhaust port was built into the back plate. In order to prevent the quartz tubing from cracking at the ends when in contact with the stainless-steel plates, o-rings were placed in between the quartz and the plates. The reaction tube was sealed by the compression of viton o-rings by steel flanges, denoted as (1) in Figure 2.7. The stainless-steel plates were water cooled and cooling fans were directed on them to prevent excessive heating. The steel back plate (denoted as (2) in Figure 2.7) also had a hinged door (denoted as (3) in Figure 2.7) to allow access into the reaction chamber for loading/unloading of samples and cleaning of the reaction tube. The door had an Ar-purged stainless steel tube with a quartz view port (denoted as (4) in Figure 2.7) attached which served as the pyrometer window. The temperature of the susceptor was again estimated using the Si melt test procedure outlined in Section 2.4.1. Unlike the 75 mm reactor, the 200 mm reactor did not have a water-cooling jacket built around the reaction tube. This was not needed as the reactor design was meant to be a hot-wall system only, which does not require additional reaction tube cooling.

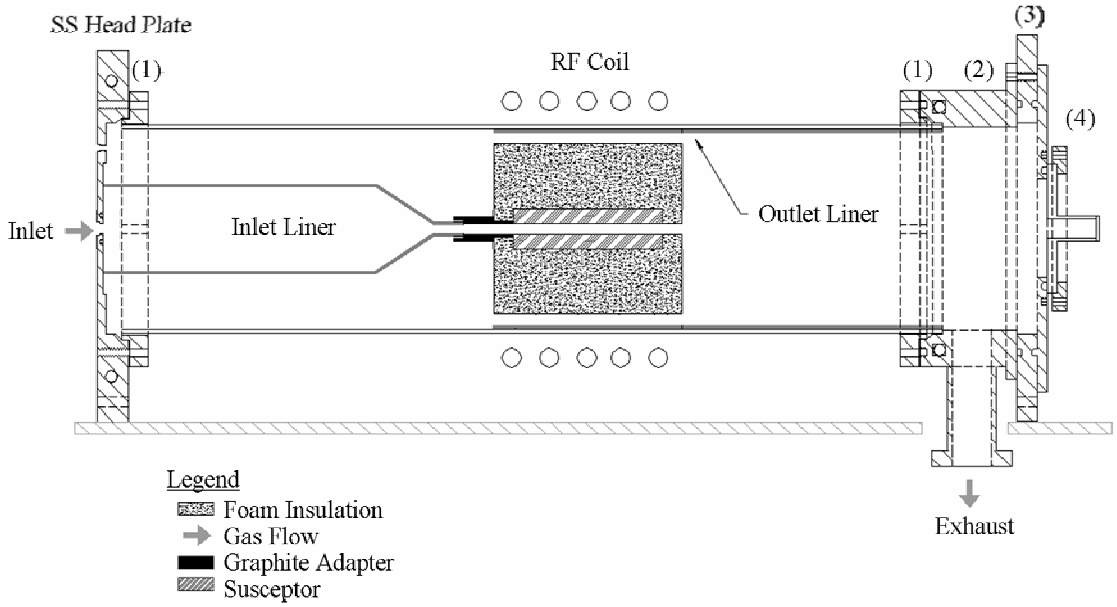

Figure 2.7 Sketch of the 200 mm horizontal hot-wall reactor including head plate, foam insulation, adapter, RF coil, inlet and foam liners, drum (back plate). (1) Denotes steel flanges, (2) denotes back plate, (3) denotes hinged door, and (4) denotes view port. Sketch provided by I. Haselbarth, University of South Florida.

The susceptor for the 200 mm reactor was similar to that of the susceptor for the 75 mm reactor shown in Figure 2.6, except the dimensions were larger. The width and length of the susceptor were 95 and 150 mm, respectively, and the thickness of the susceptor's top and bottom parts were 15 mm. The distance from the bottom of the susceptor to the ceiling was 10 mm. This susceptor also consisted of a top and bottom part; the top being SiC coated dense graphite and the bottom being TaC coated dense graphite. There was a machined hole in the top portion of the susceptor to provide a more isothermal environment for the pyrometer readings. A cross-sectional sketch of the hot-zone is shown in Figure 2.8.

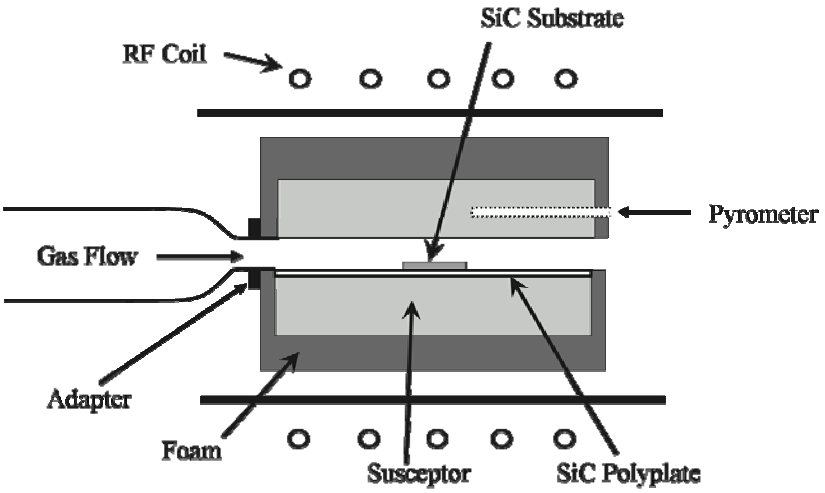

Figure 2.8 Cross-section schematic drawing of 200 mm horizontal hot-wall CVD reactor hot-zone, showing gases entering on the left and exiting the right. The top part of the susceptor has a machined hole for pyrometer readings. The inlet gases enter through a quartz tube which guides the gases to the susceptor.

Note that a polycrystalline plate was loaded into the growth zone, as shown in Figure 2.8. A few different types of polycrystalline plates with machined recesses were used to accommodate samples of different sizes as shown in Figure 2.9. The dimensions of the polycrystalline plates and the recesses are detailed in the figure. The depth of each recess is 0.5 mm (typical 4H-SiC substrates have a thickness of 0.4 mm). The use of the polycrystalline plates allows easy loading/removal of the sample and enables repeatable sample placement from growth run to growth run.

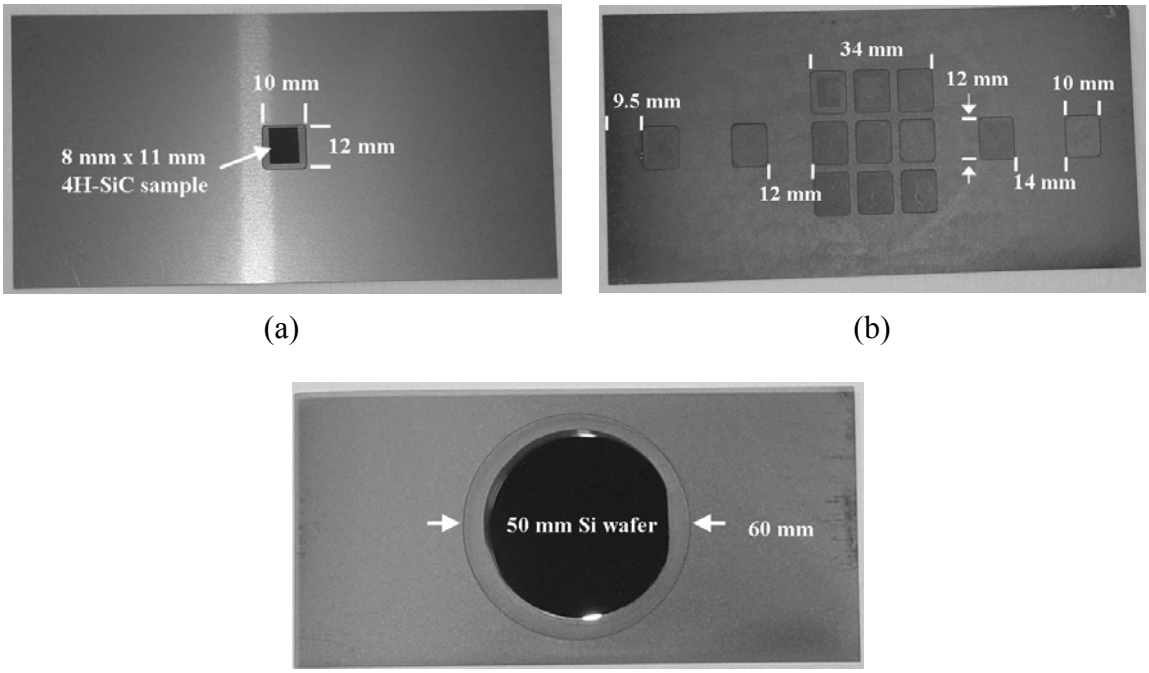

(a) (b)

(c)

Figure 2.9 SiC polycrystalline plates with (a) one 12 mm x 12 mm recess, (b) thirteen 10 mm x 12 mm recesses, and (c) one 60 mm diameter recess. The total length and width of each polycrystalline plate is 145 mm and 73 mm, respectively, which roughly corresponds to the dimensions of the bottom portion of the susceptor.

The foam insulation was placed inside a liner tube, which acted as a sacrificial quartz liner. The liner prevented the reaction tube from getting worn down due to the reaction between the graphite foam and the quartz tube. When the foam was heated in the 75 mm system, the quartz tube started to vitrify. With the sacrificial liner included into the 200 mm reactor design, the reaction tube remained intact without damage from the foam.

2.5 Computational Fluid Dynamic (CFD) Simulations of the 200 mm Reactor

The gas flow velocity distribution for the 200 mm horizontal hot-wall CVD reactor has been simulated and is presented in this section. The simulations are needed to validate any design changes to the hot zone so that uniform deposition can be realized across a 50 mm wafer. The program used to perform the simulations was Femlab [54], which is a computational fluid dynamics (CFD) simulation software package that has been used throughout this work [49]. The velocity profile is based on the equation of motion (momentum balance) and the equation of continuity (mass balance), which are [55]:

$$\rho(u\cdot\nabla)u = \nabla\cdot\left[-PI+\eta\left(\nabla u+(\nabla u)^{*}\right)-\left(2\eta/3\right)(\nabla\cdot u)I\right] \tag{2.26}$$

and

$$\nabla\cdot(\rho u)=0 \tag{2.27}$$

where ρ is the mass density, u is the gas velocity vector, P is the system pressure, I is the identity matrix (diagonal matrix with 'ones' on the main diagonal and 'zeroes' everywhere else), η is the dynamic viscosity, and superscript * identifies the transpose vector.

In order to perform the simulations, the reactor geometry, carrier gas and boundary conditions of the system must be specified. The reactor geometry used for the CFD simulations was shown in Figure 2.7. The boundary conditions specified for the simulations were zero velocity at all surfaces except at the inlet and exhaust outlet ports. The pressure boundary condition was set to the process pressure of 150 Torr at the exhaust, since the pressure in the system is set downstream of the process. The boundary

condition at the gas inlet port was set to the maximum velocity [55], which was 30 m/s, as determined by:

$$u_{\max} = 2 * u_{avg} \tag{2.28}$$

where u_{max} is the maximum gas velocity and u_{avg} is the average gas velocity.

The average gas velocity is found by:

$$u_{avg} = Q/A = Q/4\pi r^2 \tag{2.29}$$

where Q is the flow rate of the gas, A is the area of the reactor where the gas enters, and r is the radius.

The gas enters the inlet from a ¼" stainless steel VCR fitting; therefore, the area was calculated based on the area of the ¼" tube. The gas designated for the simulations was H_2, with a flow rate of 30 slm, since the carrier gas has a much higher concentration compared to the precursors. The temperature was set to 1565 °C. The gas velocity simulations are shown in Figure 2.10. The polycrystalline plate was included in the reactor geometry. The plate is the entire length of the susceptor and is 1 mm thick. Simulations were also performed without the polycrystalline plate, which resulted in no substantial difference between the two velocity distributions.

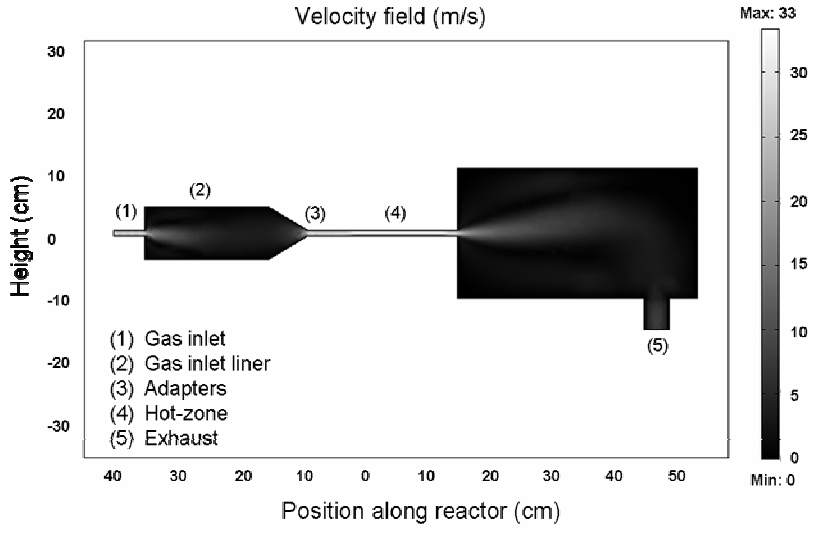

(a)

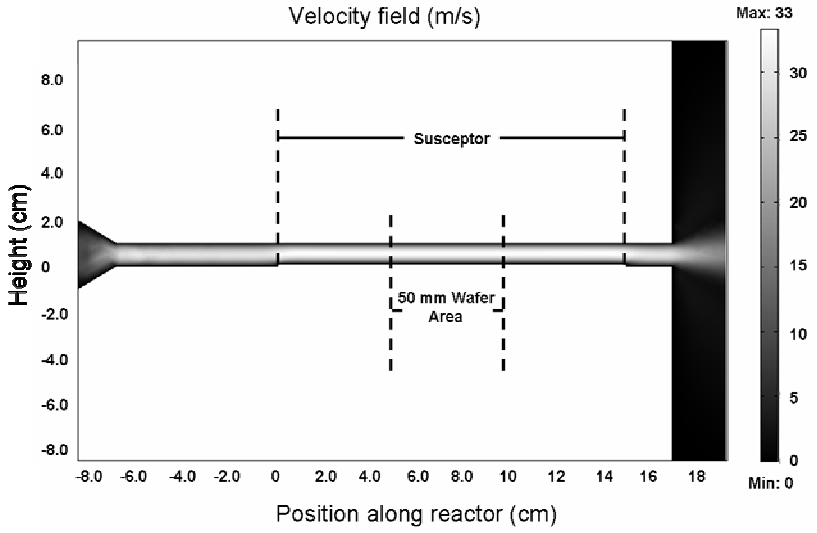

(b)

Figure 2.10 Gas velocity distribution for the 200 mm hot-wall reactor showing (a) the entire reactor cross-section and (b) an enlarged area of the hot-zone with the 50 mm wafer area and susceptor indicated. The conditions for the simulations were Q_{H2} = 30 slm, P = 150 Torr, and T = 1565 °C and zero velocity for all boundaries except inlet gas flow and outlet pressure. The simulations were performed using Femlab [54].

As seen in Figure 2.10, the gas velocity along the gas flow direction remains constant over the 50 mm wafer length. This indicates that the reactants should diffuse to

the surface at approximately the same rate since the velocity is uniform. Velocity profiles were also computed at specific distances along the susceptor and the maximum velocities were plotted versus distance. This plot is shown in Figure 2.11.

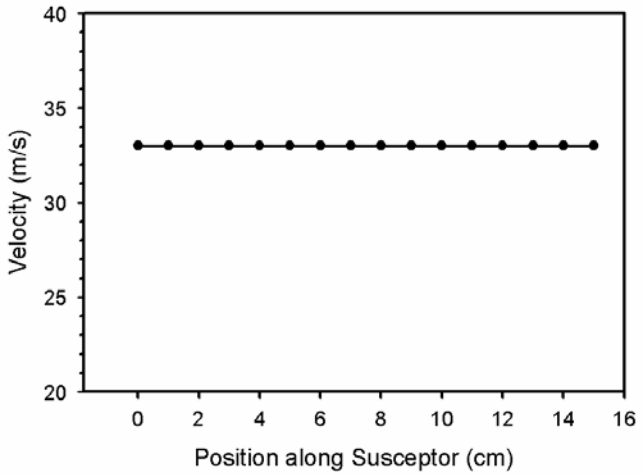

Figure 2.11 Velocity profile of the maximum gas velocity along the 200 mm hot-wall susceptor. The gas was H_2 with a flow of 30 slm, T = 1565 °C, and P = 150 Torr.

As seen from the velocity profile in Figure 2.11, the maximum velocity remains constant along the susceptor. With the high H_2 gas flow of 30 slm and the narrow area for the gases to flow, the velocity is at a maximum throughout the entire susceptor region for this particular susceptor design. Therefore, a linear boundary layer is predicted throughout this area. The results from the CFD simulations will be compared to the experimental results within the 200 mm hot-wall reactor in the following chapter. (In the next chapter, it will be shown that due to severe process issues, the susceptor was redesigned.

2.6 Summary

Deposition of SiC by means of CVD has been discussed and the theoretical underpinnings of this method have been reviewed in this chapter. Many different aspects must be considered so that predictions can be made which is helpful during CVD process development. In order to determine which chemical species may be present in the system, the minimization of Gibbs free energy method was selected as the individual reactions need not be assumed *a priori*. Simulations were performed using the NASA CEA algorithm to determine the most dominant species in the SiC CVD reaction system studied during this dissertation work, and were predicted to be H, CH_4, SiH, SiC(s) and Si.

The design of the 200 mm hot-wall reactor was similar to that of the 75 mm reactor hot-wall design which had been implemented before this dissertation research was initiated. The quartz reaction tube for the 200 mm reactor, however, was designed without a cooling water jacket and changes to the glass-to-metal seals were made to improve system reliability. The gas velocity distribution within the 200 mm hot-wall reactor was predicted using a 2D CFD simulation tool called Femlab. The predictions indicated that the velocity remained constant along the susceptor. The growth of 4H-SiC epitaxial layers in both hot-wall reactors will be presented in the following chapter.

CHAPTER 3

4H-SIC EPITAXIAL GROWTH EXPERIMENTS

The reactors used during this dissertation research work were horizontal hot-wall CVD reactors capable of process temperatures up to 1850°C. The typical growth temperature was from 1560°C to 1585°C. This chapter describes the development of the 4H-SiC epitaxial process using two reactor configurations: a 75 mm tube and a 200 mm tube. The latter is capable of growth on 100 mm substrates, however at the time of this work, the reactor was configured for 50 mm substrates, as that was the most common wafer size commercially available.

3.1 Characterization Techniques

Before going into the experimental development of the 4H-SiC growth process, the characterization techniques used will be described. To develop the growth process, characterization of the 4H-SiC films was needed to determine the morphology, thickness, doping, and structural quality of the material. The surface morphology and thickness were analyzed using a Hitachi S-800 Scanning Electron Microscope (SEM). The thickness was found by cleaving the samples and looking at the cross-section of the epitaxial layer using the SEM. The surface roughness of the films was measured using a Digital Instruments Nanoscope Dimension 300 Atomic Force Microscope (AFM). The

tool was used to determine whether the films had any surface defects such as step-bunching, which are large steps on the surface which occurs when atomic steps combine [34], or 3D features. The structural quality was analyzed using a Phillips Analytical X'pert Pro X-ray Diffraction (XRD) System. The film quality was assessed based on FWHM values of X-ray rocking curves of the (0004) diffraction peak. The electrical characteristics of the epitaxial films were analyzed by performing current-voltage (I-V) measurements, using a HP 4145B Semiconductor Parameter Analyzer and capacitance-voltage (C-V) measurements taken using a HP 4280A C-V meter. The net carrier concentration of the films was found using these two techniques. Finally, select samples were sent to the University of Pittsburgh where they were analyzed using low temperature photoluminescence (LTPL) (Professor W. J. Choyke's research group). The characterization tools used during this research are detailed in Appendix B.

3.2 75 mm Hot-Wall Reactor Experiments

The growth of 4H-SiC epitaxial films was initially developed in the 75 mm cold-wall reactor capable of atmospheric pressure (AP) growth. The details can be found in M. Smith's Master's Thesis [49]. Growth could be carried out on a full 50 mm wafer in the cold-wall reactor system. The system was then modified to grow epitaxial films at low pressure (LP) [49]. The reactor was then modified with a hot-wall insert to realize a hot-wall design (refer to Figure 2.5 for reference). Due to the size constraints, the hot-wall reactor was capable of holding a maximum sample size of 2 cm in diameter. The 4H-SiC

process for the hot-wall reactor was established starting with the process schedule developed for the cold-wall design, which is given in Table 3.1.

Table 3.1 4H-SiC baseline process in the 75 mm LP horizontal cold-wall reactor.

Pressure (Torr)	Temperature (°C)	Q_{H2} (slm)	Q_{SiH4}* (sccm)	Q_{C3H8}** (sccm)	Si/C	Growth rate (μm/h)
150	1550-1580	10	120	80	0.33	2.0

* 2% in H_2; ** 3% in H_2

Secondary electron microscopy (SEM) micrographs from a representative sample for the 4H-SiC growth process in the horizontal hot-wall 75 mm reactor are shown in Figure 3.1. The morphology of the film was observed to be smooth and specular. A typical growth rate for this process was approximately 16 μm/h. By comparison, growth rates presented in the literature for horizontal hot-wall reactors operating at similar temperatures, around the time of development of the 16 μm/h growth process in the 75 mm hot-wall CVD reactor (late 2003), were between 5 and 20 μm/h [19,56]. The morphology of a film from reference [19] was very similar to the morphology of a typical sample shown in Figure 3.1.

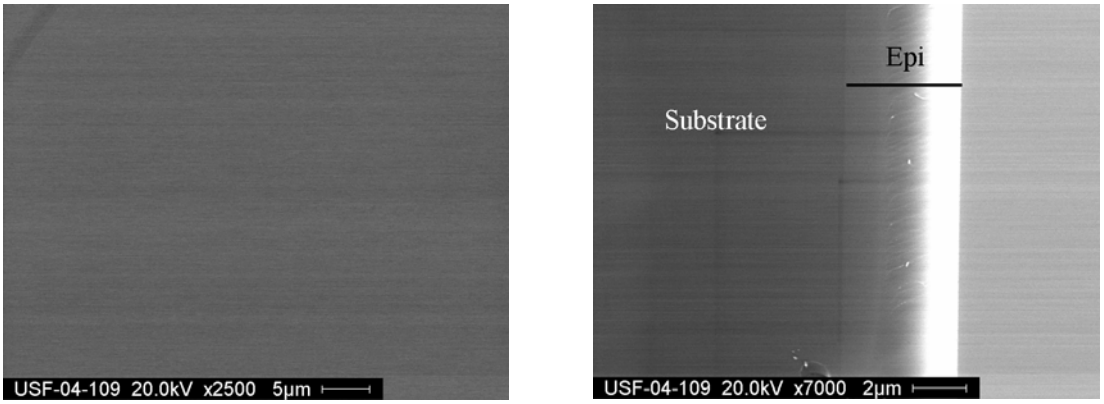

(a) (b)

Figure 3.1 4H-SiC epitaxial film grown in the 75 mm LP horizontal hot-wall reactor for 15 min. (a) Plan-view SEM micrograph showing a smooth, specular film surface, and (b) cross-section SEM micrograph of cleaved edge showing film thickness of ~4.3 µm, yielding a V_g ~ 17 µm/h (t = 15 min).

In order to grow films on 50 mm wafers, and potentially up to 100 mm in diameter, the area of the reactor needed to be increased. The reactor was thus scaled-up to allow for the possibility to accommodate larger samples. The development of the growth process in the 200 mm reactor is detailed next.

3.3 200 mm Reactor Process Development

The hot-wall hot-zone insert (graphite susceptor and insulating foam) were scaled-up in size from the 75 mm hot-wall reactor to permit growth on 50 mm substrates (i.e., the 200 mm reactor). The foam was originally designed with a cylindrical geometry to fit the inside diameter of a sacrificial quartz liner (a quartz tube cut to match the hot-zone length), as shown by the sketch in Figure 3.2(a). With the full circular cross-section foam insulation design, there were RF impedance matching issues which prevented the RF generator from turning on (it was believed that the coil inductance was too large and

beyond the tuning range of the Ameritherm L-80 RF Generator [57]). The foam geometry was re-designed by shaving the mass of the cylindrical foam into the shape shown in Figure 3.2(b), which allowed the RF generator to be able to match the load impedance. The foam design in Figure 3.2(b) was used for the thermal insulation of the 200 mm reactor and all subsequent process development was conducted with this design.

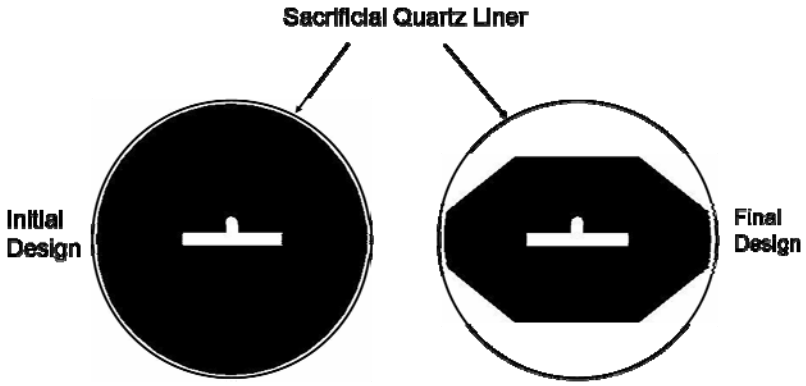

Figure 3.2 Sketch of insulating foam cross-sections for the 200 mm reactor with (a) initial circular geometry and (b) modified design to enable RF coupling of foam and susceptor.

Two different susceptor designs were explored in the 200 mm hot-wall CVD reactor. The first version of the susceptor had the same design as the one used in the 75 mm hot-wall reactor. This susceptor had a flat ceiling and was essentially a scaled-up replica of the 75 mm reactor susceptor. It was quickly determined that in the new 200 mm tube design, the susceptor needed to be modified due to precursor depletion at the inlet to the hot-zone. The modified susceptor had an angled ceiling intended to reduce the depletion at the inlet. The experimental growth process developed using the flat and angled ceiling designs is described in the next section.

3.3.1 Flat Ceiling Susceptor Design

The initial design of the 200 mm hot-wall reactor was based on the 75 mm hot-wall reactor, which was described earlier in Chapter 2, Section 2.4.2. Replicating the susceptor design from the smaller reactor, the susceptor originally had a flat ceiling as shown in Figure 3.3.

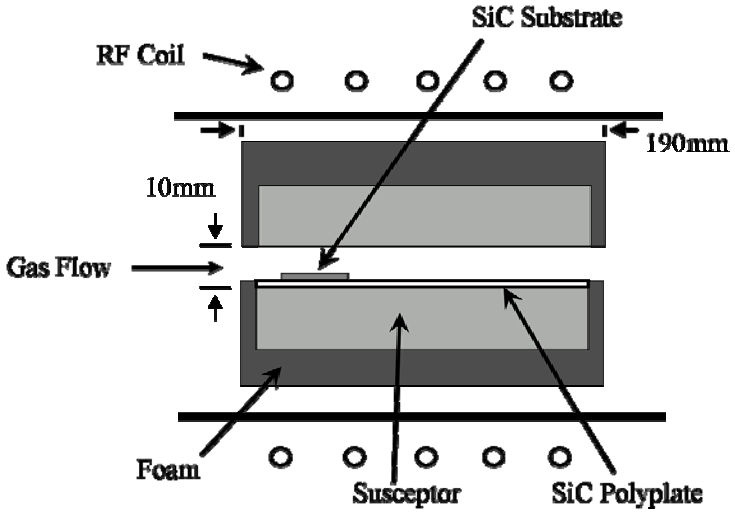

Figure 3.3 Cross-section sketch of the hot-wall CVD reactor hot-zone including graphite foam, flat graphite susceptor, SiC polycrystalline plate (SiC polyplate), RF coils, and SiC substrate.

The flat ceiling design in the 75 mm reactor produced a uniform deposition across the hot-zone. However, the flat ceiling design in the 200 mm reactor produced non-uniform deposition within the larger hot-zone. The reactants were being depleted at the entrance (inlet) of the susceptor, as there were lots of deposits on the polycrystalline plate at the front end. No growth occurred in the center or back end of the susceptor, as no deposits were seen in these areas. Looking at the gas velocity distributions in Chapter 2, Figure 2.10, the velocity is high at the entrance to the susceptor. Therefore, the boundary layer would be thin at this point and the reactants could easily diffuse to the surface at the

front of the susceptor. Also, the efficiency of SiH_4 cracking was very high at the entrance due to the high temperature at the front of the susceptor, enabling the reactants to be easily consumed by the reaction. This in turn left little reactants for growth downstream of the hot-zone. The samples had to be placed at the front of the susceptor, as shown in Figure 3.3, in order to realize growth. With the flat ceiling design, growth on a 50 mm wafer could not be carried out since the deposition only took place at the front of the susceptor, which defeated the purpose of scaling up the reactor for growth on 50 mm wafers. The modification, which was made to eliminate the excessive depletion of reactants at the growth zone entrance, is discussed in Section 3.3.2.

The development of the growth process of 4H-SiC in the 200 mm horizontal hot-wall reactor was initiated by using the process parameters of the 75 mm reactor as described in Section 3.2. However, the flow rates of H_2, C_3H_8, and SiH_4 were doubled compared to what was used for the 75 mm reactor process. This was done because the area of the growth zone in the 200 mm reactor was double that of 75 mm reactor, thus the flow rates were scaled accordingly so that a similar gas velocity would be achieved. The pressure and temperature were maintained at 150 Torr and ~1550°C, respectively. With these parameters and the doubled flow rates, there was not any epitaxial film growth. This was an indication that only etching was occurring due to excess H_2 flow. It is known that H_2 etches SiC [58] and the technique is often used to remove surface damage on a sample prior to deposition [20,27]. Therefore, to eliminate etching effects, the H_2 flow rate was decreased to 7slm and Q_{SiH4} (2% in H_2) and Q_{C3H8} (3% in H_2) were increased to 300 sccm and 220 sccm, respectively. Along with reducing the H_2 flow to 7 slm, Ar was introduced (10 slm) to maintain a high carrier gas flow. Argon is an inert gas and does

not etch SiC as much as hydrogen. With these process parameter changes, growth was achieved and the resulting films were highly mosaic, if not polycrystalline, in structure with growth rates of around 2.4 – 4.0 μm/h. An example of the resulting morphology is shown in Figure 3.4. As seen in the plan-view micrographs, the film surface was very rough with large grain boundaries and many 3D features (which are the white features in the micrographs), indicating further development of the process was needed.

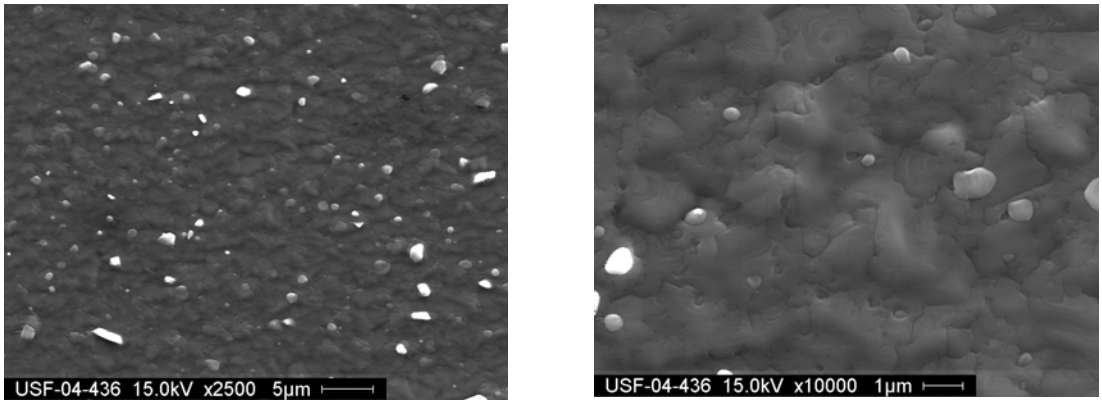

(a) (b)

Figure 3.4 Plan-view SEM micrographs of a 4H-SiC film grown in the 200 mm reactor at a magnification of (a) 2500x and (b) 10000x. The process pressure and temperature were 150 Torr and ~1550°C, respectively. The Q_{H2}, Q_{Ar}, Q_{SiH4} (2% in H_2) and Q_{C3H8} (3% in H_2) were 7 slm, 10 slm, 300 sccm, and 220 sccm, respectively. Data taken by Dr. S. Rao, University of South Florida.

The precursor flow rates were increased not only to suppress H_2 etching, but to supply an excess amount of reactants to the surface. This was done to achieve sufficient amounts of reactants at the inlet of the hot-zone (which were being depleted at the inlet with the lower flow rates) as well as have enough reactant left over to supply reactions further along the growth zone. Even with increased precursor flow rates, there was still no deposition observed anywhere in the hot-zone except at the front entrance. This was determined by inspecting the polycrystalline plate for the deposition pattern in the hot-

zone. In order to achieve uniform deposition through the hot-zone, the pressure was decreased from 150 Torr to 90 Torr to allow a higher gas velocity which would also increase the diffusion of the reactants to the substrate surface at the back end area of the hot-zone. Decreasing the pressure did in fact bring the reactants farther downstream as deposition was observed near the center of the polyplate. However, the film morphology was still polycrystalline in structure. The argon was then eliminated, leaving 7 slm of hydrogen as the carrier gas. This produced a film with less texture on the surface than that shown in Figure 3.4.

Clearly, radical changes were required to realize an acceptable 4H-SiC epitaxial growth process in the 200 mm reactor. Once the morphology was improved by eliminating Ar as the carrier gas, the next step was to increase the growth rate. The Q_{C3H8} (3% in H_2) and Q_{SiH4} (2% in H_2) were increased from 220 sccm and 300 sccm, to 300 sccm and 800 sccm, respectively. Since the pressure at 90 Torr did not produce good film morphology, the pressure was set back to 150 Torr. The H_2 flow was also increased from 7 to 24 slm. The increase in H_2 was used to push the reactants further into the hot-zone. With the large precursor flow rates, H_2 etching of the substrate instead of growth should not have been an issue. The flows described above produced an improved film with step bunching (shown in Figure 3.5) and a growth rate of 16-24 μm/h. The thickness uniformity varying across the sample was 40 %. This value was calculated by taking the difference between the high and low thickness values and dividing by the mean.

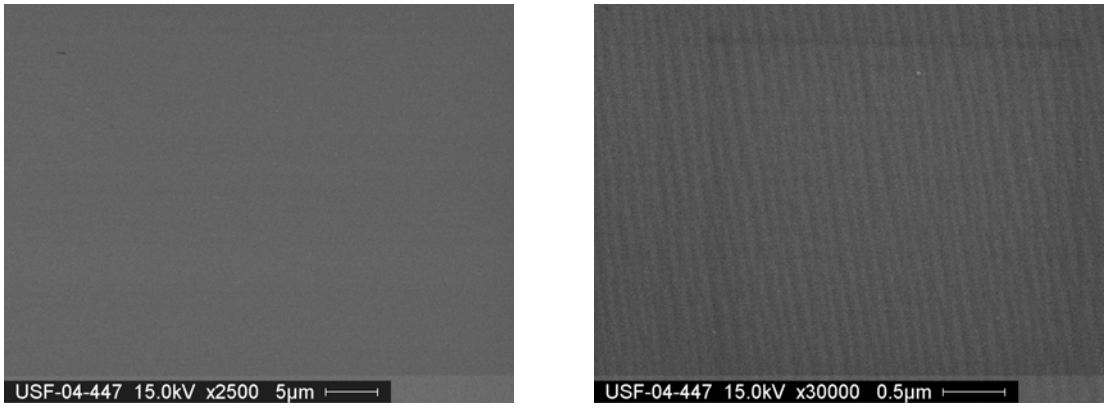

(a) (b)

Figure 3.5 Plan-view SEM micrographs of a 4H-SiC epitaxial film grown for 15 minutes at a magnification of (a) 2500x and (b) 30000x. Micrograph of part (b) shows step bunching. Data taken by Dr. Y. Shishkin, University of South Florida.

With the severe depletion of reactants at the front of the susceptor, growth on a full 50 mm wafer could not be carried out to produce a uniform film thickness. Therefore, the susceptor was modified to push the reactants farther downstream in the hot-zone, enabling a more uniform deposition. The susceptor top was exchanged with a tilted ceiling design. The 4H-SiC epitaxial growth process development then continued as described next.

3.3.2 Angled Ceiling Susceptor Design

For CVD systems, the bottom portion of the susceptor is usually angled so that precursor depletion downstream can be overcome [5]. However, the bottom portion remained flat, while the top portion was redesigned to have an angled ceiling. The angled ceiling design ($\alpha \sim 23$ ° from the horizontal) of the 200 mm reactor susceptor is shown in

Figure 3.6. This design would allow for future wafer rotation which is commonly used in SiC CVD to ensure epitaxial film uniformity over a full wafer [5].

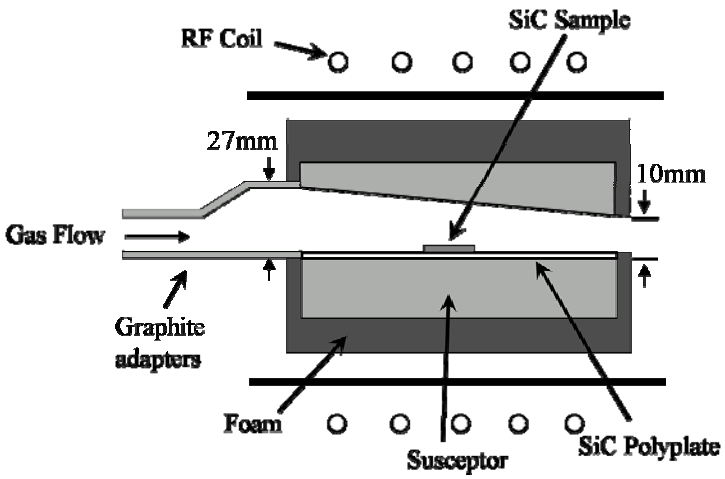

Figure 3.6 Cross-section sketch of the hot-wall CVD reactor hot-zone including graphite foam, angled graphite susceptor, graphite adapters, SiC polycrystalline plate (SiC polyplate), RF coils, and SiC substrate.

With the angled ceiling, the boundary layer above the susceptor surface becomes more uniform across the entire susceptor. This is accomplished by having a lower gas velocity at the entrance of the susceptor due to the larger volume, and a higher gas velocity at the outlet from the constriction due to the tilt [33]. This ultimately produces a thinner boundary layer downstream of the susceptor for reactants to diffuse through [5,33], thus increasing the deposition rate downstream. Figure 3.7 shows sketches of the boundary layer without a tilted susceptor and with a tilted susceptor. Note that the bottom of the susceptor is angled, however, the same principle should apply with the angle being on the ceiling of the susceptor.

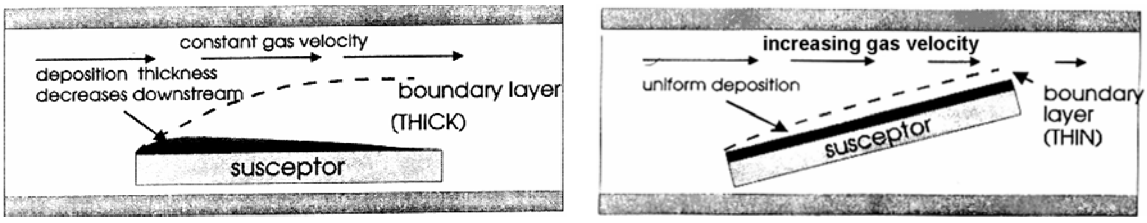

(a) (b)

Figure 3.7 Sketch of the boundary layer above the susceptor with a (a) flat bottom and (b) tilted bottom. The gas velocity for the tilted bottom susceptor increases farther downstream along the flow direction producing a thinner boundary layer at the back end of the susceptor [59].

CFD simulations were performed to predict the velocity distribution within the 200 mm hot-wall reactor with a tilted susceptor ceiling. CFD simulations for the flat ceiling susceptor design were described in Chapter 2, Section 2.5. The reactor geometry for the simulations was similar to the reactor sketch shown in Chapter 2, Figure 2.7; however, the susceptor geometry simulated was that of the sketch in Figure 3.6. The simulated gas velocity distribution for the 200 mm hot-wall CVD reactor with the tilted ceiling is shown in Figure 3.8. As seen in Figure 3.8(b), the velocity increases along the length of the susceptor, as expected, due to narrowing of the flow cross section. With the lower velocity at the inlet of the susceptor, the boundary layer would be slightly thicker there compared to that the back end of the susceptor, which has a higher gas velocity.

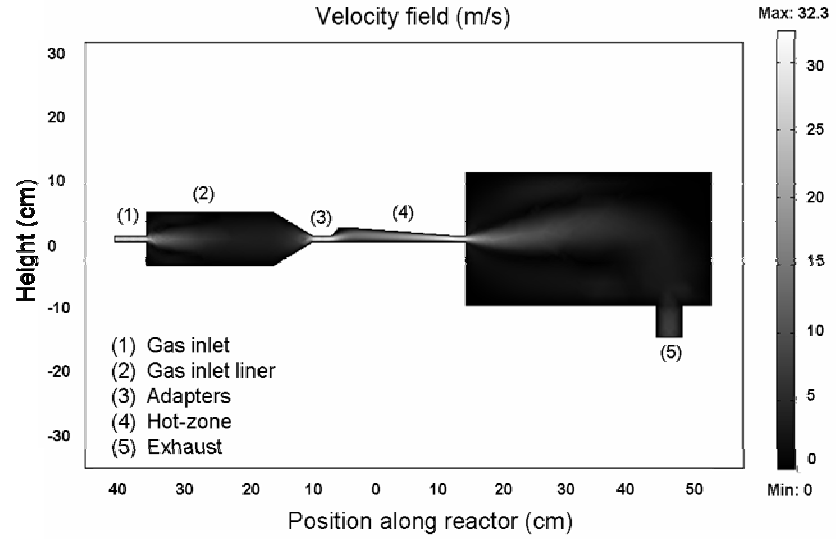

(a)

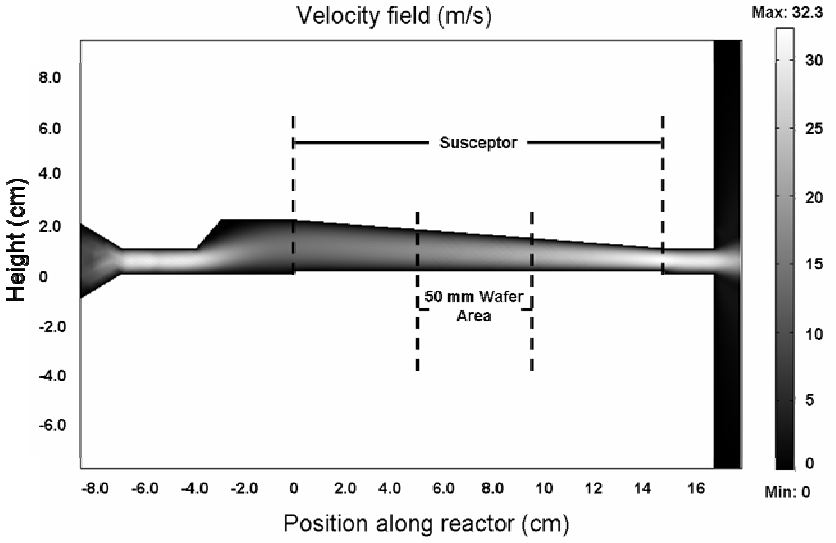

(b)

Figure 3.8 Simulated gas velocity distribution for the 200 mm hot-wall reactor with angled susceptor ceiling showing (a) the entire reactor cross-section and (b) an enlarged view of the hot-zone with the 50 mm wafer area and susceptor indicated by vertical dashed lines. The boundary conditions were $u = 0$ for all surfaces, except inlet flow of Q_{H2} = 30 slm, P = 150 Torr, and T = 1565 °C. The simulations were performed using Femlab [54].

Velocity profiles were also computed at specific distances along the susceptor and the maximum velocities were plotted versus distance. The plot is shown in Figure 3.9. The velocity increases from a velocity of ~ 14 m/s to a velocity of ~ 30 m/s along the susceptor. With this susceptor design, the boundary layer will be thicker at the front of the susceptor than at the back (exhaust) end. This should theoretically help to reduce the depletion of reactants at the front of the susceptor, as was observed to be the case experimentally for the flat ceiling design. With the higher gas velocity at the back end of the susceptor, the reactants will be able to diffuse through the stagnant layer faster, which will provide more reactants at the surface for the reaction to take place. Therefore, the titled susceptor ceiling design should improve the uniformity of the deposition and allow growth downstream of the susceptor. Indeed this was found to be the case as will be described shortly.

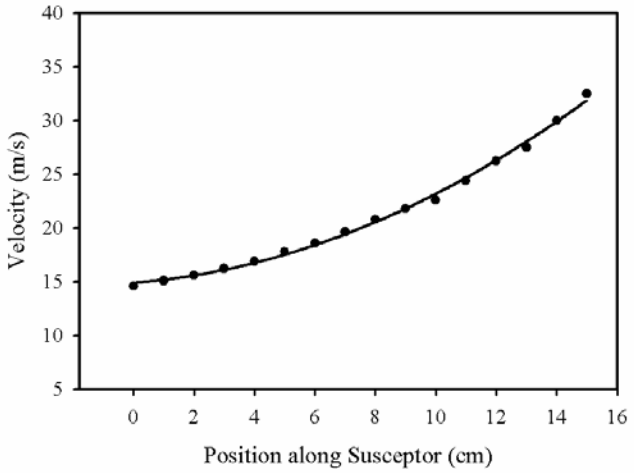

Figure 3.9 Velocity profile of the maximum gas velocity along the 200 mm hot-wall susceptor with the angled ceiling. The gas velocity profile was carried out with a H_2 flow of 30 slm, T = 1565 °C, and P = 150 Torr. Trend line to aid eye only.

Another benefit to the angled susceptor design is that silane is less efficiently cracked at the inlet, thus allowing for un-cracked reactants to be available farther downstream for deposition. This is likely due to the susceptor ceiling and bottom being farther apart, resulting in less efficient gas heating at the susceptor inlet compared to that of the flat ceiling design. The susceptor modification was one of the main factors used to improve the growth rate and surface morphology of the 4H-SiC epitaxial process in the new 200 mm reactor.

Along with changing the susceptor geometry, the precursor gas mixture was also changed from 2% and 3% in H_2 to 100% silane and propane concentrations, respectively. This change was made to extend the life of the gas bottle by using a higher concentration gas source. Another reason is that the precursor MFC's have a specific maximum value. When the precursor flows (at the low mixture percentages (2% and 3% in H_2 for SiH_4 and C_3H_8, respectively)) were increased, the majority of the increase was due to H_2 gas. By having 100% concentration of precursors, a larger range of the actual precursor gas flow was permitted. With the new susceptor ceiling and gas concentrations, the experiment that produced the best result before these changes took place (V_g = 16-24 μm/h) was repeated. As a note, the sample placement, in both the flat ceiling and the first few experiments in the tilted ceiling design, for all experiments described was towards the entrance of the susceptor. The resulting film was smooth and specular. The growth rate was found to be 6.4 – 7.2 μm/h, with a much higher degree of thickness uniformity (7.5%) across the sample surface. SEM micrographs of the surface morphology and the thickness of the film are shown in Figure 3.10.

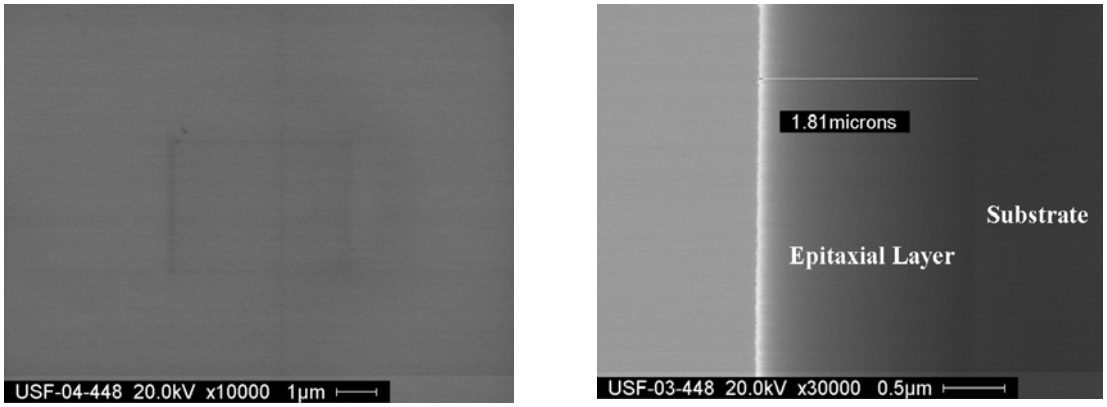

(a) (b)

Figure 3.10 SEM micrographs of the first 4H-SiC epitaxial film grown in the hot-wall CVD reactor with angled ceiling. (a) Plan-view micrograph of smooth surface and (b) cross-section micrograph of film grown for 15 minutes resulting in a V_g of ~7 µm/h. Note the growth parameters were not yet optimized. Data collected by Dr. S. Rao, University of South Florida.

The growth parameters clearly needed to be optimized to account for the angled ceiling. The carrier gas (H_2) was increased to 30 slm and the precursors (SiH_4 and C_3H_8) were each increased to 10 sccm, producing a Si/C ratio of 0.33. The morphology of the films produced using this process was smooth and the growth rate was determined to be 9.2 µm/h. In an effort to enhance the growth rate further, the silane flow rate was increased while maintaining a constant propane flow rate. A sequence of films was grown with increasing silane flow rate until the surface morphology deteriorated. The maximum silane flow rate that resulted in a smooth film surface was 30 sccm, giving a growth rate of 22 µm/h. The Si/C ratio was 1.0 for this experiment. For Si/C ratios higher than 1.0, the surface degraded.

The surface morphology of a film with excess SiH_4 flow is shown in Figure 3.11. The surface of the film was rough and severely step-bunched. This is likely due to the silane flow rate being too high for the growth temperature used. That is, the partial

pressure of the precursor may be too high to supply reactants for growth at this temperature [17]. The growth temperature used for the experiment was 1535 °C. However, later experiments were performed at higher growth temperatures of ~1560 °C. The morphology may have been improved by increasing the growth temperature beyond 1560 °C, however, the higher temperature was not pursued at the time of the experiment shown in Figure 3.11.

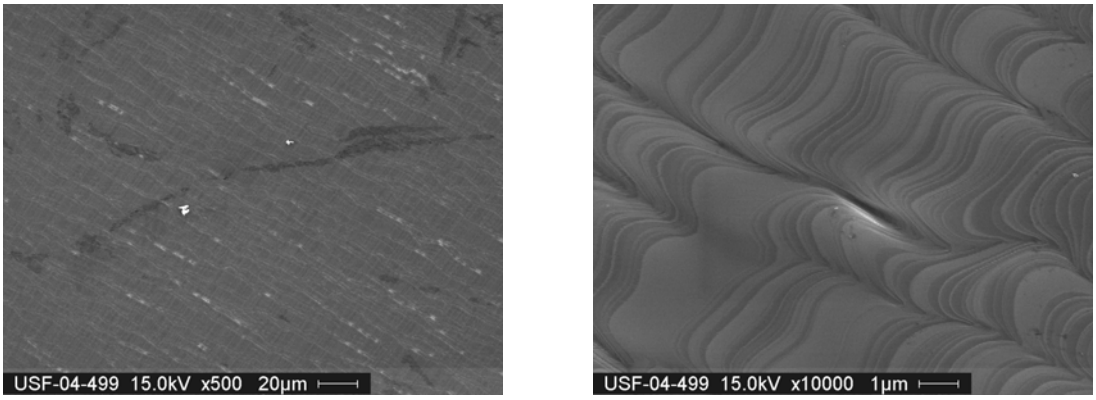

(a) (b)

Figure 3.11 Plan-view SEM micrographs showing poor film morphology caused from excess precursor flow rates at a magnification of (a) 500x and (b) 10000x. The silane flow rate was 48 sccm, with a Si/C ratio of 1.0. Process temperature and pressure were ~ 1535°C and 150 Torr, respectively. Data taken by Dr. Y. Shishkin, University of South Florida.

Once the process parameters were determined as described above, the samples were placed in the center of the polycrystalline plate as deposition was observed to take place across the entire susceptor. At the center, a growth rate of 28 µm/h was observed. A diffuser plate was then incorporated into the system at the inlet port of the gas stream, as shown in Figure 3.12, to potentially eliminate gas jetting effects. Jetting may occur when the gas flows out of the inlet without dispersion. The diffuser was meant to help disperse the gases throughout the inlet liner, shown in Figure 3.12(b). By implementing this

diffuser into the system, there was a slight growth rate increase from 28 μm/h without the diffuser, to 30 - 32 μm/h with the diffuser. The addition of the diffuser may have been the reason for the increase in growth rate.

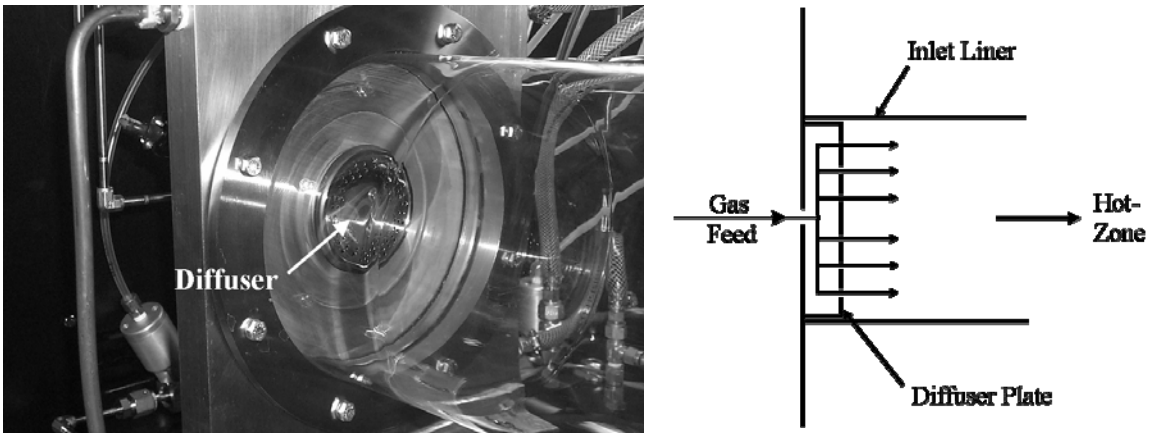

(a) (b)

Figure 3.12 (a) Photograph of the gas inlet port of 200 mm hot-wall reactor showing diffuser plate. (b) Cross-section sketch of diffuser plate demonstrating the dispersion of the inlet gas into the inlet liner.

With all of the modifications to the 200 mm system described in Section 3.3.2, the growth rate increased from 4 μm/h (with the sample placed at the front of the susceptor entrance) to 30 – 32 μm/h (with the sample place in the center of the susceptor). The modification of the susceptor from a flat ceiling to an angled ceiling, the increase in precursor and carrier flows, and the addition of a diffuser plate were crucial to the development of the 4H-SiC baseline process. This baseline process will be summarized next along with characterization performed on the films grown using this process.

3.4 200 mm Reactor Process

The work performed during this research for the development of a 4H-SiC epitaxial growth process has led to two publications [60,61]. The growth rate of 32 μm/h is the highest reported rate to date for a horizontal hot-wall CVD reactor using standard process chemistry of H_2 - SiH_4 – C_3H_8 at low (~ 1600°C) growth temperatures. The process parameters used to achieve this high growth rate are as follows: P = 150 Torr, T ~ 1600°C, Q_{H2} = 30 slm, Q_{SiH4} = 30 sccm (100%), Q_{C3H8} = 10 sccm (100%), and Si/C = 1.0. Note the temperature of the process generally shifts. Therefore, when growing the epitaxial layers using the same process flows and pressure described above, the temperature may be somewhere within the range shown above to produce smooth films. The process schedule developed is shown in Figure 3.13. The step-by-step experimental procedure to grow the epitaxial layers using this process is detailed in Appendix C.

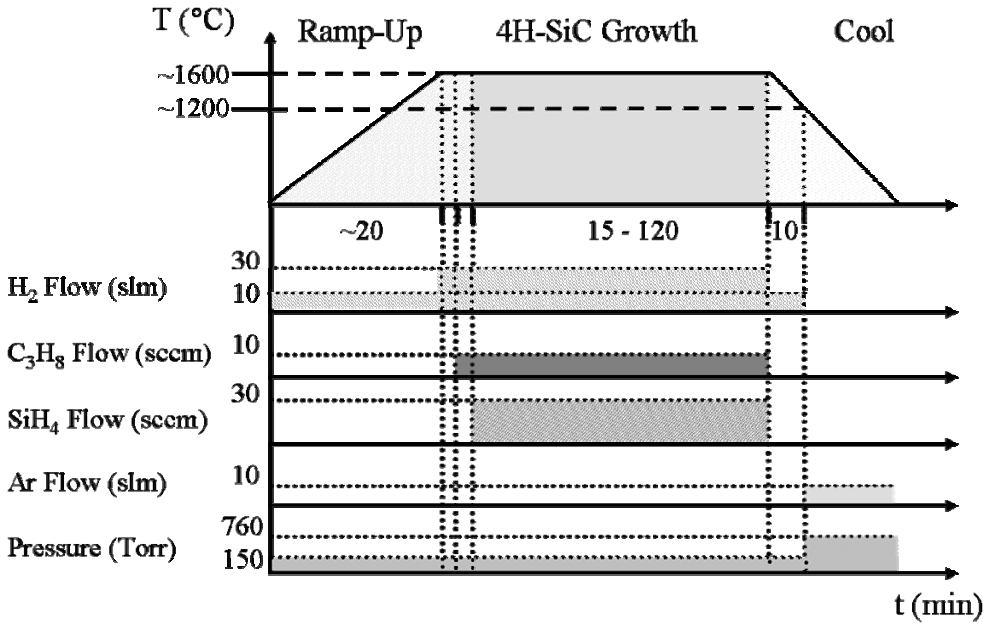

Figure 3.13 4H-SiC epitaxial growth process schedule developed for the 200 mm LP horizontal hot-wall reactor with angled ceiling. Note, the reactor was configured for growth on a 50 mm wafer.

Comparatively speaking, the amount of silane and propane needed for the baseline growth process in the 200 mm reactor is higher than that needed in the 75 mm reactor. The mole fractions of the precursors, found by taking the flow rate of the desired specie divided by the total flow rate (added flow rates of carrier gas and precursors), for the 75 mm reactor baseline process were 2.36×10^{-4} for both silane and propane. In the 200 mm reactor baseline process, the mole fractions are 9.99×10^{-4} and 3.33×10^{-4} for silane and propane, respectively. This may be due to the difference in reactors. Typically the growth process of one reactor can not be used to produce the same results of surface morphology and growth rate for another reactor. Therefore, the difference in mole fractions between the two reactors may be due to the reactors being different. The different reactors need different process parameters to achieve smooth, specular films.

Plan- and cross-section view micrographs of a representative epitaxial film grown for 45 minutes using the developed baseline process in the 200mm reactor are shown Figure 3.14. As seen in the figure, the morphology of the film was smooth and specular, and the growth rate was approximately 31 μm/h.

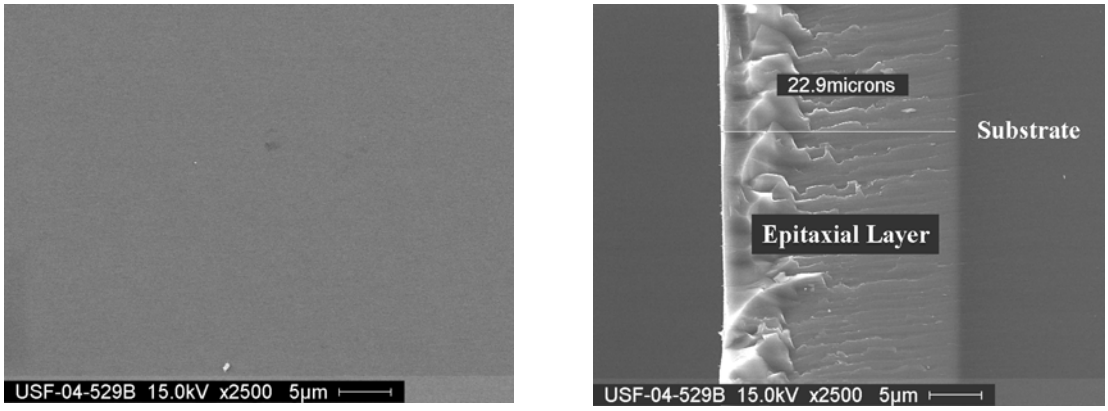

(a) (b)

Figure 3.14 4H-SiC epitaxial layer grown with the baseline process for 45 minutes in the 200 mm reactor. (a) Plan-view SEM micrograph showing a smooth, specular 4H-SiC film and (b) cross-section SEM micrograph of the same sample showing a thickness of 23 μm for a growth rate of 31 μm/h. Data taken by Dr. Y. Shishkin, University of South Florida.

Structural and optical analysis was performed on the sample shown in Figure 3.14 using XRD and LTPL, respectively. Defects influence the diffraction of X-rays, therefore, X-ray diffraction measurements may be used to evaluate the quality of the films. Using LTPL, donor and acceptor impurities may be investigated within the film. The X-ray rocking curve of the (0004) reflection peak for sample USF-05-529C, grown in the same run as the sample shown in Figure 3.14, is shown in Figure 3.15. The full width at half maximum (FWHM) of the (0004) diffraction peak was approximately 36 arcsec. This indicates the film is of reasonable quality, however, higher quality films have been produced with FWHM values between 5.2 and 10 arcsec, grown in vertical and horizontal hot-wall reactors as well as vertical radiant-heating reactors [18,24,27]. While the quality of the film in Figure 3.14 is not as high as that reported for the films in [18,24,27], other films have since been produced in the 200 mm reactor with higher quality. A reason for the high FWHM value (36 arcsec) of the (0004) diffraction peak

may be that defects from the substrate propagated into the epitaxial layer, producing a lower quality film. The characterization results of these films will be shown in Section 3.5.3.

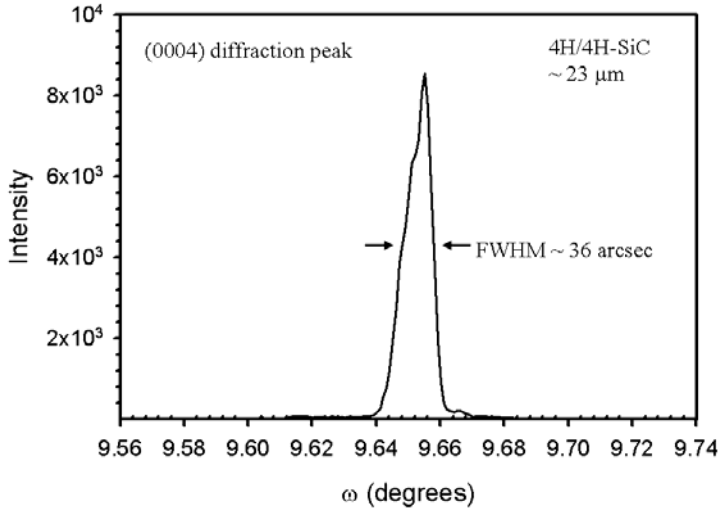

Figure 3.15 X-ray diffraction rocking curve of the (0004) diffraction peak for a 4H-SiC epitaxial film grown for 45 min at a temperature of ~ 1520°C and a process pressure of 150 Torr. Sample ID: USF-04-529C.

The film quality was also analyzed using LTPL (collected at 2K), which was provided by Professor W. J. Choyke's group at the University of Pittsburgh. The near bandedge spectrum of film USF-04-529B (refer to Figure 3.14) is shown in Figure 3.16. In the spectrum, it can be seen that the intrinsic peak, labeled I_{75}, is strong which is an indication of a high quality film [62]. The doping of the epitaxial layer was estimated by taking the ratio of the Q_o peak to the I_{75} peak [63]. The net carrier concentration, N_d-N_a, was found to be approximately 1.75 x 10^{15} cm^3, which is comparable to the doping concentration found using C-V measurements conducted. A four-particle aluminum complex peak is seen between P_0 and Q_0 lines, indicating there is a source of Al contamination present in the CVD reactor. The source of the Al contamination may be

caused from a high concentration of Al in the graphite adapters. The graphite adapters used in this dissertation work had recently been replaced, and the films grown with the new adapters contained lower concentrations of Al.

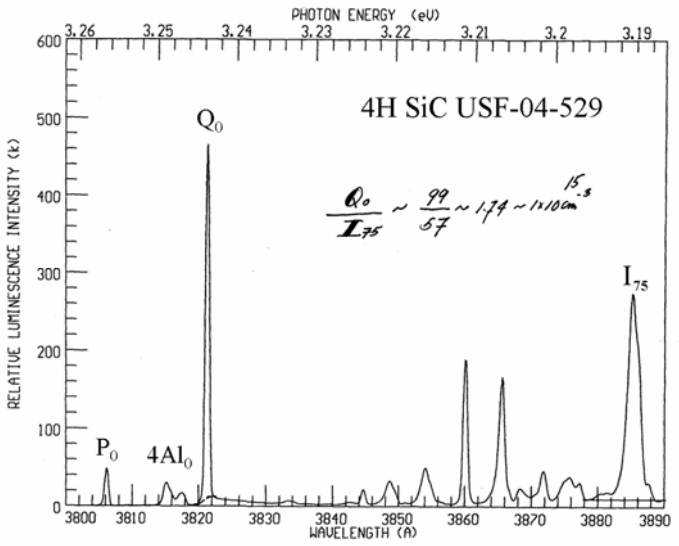

Figure 3.16 Near bandedge LTPL spectrum (taken at 2K) of a 23 μm thick 4H-SiC film grown at 31 μm/h. The process temperature ~ 1520°C, pressure = 150 Torr, and Si/C = 1.0. Data courtesy of Professor W. J. Choyke, University of Pittsburgh.

With the baseline 4H-SiC epitaxial film process developed, the growth parameter space was explored to characterize the reactor. The only parameter which was left unchanged was *T*. The growth rate was studied as a function of silane flow, pressure, and growth time. The results of the reactor characterization will be presented in the next section of this dissertation.

3.5 200 mm Reactor Growth Characterization

The characterization of the 200 mm reactor is important as there are many parameters (i.e. pressure, silane flow rate, etc) that influence the growth of the epitaxial

layers. By investigating growth parameters such as the silane flow rate and the Si/C ratio, the ability to grow at different speeds or vary the doping concentration (within a certain range) may be examined. This work has recently been published in the *Journal of Crystal Growth* [61].

3.5.1 Growth Rate as a Function of Silane Flow

The ability to grow epitaxial films at different speeds in the hot-wall CVD reactor was investigated by varying the SiH_4 flow rate while maintaining the same Si/C ratio. The baseline process described in Section 3.4 was the starting point for this experiment. The silane flow was varied from 12 sccm to 39 sccm. The pressure, temperature, and H_2 carrier gas flow rate were maintained at 150 Torr, ~ 1600°C, and 30 slm, respectively. Figure 3.17 shows the result of the experiment.

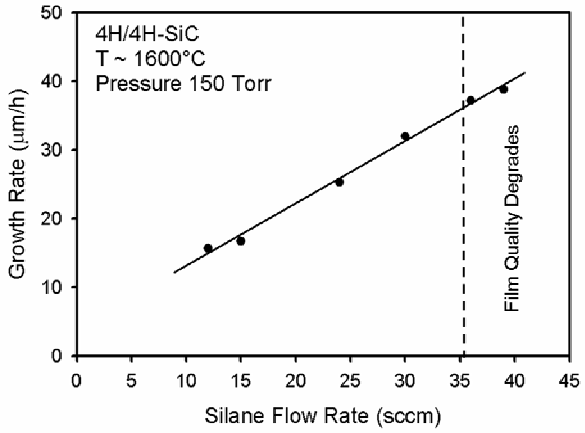

Figure 3.17 4H-SiC epitaxial growth rate dependence on silane flow rate in the 200 mm LP hot-wall reactor with angled ceiling. Carrier gas flow rate and the Si/C ratio maintained at 30 slm and 1.0, respectively. The solid trend line shown to aid eye only [60,61].

As seen in Figure 3.17, the growth rate is a linear function of silane flow rate, in which it increased from 16 to 39 μm/h. The lowest flow rate for silane (12 sccm) produced a film with black features on the surface, shown in Figure 3.18, and a growth rate of 16 μm/h. The features may be due to the substrate or from the low silane flow rate. If there were defects or there was surface damage on the substrate prior to growth, the epitaxial film could be affected by it. If the features were caused by the lower silane flow, there may not have been enough precursors to support growth of a smooth film.

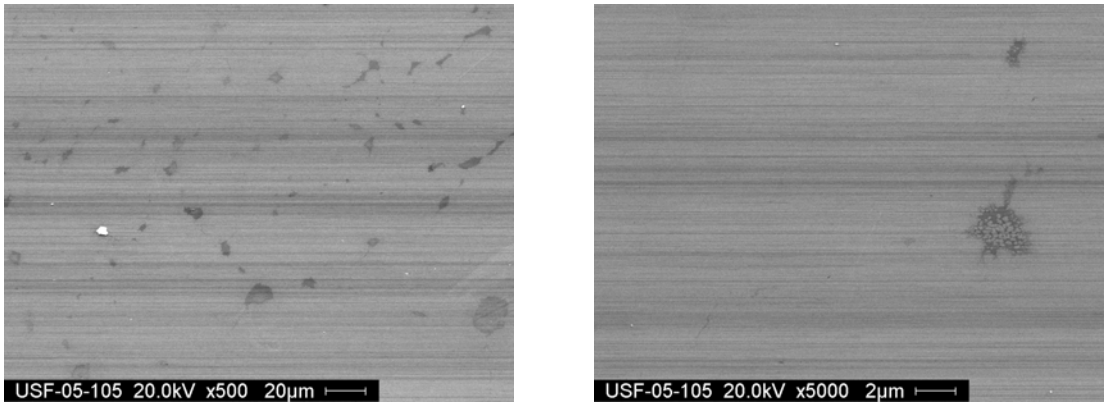

(a) (b)

Figure 3.18 Plan-view SEM micrograph of 4H-SiC grown for 15 minutes with a silane flow rate of 12 sccm and a Si/C ratio of 1.0 at a magnification of (a) 500x and (b) 5000x.

When the silane flow rate was increased to 15 sccm, the growth rate increased slightly to ~ 17 μm/h, resulting in decent film morphology without the black features as those seen in Figure 3.18. With a silane flow increased from 15 sccm up to 30 sccm, the growth rate increased. At the same time, the morphology of the films was found to be smooth, similar to one in Figure 3.14. The first sign of film deterioration began when the silane flow rate was increased from 30 to 36 sccm. Occasional triangular defects were observed on the surface by plan-view SEM (not shown). When the flow was increased

further to 39 sccm, the surface morphology became wavy, which may have indicated the growth rate was too fast for this temperature [17] (without the addition of any other precursors, which will be discussed in Chapter 4). The morphology of the film grown at 39 sccm of SiH_4 flow is shown in Figure 3.19.

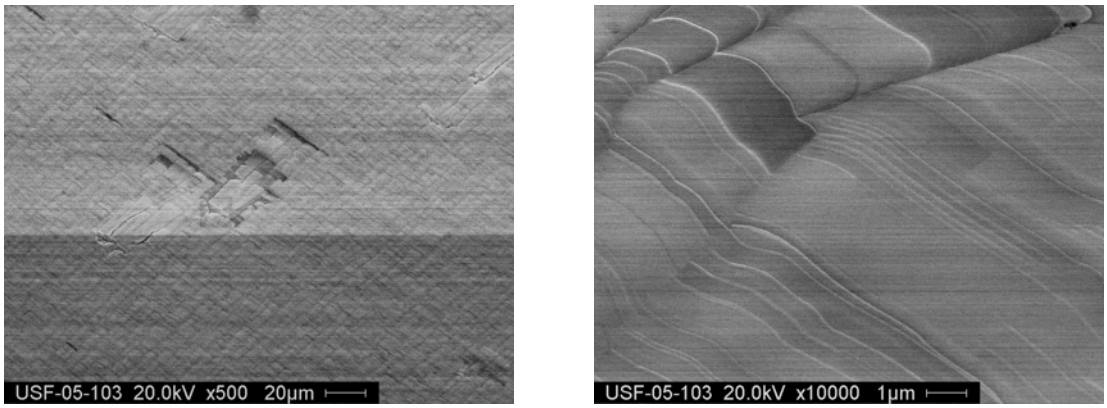

(a) (b)

Figure 3.19 Plan-view micrographs of a 4H-SiC epitaxial sample grown at a growth rate of 39 µm/h using a flow rate of SiH_4 at 39 sccm. The magnifications are (a) 500x and (b) 10000x.

When excess SiH_4 is added to the process, homogeneous nucleation in the gas phase is likely to occur. Homogeneous gas phase nucleation can result in Si clusters which may descend onto the surface of the film. These clusters become detrimental to the film by incorporation of large 3D particles [17,21]. With the film deterioration at the higher silane flow rates, this may be an indication the supersaturation limit for this Si/C ratio and temperature is being approached. In Chapter 4, research using HCl as a growth additive to reduce the homogeneous gas phase nucleation will be discussed. Adding HCl to the precursor mixture allowed the possibility of increasing in the silane flow up to 45 sccm without significant detrimental effects on the film morphology.

3.5.2 Growth Rate as a Function of Process Pressure

The pressure plays a crucial role in chemical vapor deposition. If the pressure is too high, the growth rate can decrease due to a thicker boundary layer making it more difficult for the reactants to diffuse through [33]. When the pressure is excessively low, a crowning effect can occur, in which the epitaxial deposition takes place mostly at the edges of the sample. Therefore, the evaluation of the reactor based on the process pressure is important. Figure 3.20 shows the obtained growth rate dependence on process pressure, which was varied from 100 to 450 Torr.

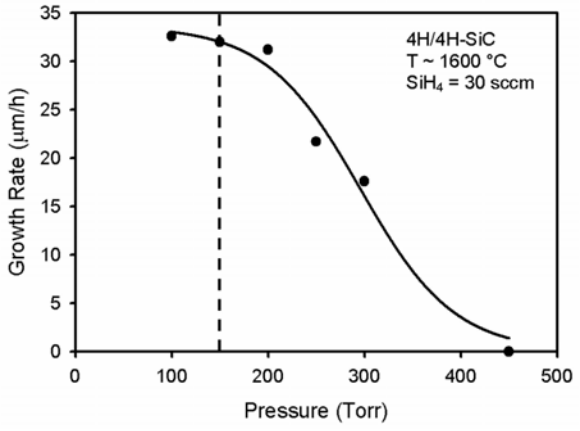

Figure 3.20 4H-SiC epitaxial growth rate vs. process pressure in the 200 mm horizontal hot-wall reactor with angled ceiling. The H_2 flow and the Si/C ratio maintained at 30 slm and 1.0, respectively. Solid trend line shown to aid eye only. Vertical dashed line indicates baseline process pressure of 150 Torr.

As demonstrated in the Figure 3.20, the growth rate was at a maximum (33 μm/h) at P = 100 Torr. The process pressure could not be decreased much below 100 Torr as the lowest achievable pressure with the existing vacuum system was 90 Torr for the experimental conditions of interest. The growth rate at 150 Torr (32 μm/h) was approximately the same as that at 100 Torr. The growth rate may be highest at these process pressures because the boundary layer is thinner, allowing the reactants to diffuse

quickly to the surface where the reaction may take place. The resulting morphologies at both pressures were very similar to the morphology of the sample shown in Figure 3.14.

As the pressure was increased to 250 Torr, the growth rate reduced by more than 25% to approximately 22 μm/h. With a further increase in pressure to 450 Torr, no growth was observed. An explanation could be that homogeneous nucleation occurs at the higher pressures thus reducing the amount of Si available to supply the reaction. At elevated pressures, homogeneous nucleation of the SiH_4 precursor limits the deposition rate [17]. It may also be that at the higher pressure, the gas flow velocity is decreased and the reactants may not be getting to the substrate fast enough for growth to take place. A final explanation for the decrease in growth rate at the 450 Torr pressure may be that, the process parameters are not optimized for this pressure. The temperature may need to be adjusted to allow growth at this high of pressure. The temperature was not adjusted during these experiments.

3.5.3 Analysis of Thick Films

When growing thick epitaxial films, it is important to verify that the growth rate is maintained for extended amounts of time. This is an essential piece of information in the characterization of the reactor as it provides insight into process stability and reliability. For example, if a film thickness of 75 μm is desired and the growth rate is 15 μm/h, then it is important to know that growing for 5 hours will truly result in this thickness. If the growth does not produce a film of preferred thickness and quality, then the growth process is not stable or reliable. Therefore, experiments were conducted in which the

baseline process was used and films were grown for various lengths of time, as shown in Figure 3.21. The Si/C ratio was, however, 1.2 instead of 1.0 in order to produce an n-type epitaxial layer during these experiments (for reasons explained in Section 3.5.4).

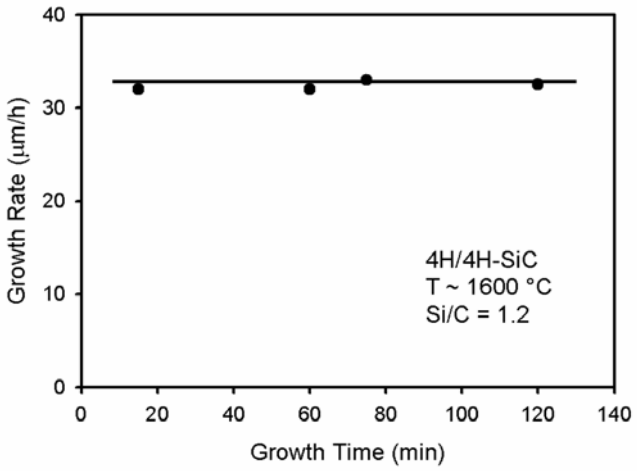

Figure 3.21 Growth rate of 4H-SiC as a function of growth time in the 200 mm LP hot-wall CVD reactor with angled ceiling. The process pressure and the silane flow rate were 150 Torr and 30 sccm, respectively. Solid trend line shown to aid eye only. Note the growth rate is invariant with respect to growth time.

The substrates were polished using chemical mechanical polishing (CMP) by NovaSiC prior to deposition [64]. The growth of epitaxial films was conducted for a few different periods of time between 15 and 120 minutes. The epitaxial layer thicknesses were determined via cross-section SEM and the average growth rates were calculated as described in Section 3.1. As seen in Figure 3.21, the growth rate remained constant (V_g ~ 32 μm/h) for all growth runs. Thus, this data showed that longer growth runs should produce the desired film thickness based on the nominal growth rate of 32 μm/h.

The morphology of the films was similar to that shown in Figure 3.14(a). However, occasional triangular and carrot-like defects were observed in the films thicker than 30 μm. When thick epitaxial layers are grown, the defects from the substrate may

propagate into the film and increase in size [52]. Triangular defects are inclusions of 3C-SiC in the 4H-SiC films which may be developed from imperfections in the substrate [20]. Carrot-like defects are extended line defects which also propagate from the substrate interface [17]. Defects within the epitaxial layers reduce the minority carrier lifetime, which affects the device performance.

The quality of the film surface is typically evaluated by a quantity known as surface roughness RMS which is obtained by performing AFM scans of the surface. The RMS roughness is the root mean square value of vertical deviations from the mean horizontal surface [65]. The surface roughness of the films from the experiment in Figure 3.21 was investigated. The plot of surface roughness as a function of film thickness is shown in Figure 3.22.

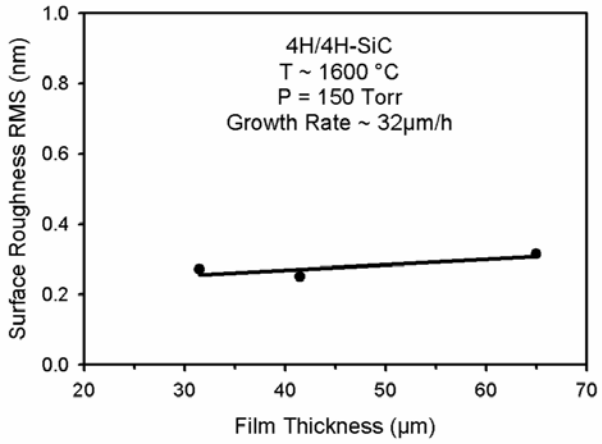

Figure 3.22 Dependence of surface roughness of 4H-SiC films on film thickness as measured by AFM. Growth conditions were maintained at 30 slm of H_2, 30 sccm of SiH_4 and a Si/C ratio of 1.2. Data taken by Dr. Y. Shishkin, University of South Florida.

The surface roughness for the 30 μm film was 0.27 nm RMS, while that of the 65 μm film was 0.32 nm RMS. This is only a slight increase in surface roughness when the film thickness was doubled, indicating that the epitaxial growth in hot-wall CVD for

prolonged periods of time should not significantly affect the surface roughness of the grown films. An AFM scan of the 65 μm thick film is shown in Figure 3.23. In the literature, films were grown at 11 - 15 μm/h resulting in 60 μm thick films which had a surface roughness between 0.2 and 0.7 nm RMS [66]. In another work [16], approximately 100 μm thick films were grown with surface roughness values from 0.2 and 0.3 nm RMS. Therefore, the surface roughness of the thick films grown in the 200 mm reactor is of reasonable value.

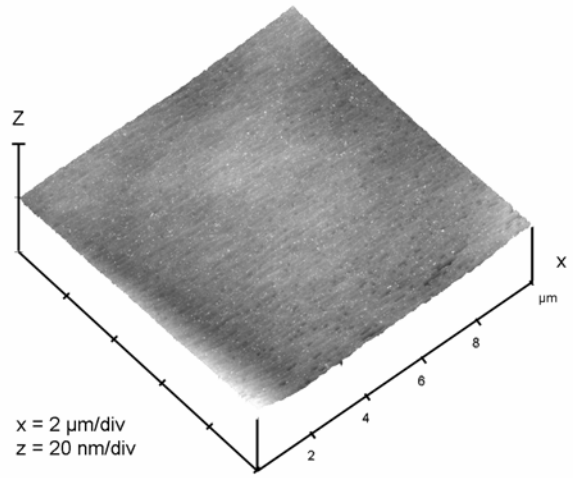

Figure 3.23 AFM scan of a 65 μm thick 4H-SiC film grown for 120 minutes at a rate of 32 μm/h. Surface roughness is 0.32 nm RMS. The scan area was 10 μm x 10 μm. Data taken by Dr. Y. Shishkin, University of South Florida.

The structural quality of the 65 μm film was analyzed using XRD. A rocking curve taken of the (0004) reflection peak is shown in Figure 3.24. The X-ray rocking curve is customarily used to measure the semiconductor crystal perfection. In order for a film to be considered high quality, the diffraction peak must be narrow and result in a low FWHM value. If the crystal was perfect, diffraction would only occur at one specific angle, the Bragg angle. However, for real crystals, the peak broadens due to

imperfections in the lattice called defects. Therefore, the lower the FWHM value, the more perfect the crystal structure. The FWHM for the 65 μm thick film is approximately 11 arcsec which is comparable to other high quality films grown using hot-wall CVD [18,24].

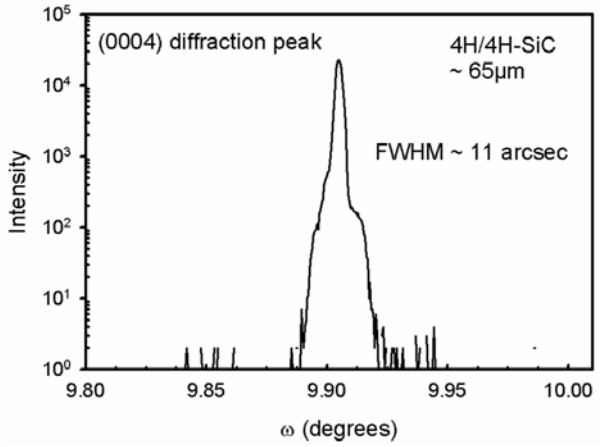

Figure 3.24 X-ray diffraction rocking curve of the (0004) peak for the 65 μm thick 4H-SiC epitaxial film. The FWHM is approximately 11 arcsec.

3.5.4 Analysis of Doping Concentration

The results of the experiments aimed to determine the carrier concentration, $|N_d - N_a|$, as a function of Si/C ratio in the gas phase are shown in Figure 3.25. The films grown during these experiments were not intentionally doped. However, Al and N atoms are known contaminants in the reactor, as determined by LTPL. It is speculated that the contaminants may be out-diffusing from the graphite adapters during growth. The doping concentration of films grown in the 200 mm reactor was explored by changing the Si/C ratio, which was performed by varying the C_3H_8 flow rate while maintaining a constant SiH_4 flow rate. During the growth of SiC, the Al (p-type dopant) atoms compete with Si atoms and N (n-type dopant) atoms compete with C for vacant lattice sites [35]. To

produce an n-type doped epitaxial layer, the Si/C ratio is increased, providing a lower concentration of C atoms which presents a greater chance for N atoms to occupy the vacant lattice sites. On the other hand, to create a p-type epitaxial layer, the Si/C ratio is decreased. This is accomplished by reducing the amount of Si in the system, which enables the Al atoms to more easily occupy the vacant lattice sites.

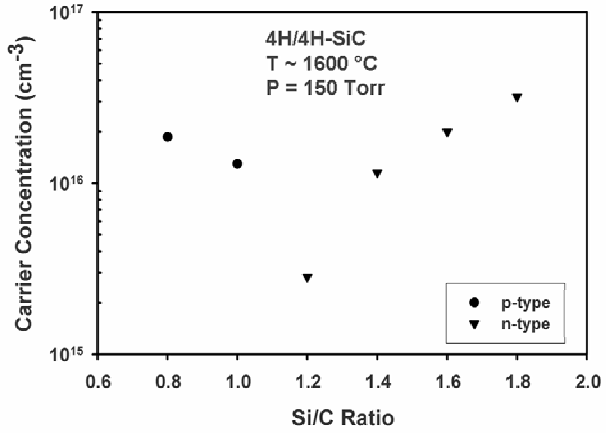

Figure 3.25 Net carrier concentration of 4H-SiC epitaxial films as a function of Si/C ratio as measured with the C-V technique. The 200 mm LP hot-wall reactor with angled ceiling was used. H_2 and SiH_4 flow rates maintained at 30 slm and 30 sccm, respectively. Doping concentrations of p-type layers indicated by circles while doping concentrations of n-type layers indicated by triangles. Data provided by Dr. S. Rao and J. Walker, University of South Florida.

The Si/C ratio was varied between 0.8 and 1.8 by fixing the amount of available silicon and varying the amount of carbon. As shown in Figure 3.25, the Si/C ratios of 0.8 and 1.0 resulted in p-type epitaxial layers. When the Si/C ratio was increased from 1.0 to 1.2, the conductivity type conversion occurred. At and beyond a Si/C ratio of 1.2, the films were n-type with increasing carrier concentrations as the Si/C ratio increased. The lowest value of $|N_d - N_a|$ obtained was ~ 2 x 10^{15} cm^{-3} at a Si/C ratio of 1.2. The p-type epitaxial layers were grown at the lower Si/C ratios, where more C atoms are available to

occupy the vacant lattice sites, resulting in a lower concentration of N atoms. With less n-type dopants, the material became p-type since there was the same amount of Al contaminants in the system as with a higher concentration of C atoms. As the Si/C ratio was increased, by decreasing the C concentration, the doping concentration of the p-type films decreased and type conversion occurred. With the higher Si/C ratios, there were less C atoms to compete with the N atoms, resulting in films with higher n-type conductivity.

The morphology of the films was also examined as a function of Si/C ratio. With a Si/C of 0.6, the resulting film surface was wavy which may have been caused by a carbon-rich process [26] or too low of a growth temperature [17]. With an increase in carbon, films may roughen at one specific growth temperature. However, smooth film surfaces may be produced when there is a higher amount of carbon present by increasing the growth temperature [25]. When the Si/C ratio was increased to 0.8, triangular defects were observed on the surface. The triangular defects, which are 3C inclusions in the film, are common when Si/C ratios are low [52]. To reduce this problem, the Si/C ratio may be increased. The morphology was smooth and specular for the Si/C ratios between 1.0 and 2.0. At a Si/C ratio of 2.5, the film contained Si droplets on the surface caused by excess Si not consumed by the reaction.

The growth rate was not affected by variation of the Si/C ratio between 0.8 and 1.4, resulting in growth rates of approximately 30 μm/h. With a Si/C ratio above 1.4, the growth rate started decreasing. The growth rate was approximately 26.5 μm/h for the Si/C ratio of 1.6, and decreased down to 17 μm/h for the Si/C ratio of 2.0. Since the

amount of Si was fixed, this may have been caused by a carbon-limited process in which not enough carbon is being supplied to the reaction.

3.5.5 Growth Variation in Hot-Zone

In order to determine the growth rate, film quality, and doping variation along the hot-zone, an experiment was carried out to simulate growth on a 50 mm wafer. Five samples were loaded onto the polyplate as shown in Figure 3.26. The size of each sample was 8 mm x 11 mm. This was done to reduce the substrate cost of growing on an actual whole wafer. The growth was carried out using the baseline process with a Si/C ratio of 1.2 to produce n-type epitaxial film at 30 - 32 μm/h. The films were grown for 30 minutes which resulted in ~ 17 μm thick films. The results of the experimental analysis are shown in Table 3.2.

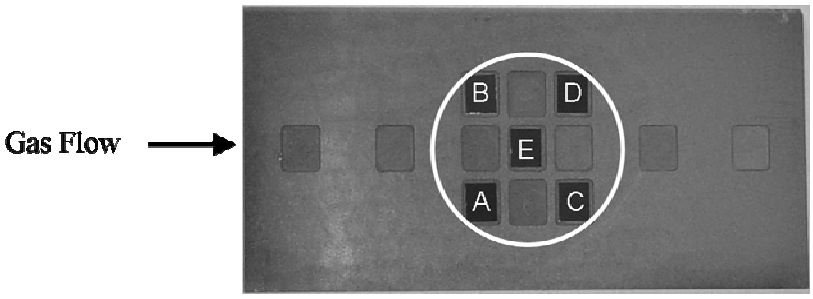

Figure 3.26 Picture of the polycrystalline plate used to simulate growth on a 50 mm wafer. Note the lettering is used to designate placement of samples. The circle shown indicates the simulated 50 mm wafer position.

The thickness of the films across the simulated wafer was observed to be fairly uniform in both the gas flow direction and perpendicular to it. It must be noted that the reactor does not currently have wafer rotation. Without rotation, the thickness uniformity was found to be approximately 4%. This value was calculated by using:

$$\%Uniformity = \sigma / mean * 100\% \tag{3.1}$$

where

$$\sigma = \sqrt{1/N \sum_{i-1}^{N} (\bar{x} - x_i)^2} \tag{3.2}$$

such that $\bar{x}$ is the average of all thicknesses (mean) and x_i is the value of the individual thickness measurement, and N is the number of measurements.

Typical thickness uniformities (with wafer rotation) given in the literature are approximately 5% for 50 mm and 35 mm diameter wafers [19,21]. With the addition of wafer rotation, the thickness uniformity of the process should improve.

Table 3.2 Experimental results of growth over a 50 mm wafer area. T ~ 1600 °C, P = 150 Torr, Q_{SiH4} = 30 sccm, and Si/C ratio = 1.2.

Sample ID USF-05-346	Thickness (μm)	Growth Rate (μm/h)	$\lvert N_d - N_a \rvert$ (cm^{-3}) n-type layers	(0004) XRD FWHM (arcsec)
A	17.2	34.5	4.55×10^{15}	8.0
B	17.3	34.7	5.16×10^{15}	16.0
C	18.0	36.0	7.09×10^{15}	12.0
D	17.0	34.0	7.53×10^{15}	9.7
E	16.0	32.0	4.30×10^{15}	10.5

Typical reported doping uniformities across 35 mm diameter wafers [21,67] with wafer rotation are 10 – 12%. The doping concentration of the films across the simulated 50 mm wafer slightly increased along the gas flow direction from ~ 5×10^{15} to ~ 7×10^{15} cm^{-3} as shown in Table 3.2. The doping uniformity was found to be approximately 24%

using equations (3.1) and (3.2); however, $\bar{x}$ and x_i were the average value and the values of individual measurements of the net carrier concentration, respectively. From the LTPL data presented in Figure 3.16, Al contamination is present in the reaction system. Recent investigations show that the graphite adapters are the likely source of the contamination. It is speculated that Al impurities might be consumed at the inlet of the reactor, reducing the amount of Al downstream. This would in turn reduce the acceptor concentration and produce a higher n-type doping concentration.

The structural quality of all the films in the simulated 50 mm growth run is very good. The FWHM values of the rocking curve of the (0004) X-ray diffraction peak ranged between 8 and 16 arcsec. The films placed in the "A" and "B" positions on the polycrystalline plate resulted in the largest difference in the structural quality. Representative rocking curves from the simulated wafer experiment are shown in Figure 3.27.

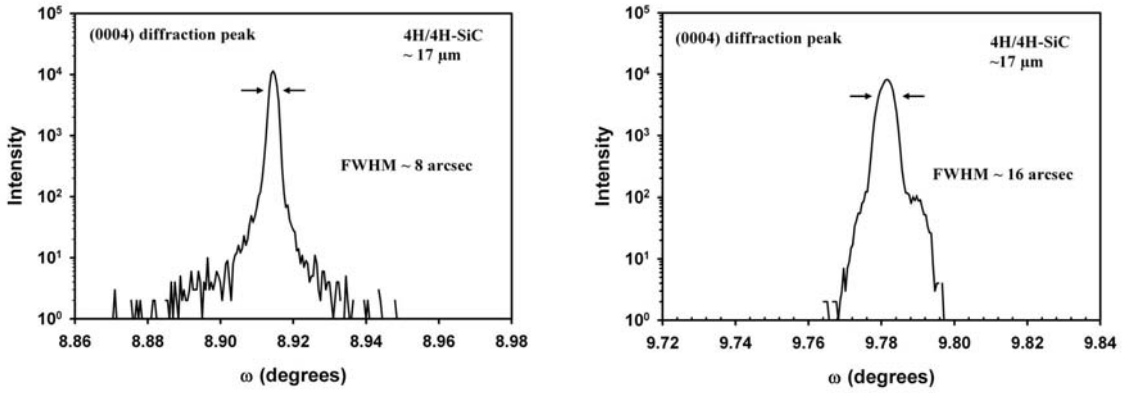

(a) (b)

Figure 3.27 X-ray diffraction rocking curves of 4H-SiC epitaxial films grown for 30 minutes placed on the polycrystalline plate in (a) sample placement A and (b) sample placement B from Figure 3.26. Data provided by Dr. Y. Shishkin, University of South Florida.

In Figure 3.27(a), a rocking curve of the film placed in position "A" on the polyplate (Figure 3.26) is shown. The FWHM (~ 8 arcsec) of this film was the lowest value of the five samples. The FWHM for the sample in Figure 3.27(b) (sample placement "B") was the highest value of 16 arcsec. The lower quality of the film placed in position "B" may have been caused by the substrate. If there were initially a higher amount of defects on this substrate, which could be possible since micropipes tend to cluster, they could have propagated through the epitaxial layer, causing a lower quality film compared to the other samples in this experiment. While the FWHM value for sample placement "B" is twice that of the film set in placement "A", the peak is still fairly narrow indicating a good quality film.

3.6 Summary

The development of a baseline 4H-SiC epitaxial growth process in the USF 200 mm hot-wall CVD reactor has been completed. The obtained growth rate of 32 μm/h is the highest reported for this type of reactor to date at temperatures around 1600 °C [61]. It was demonstrated that a tilted susceptor ceiling was necessary to enable a uniform thickness deposition (~4 %) across the hot-zone. Simulated velocity distributions predicted the boundary layer to be higher at the entrance of the tilted susceptor design to that at the back end. With an increase in silane flow, the growth rate increased, as expected; however, the morphology degraded when excessive flows (≥ 36 sccm) were used. In addition to silane flow, the growth rate increased with a decrease in process pressure, ultimately producing the best surface morphology at a process pressure between

100 and 150 Torr. 150 Torr was chosen as the baseline the process pressure since this would allow for higher process flows in the future (e.g. 100 mm wafer growth process development). The pump is only capable of achieving a certain process pressure with certain flow rates. A process pressure of 150 Torr would be achievable with the pump for higher flow rates, however, a pressure of 100 Torr may not be obtainable. A 65 μm thick film was grown and the surface roughness was found to be 0.32 nm RMS, which is a comparable surface roughness value to films, of approximately the same thickness, in the literature. The structural quality of the 65 μm thick film was evaluated by an X-ray diffraction rocking curve of the (0004) peak. The FWHM value was 11 arcsec, indicating a high quality film. The uniformity in carrier concentration and thickness was 24% and 4%, respectively, for films of ~ 17 μm thickness grown to simulate a 50 mm wafer. The thickness uniformity is high given the reactor does not have wafer rotation.

CHAPTER 4

4H-SIC EPITAXIAL GROWTH USING HCL AS A GROWTH ADDITIVE

The main goal of this dissertation research has been to increase the growth rate of 4H-SiC in the horizontal hot-wall CVD reactor. It was detailed in Chapter 3 that the growth rate could be increased from 4 μm/h to 32 μm/h by optimizing the input parameters and tilting the susceptor ceiling. There are other ways to increase the growth rate further while maintaining smooth morphology, for example, by elevating the growth temperature, changing the process pressure, or changing the carrier gas flow rate of the system. The most effective method is to increase the SiH_4 flow rate, which, in turn, provides more Si species at the substrate surface to supply the reaction which increases the growth rate. When excessive amounts of SiH_4 are present, gas phase homogeneous nucleation commonly occurs as discussed in Section 3.5.1. To overcome gas phase homogeneous nucleation, HCl was added to the process chemistry. The details and results of the addition of this chlorinated precursor to the growth process will be presented in this chapter.

4.1 Proposed HCl Mechanism

In order to increase the growth rate, the supply of the silicon containing precursor, in this case SiH_4, may be elevated to provide more Si vapor to feed the growth reaction. However, it was shown in Section 3.5.1 that with higher SiH_4 flow rates, the film morphology deteriorated. As the SiH_4 flow rate is increased, gas phase homogeneous nucleation may occur producing a supersaturation of Si which may result in Si clusters or precipitates [68]. Si clusters do not aid in the growth of SiC. Instead they reduce the amount of Si reactants available for 2D film growth, thus limiting the growth rate. The precipitates form and may deposit onto the surface of the film, creating 3D features. One way to prevent homogeneous nucleation from occurring is to increase the growth temperature. By doing this, the Si clusters may evaporate into Si vapor, thus providing more of the reactant for growth [26].

Another way to reduce the gas phase homogeneous nucleation of Si is to add chlorine (Cl) into the H_2-C_3H_8-SiH_4 gas mixture [31]. For this dissertation work, hydrogen chloride (HCl) was selected as the Cl precursor. Two mechanisms were proposed where HCl may be used, in addition to an increase of silane flow rate, to produce elevated epitaxial growth rates while maintaining smooth films. The first proposed mechanism is that the HCl etches away the 3D particles which may have fallen onto the surface due to homogeneous nucleation. This would result in a smooth film surface, albeit at a reduced growth rate. HCl diluted in H_2 has been used to pre-treat the SiC surface prior to growth to suppress dislocation-related growth pits caused by selective H_2 etching [67]. Xie, *et al.* [58] performed a study on the difference between H_2 etching and H_2 etching with the addition of HCl of SiC, proving that HCl does in fact

etch SiC at elevated temperatures of ~ 1400 °C. Excess silicon may create Si clusters, which in turn produce a deteriorated film surface. Knowing that HCl etches Si and SiC, it is possible that HCl vapor may be etching the particles that fall onto the film surface from the Si clusters, leaving a smooth surface behind. A sketch of this proposed mechanism is shown in Figure 4.1.

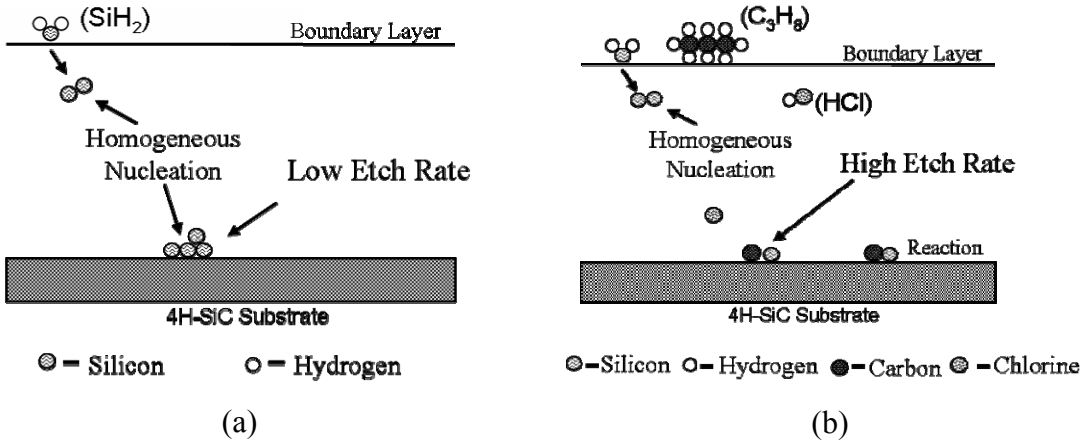

Figure 4.1 Sketch of the first proposed HCl mechanism where (a) homogeneous nucleation occurs with low etch rate of the Si clusters on the substrate surface and (b) high etch rate with the addition of HCl into the gas mixture resulting in a smooth surface and no Si clusters.

Figure 4.1(a) is a sketch of what may occur during homogeneous nucleation. Without the addition of HCl, Si clusters form in the gas phase and deposit onto the growth surface and create 3D features. With the standard chemistry of H_2-C_3H_8-SiH_4 at elevated SiH_4 flow rates, there may be a low etch rate of the particles, thereby deteriorating the surface of the film. However, when HCl is added to the standard gas mixture (shown in Figure 4.1(b)), there may be a high etch rate of the precipitates on the surface, due to etching with HCl. As detailed in [58], H_2 with the addition of HCl etches SiC faster than H_2 alone. This may explain why the 3D particles are not etched away fast

enough when in the presence of the standard chemistry, but are etched away when HCl is added to the mixture. Also, since there is a higher surface area with the 3D features, the HCl may be able to etch the features at a faster rate than the flat surface of SiC.

The second proposed mechanism is that the HCl suppresses the homogeneous nucleation from occurring in the first place. Figure 4.2(a) shows a sketch of the reactions occurring during growth. The precursors diffuse through the boundary layer as described in Chapter 2, Section 2.2. Pyrolysis occurs above and throughout the boundary layer, in which case the precursors decompose into the separate species providing the Si and C containing reactants. With excess Si precursors in the system, homogeneous nucleation is likely to occur. Homogeneous gas phase nucleation may be seen with the naked eye and is viewed as 'white smoke' within the reactor when growth takes place at elevated SiH_4 flow rates or at very low temperatures. When HCl is introduced into the gas mixture, or other chlorinated precursors are added, this phenomenon may be suppressed. When the HCl and SiH_4 molecules decompose, it is proposed that the chlorine attaches to the Si atoms to create Si_xCl_y compounds. This behavior is sketched in Figure 4.2(b). Indeed simulations performed by M. Reyes showed this to be the case thermodynamically [69]. With the Cl combining with the Si, the Si cluster compounds, such as Si_2, Si_2C, etc, formation is reduced. This eliminates the gas phase homogeneous nucleation of Si at higher partial pressures of SiH_4, thereby allowing growth to proceed at high growth rates and result in smooth surface morphology films.

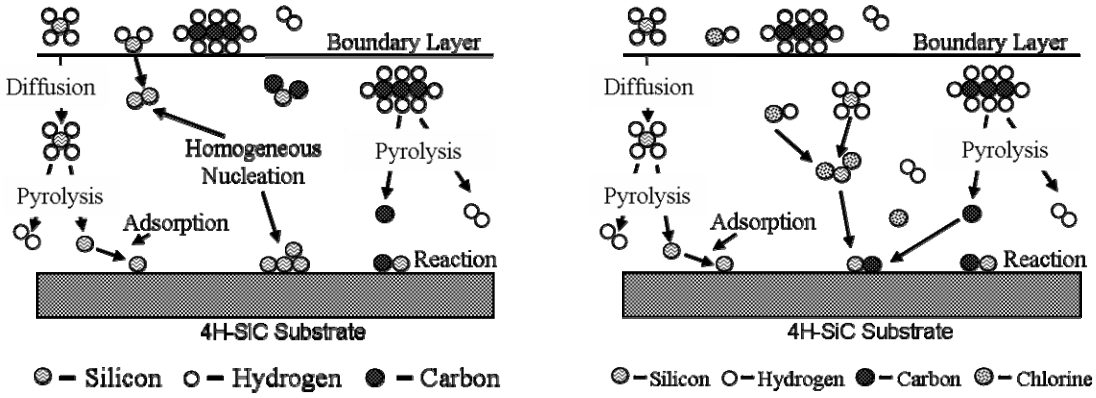

(a) (b)

Figure 4.2 Sketch of second proposed HCl mechanism to suppress homogeneous nucleation. (a) Homogeneous nucleation occurs, creating Si clusters and (b) HCl suppresses the gas phase homogeneous nucleation of Si.

Thermodynamic simulations were used to predict the dominating chemical species within the CVD system when HCl was added to the standard chemistry of H_2-C_3H_8-SiH_4. The simulations were performed using the NASA CEA code [40]. The process parameters of the baseline process for the 75 mm hot-wall CVD reactor, described in Chapter 3, Table 3.1, were used as the input parameters for the simulations. The standard chemistry thermodynamic simulations without the addition of HCl are shown in Figure 4.3(a) and those with the addition of HCl are shown in Figure 4.3(b). The H_2 flow was input as 10 slm and the precursors SiH_4 (2% in H_2) and C_3H_8 (3% in H_2) were input as 120 and 80 sccm, respectively. The process pressure was 150 Torr and Si/C was 0.33 for both cases. The Si/Cl ratio for the simulations including HCl was chosen to be 1.0. It was assumed that the same amount of chlorine moles were needed as that of silicon moles to suppress homogeneous gas phase nucleation.

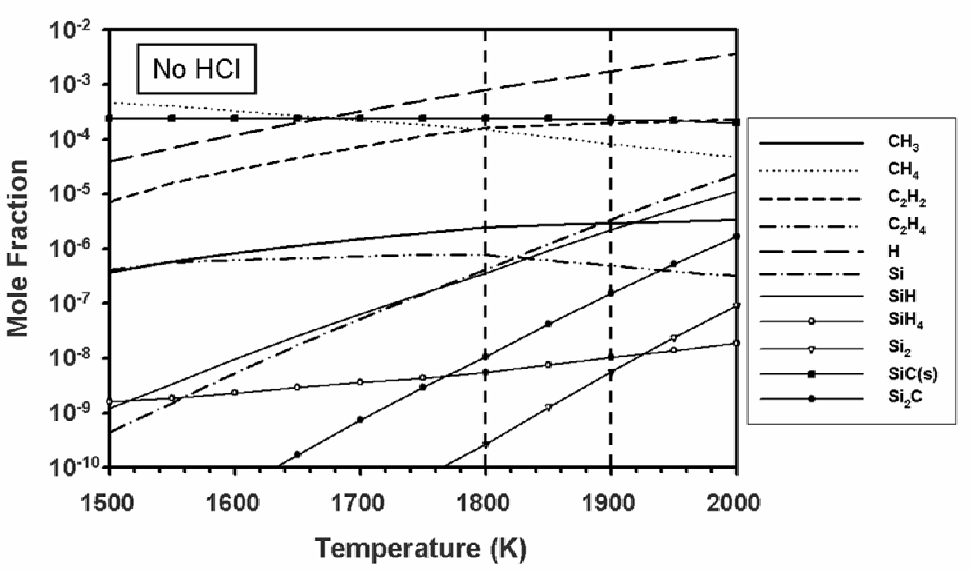

(a)

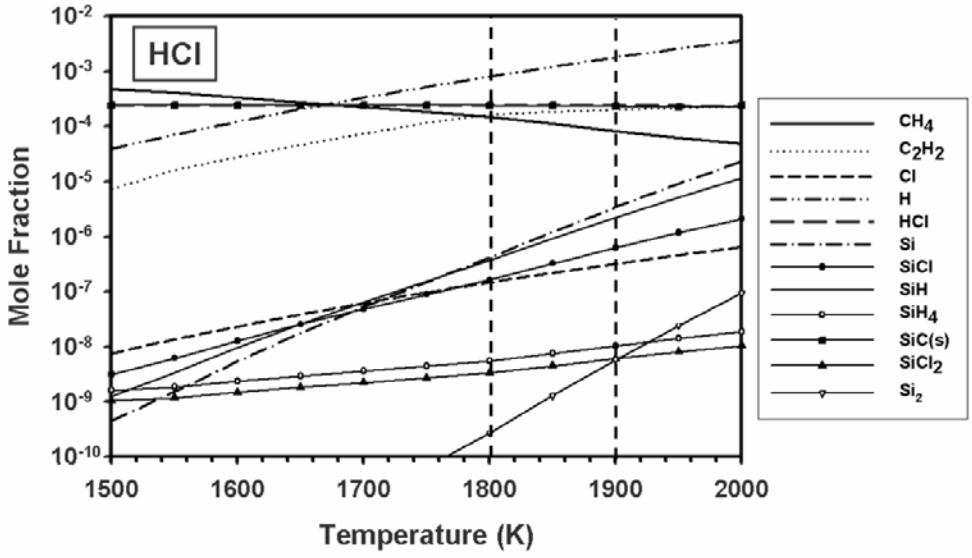

(b)

Figure 4.3 Thermodynamic simulations of the mole fraction of gaseous species for the chemistry of H_2-C_3H_8-SiH_4 in the 200 mm CVD reactor (a) without the addition of HCl gas and (b) with the addition of HCl. Simulations were performed using the NASA CEA code [40].

In Figure 4.3(a) and (b), it can be seen that the dominating species at the growth temperature for the baseline process, ranging between 1800 and 1860 K (1520 and 1580

°C), are H, solid SiC, C_2H_2, and CH_4. The Si specie has the highest mole fraction for the silicon source. Molecular hydrogen is again not shown as it has a higher mole fraction than all of the species shown, ~ 1. The specie Si_2C is present in the standard chemistry simulation, however, with the addition of HCl, there is no Si_2C specie. In the simulations with HCl additive, there are two species with both Si and Cl which are SiCl and $SiCl_2$. In Si CVD, the main specie of interest when chlorinated precursors are added is $SiCl_2$ [70].The Cl may be combining with the Si_2C to create these species. Based on the results of the thermodynamic simulations, the CVD growth experiments were carried out at elevated precursor partial pressures with the addition of HCl. These experiments will be discussed in the following sections of this chapter.

4.2 HCl Manifold

With the prediction that HCl would be effective in allowing for high growth rates of SiC, an HCl gas source was incorporated into the CVD gas handling system. Careful planning was needed as HCl is a corrosive gas when it comes into contact with water vapor. When hydrogen chloride gas combines with moisture, hydrochloric acid (a liquid) is produced, which is also highly toxic and corrosive. Therefore, the gas lines that would be in contact with the HCl gas were welded to prevent moisture from getting into the lines. Another preventative measure to reduce moisture in the lines was adding a moisture purifier. This was put in the system to lessen any moisture that could have possibly seeped into the lines from the VCR connections. To reduce the corrosion rate of the gas lines, electropolished stainless steel (SS) tubing was used. Electropolished stainless steel

is different from standard stainless steel in that it has a much smoother surface, thereby reducing the surface area that the HCl can attack. In addition to welding the lines, a purge panel, shown in Figure 4.4, was implemented into the system near the HCl bottle. The panel was used to remove HCl gas from the gas line and replace it with Ar when the lines were not utilized for extended periods of time. The next paragraph describes the operation of the HCl panel.

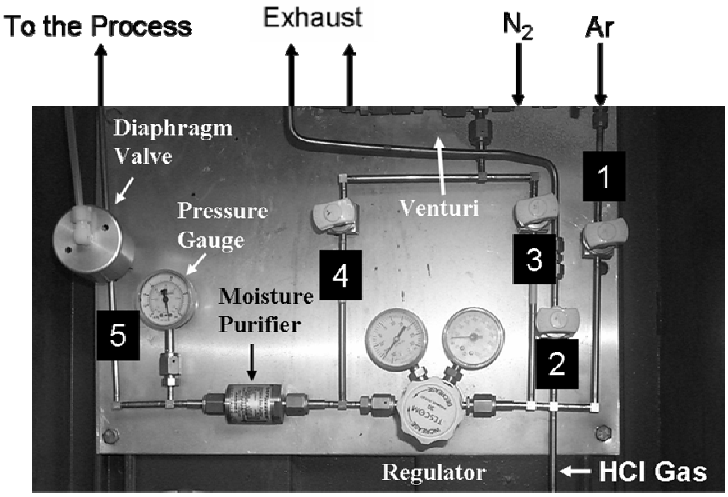

Figure 4.4 HCl purge panel near the HCl gas bottle which was used to replace HCl with Ar in the gas lines to help prevent corrosion. Numbers in the picture represent valve numbers.

The HCl gas flows from the bottle (not shown; bottom of photograph) through the gas line (labeled "HCl gas" in Figure 4.4), through a dual-stage pressure regulator into the moisture purifier and out to the process line. The diaphragm valve was used as a safety valve to isolate the HCl gas panel from the mainstream gas line and is actuated by the user by closing a switch on the CVD control panel. It is closed at all times when the system is not in operation. Detailed operation of the HCl panel is described in Appendix D.

4.3 HCl Growth Additive Experiments: 75 mm Reactor

The 75 mm reactor, described in Chapter 2, Section 2.4.1, was used for the first experiments using HCl as a growth additive. With all the modifications to the system finished to allow HCl gas to be safely supplied to the reactor, the experimental evaluation of the HCl additive was initiated. The experimental study of increasing the growth rate by increasing the precursor flows and adding HCl is discussed next.

4.3.1 Experimental Results

The goal of adding HCl to the standard chemistry of H_2-C_3H_8-SiH_4 was to increase the growth rate, by increasing the SiH_4 flow rate, while maintaining a smooth surface morphology with a low amount of surface defects. The theory of adding HCl to the standard chemistry to reduce homogeneous nucleation and increase the growth rate was investigated. A small amount of HCl gas (100%) was added to the baseline process described in Section 3.2. The flow rate of HCl was set to a very low, but controllable, value of 0.5 sccm with the HCl MFC. This flow rate produced a Si/Cl ratio of 4.8, which is the ratio of the number of moles of Si and the number of moles of Cl in the inlet gas mixture. Plan- and cross-section view SEM micrographs of the films grown are shown in Figure 4.5.

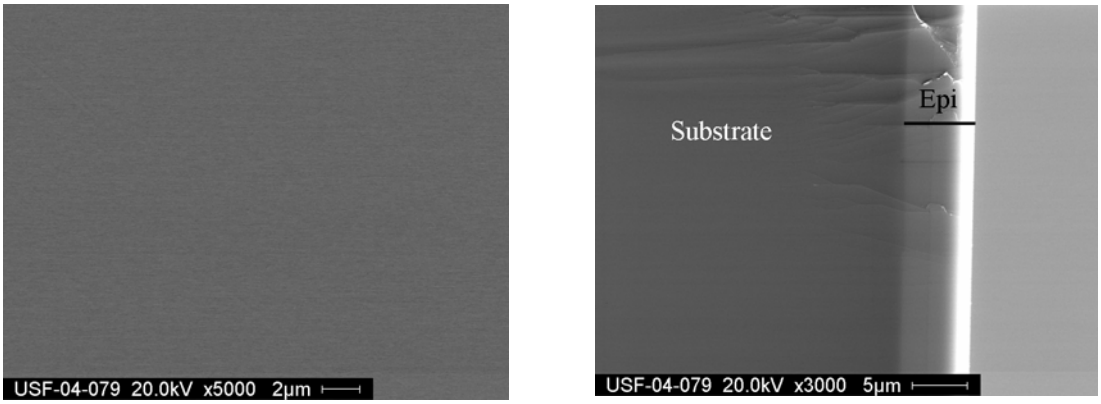

(a) (b)

Figure 4.5 4H-SiC epitaxial film grown using the baseline process (from Section 3.2) with the addition of 0.5 sccm of HCl in the LP horizontal hot-wall reactor. (a) Plan-view micrograph showing the resulting smooth film surface and (b) cross-section micrograph of cleaved edge showing a film thickness of 6.5 µm. (t = 15 min).

As shown in the micrograph in Figure 4.5(a), the film surface was smooth and specular. The growth rate using this process was 26 µm/h, which is considerably higher than the growth rate of the baseline process of 16 µm/h for the 75 mm reactor. With the addition of HCl, there may be an increase in Si vapor to supply the reaction, resulting in a higher growth rate. This would support the theory that the Si clusters are not being formed when HCl is added to the growth process, which would provide more Si for deposition.

Further experiments were conducted on the baseline process with the addition of HCl to determine the effects on the surface morphology due to increasing the HCl flow rate beyond 0.5 sccm. The highest flow rate of HCl added to the baseline process was 5 sccm resulting in a Si/Cl ratio of ~ 0.5. Plan-view micrographs of a film grown using the baseline process and the addition of 1.0 sccm of HCl to produce a Si/Cl ratio of 2.4, are shown in Figure 4.6.

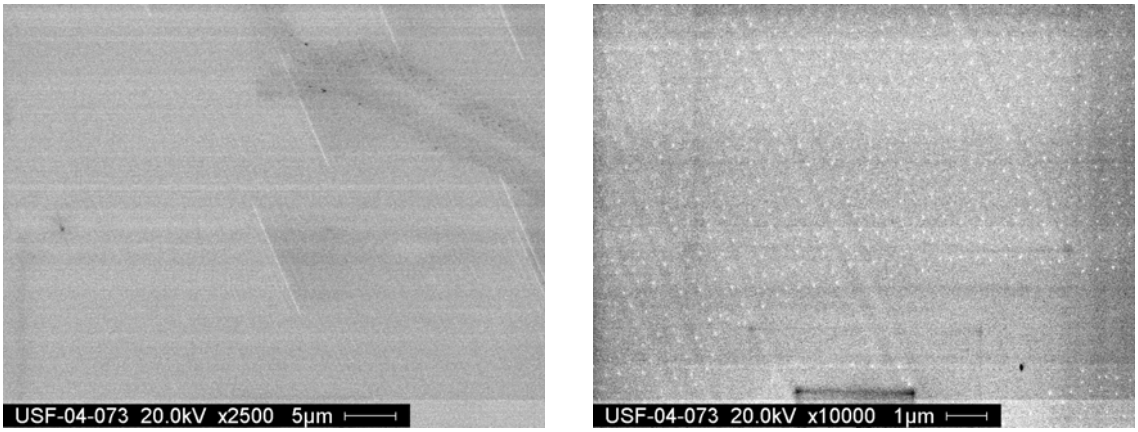

(a) (b)

Figure 4.6 Plan-view micrographs of 4H-SiC epitaxial growth run in the 75 mm horizontal hot-wall reactor with the addition of 1.0 sccm of HCl to the baseline process (see Section 3.2 for details) showing step-bunching at a magnification of (a) 2500x and (b) 10000x. V_g = 14.4 µm/h. Data taken by Dr. S Rao, University of South Florida.

From the micrograph in Figure 4.6(a), there is slight step-bunching on the surface of the film which may indicate there is too much HCl in the gas mixture causing some etching effects. Nakamura, *et al.* [71] found that etching of 6H-SiC surfaces with 3 sccm of HCl in 1 slm of H_2 at 1300 °C for 10 minutes resulted in step bunching. Therefore, at elevated HCl flows during growth of 4H-SiC, step-bunching may occur and could be the reason for the step-bunched surface. At a magnification of 10000x (Figure 4.6(b)), there are white dots on the surface which are of higher contrast than the flat surface. Unfortunately, the cause of these white spots is unknown. The growth rate of the film (14.4 µm/h) was slightly lower than the baseline process growth rate of 16 µm/h. The surface of a film grown with 5 sccm of HCl added to the baseline process was similar to that shown in the micrographs in Figure 4.6, however, there was a higher amount of step-bunching and no white spots were seen at the higher magnification. Also, the growth rate was reduced even further to ~ 11 µm/h. From these experiments, it was determined that

the amount of HCl needed to produce a smooth film using the baseline process was 0.5 sccm.

With the baseline process evaluated, the precursor flow rates were doubled from 80 sccm of SiH_4 and C_3H_8 (both 3% in H_2) to 160 sccm. This was done for two reasons. The first was to determine how high the growth rate could be increased. With increasing the silane flow rate and keeping a constant Si/C ratio, there might be a limit to how high the precursors can be increased while still increasing the growth rate and maintaining a smooth surface morphology. The second was to determine whether HCl could improve the morphology at higher precursor flow rates. At a certain flow rate of precursors, the HCl might not suppress the gas phase homogeneous nucleation which would result in deteriorated film surfaces.

The growth parameters for the increased precursor flow experiments were maintained at T = 1535 °C, P = 150 Torr, and Si/C = 0.33. The initial growth was carried out using the same amount of HCl flow as the one found in the baseline process (0.5 sccm). The resulting film of the experiment was polycrystalline in structure and a plan-view image of the film surface is shown in Figure 4.7(a). The growth rate of the film was 33 μm/h, which is double the baseline process growth rate. Although this is a high growth rate, the film is polycrystalline in nature.

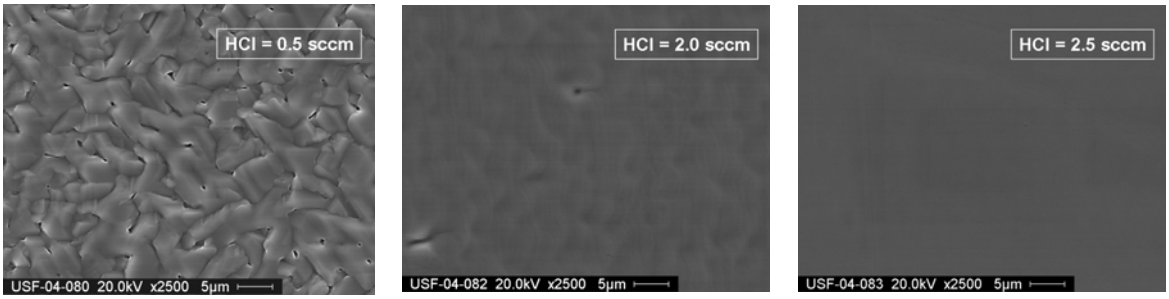

(a) (b) (c)

Figure 4.7 SEM micrographs of 4H-SiC epitaxial films grown at Q_{SiH4} and Q_{C3H8} (3% in H_2)) of 160 sccm with the addition of HCl [5]. (a) 33 µm/h growth rate with 0.5 sccm of HCl, (b) 31 µm/h growth rate with 2.0 sccm of HCl, (c) 28 µm/h growth rate with 2.5 sccm of HCl flow. Data of USF-04-082 taken by Dr. S. Rao, University of South Florida.

Since the epitaxial layer in Figure 4.7(a) was polycrystalline, the HCl flow rate was increased further to 2.0 sccm. The growth rate of the film decreased slightly from 33 to 31 µm/h. With the increased HCl flow rate, the surface of the epitaxial layer was much smoother (see Figure 4.7(b)). There was still a wavy texture to the surface, but the film was not polycrystalline in structure. The amount of HCl was then increased further to 2.5 sccm. The growth rate for this experiment was 28 µm/h. Although the growth rate slightly decreased from 33 to 28 µm/h with the increase of HCl flow from 0.5 to 2.0 sccm, the surface morphology of the film grown was very smooth (see Figure 4.7(c)). Therefore, the HCl mechanism of reducing homogeneous gas phase nucleation at elevated SiH_4 flow rates to produce smooth morphology films was shown to be the reason behind the increased growth rate with HCl. The precursor flow rates could be increased to 160 sccm of SiH_4 and C_3H_8 (both 3% in H_2), resulting in an overall increase of growth rate from the baseline process (16 µm/h) in the 75 mm hot-wall CVD reactor to 28 µm/h.

The SiH_4 precursor was again increased by an additional 25% to a flow of 200 sccm (3% in H_2), while maintaining the Si/C ratio of 0.33, in order to determine whether the growth rate could be improved further. The H_2 carrier gas flow and process pressure were maintained at 10 slm and 150 Torr, respectively. The HCl flow rate was set to 2.5 sccm, however, the film resulted in large mosaic structures over the entire surface. As seen in Figure 4.8, the morphology was much different than that of the film grown at a SiH_4 flow rate of 160 sccm. The surface was highly mosaic, if not polycrystalline, with large grain boundaries, as evident from the 2500x magnification image in Figure 4.8(b).

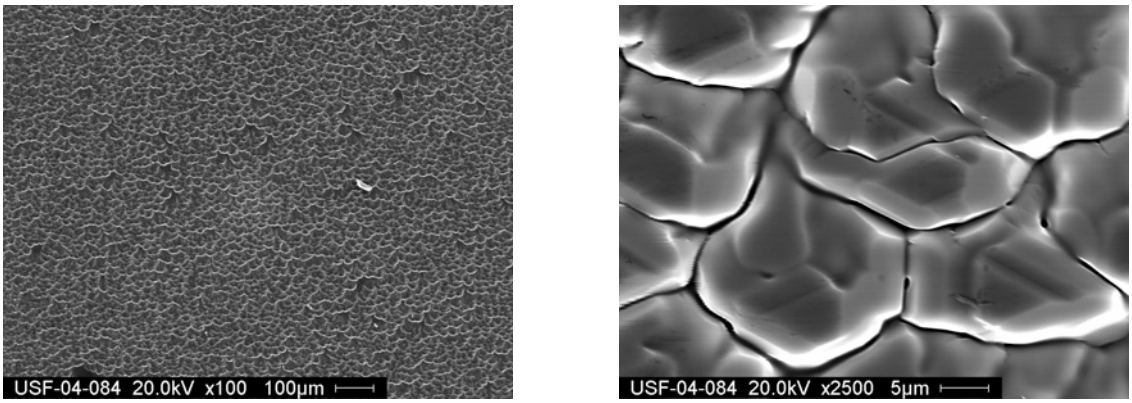

(a) (b)

Figure 4.8 Plan-view SEM micrographs at a magnification of (a) 100x and (b) 2500x of an epitaxial film grown for 15 minutes in the LP hot-wall reactor. Q_{SiH4} and Q_{C3H8} were both 200 sccm (3% in H_2) and Q_{HCl} = 2.5 sccm. V_g = 46 µm/h. Data taken by Dr. S. Rao, University of South Florida.

In an effort to improve the morphology of the film grown at a SiH_4 flow rate of 200 sccm (3% in H_2), the amount of HCl gas was increased. Polycrystalline films were produced for each HCl flow rate attempted, between 2.5 and 6.0 sccm. Therefore, it was determined that at high precursor flow rates, the morphology could not be improved with the addition of HCl. This may indicate that the SiH_4 flow rate limit at this temperature has been reached. The growth rate was ~ 56 µm/h with the SiH_4 precursor flow rate at

200 sccm (3% in H_2) and the HCl flow rate at 4.0 sccm. The experimental results of the HCl additive experiments are presented in a graph shown in Figure 4.9.

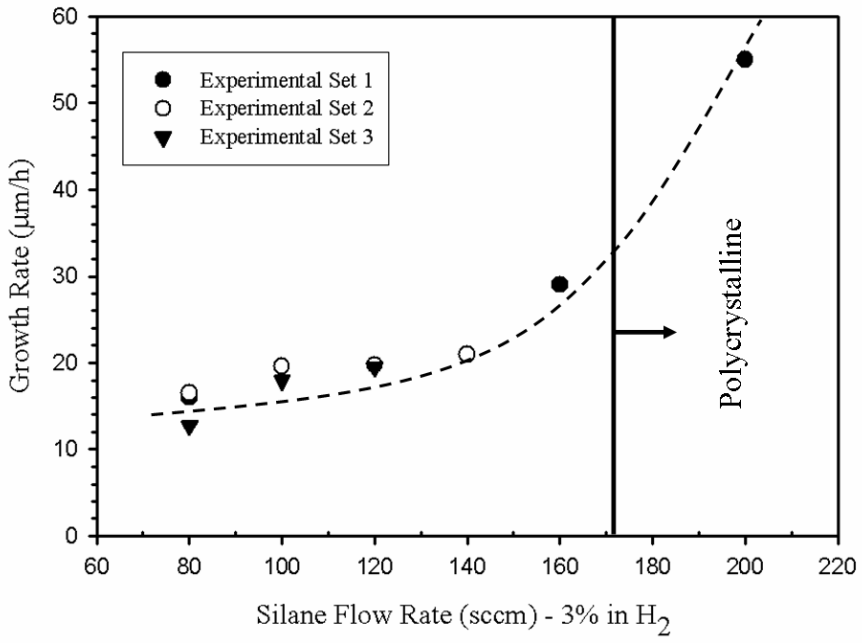

Figure 4.9 Growth rate of 4H-SiC as a function of silane flow rate for three separate experimental sets with the addition of HCl [5]. T = 1530 °C and P = 150 Torr. Curve is used to aid the eye only.

As shown in Figure 4.9, the silane flow rate was increased from 80 sccm to 200 sccm (3% in H_2). The H_2 carrier gas, process temperature, and Si/C ratio for the experiments were maintained at 10 slm, ~ 1530 °C, and 0.33, respectively. As seen in Figure 4.9, with an increase in silane flow rate, the growth rate of the 4H-SiC also increased. All films had smooth, specular surface morphology except for the film grown with a SiH_4 flow rate of 200 sccm (3% in H_2). There are three experimental sets shown in Figure 4.9. The first experimental set was conducted to determine whether the HCl additive process could increase the growth rate. The second set was to provide results for the SiH_4 flow rates between 80 sccm and 140 sccm that were not evaluated in the first set.

The third experimental set was performed to investigate the reliability of the growth rates with higher precursor flow rates.

The amount of HCl needed to produce smooth epitaxial layers at Q_{SiH4} between 80 and 160 sccm (3% in H_2) are shown in a graph in Figure 4.10. The amount of HCl needed to maintain smooth film surfaces increased when the SiH_4 flow increased, as expected. The HCl flow rate for the 80 sccm flow rate of SiH_4 (3% in H_2) experiments remained relatively constant. At Q_{SiH4} of 100 and 120 sccm (3% in H_2), the HCl flow rate varied considerably between the three experiments for each SiH_4 flow. The reason for the high error in HCl flow may have been that the HCl MFC was starting to corrode and the actual flow rate of HCl was different than what was believed to be flowing. Experiments for the higher SiH_4 flow rates of 140 and 160 sccm were not repeated as there were MFC problems due to corrosion and the HCl system was taken down for repair.

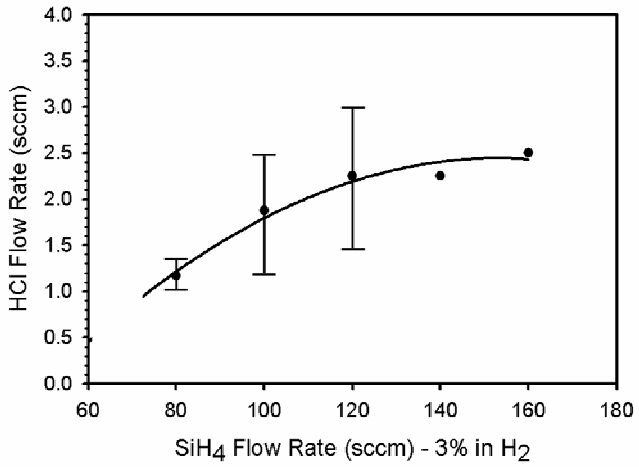

Figure 4.10 HCl flow rate as a function of silane flow rate for the experiments displayed in Figure 4.9. Process temperature and pressure were ~ 1530 °C and 150 Torr, respectively. Curve is used to aid the eye only.

The growth rate as a function of HCl flow rate was also investigated in the 75 mm hot-wall reactor and the results are shown in Figure 4.11. The process conditions were maintained for all experiments at Q_{SiH4} = 80 sccm (3% in H_2), T = 1535 °C, P = 150 Torr, and Si/C = 0.33. The HCl flow rate was varied between 1 and 5 sccm. As seen in Figure 4.11, the growth rate increased with an initial increase of HCl flow from 1.0 to 2.5 sccm. The maximum growth rate of ~ 23 μm/h was produced with an HCl flow rate of 2.5 sccm. As the HCl flow was increased above 2.5sccm, the growth rate began to decrease, indicating the HCl was beginning to etch the film surface. The morphology of the films grown with an HCl flow rate between 1.5 sccm and 2.5 sccm was smooth and specular. However, at an HCl flow rate of 3.0 sccm, growth pits were present on the film surface. Finally, at an HCl flow rate of 5.0 sccm, the resulting film surface displayed severe step-bunching.

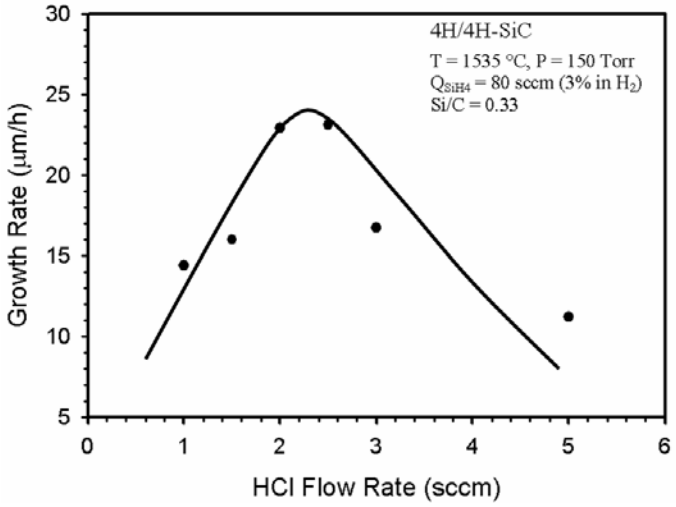

Figure 4.11 Growth rate of 4H-SiC as a function of HCl flow rate in the 75 mm hot-wall CVD reactor. Q_{SiH4} = 80 sccm (3% in H_2), T = 1535 °C, P = 150 Torr, and Si/C = 0.33. Curve is to aid the eye only.

This data is in general agreement with what is normally encountered in the growth of Si films using chlorinated chemistry. Figure 4.12 shows an example of Si growth using silicon tetrachloride ($SiCl_4$), where a clear boundary between growth and etching has been shown for reference. While a similar plot can be generated from this dissertation work with additional experiments, resources did not permit this to be achieved and it is comforting to note from Figure 4.11 that the same qualitative behavior in SiC epitaxy with Cl has been observed.

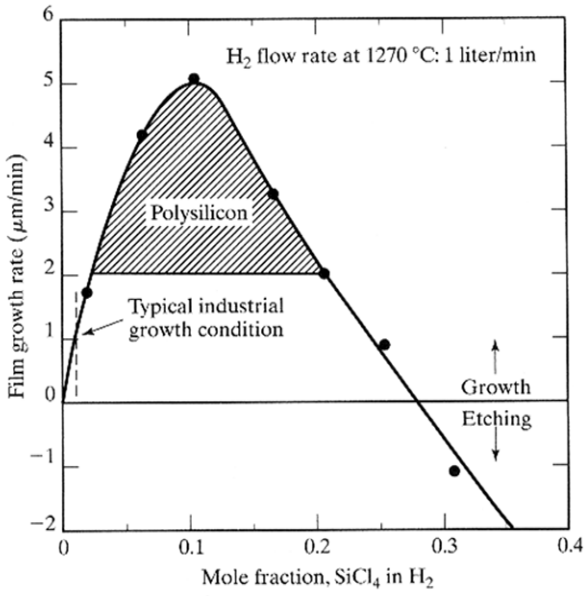

Figure 4.12 Growth rate of Si versus mole fraction of $SiCl_4$ in H_2 [70]. Note that the growth rate increases rapidly for mole fractions below 0.1, then increases steadily for higher mole fractions. Etching occurs for mole fractions above ~ 0.275. This data is in qualitative agreement with Figure 4.11 for 4H-SiC growth using HCl as a growth additive.

4.3.2 Characterization (AFM, XRD, and LTPL)

The structure of the sample shown in Figure 4.7(c) was analyzed using XRD to confirm that the film was single crystal. The samples, whose micrographs are shown in

Figure 4.7(a) and (b), had polycrystalline and wavy surface structures, respectively. If the epitaxial film shown in Figure 4.7(c) was actually polycrystalline and the HCl was only smoothing the surface, then the XRD scan would show a diffraction pattern for a polycrystalline film. The 2θ/ω scan, which is an X-ray diffraction scan used to determine the phase of the crystalline film, is shown in Figure 4.13.

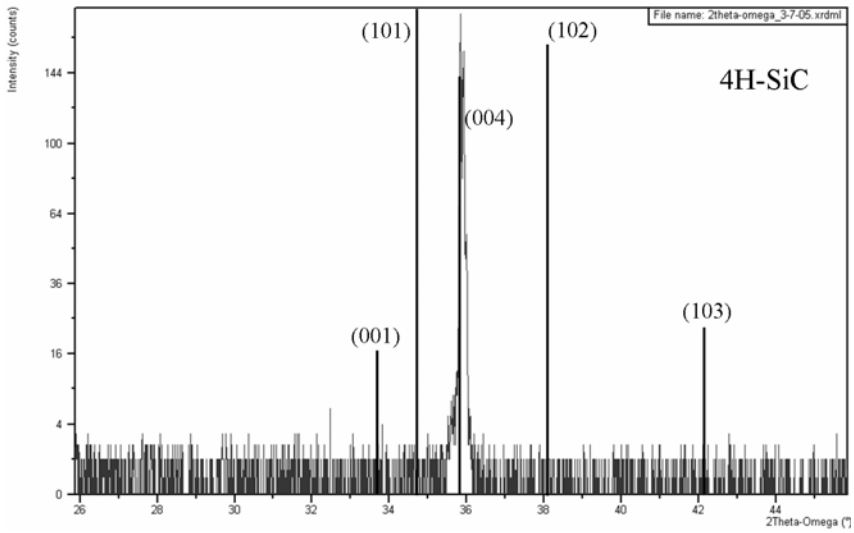

Figure 4.13 XRD 2θ/ω diffraction scan of the sample shown in the SEM micrograph of Figure 4.7(c). The reference pattern for a polycrystalline 4H-SiC film is shown by black vertical lines and the labels indicate the possible reflecting planes. This experiment indicates the film to be single crystal.

The diffraction peak shown in Figure 4.13 is indicative of a single crystal film. The vertical straight lines in Figure 4.13 are the reference peaks for a polycrystalline 4H-SiC film. As seen in the 2θ/ω scan, there is only one peak which is seen at the (004) reflecting plane. The peak is broad because this was a low resolution scan to test the crystallinity of the film. If there were more diffraction peaks the sample would be polycrystalline in nature. It can be stated from these results that the HCl is not etching polycrystalline films into smooth, flat surfaces. The films are actually single crystal.

Comparisons between films grown with and without the addition of HCl as a growth additive were made using AFM analysis of the grown films. The process parameters for both samples were from the baseline process described in Section 3.2, which were T = 1530 °C, P = 150 Torr, and Q_{SiH4} (3% in H_2) = 80 sccm. The AFM surface scans of the films are shown in Figure 4.14. The surface roughness of the sample grown (4.4 μm thick) without HCl was 0.30 nm RMS, while that of the sample grown (3.9 μm thick) with 1.0 sccm of HCl additive was 0.25 nm RMS. These films were chosen to be analyzed as they were representative samples for the baseline process and the baseline process with HCl additive. From the surface roughness values, it may be concluded that the addition of HCl has little to no effect on the films surface roughness. In fact, it may be slightly improving the film surface. It is important to note that this was a comparison of only one experiment from each process (with and without HCl additive). To make a definitive conclusion, more statistical data would be needed. However, the resources were not available for additional experiments.

The film thickness was thinner for the film grown with 1.0 sccm of HCl compared to that grown without the addition of HCl to the baseline process. This is contradictory to the results of the film presented in Figure 4.5, in which the growth rate increased from 16 μm/h for the baseline process to 26 μm/h when HCl was added.

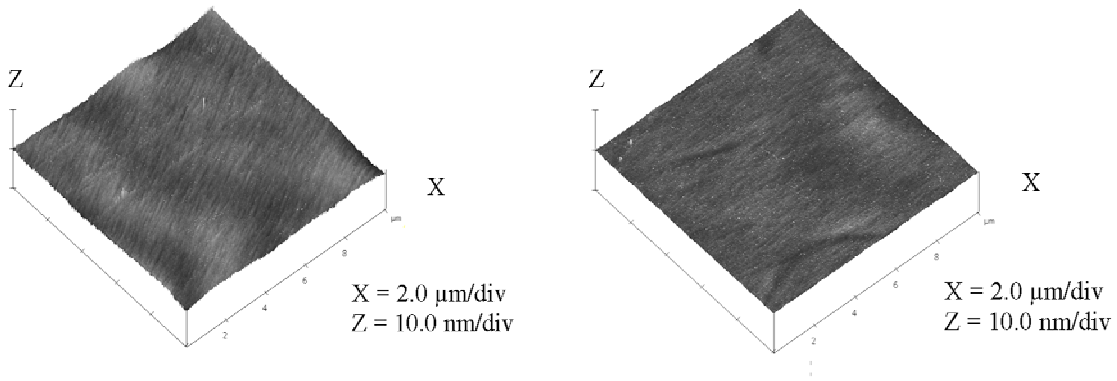

(a) (b)

Figure 4.14 AFM surface scans of 4H-SiC epitaxial films grown for 15 minutes [5] (a) without the addition of HCl and (b) with the addition of 1.0 sccm of HCl, resulting in surface roughness of ~ 0.30 and ~ 0.25 nm RMS, respectively. The AFM scan area was 10 µm x 10 µm. AFM scan of (a) was taken by Dr. S. Rao, University of South Florida.

The structural quality of films grown with and without the addition of HCl were investigated using XRD. X-ray rocking curves of the (0004) diffraction peak were analyzed to determine whether the addition of HCl to the standard chemistry degraded the film quality. A representative 9 µm thick film grown with the baseline process in the 75 mm reactor, described in Chapter 3, Section 3.2, was analyzed. A sample (3.4 µm thick) which was grown with the baseline process and the addition of 1.0 sccm of HCl was also investigated. The X-ray rocking curves for both films are shown in Figure 4.15.

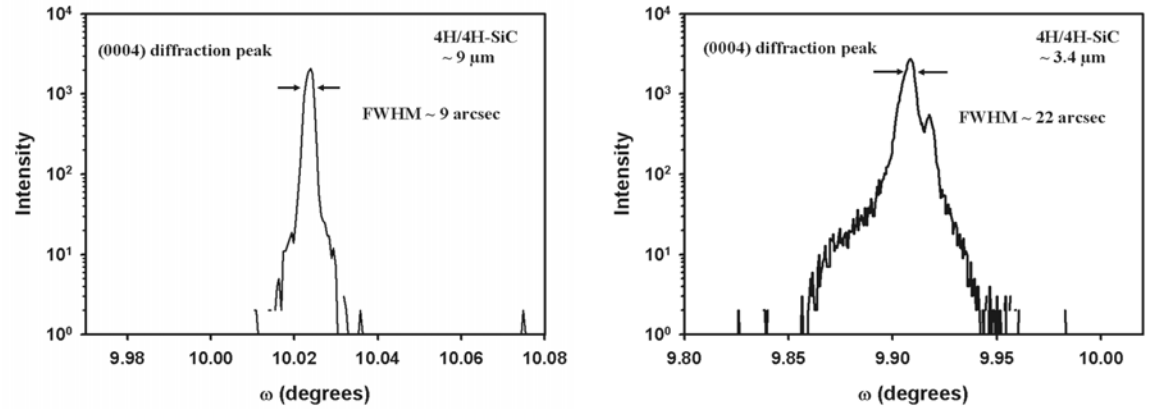

(a) (b)

Figure 4.15 X-ray rocking curve of the (004) diffraction peak for 4H-SiC epitaxial films. (a) Sample grown (USF-04-088) with the baseline process described in Section 3.2. (b) Sample grown with baseline process and the addition of 1.0 sccm of HCl.

The FWHM of the (0004) diffraction peak was 9 arcsec for the film grown without HCl, indicating a high quality film. The film grown with HCl had a FWHM value of the (0004) X-ray diffraction peak of 22 arcsec. The thickness of the film grown with HCl is much thinner than that of the film grown without HCl. This may have been the reason for the higher FWHM value of the diffraction peak. As seen in Figure 4.15(b), there is a double diffraction peak, which may be due to diffraction from both the thin film and the substrate.

The structural analysis of a film grown at a higher silane flow rate of 140 sccm (3% in H_2), which resulted in a growth rate of ~ 21 µm/h, was also analyzed using XRD. The amount of HCl needed to produce a smooth film morphology was 2.25 sccm. An X-ray rocking curve of the film is shown in Figure 4.16. The FWHM value of the (0004) diffraction peak was approximately 19 arcsec. This is comparable to the FWHM value (22 arcsec) from the diffraction peak of the sample grown with the baseline process and the addition of 1 sccm of HCl presented above, which had a growth rate of ~ 13 µm/h.

The increase in SiH_4 flow (which in turn increased the growth rate) and HCl flow rates appear to have little effect on the structural quality of the 4H-SiC epitaxial films from the two experiments conducted. The growth rate increased from 13 μm/h to 21 μm/h by increasing the silane flow rate and increasing the HCl flow rate to produce smooth films. With this increase, the quality remained relatively the same.

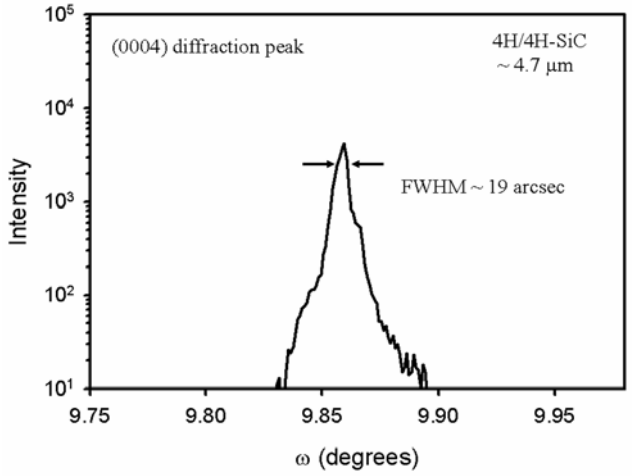

Figure 4.16 X-ray rocking curve of the (0004) diffraction peak of a 4H-SiC epitaxial film grown at a Q_{SiH4} (3% in H_2) of 140 sccm with the addition of Q_{HCl} at 2.25 sccm. The film thickness was 4.7μm.

Low temperature PL, collected at a temperature of 2K at the University of Pittsburgh (Professor W. J. Choyke's group), was used to characterize the films as well. The 9 μm thick film grown using the baseline process of the 75 mm reactor without the addition of HCl, whose XRD rocking curve was shown in Figure 4.15(a), was characterized using LTPL. A 6.4 μm thick film grown using the baseline process with the addition of 0.5 sccm of HCl was also investigated. The near bandedge spectra of the two films were overlayed on one another and shown in Figure 4.17. The two near bandedge

spectra are similar within this wavelength range, indicating that the addition of HCl may not change the quality of the epitaxial film.

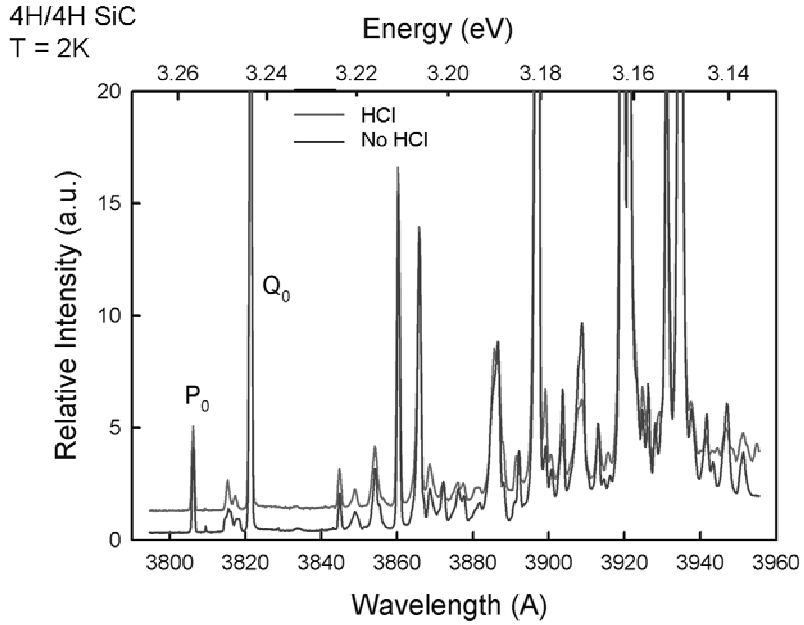

Figure 4.17 Near bandedge LTPL spectra of 4H-SiC epitaxial layers (collected at 2K). Sample USF-04-088 was grown using the baseline process described in Section 3.2, producing a thickness of a 9 μm. The spectrum was overlaid on the spectrum of sample USF-04-089 (6.4μm thick) grown with 0.5 sccm of HCl. Data courtesy of Professor W. J. Choyke, University of Pittsburgh.

The LTPL spectrum at longer wavelengths, between 3980 and 4300 Å, for samples USF-04-088 and USF-04-089 are shown in Figure 4.18. The L_1 defect line is present in the spectrum of the 4H-SiC epitaxial film grown with the baseline process from Section 3.2. However, when 0.5 sccm of HCl gas was added to the same process, the L_1 defect line was not observed in the LTPL spectrum. The L_1 defect line is a zero phonon line that appears in the spectra at 2.901 eV in 4H-SiC. This defect complex may be formed from antisites, interstitials, or Si vacancies [72]. Without the incorporation of HCl into the gas mixture, there may be more Si vacancies. This may be due to the high

concentration of Si_2C present, shown in the thermodynamic simulations in Figure 4.3(b). However, when HCl was added to the gaseous mixture, the Si_2C species were not present in the simulations, as shown in Figure 4.3(a). This may indicate that the Si vacancies are decreasing within the epitaxial films, thus resulting in a reduced/eliminated the L_1 defect line in the LTPL spectrum.

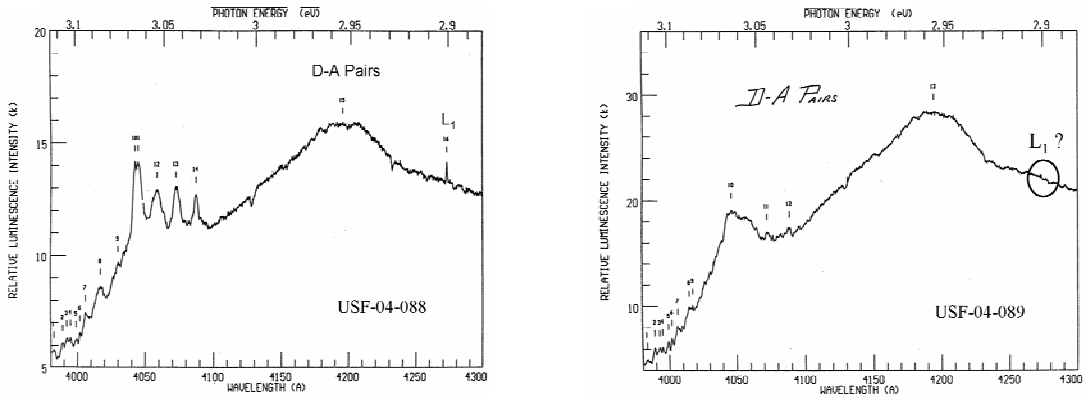

(a) (b)

Figure 4.18 2K LTPL spectra at longer wavelengths, compared to Figure 4.17, showing (a) the presence of the L_1 defect line in the sample grown without HCl and (b) no L_1 defect line present for 4H-SiC epitaxial film grown with the addition of 0.5 sccm of HCl. Data provided by Professor W. J. Choyke, University of Pittsburgh.

Characterization was also performed on three samples to make a definitive analysis whether the growth rate and HCl additive deteriorate the quality of the films. The corresponding near bandedge spectra are shown in Figure 4.19. The 4H-SiC samples in Figure 4.19(a), (b) and (c) were grown with; a Q_{SiH4} of 80 sccm with the addition of 1 sccm of Q_{HCl}, a Q_{SiH4} of 100 sccm with the addition of 1.25 sccm of Q_{HCl} and a Q_{SiH4} of 140 sccm with the addition of 2.25 sccm of Q_{HCl}, respectively. Comparing Figure 4.19(a), (b) and (c), the near bandedge emission does not change with an increase of growth rate.

Also noted was that the L_1 defect line (spectra not shown) was reduced or eliminated with the addition of HCl for all samples.

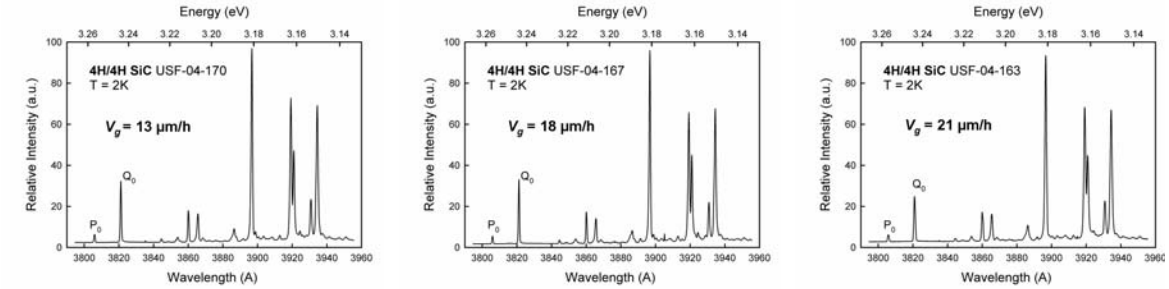

(a) (b) (c)

Figure 4.19 Near bandedge LTPL spectra taken at 2K of 4H-SiC epitaxial films grown using HCl as a growth additive. (a) Sample USF-04-170 with a V_g of 13 µm/hr, (b) sample USF-04-167 with a V_g of 18 µm/hr, and (c) sample USF-04-163 with a V_g of 21 µm/hr. Data courtesy of Professor W. J. Choyke, University of Pittsburgh.

Although the results from the characterization of the 4H-SiC epitaxial films grown with the addition of HCl were very promising, modifications to the CVD reactor had to be made. The amount of HCl needed to produce smooth film surfaces varied from one experimental set to another when the same SiH_4 flow rates were used. Therefore, a new HCl manifold had to be incorporated into the system to provide more reliable HCl flows. Along with adding the HCl gas manifold, the reaction tube was enlarged to accommodate 50 mm wafers.

4.4 HCl Growth Additive Experiments: 200mm Reactor

The 75 mm diameter reaction tube was enlarged to a 200 mm diameter. Details of the reactor modification were presented in Chapter 2, Section 2.4. This enabled the ability to grown on wafers up to 100 mm in diameter, although the 200 mm reactor was

configured to accommodate 50 mm during this research. While upgrading the reactor hardware, the HCl gas manifold was replaced and a methyl chloride gas line was added to the same manifold (which was kept separate from the main manifold to reduce corrosion of the other gas lines). With the new HCl gas manifold and larger reaction tube, HCl experiments were continued and the results are detailed next.

4.4.1 Growth Rate as a Function of Silane Flow

During these experiments, the SiH_4 and C_3H_8 precursors were 100% concentrations instead of the 2% and 3% mixes in H_2, respectively. The development of 4H-SiC epitaxial growth with the addition of HCl in the 200 mm reactor began by adding HCl to a process that was similar to the baseline process detailed in Chapter 3, Section 3.4. The only difference was that the SiH_4 precursor was increased from 30 sccm to 36 sccm, while all other process parameters were held constant. Initially, the amount of HCl added to the process was 15 sccm to achieve a Si/Cl ratio of 2.4, which was approximately what was used in the 75 mm reactor process. The flow of HCl was varied from 5 sccm to 17 sccm, all resulting in degraded surfaces of the grown films compared to the films grown using the baseline process without HCl gas. When an excessive amount of HCl was added to the process with 36 sccm of SiH_4 flow, there was etching of the film surface. An example of a sample with excessive etching is shown in Figure 4.20. The morphology of the film is nearly the same as that shown in Figure 3.11, which was caused from excess precursor flows. Comparing the two images, it seems as though the

surface morphology for excess etching and excess precursor flow rates result in the same morphology.

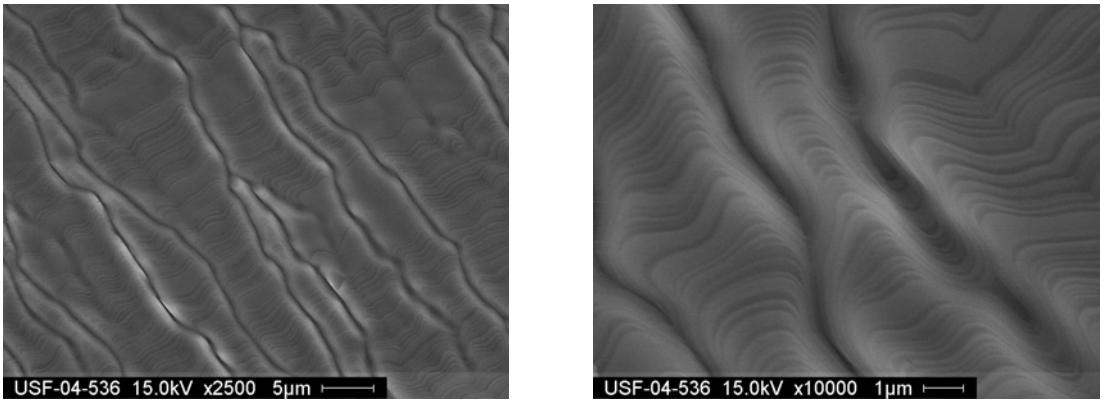

(a) (b)

Figure 4.20 Plan-view SEM micrographs of a 4H-SiC epitaxial film grown in the 200 mm hot-wall reactor with 17 sccm of HCl additive at a magnification of (a) 2500x and (b) 10000x. The Si/C and Si/Cl ratios were 1.0 and 2.0 respectively. $T \sim 1550$ °C. Data taken by Dr. Y. Shishkin, University of South Florida.

It was then determined that it would be best to start out with the baseline process and then slowly add HCl to it, while maintaining a smooth surface morphology. After finding the 200 mm reactor process with HCl additive, then the precursor flows could be increased. This was how the experimental flow occurred for the 75 mm reactor, outlined in Section 4.3.1, so it was logical to follow the same approach for the new reactor. The amount of HCl added to the baseline process (30 sccm of SiH_4) that produced a smooth film morphology was 7.5 sccm, with a Si/Cl of 4.0.

The SiH_4 precursor flow rate was then increased to 35 sccm. The amount of HCl needed to produce a smooth morphology film was 8.75 sccm. The flow rates were incrementally increased by 5 sccm until a SiH_4 flow rate of 45 sccm was achieved. When the precursor flows were increased beyond this point, the film morphology could not be

improved with the addition of HCl. The resultant morphology of films grown beyond a flow rate of 45 sccm was similar to that in Figure 4.20. Plan-view images of samples grown with a SiH_4 flow of 45 sccm are shown in Figure 4.21.

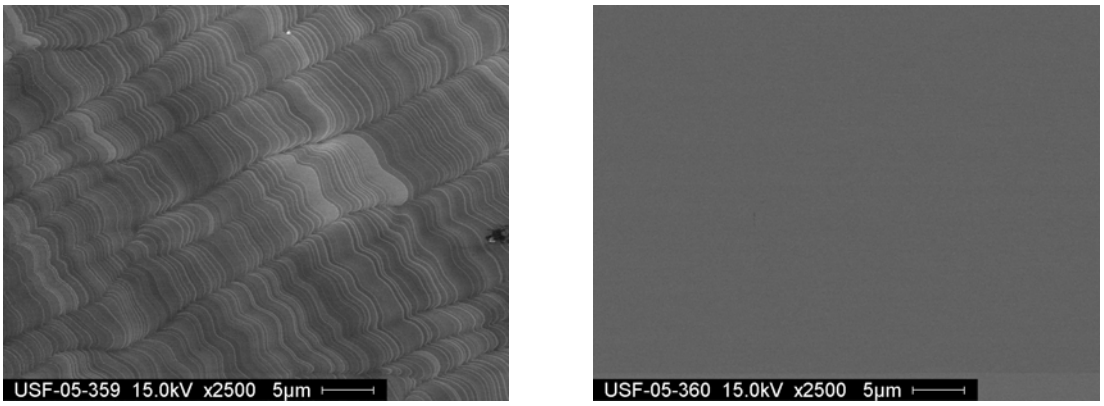

(a) (b)

Figure 4.21 Plan-view SEM micrographs of 4H-SiC grown with a Q_{SiH4} of 45 sccm. The amount of HCl added was (a) 9.75 sccm resulting in a rough surface with a V_g of 44 µm/h and (b) 10.25 sccm resulting in smooth surface with a V_g of 49 µm/h. Data taken by Dr. Y. Shishkin, University of South Florida.

The micrograph in Figure 4.21(a) displays a film surface that has large grooves and is similar to that in Figure 3.11 indicating that not enough HCl was added. The surface of the film shown in Figure 4.21(a) may be caused from Si clusters in the gas phase which deteriorated the film morphology. When a slightly higher flow of HCl (from 9.75 to 10.25 sccm) was added, the film morphology became smooth, as shown by a plan-view SEM micrograph in Figure 4.21(b). The growth rate also increased from 44 µm/h to 49 µm/h with the elevated HCl flow. This may be indicative that the suppression of Si clusters had been achieved.

The results of the growth rate as a function of SiH_4 flow are displayed in the graph in Figure 4.22. All film morphologies were similar to the morphology shown in the plan-view micrograph in Figure 4.21(b).

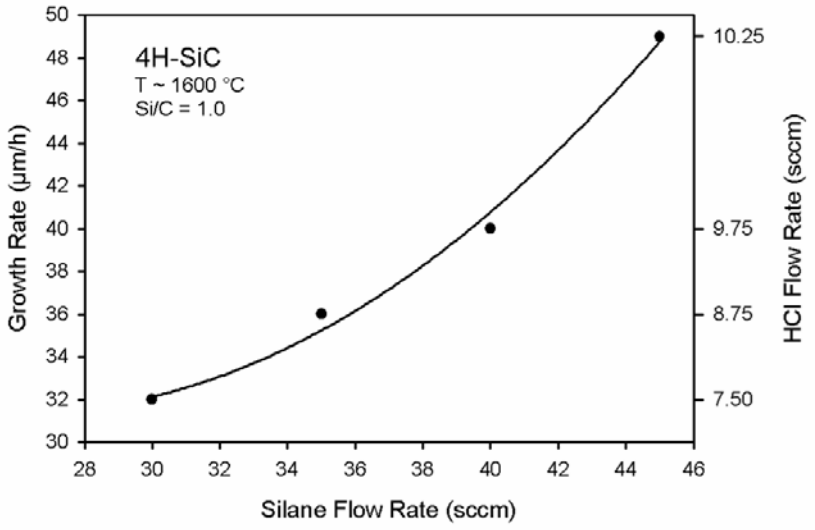

Figure 4.22 200 mm reactor growth rate as a function of SiH_4 flow rate. The HCl flow rates needed to produce films of smooth morphology are displayed on the right vertical axis. Solid trend line to aid eye only.

As shown in Figure 4.22, the growth rate increased with an increase in SiH_4 flow rate. The amount of HCl flow needed to produce smooth morphology films also increased with an increase in silane flow rate, as expected. With an increase of silane flow by 50%, the growth rate increased by ~50% and the HCl needed for the process increased by ~40%. The highest growth rate achieved in the 200 mm reactor with smooth morphology was 49 µm/h. Unfortunately, the HCl MFC failed again, so the experiments were not pursued further. The growth rate might have been increased beyond this value had the process been stable. With an increase in SiH_4 flow rate, an increase in HCl flow was needed as well. The ratio of Si/Cl was not constant for the increase in SiH_4 flow rate. The Si/Cl ratio was maintained at 4.0 for the experiments performed with a silane flow rate of

30 and 35 sccm. However, the ratio increased to 4.1 for a SiH_4 flow of 40 sccm and increased additionally to 4.4 for a SiH_4 flow of 45 sccm. This implies that Si/Cl ratio needed to suppress the gas phase homogeneous nucleation varies for higher SiH_4 flow rates.

The thickness of each sample presented in the graph in Figure 4.22 was measured using FTIR to confirm the thickness of the HCl samples grown in the 200 mm reactor. The method used to determine the correct film thickness is detailed in Appendix E. A comparison of an FTIR spectra compared to a cross-section SEM micrograph, used to determine the thickness of a film is shown in Figure 4.23.

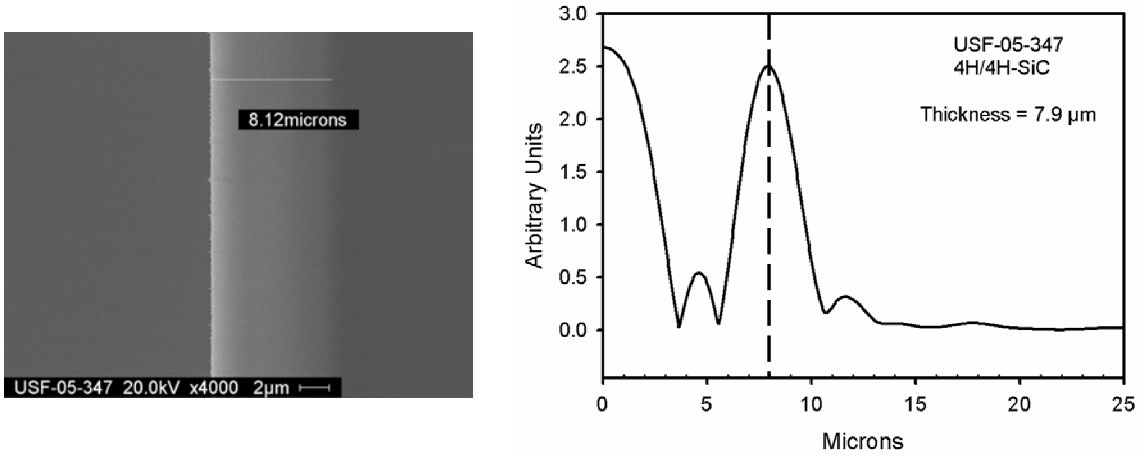

(a) (b)

Figure 4.23 Thickness results for a 4H-SiC epitaxial film grown with the 200 mm reactor baseline process with 30 sccm of SiH_4 and 7.5 sccm of HCl. (a) Cross-section SEM micrograph of bottom edge showing thickness of 8.12 µm and (b) Fourier transform of the reflectance spectrum showing thickness of ~ 8 µm.

The thickness of a 4H-SiC film, using the 200 mm baseline process with a SiH_4 flow of 30 sccm and an HCl flow of 7.5 sccm, determined by cross-section SEM micrograph and FTIR are in very close agreement. The percent error between the two measurements was approximately 3%. The same comparison was made for the other

three sample thicknesses presented in Figure 4.22. The percent error of thickness comparing the cross section SEM micrograph and the FTIR spectrum techniques are ~ 8% for the 35 sccm of SiH_4 sample, 2.5% for the 40 sccm of SiH_4 sample, and ~ 1.5% for the 45 sccm of SiH_4 sample. Therefore, from the comparison of these measurements, it can be concluded that the thicknesses of the HCl samples presented in Figure 4.22 are correct.

Electrical, structural and surface characterization of the films presented in Figure 4.22 was performed. The results are presented in the next section.

4.4.2 Characterization

To determine whether the increased growth rate and the addition of HCl had an affect on the doping of the samples, the net carrier concentration of the samples from the experiments described in Section 4.4.1 was evaluated using the C-V technique. The results are shown in Figure 4.24 and summarized in Table 4.2. From the graph, the doping of the films remained relatively constant with an increase in growth rate. The doping concentration was found to be in the low 10^{16} cm^{-3} range. Comparing the doping of a baseline process sample to a sample with the addition of HCl, the carrier concentrations are similar. This indicates that the addition of HCl used to increase the growth rate has little effect on the net carrier concentration of the films.

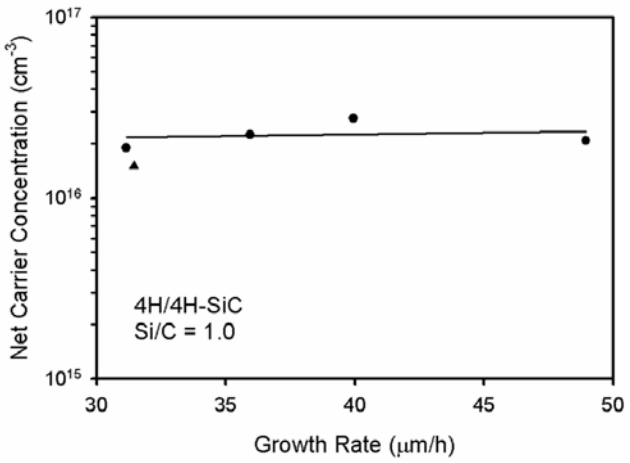

Figure 4.24 Net carrier concentration of 4H-SiC films grown with the addition of HCl at elevated growth rates. The closed-circle data points are the experiments from Figure 4.22. The triangle data point is the doping density of a baseline process sample. The trend line is to aide the eye only.

The surface roughness of a film grown with the baseline process (V_g = 32 μm/h) was compared to that of a film grown with HCl additive at a higher SiH_4 flow rate of 45 sccm. The corresponding AFM scans are shown in Figure 4.25. The film grown with HCl (V_g = 49 μm/h) was produced from an HCl flow of 10.75 sccm. The surface is very smooth for the baseline process sample. The sample grown with added HCl does have a groove on the surface which could have been a defect extended from the substrate. The surface roughness values for the films grown without and with HCl additive were 0.6 nm RMS and 0.9 nm RMS, respectively. Comparing the two films, the surface roughness did not increase by much for the higher growth rate film.

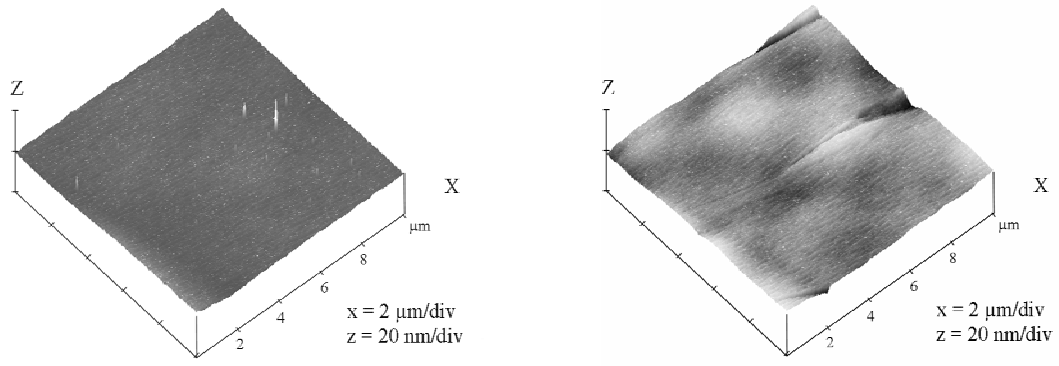

(a) (b)

Figure 4.25 AFM surface scans of 4H-SiC epitaxial films grown in the 200 mm LP hot-wall CVD reactor. Film grown (a) using baseline process (USF-05-099) and (b) with SiH_4 flow of 45 sccm and HCl flow of 10.25 sccm (USF-05-360). The resulting surface roughness values were 0.6 nm RMS and 0.9 nm RMS, respectively. Process $T \sim 1600$ °C.

The structural quality of the films was analyzed using XRD. The results of this analysis are displayed in Table 4.2. The FWHM values of the (0004) diffraction peak ranged between 8.3 and 13.6 arcsec for SiH_4 flow between 30 and 45 sccm. The increased growth rate does not seem to be a large factor in the quality of the films. The (0004) diffraction peaks do broaden slightly with an increase in growth rate, however, the FWHM values prove the 4H-SiC epitaxial films to be of good quality.

Table 4.1 200 mm CVD reactor film properties versus growth rate.

Sample ID	Q_{SiH4} (sccm)	Q_{HCl} (sccm)	V_g [1.] (μm/h)	Net Carrier [2.] Concentration (cm^{-3})	XRD[3.] FWHM (arcsec)
USF-05-347	30	7.5	31.2	1.89×10^{16}	8.30
USF-05-348	35	8.75	36.0	2.24×10^{16}	10.5
USF-05-350	40	9.75	40.0	2.76×10^{16}	12.6
USF-05-360	45	10.25	49.0	2.08×10^{16}	13.6

T ~ 1600 °C, P = 150 Torr, and Si/C =1.0.
1.) As determined by cross-section SEM analysis
2.) As determined by the C-V technique
3.) As determined by XRD rocking curve analysis of the (0004) plane.

The rocking curve of the film with the highest growth rate of 49 μm/h is shown in Figure 4.26. The FWHM of the (0004) diffraction peak is 13.6 arcsec. This is a reasonable value compared to other films grown in hot-wall CVD reactors from the literature [18,24]. The FWHM values of the (0004) diffraction peak for other films grown with high growth rates during this work are slightly lower than 13.6 arcsec.

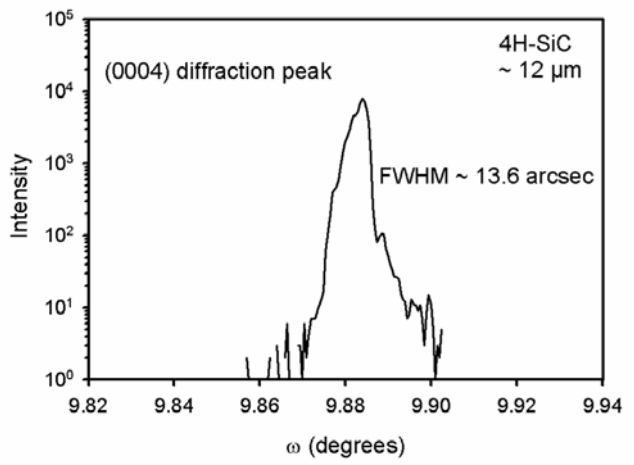

Figure 4.26 X-ray diffraction rocking curve of the (0004) diffraction peak for the 4H-SiC film with the highest growth rate (49 µm/h), indicated in Figure 4.22. The FWHM value for the 12 µm thick film is 13.6 arcsec. Data taken by Dr. Y. Shishkin, University of South Florida.

4.5 Summary

The growth of 4H-SiC epitaxial films with the addition of HCl has been demonstrated in a hot-wall CVD reactor. The growth rate has been increased from the baseline process of 30-32 µm/h to 49 µm/h in the 200 mm reactor. This has been accomplished by increasing the partial pressure of the precursors and adding HCl to the process. When the SiH_4 flow rate was increased, the growth rate increased when the correct amount of HCl was added to the process (shown in Figure 4.21). The mechanism for this effect was proposed, in which the HCl suppresses gas phase nucleation of Si. Comparing the baseline process without and with the addition of HCl, the surface roughness only slightly increased. The film quality did not degrade with the introduction of HCl as shown by LTPL analysis (for the 75 mm reactor process) and XRD (for both the 75 mm and 200 mm reactor processes). Overall, the growth rate increased by approximately 1.5 times the baseline process for both reactors (the 75 mm and the 200

mm). With the malfunctioning of the HCl MFC, the growth rate investigation could not be pursued further. Future work regarding the higher growth rates will be discussed in Chapter 5.

CHAPTER 5

SUMMARY AND FUTURE WORK

5.1 Summary

The development and characterization of a high-growth rate 4H-SiC epitaxial growth process in a 200 mm horizontal hot-wall CVD reactor was completed during this dissertation work. The process development focused on the growth rate and the surface morphology of the grown films. Characterization of the films was carried out using optical (LTPL), electrical (CV-IV) and structural (X-ray, AFM and SEM) analysis. Using standard SiC CVD chemistry to develop a baseline CVD process resulted in the highest growth rate (32 μm/h) to date using a horizontal hot-wall reactor at temperatures around 1600 °C. Epitaxial layers were also grown by introducing hydrogen chloride into the gaseous mixture which permitted an increase in the silane flow rate and, thus, a maximum growth rate of 49 μm/h.

Thermodynamic simulations for the baseline process were carried out to determine the dominant chemical species in the reacting system. The simulations were also performed on the growth process which included the addition of HCl gas. The simulations were used to predict if homogeneous gas phase nucleation of Si was expected in the system for the growth parameters studied. The analysis was able to predict where

the highest concentrations of the dominant chemical species (SiH_2, Si, and CH_4) were developing within the reactor. This type of information could be helpful if growth was not occurring within the hot-zone. By predicting which species are generated within the hot-zone, one can decide whether the temperature or pressure, or any other parameter is needed to be changed to improve the growth.

A growth rate of 16 μm/h was previously obtained using the 75 mm hot-wall reactor. The downside to this reactor size was that the maximum substrate size was only 2 cm in diameter. During this research the reactor diameter was scaled up to accommodate substrates up to 100 mm in diameter, however, the reactor was configured for 50 mm diameter substrate sizes for the experiments performed. A growth process for 100 mm substrates will be developed in the future. The development of the 4H-SiC baseline process for the 200 mm reactor was initiated by using the 75 mm hot-wall reactor process parameters developed previously. The process development of the 200 mm reactor entailed changing various process parameters such as pressure, silane flow rate, and Si/C ratio. The characterization of the grown films, by SEM analysis, was used to adjust the process parameters from run to run, to finally achieve films with smooth morphology at the highest growth rates possible. LTPL and XRD were later used to assess the optical and structural quality of the films, respectively. The surface morphology of the films was smooth and specular, with little to no surface defects observed for films of thickness less than 30 μm. AFM analysis was performed on thick films (30 and 65 μm) and it was found that the surface roughness was approximately 0.3 nm RMS for both films which is quite respectable. When thicker films were produced (> 30 μm), occasional defects were seen on the surface such as carrot-like and triangular defects which are known to develop

with thicker films. The LTPL response was measured at 2K on a 23 μm thick film. Near band-edge spectrum showed a strong intrinsic peak, which is an indication of good crystalline quality. The four-particle Al complex peak was also seen via LTPL indicating Al contamination of the films was occurring during growth. The contamination source is still unknown and should be investigated in the future. The X-ray rocking curves of the (0004) diffraction peak were sharp with the lowest FWHM value being 9 arcsec, which is comparable to the best values reported in the literature (~ 5 arcsec [27]).

After the development of the baseline process in the 200 mm hot-wall reactor, the process was altered to achieve even higher growth rates. This was accomplished by increasing the silane flow rate, which in turn increases the growth rate. There are some issues with increasing the silane flow alone. When excessive amounts of SiH_4 is injected into the growth zone, a supersaturation of gas phase reactions typically occur creating Si clusters which are detrimental to the epitaxial surface morphology. To reduce or eliminate this problem, HCl was introduced into the standard H_2-C_3H_8-SiH_4 chemistry. By increasing the silane flow rate and introducing HCl gas, the growth rate was incrementally increased from 32 to 49 μm/h. The morphology and structural quality of the films were found to be similar to that of the baseline process. Unfortunately, there were some limitations to this process. The HCl mass flow controller (MFC) and other plumbing parts were corroding due to the highly corrosive HCl gas. Corrosion affected the repeatability of the growth process and the possibility to increase the growth rate further. During the HCl additive experiments, the silane flow rate was increased in increments, and, at each flow, a specific HCl flow rate was needed to produce films of smooth morphology. However, when the process was repeated at a later time using the

SiH_4 and HCl flows found initially, the flows did not produce the same quality of epitaxial layers. This indicated there was some problem with the HCl gas delivery system, mainly the HCl MFC. The 4H-SiC epitaxial process was not evaluated beyond a flow rate of 50 sccm for SiH_4 due to the HCl MFC failure. The maximum growth rate achieved during this research was therefore 49 μm/h, for a silane flow of 50 sccm, which may not yet be the upper limit for the process. Due to the corrosion of the system, the research using HCl additive to the standard chemistry process for 4H-SiC epitaxial growth was terminated.

5.2 Recent and Future Work

5.2.1 Chemistry

The growth of 4H-SiC epitaxial layers using HCl as a gas additive proved to be a promising technique to increase the growth rate. However, as explained above, the corrosion of the reactor system is a significant problem not only to the reactor parts, but also to establishing a repeatable growth process using this approach. An alternative to adding HCl gas, while still achieving the basic principle of suppressing homogeneous gas phase nucleation via the presence of chlorine in the gas mixture, is to use methyl chloride (CH_3Cl) instead of HCl. CH_3Cl would not necessarily replace C_3H_8 as the carbon source. The reason is that in order to maintain both constant Si/C and Si/Cl ratios, propane must also be added to the process along with the CH_3Cl gas. Using CH_3Cl instead of HCl may help to reduce the corrosion of the system (i.e. gas lines, etc.) since only cracked CH_3Cl would lead to corrosion and might prove to be a precursor which could produce more

stable and repeatable results. Corrosion will still occur, but at a much slower rate than when using HCl gas.

Preliminary experiments had been performed to determine the difference in surface morphology and growth rate for growth processes which included HCl and that which included CH_3Cl. There was no substantial difference in the surface morphology using the process parameters which produced the same Si/C and Si/Cl ratios. SEM micrographs of the surface morphology for the film grown with HCl and the film grown with CH_3Cl are shown in Figure 5.1. The horizontal lines on the micrograph are noise from the SEM tool and are not actual surface structures. The growth rate for the HCl additive sample was 33 μm/hr, while that of the CH_3Cl additive sample was 37 μm/hr. There was a slight increase in growth rate; however, only one experiment was performed due to resource limitations. Further analysis is needed to determine the differences between the two techniques.

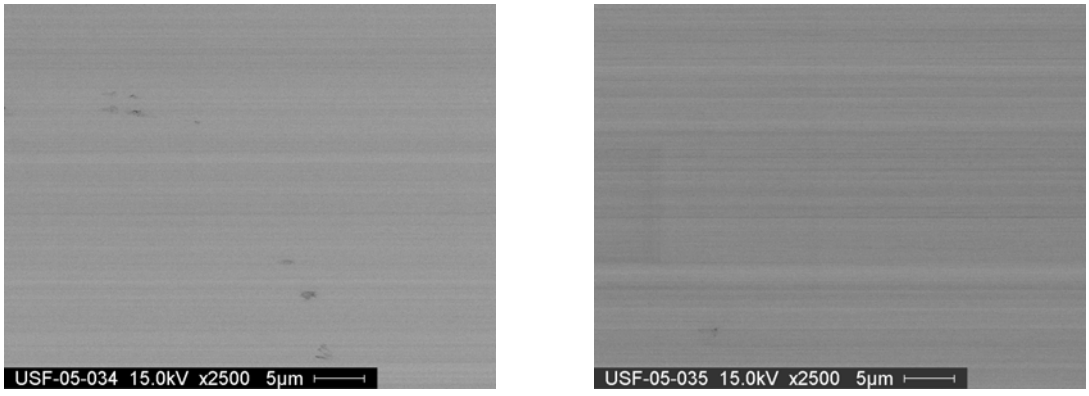

(a) (b)

Figure 5.1 Plan-view SEM micrographs of 4H-SiC grown with (a) HCl additive and (b) CH_3Cl additive to the standard chemistry of H_2-C_3H_8-SiH_4. P = 150 Torr, T = 1550 °C, Si/C = 1.0 and Si/Cl = 4.0. The growth rates were 33 and 37 um/h, respectively.

Thermodynamic simulations were performed to predict differences in the mole fractions of the dominant species in the system when growing with HCl and CH_3Cl as a gas additive. The results of the simulations are shown in Figure 5.2. The Si/C and Si/Cl ratios for each additive were the same at 1.0 and 4.0, respectively. In order to obtain the same values, C_3H_8 was added along with CH_3Cl. The most dominant specie in the system is, as expected, hydrogen. However, H_2 is not shown in the figure as it has a much higher mole fraction, approximately 1, compared to the other species. As seen in Figure 5.2, the mole fractions for all species are approximately the same when using HCl as an additive versus CH_3Cl. This should be the result because the same number of moles of carbon, silicon, and chlorine are being added into the system. The highest mole fraction below 1800 °C is solid SiC. The following highest mole fractions are atomic H and HCl for both cases. The dominant carbon source is CH_4, while the dominant Si source species are Si and SiH. The simulations are an indication that the growth process should be similar for either additive, as long as the Si/C and Si/Cl ratios are maintained.

Comparing the results of the simulations presented in Figure 5.2 to that presented in Chapter 2, Figure 2.1, the process with the added chlorinated gas has many more species than that of the standard 4H-SiC baseline process. The reason for this is that either HCl or CH_3Cl was added into the gas mixture, creating species that have Cl. This is what accounts for the added species in the list presented in Figure 5.2.

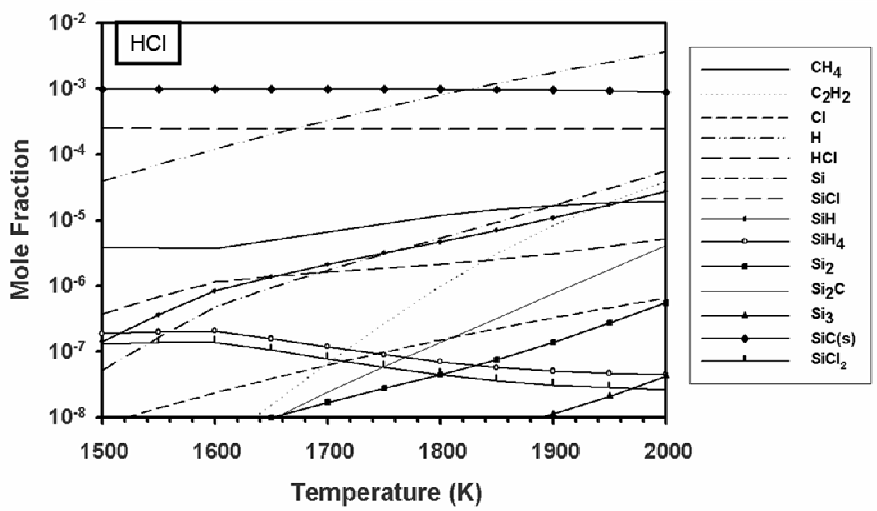

(a)

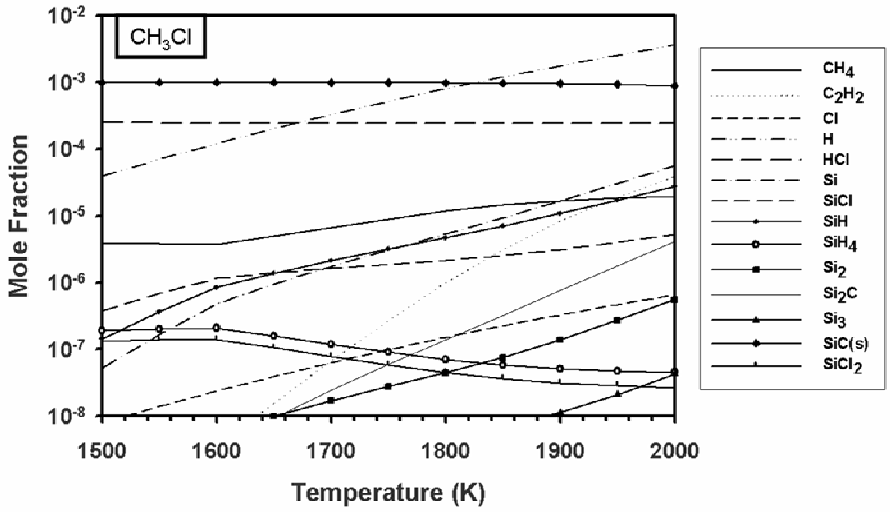

(b)

Figure 5.2 Thermodynamic simulations of the standard CVD growth chemistry with the addition of (a) HCl additive and (b) CH_3Cl additive. The Si/C ratio and Si/Cl ratio were 1.0 and 4.0, respectively. H_2 is excluded from graphs. Simulations performed using NASA CEA code [40].

Koshka, *et al*. [73] reported on the growth of 4H-SiC epitaxial layers using CH_3Cl to replace C_3H_8 as the carbon source,. A comparison between the two carbon precursors was made at a temperature of 1600 °C. The surface morphology for the film grown with

CH_3Cl was smooth resulting in a growth rate of 7 μm/h. However, growth conducted with C_3H_8 while using the same silane flow rate as with the CH_3Cl experiment resulted in film degradation and a lower growth rate of 2.6 μm/h. Koshka, *et al*. [74] also reported on a 4H-SiC epitaxial growth process using CH_3Cl, to again replace C_3H_8, at reduced growth temperatures of ~ 1300 °C. The film surface morphology was mirror-like and a growth rate of 2 μm/h was achieved. LTPL was performed on the sample and the spectrum indicated a good film quality which was as good as that of the films grown at 1700 °C. From [73,74], it can be seen that CH_3Cl may, in fact, be a precursor worth investigating for future work on 4H-SiC halocarbon epitaxial growth.

The epitaxial growth of 4H-SiC using CH_3Cl as a growth additive may be carried out in the same fashion as the HCl additive experiments. A suggestion would be to start with the baseline process (standard chemistry H_2-C_3H_8-SiH_4). Then introduce CH_3Cl into the baseline process at a low flow rate to a point where the surface morphology remains smooth and specular. Then increase the SiH_4 flow rate to increase the growth rate while maintaining the CH_3Cl flow rate from the first experiment. If needed, increase the CH_3Cl flow rate until a smooth film surface is produced. Then proceed to a higher silane flow rate and perform the experiments by the method of increasing the SiH_4 flow rate and then introducing more CH_3Cl until a smooth morphology is achieved. The films should be characterized using FTIR for thickness measurements, AFM for surface roughness, XRD for structural quality and LTPL for optical quality. An interesting investigation would be to determine whether the samples using the same Si/C and Si/Cl ratios, but using the two different additives, would result in the same structural and optical quality.

5.2.2 Temperature Uniformity

Another issue to look into is the temperature distribution across the 50 mm wafer area within the hot-zone. Currently, there is approximately a 20 -25 °C ΔT across this area with a P = 150 Torr and Q_{H2} = 30 slm, with a 120 °C ΔT across the entire susceptor and a 20 °C ΔT from the middle to the back end of susceptor. Experiments have been performed by M. Reyes and S. Harvey growing 3C-SiC on a 50 mm Si wafer at ~ 1380 °C in the center of the growth zone. The backend of the wafer melted while the front end of the wafer resulted in polycrystalline film. The only single-crystal material was in the center of the wafer. This is an indication that there is a temperature uniformity issue, the temperature being too low in the front and too high in the back of the growth zone. Based on these experiments, growth on a 50 mm wafer could not be successfully carried out with this temperature gradient. Interestingly, characterization of the reactor during this research using 4H-SiC did not indicate such a high degree of growth non-uniformity but that is a different process and at a higher temperature.

The temperature uniformity issue has been studied recently due to the problems encountered as described above. The RF coils were adjusted to determine whether any significant improvement to the temperature profile could be produced. The coils were put closer together at the front of the hot-zone and spread further apart in the back. This was done to increase the temperature at the front end of the susceptor while decreasing the temperature at the backend (this had been successfully used in the past to level out the temperature uniformity in the cold-wall reactor). Unfortunately this resulted in a higher ΔT, increasing to 150 °C across the entire susceptor and 25 °C from the middle to the backend of susceptor. Another experiment performed to improve the temperature

uniformity was to raise the polycrystalline plate off the susceptor's backend which would reduce the temperature of the substrate since the plate would not be in intimate thermal contact with the susceptor. This improved the temperature profile by 5 °C from the middle to the backend of susceptor. Since this experiment improved the profile slightly, the bottom susceptor had some of the mass removed which was done to reduce the thermal mass in that area. This was accomplished by removing a portion of the bottom of the bottom susceptor, starting at the center and creating an angle upward toward the back end. The same was done on the top of the bottom susceptor. The backend was changed from a thickness of 15 mm to 12 mm, initially. A schematic drawing of this is shown in Figure 5.3.

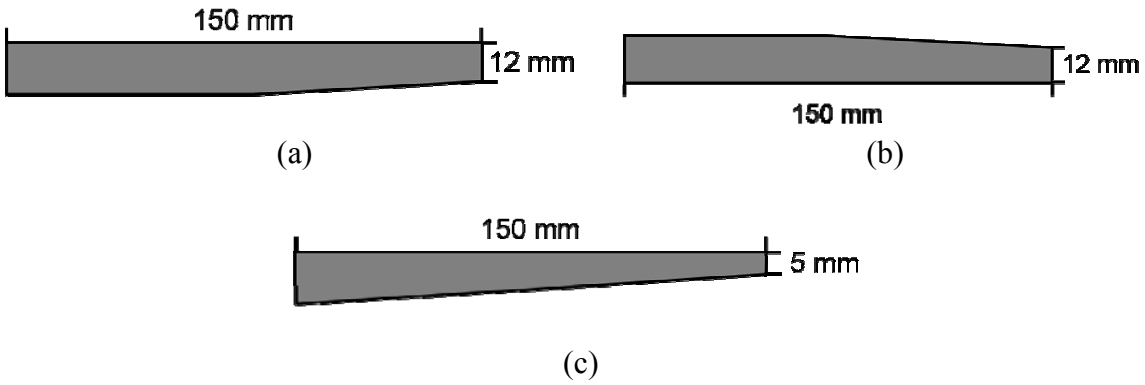

Figure 5.3 Cross-section schematic drawing of the 200 mm reactor susceptor bottom with a portion of the (a) bottom removed and (b) top removed to produce a backend thickness of 12 mm, (c) bottom removed additionally from (a) to produce a backend thickness of 5 mm.

The modifications shown in Fig. 5.3(a & b) resulted in a profile that was slightly improved with a measured ΔT of 10 °C from the middle to backend of the susceptor. Since this design improved the temperature distribution, the susceptor had even more mass removed from the bottom of the bottom susceptor in both designs by extending the

shaved area to the front end of the susceptor and making the thickness at the backend to be 5 mm (shown in Figure 5.3(c)). The temperature distribution with this design had approximately a 15 °C ΔT from middle to back of the susceptor. Since the additional shaving of the susceptor from the bottom did not improve the temperature distribution enough, then the mass of the top susceptor may need to be reduced. This trial and error process needs to be continued until there is at most a 5 °C temperature difference from front to back across the 50 mm wafer area. Another issue may be that the susceptor top and bottom portions are so close together at the backend of the susceptor that the area close to the backend will always be hotter with this design. A suggestion would be to increase the distance between them, i.e. decrease the angle of the top portion of the susceptor to increase the distance between top and bottom portions at the backend of the susceptor. Once the temperature uniformity is improved, growth on a 50 mm wafer will be possible. The epitaxial films may then be characterized across the entire wafer to determine doping and thickness uniformity of the layer.

5.2.3 CVD Simulations

One of the most important tasks that has yet to be fully addressed is the complete modeling of the hot-wall CVD process. At the 2005 ONR Electronic Materials Program Review, Dr. Y. Makarov of Semitech [75] presented simulations of a CVD reactor, which were performed using Semitech software. At the same review, Dr. Saddow presented results of 4H-SiC epitaxial layers grown in the 200 mm reactor during this dissertation work (see Chapter 3). Dr. Y. Makarov was very interested in the epitaxial growth results

and offered to model the 200 mm reactor to predict the distribution of species and growth rate within the reactor.

As stated in Chapter 2, a system of equations must be developed that encompass all phenomena involved in order to model this or any CVD process. The flow of the reactants, reactor temperature distribution, and reactant species distribution are required to simulate the process. CVD reactor models involve non-linear partial differential equations that represent conservation of momentum and energy, and track individual chemical species [46,47,76]. Along with the transport equations, the homogeneous reactions and surface reaction equations must be solved [77]. Many computer programs have been created to solve such equations and to model CVD reactors. The final 200 mm horizontal hot-wall reactor design was modeled by Dr. Y. Makarov and Dr. A. Galyukov of Semitech [75] using a software program called CVD-Module ™. The geometry used for the simulations is that shown in the reactor cross-section sketch, Figure 3.7. Since any hot graphite part can affect the reaction, it is critical to include the graphite adapters as well (e.g. silane may crack and SiC may form on the adapters, thus robbing reactants from the growth zone farther downstream).

The information needed to perform the computational analysis was the reactor geometry (Figure 3.6), the gas flow rates, the process temperature and pressure, and the hot-zone temperature profile. The temperature profile was determined by performing multiple Si melt tests along the susceptor in the 200 mm reactor. The Si melt test samples were placed 15 mm, 39 mm, 61 mm, 73 mm, 107 mm and 131 mm along the flow direction starting at the front (gas inlet side) of the susceptor. Figure 5.4 shows the measured temperature profile as determined by the Si melt tests. The temperatures along

the vertical-axis correlate to the relative temperature with respect to the center of the hot-zone. As seen in Figure 5.4 there is a temperature difference of about 20 – 25 °C in the center of the hot-zone for an area corresponding to a 50 mm wafer. The lateral temperature gradient (not shown) was measured to be ~ 1-5 °C, which is essentially negligible.

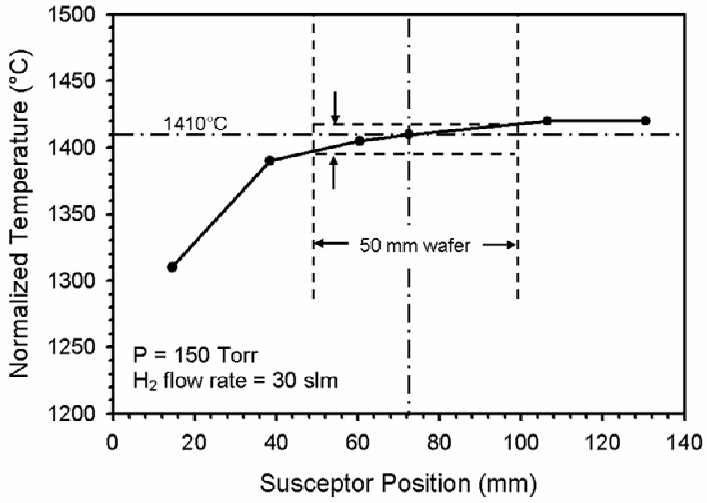

Figure 5.4 Temperature profile measured at the bottom of the susceptor in the 200 mm horizontal hot-wall reactor. Vertical dotted lines indicate the position of a 50mm wafer and horizontal dotted lines represent the corresponding temperature difference. A 20 - 25 °C temperature gradient was measured, with the hottest position being towards the hot-zone outlet. Data is normalized with respect to the hot-zone center as indicated by the dashed lines.

Along with the measured temperature profile, the process parameters used for the simulations were those similar to the baseline process in the 200 mm reactor, Section 3.4. The parameters were: P = 150 Torr, T = 1565 °C, Q_{H2} = 30 slm, Q_{C3H8} = 8 sccm, Q_{SiH4} = 30 sccm (Si/C = 1.2). With the process parameters, reactor geometry, and temperature profile, the following simulations, shown in Figure 5.5 and Figure 5.6, were generated. The temperature profile of the reactor was used to input information about the actual

process into the simulations. With the measured data, the simulated temperature profile should be more realistic. Note that the temperature of the ceiling of the susceptor was assumed to have the same temperature distribution as the bottom since the Si melt test could only be performed on the bottom of the susceptor. The computed temperature profile of the 200 mm horizontal hot-wall reactor is shown in Figure 5.5.

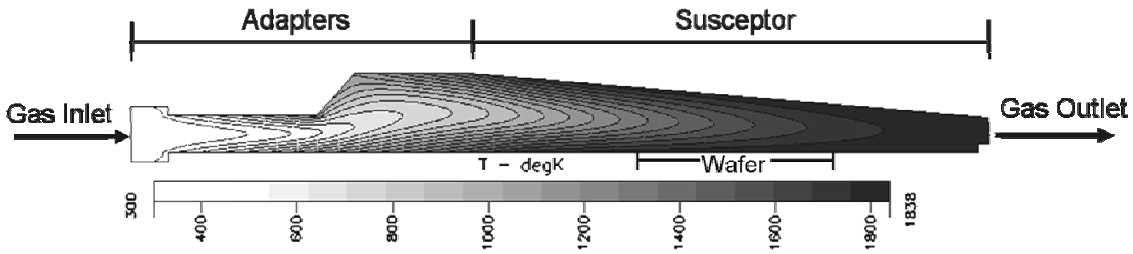

Figure 5.5 Computed 2D temperature profile in the 200 mm horizontal hot-wall CVD reactor. Temperature profile scale is in Kelvin. Data provided by Dr. Y. Makarov and Dr. A. Galyukov [75].

The 2D simulation represents the cross section of the reactor hot-zone which includes the adapters and the susceptor. The geometry shown in the 2D temperature profile in Figure 5.5 is the shape of the 200 mm reactor area where the gases flow through the graphite parts. The gases enter the left hand side from the gas inlet port (inlet) and exit the right side (outlet). The susceptor position is also shown. The simulations predict that the temperature increases starting at the inlet of the hot-zone and reaches a maximum at the outlet. When looking at a specific distance along the reactor, there is a temperature gradient going from the susceptor bottom to the susceptor ceiling, in which the center is the coolest section. This is due to the ceiling and bottom portions being hotter than the gases between them. However, the ceiling and bottom are very close to

each other near the outlet (10 mm spacing), in which the simulations predict there is a small temperature gradient in that area.

The mass fractions of the dominant species (CH_4, SiH_2, and Si) from the thermodynamic simulations in Figure 2.1, as well as SiH_4, were also modeled for the reactor. The distributions are shown in Figure 5.6. The methane, CH_4, mass fraction distribution shows that methane is not present at the entrance of the reactor, but is generated approximately half way down the hot-zone. This is likely caused by C_3H_8 cracking and dissociating into CH_4 as the propane gas is heated along the direction of gas flow. From the temperature distribution in Figure 5.5, the temperature when methane generation becomes significant is approximately 1250 K (~ 970 °C). The highest mass fraction for CH_4 is above the 50 mm wafer area, indicated as 'wafer' in Figure 5.6(a). Silane has a totally different profile as seen in Figure 5.6(b). The amount of SiH_4 at the entrance is initially large, and as the gas is heated up along the hot-zone, the SiH_4 dissociates, resulting in a lower mass fraction. Approximately 1/3 the distance along the wafer zone, there is a very small amount of SiH_4 remaining, indicating that most of it has been dissociated, most likely into SiH_2 and Si, or consumed in the surface reaction.

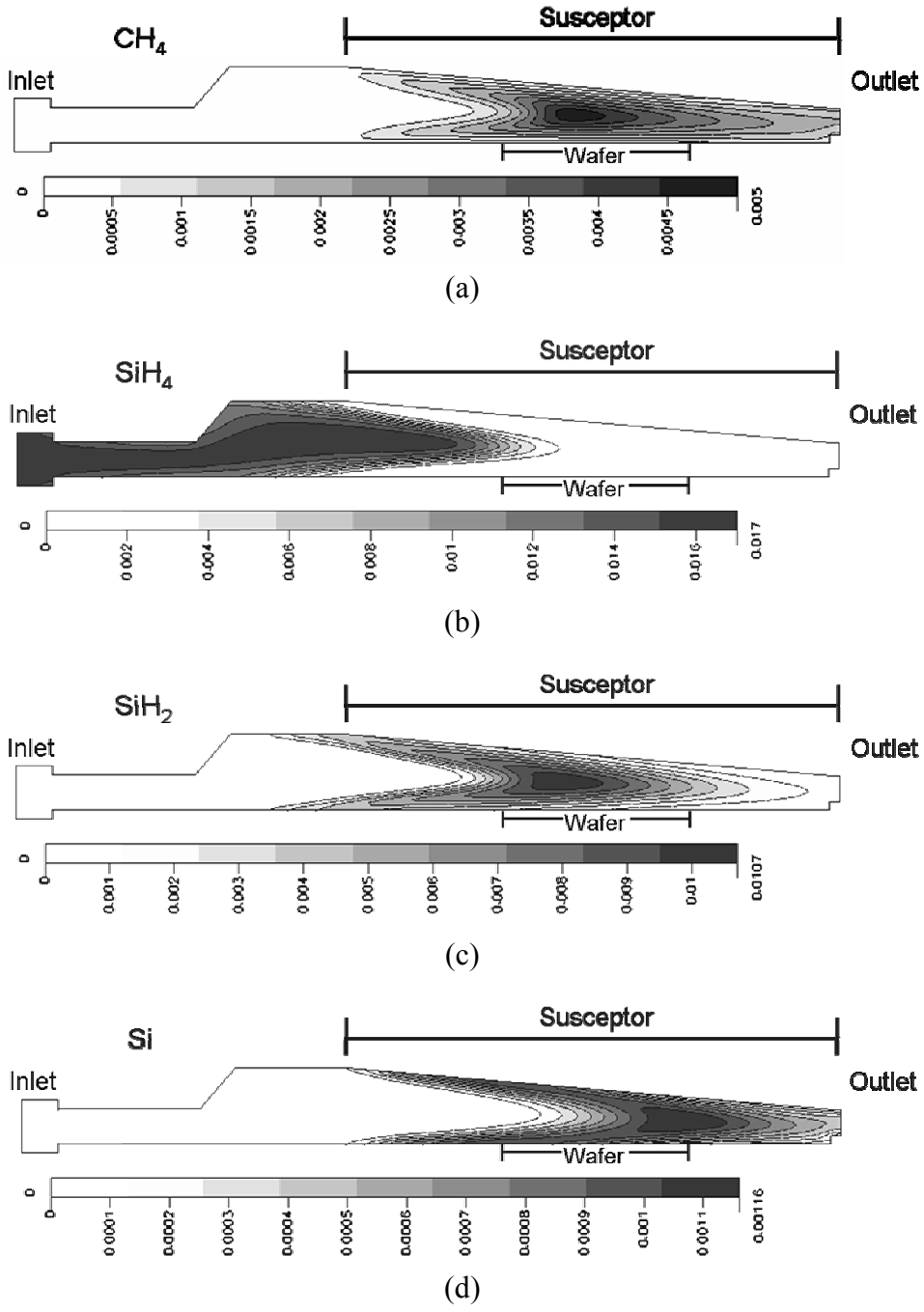

Figure 5.6 Mass fraction distributions of the dominant species (a) CH_4, (b) SiH_4, (c) SiH_2, and (d) Si at a temperature of 1565 °C for the 200 mm horizontal hot-wall reactor geometry. Data provided by Dr. Y. Makarov and Dr. A. Galyukov [75].

Silylene, SiH_2, has a similar profile as CH_4, which can be seen in Figure 5.6(c).

There is little SiH_2 gas at the entrance of the hot-zone because initially the silicon source

enters as SiH_4. As silane is heated, it dissociates into SiH_2. This occurs approximately 1/3 of the distance into the susceptor along the gas flow direction. The highest concentration of SiH_2 is around the area of the wafer. Finally, the Si specie is predicted to behave in a similar fashion to SiH_2, as can be seen from Figure 5.6(d). The Si specie is not present at the beginning of the hot-zone. However, Si is generated further along the hot-zone. The difference between the SiH_2 and the Si distribution is that the Si specie develops farther downstream in the hot-zone. This is most likely due to SiH_2 dissociation. Comparing SiH_2 and Si mass fraction distributions, the Si concentration increases close to the area where the SiH_2 starts to decrease.

Comparing the mass fraction results in Figure 5.6 to those from the thermodynamic simulations shown in Figure 2.1(b), there are some discrepancies between the two simulations. The mass fractions in Figure 5.6 are much higher than those from the thermodynamic simulations in Figure 2.1(b). Also, the CH_4 mass fraction is higher than Si in the thermodynamic simulations, however, the mass fraction is for CH_4 than Si for the simulations in Figure 5.6. The temperature of course is different between the two simulations, however, the mass fractions at the lower temperature scale in Figure 2.1(b) are decreasing. Therefore, the mass fractions would be even lower, making the difference between the two simulations greater. An explanation could be that the simulations are performed using two different software techniques. The thermodynamic simulations (Figure 2.1) use the minimization of Gibbs free energy to calculate the mass fractions, while the CVD-Module simulations take into account the mass transport, homogeneous and heterogeneous chemistry, and gas phase nucleation. Therefore, the

simulations in Figure 5.6 interpret the CVD process more realistically compared to the thermodynamic simulations in Figure 2.1(b).

The growth rate of SiC across the hot-zone was predicted and is shown in Figure 5.7. The growth rate of SiC within the 50 mm wafer area is the most important information for growth purposes because this is where the samples were placed during growth experiments. The growth rate was found using the equation [78]:

$$V_g = \sum_{i=1}^{N_s} M_i \sum_{r=1}^{N_{sr}} \frac{\nu_{ir} R_r}{\rho} \tag{5.1}$$

where V_g is the growth rate, M_i is the molecular weight of the i^{th} specie, ν_{ir} is the stoichiometric coefficient of the i^{th} specie in the r^{th} reaction, R_r is the rate of r^{th} surface reaction, ρ is the surface material density, N_s is the number of species, N_{sr} is the number of species involved in the reactions.

The simulations show that the growth rate will be at a maximum near the center of the 50 mm area and then will dramatically decrease for the maximum reactor temperature of 1565 °C. In order for this to happen looking at equation (5.1), the reaction rates must be increasing in that area. The growth rate may decrease after the center of the wafer because the reactants are being consumed in the reaction. The Si/C ratio for all cases shown in Figure 5.7(b) decreases across the wafer zone. This is likely due to the Si being consumed. However, when looking at the mass fraction distribution of CH_4 in Figure 5.6(a), the highest concentration is in the wafer zone. Therefore, it may be that there is more C from the C_3H_8 cracking in this area causing the Si/C ratio to decrease.

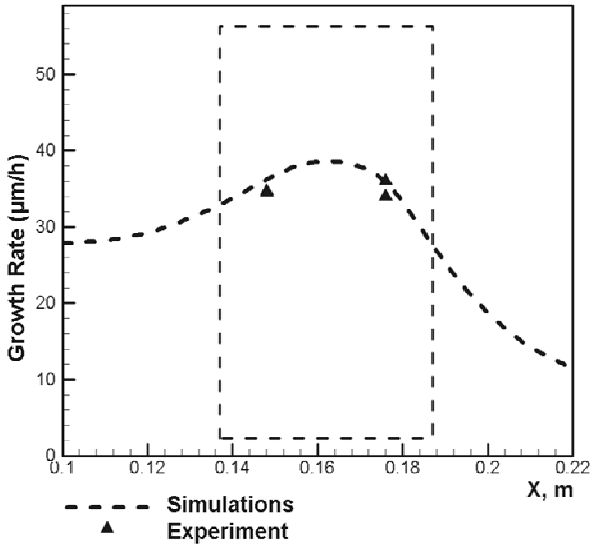

(a)

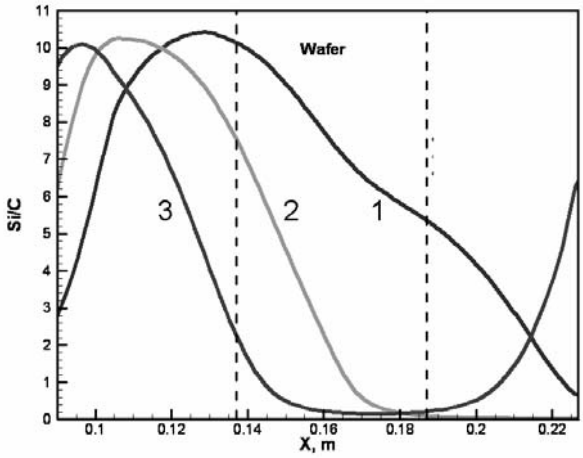

(b)

Figure 5.7 Calculated (a) growth rate and temperature profiles along the reactor hot-zone for a maximum reactor temperature of 1565 °C and (b) Si/C ratio across the reactor. Case 1, 2 and 3 are for maximum reactor temperatures of 1410, 1565 and 1710 °C, respectively. Data courtesy of Dr. Y. Makarov and Dr. A. Galyukov [75].

Comparing the experimental thickness results across the simulated 50 mm wafer zone shown in Table 3.2 and the computational analysis of the growth rate (at T = 1565 °C) (shown in Figure 5.7(a)), the results tend to correlate. However, the simulations were performed assuming the temperature profile on the bottom of the susceptor is the same as

that at the ceiling of the susceptor. Recent experiments indicate that the temperature at the susceptor ceiling is approximately 70°C hotter than the bottom portion of the susceptor. Therefore, new simulations should be carried out with the correct ceiling temperature to determine if the simulations and experimental results are still in agreement with one another.

Comparing the doping concentration experimental results from Table 3.2 with the simulations presented Figure 5.7(b), the results are opposite to each other. The reason for this may be that the calculated simulations do not account for the impurities within the reactor. It is known, from the LTPL data presented in Chapter 3, Section 3.4, that there are Al contaminants in the reaction system likely caused by the graphite parts. The Al impurities might be consumed at the inlet of the reactor, reducing the amount of Al present downstream. This would in turn reduce the acceptor concentration and produce a higher n-type doping concentration. Another explanation for the decrease in growth rate may be that the Si is being consumed at the inlet of the susceptor. This would deplete the available Si, resulting in a lower deposition farther along the susceptor.

Work must be continued to find a revised correlation between the simulations of the 200 mm hot-wall CVD reactor performed by Dr. Y. Makarov and Dr. A. Galyukov (Figure 5.7) and the experimental results presented in Chapter 3. The corrected temperature profile for the bottom and ceiling portions of the susceptor must be included in the simulations. The CVD simulations may be used to predict the outcome of SiC growth if the 200 mm reactor is modified further, or a new reactor comes online.

REFERENCES

[1] P. Masri, "Silicon carbide and silicon carbide-based structures The physics of epitaxy", *Surface Science Reports* 48 (2002) 1-51.

[2] http://www.ecn.purdue.edu/WBG/Introduction/Index.html, "Purdue Wide Band Gap Research", 2004.

[3] A. R. Powell and L. B. Rowland, "SiC Materials - Progress, Status and Potential Roadblocks", *Proceedings of the IEEE* 90 (2002) 942-955.

[4] C. Zetterling, *Process Technology for Silicon Carbide Devices*, INSPEC, London, 2002.

[5] S. E. Saddow and A. Agarwal, *Advances in Silicon Carbide Processing and Applications*, Artech House, Inc, Norwood, 2004.

[6] J. B. Casady and R. W. Johnson, "Status of Silicon Carbide (SiC) as a wide-bandgap semiconductor for high-temperature applications: A review", *Solid-State Electronics* 39 (1996) 1409-1422.

[7] I. Khan and Jr. J. A.Cooper, (http://www.ecn.purdue.edu/WBG/Basic_Measurements/Transport/Index.html, 2000).

[8] K. D. Hobart, F. J. Kub, M. Fatemi, C. Taylor, E. Eshun, and M. G. Spencer, "Transfer of Ultrathin Silicon Layers to Polycrystalline SiC Substrates for the Growth of 3C-SiC Epitaxial Films", *Journal of Electrochemical Society* 146 (1999) 3833-3836.

[9] R. L. Myers, *CVD Growth of SiC on Novel Si Substrates*, MS Thesis, University of South Florida, Tampa, 2003.

[10] R. L. Myers, S. E. Saddow, S. Rao, K. D. Hobart, M. Fatemi, and F. J. Kub, "Development of 3C-SOI structures using Si on polycrystalline SiC wafer bonded substrates", *Materials Science Forum* 457-460 (2003) 1511-1514.

[11] M. Reyes, M. Waits, S. Harvey, Y. Shishkin, B. Geil, J. T. Wolan, and S. E. Saddow, "Growth of 3C-SiC on Si molds for MEMS applications", *Materials Science Forum, in press* (2005).

[12] C. H. Park, B. Cheong, K. Lee, and K. J. Chang, "Structural and electronic properties of cubic, 2H, 4H, and 6H SiC", *The American Physical Society* 49 (1994) 4485-4493.

[13] T. Kimoto, S. Nakazawa, K. Fujihira, T. Hirao, S. Nakamura, Y. Chen, K. Hashimoto, and H. Matsunami, "Recent Achievements and Future Challenges in SiC Homoepitaxial Growth", *Materials Science Forum* 389-393 (2002) 165-170.

[14] T. Tawara, H. Tsuchida, S. Izumi, I. Kamata, and K. Izumi, "Evaluation of Free Carrier Lifetime and Deep Levels of the Thick 4H-SiC Epilayers", *Materials Science Forum* 457-460 (2004) 565-568.

[15] U. Forsberg, Ö. Danielsson, A. Henry, M. K. Linnarsson, and E. Janzén, "Nitrogen doping of epitaxial silicon carbide", *Journal of Crystal Growth* 236 (2002) 101-112.

[16] H. Tsuchida, I. Kamata, T. Jikimoto, and K. Izumi, "Growth of thick 4H-SiC epilayers in a vertical radiant-heating reactor", *Materials Research Society Symposium* 640 (2001) H2.12.1-H2.12.6.

[17] A. Ellison, J. Zhang, A. Henry, and E. Janzén, "Epitaxial growth of SiC in a chimney CVD reactor", *Journal of Crystal Growth* 236 (2002) 225-238.

[18] S. Nakazawa, T. Kimoto, K. Hashimoto, and H. Matsunami, "High-purity 4H-SiC epitaxial growth by hot-wall chemical vapor deposition", *Journal of Crystal Growth* 237-239 (2002) 1213-1218.

[19] J. Zhang, J. Mazzola, C. Hoff, Y. Koshka, and J. Cassady, "High Growth Rate (up to 20 μm/h) SiC Epitaxy in a Horizontal Hot-wall Reactor", *Materials Science Forum* 483-485 (2005) 77-80.

[20] A. O. Konstantinov, C. Hallin, O. Kordina, and E. Janzén, "Effect of vapor composition on polytype homogeneity of epitaxial silicon carbide", *Journal of Applied Physics* 80 (1996) 5704-5712.

[21] R. Rupp, A. Wiedenhofer, P. Friedrichs, D. Peters, R. Schörner, and D. Stephani, "Growth of SiC Epitaxial Layers in a Vertical Cold Wall Reactor Suited for High Voltage Applications", *Materials Science Forum* 264-268 (1998) 89-96.

[22] R. Rupp, P. Lanig, J. Völkl, and D. Stephani, "First results on silicon carbide vapour phase epitaxy growth in a new type of vertical low pressure chemical vapour deposition reactor", *Journal of Crystal Growth* 146 (1995) 37-41.

[23] K. Masahara, T. Takahashi, M. Kushibe, T. Ohno, J. Nishio, K. Kojima, Y. Ishida, T. Suzuki, T. Tanaka, S. Yoshida, and K. Arai, "High-Rate Epitaxial Growth of 4H-SiC Using a Vertical-Type, Quasi-Hot-Wall CVD Reactor", *Materials Science Forum* 389-393 (2002) 179-182.

[24] K. Fujihira, T. Kimoto, and H. Matsunami, "Fast Epitaxial Growth of High-Quality 4H-SiC by Vertical Hot-Wall CVD", *Materials Science Forum* 433-436 (2003) 161-164.

[25] J. Zhang, A. Ellison, and E. Janzén, "Morphology Control for Growth of Thick Epitaxial 4H SiC Layers", *Materials Science Forum* 338-342 (2000) 137-140.

[26] A. Ellison, J. Zhang, W. Magnusson, A. Henry, Q. Wahab, J. P. Bergman, C. Hemmingsson, N. T. Son, and E. Janzén, "Fast SiC Epitaxial Growth in a Chimney CVD Reactor and HTCVD Crystal Growth Developments", *Materials Science Forum* 338-342 (2000) 131-136.

[27] H. Tsuchida, I. Kamata, T. Jikimoto, and K. Izumi, "Epitaxial growth of thick 4H-SiC layers in a vertical radiant-heating reactor", *Journal of Crystal Growth* 237-239 (2002) 1206-1212.

[28] A. Elshabini-Riad and F. D. Barlow III, *Thin Film Technology Handbook*, McGraw Hill, New York, 1987.

[29] K. Seshan, *Handbook on Thin-Film Deposition Processes and Techniques*, Second ed., Noyes Publications, Norwich, 2002.

[30] S. Rao, *Implant Annealing of Al Dopants in Silicon Carbide using Silane Overpressure*, Dissertation Thesis, University of South Florida, Tampa, FL, 2005.

[31] C. E. Morosani, *Thin Films by Chemical Vapour Deposition*, Elsevier, Amsterdam, 1990.

[32] J. Park, *Chemical Vapor Deposition*, Vol. 2 ASM International, Materials Park, 2001.

[33] A. Sherman, *Chemical Vapor Deposition for Microelectronics: Principles, Technology, and Applications*, Noyes Publications, Park Ridge, 1987.

[34] Y. S. Park, *SiC Materials and Devices*, Vol. 52 Academic Press, Chestnut Hill, 1998.

[35] D. J. Larkin, "SiC Dopant Incorporation Control Using Site-Competition CVD", *Physica Status Solidi(b)* 202 (1997) 305-320.

[36] http://hyperphysics.phy-astr.gsu.edu/hbase/thermo/helmholtz.html, "HyperPhysics", 2005.

[37] S. Sandler, *Chemical and Engineering Thermodynamics*, Third ed., John Wiley & Sons, Inc., New York, 1999.

[38] http://chemed.chem.purdue.edu/genchem/topicreview/bp/ch21/gibbs.html, "Gibbs Free Energy".

[39] P. Atkins, *Physical Chemistry*, W. H.Freeman and Company, New York, 1998.

[40] B. McBride and S. Gordon, NASA-Glenn Chemical Equilibrium Program CEA2, 1994.

[41] S. Gordon and B. McBride, "Computer Program for Calculation of Complex Chemical Equilibrium Compositions and Applications II," Report No. NASA Reference Publication 1311 (1994).

[42] B. McBride and S. Gordon, "Computer Program for Calculation of Complex Chemical Equilibrium Compositions and Applications I," Report No. NASA Reference Publication 1311 (1996).

[43] O. Kordina, *Growth and Characterisation of Silicon Carbide Power Device Material*, Dissertation Thesis, Linköping University, Linköping, Sweden, 1994.

[44] R.V. Giles, J. B. Evett, and C. Liu, *Fluid Mechanics and Hydraulics*, Third ed., McGraw-Hill, New York, 1995.

[45] R. V. Giles, J. B. Evett, and C. Liu, *Fluid Mechanics and Hydraulics*, Third ed., McGraw-Hill, New York, 1995.

[46] W. Ji, MP. M. Lofgren, C. Hallin, C.-Y. Gu, and G. Zhou, "Computational modeling of SiC epitaxial growth in a hot wall reactor", *Journal of Crystal Growth* 220 (2000) 560-571.

[47] A. Veneroni, F. Omarini, D. Moscatelli, M. Masi, S. Leone, M. Mauceri, G. Pistone, and G. Abbondanza, "Modeling of epitaxial silicon carbide deposition", *Journal of Crystal Growth* 275 (2005) e25-e300.

[48] A. L. Hines and R. N. Maddox, *Mass Transfer*, Prentice Hall PTR, Englewood Cliffs, 1985.

[49] Matt Smith, *Design and Development of a Silicon Carbide Chemical Vapor Deposition Reactor*, Thesis, University of South Florida, Tampa, FL, Dec 2003.

[50] S. Plum, P. Graf, M. Beckers, J. Boersma, E. van den Dungen, M.Frijns, and F. Verbakel, "Advanced heating techniques for glass melting," (2002).

[51] "Experimental and Theoretical studies of nitrogen containing HF-CVD gas-phase environment", http://www.chm.bris.ac.uk/pt/diamond/jamessthesis/chapter4.htm#_edn7.

[52] O. Kordina, C. Hallin, A. Henry, J. P. Bergman, I. Ivanov, A. Ellison, N. T. Son, and E. Janzén, "Growth of SiC by "Hot-Wall" CVD and HTCVD", *Physica Status Solidi(b)* 202 (1997) 321-334.

[53] Johnson Matthey, "Gas Purification Technology", http://www.hydrogentechnology.com/html/pd_membrane_purification.html.

[54] Femlab, Comsol Multiphysics Version 3.2, 1997-2005.

[55] R. B. Bird, W. E. Stewart, and E. N. Lightfoot, *Transport Phenomena*, Second ed., John Wiley & Sons, Inc., New York, 2002.

[56] E. Janzén, J. P. Bergman, Ö. Danielsson, U. Forsberg, C. Hallin, J. ul Hassan, A. Henry, I. G. Ivanov, A. Kakanakova-Georgieva, P. Persson, and Q. ul Wahab, "SiC and III-Nitride Growth in a Hot-wall CVD Reactor", *Materials Science Forum* 483-485 (2005) 61-66.

[57] Ameritherm Inc., http://www.ameritherm.com/.

[58] Z. Y. Xie, Ch. H. Wei, L. Y. Li, Q. M. Yu, and J. H. Edgar, "Gaseous etching of 6H-SiC at relatively low temperatures", *Journal of Crystal Growth* 217 (2000) 115-124.

[59] H. O. Pierson, *Handbook of Chemical Vapor Deposition: Principles,Technology, and Applications*, Second ed., Noyes Publication, Norwich, 1999.

[60] R. L. Myers, Y. Shishkin, O. Kordina, I. Haselbarth, and S. E. Saddow, "High Epitaxial Growth Rate of 4H-SiC using Horizontal Hot-Wall CVD", *Materials Science Forum, in press* (2005).

[61] R. L. Myers, Y. Shishkin, O. Kordina, and S. E. Saddow, "High growth rates (>30μm/h) of 4H-SiC epitaxial layers using a horizontal hot-wall CVD reactor", *Journal of Crystal Growth* 285 (2005) 483-486.

[62] E. Janzén, A. Henry, J. P. Bergman, A. Ellison, and B. Magnusson, "Material characterization need for SiC-based devices", *Materials Science in Semiconductor Processing* 4 (2001) 181-186.

[63] I. G. Ivanov, C. Hallin, A. Henry, O. Kordina, and E. Janzén, "Nitrogen doping concentration as determined by photoluminescence in 4H- and 6H-SiC", *Journal of Applied Physics* 80 (1996) 3504-3508.

[64] NovaSiC, "NovaSiC Silicon Carbide and Related Materials", http://www.novasic.com/, 2003.

[65] http://www.schmitt-ind.com/support-technical-papers-scatter.shtml.

[66] H. Tsuchida, I. Kamata, T. Jikimoto, and K. Izumi, "Growth and Electrical Characterization of Lightly-Doped Thick 4H-SiC Epilayers", *Materials Science Forum* 389-393 (2002) 171-174.

[67] J. Zhang, U. Forsberg, M. Isacson, A. Ellison, A. Henry, O. Kordina, and E. Janzén, "Growth Characteristics of SiC in a Hot-Wall CVD Reactor with Rotation", *Materials Science Forum* 389-393 (2002) 191-194.

[68] R. Rupp, Y. N. Makarov, H. Behner, and A. Wiedenhofer, "Silicon Carbide Epitaxy in a Vertical CVD Reactor: Experimental Results and Numerical Process Simulation", *Physica Status Solidi(b)* 202 (1997) 281-304.

[69] M. Reyes and S. E. Saddow, "Phase I final report to Caracal, Inc., ONR STTR Phase I", December, 2004.

[70] R. C. Jaeger, *Introduction to Microelectronic Fabrication*, Vol. 5, Second ed., Prentice Hall, Upper Saddle River, 2002.

[71] S. Nakamura, T. Kimoto, H. Matsunami, S. Tanaka, N. Teraguchi, and A. Suzuki, "Formation of periodic steps with a unit-cell height on 6H-SiC (0001) surface by HCl etching", *Applied Physics Letters* 76 (2000) 3412-3414.

[72] A. Fissel, W. Richter, J. Furthmüller, and F. Bechstedt, "On the nature of the D1-defect center in SiC: A photoluminescence study of layers grown by solid-source molecular-beam epitaxy", *Applied Physics Letters* 78 (2001) 2512-2514.

[73] Y. Koshka, H. Lin, G. Melnychuk, M. S. Mazzola, and J. L. Wyatt, "Homoepitaxial growth of 4H-SiC using CH_3Cl carbon precursor", *Materials Science Forum* 483-485 (2005) 81-84.

[74] Y. Koshka, H. Lin, G. Melnychuk, and C. Wood, "Lower-temperature epitaxial growth of 4H-SiC using CH_3Cl carbon gas precursor", *ICSCRM 2005* (2005 (in press)).

[75] www.semitech.us, "Semiconductor Technology Research, Inc." 2005.

[76] S. Carrà and M. Masi, "Kinetic Approach to Materials Synthesis by Gas-Phase Deposition", *Progress in Crystal Growth and Characterization* (1998) 1-46.

[77] J. Meziere, M. Ucar, E. Blanquet, M. Pons, P. Ferret, and L. Di Cioccio, "Modeling and simulation of SiC CVD in the horizontal hot-wall reactor concept", *Journal of Crystal Growth* 267 (2004) 436-451.

[78] A. N. Vorob'ev, S. Yu. Karpov, M.V. Bogdanov, A. E. Komissarov, O. V. Bord, A. I. Zhmakin, and Yu. N. Makarov, "Numerical study of SiC CVD in a vertical cold-wall reactor", *Computational Materials Science* 24 (2002) 520-534.

[79] D. Schroder, *Semiconductor Material and Device Characterization*, Second ed., John Wiley & Sons, Inc., New York, 1998.

[80] J. H. Wittke, "Effects of Electron Bombardment", http://jan.ucc.nau.edu/~wittke/Microprobe/Interact-Effects.html, 2003.

[81] S. L. Elliot, R. F. Broom, and C. J. Humphreys, "Enhanced SEM Doping Contrast on an H-passivated Silicon Surface", http://www-hrem.msm.cam.ac.uk/research/Dopant/Dopant.html.

[82] Building and Fire Research Laboratory, "Atomic Force Microscopy (AFM)", http://www.bfrl.nist.gov/nanoscience/BFRL_AFM.htm.

[83] NanoScience Instruments, "Atomic Force Microscopy", http://www.nanoscience.com/education/AFM.html, 2005.

[84] "X-ray Diffraction and Braggs Law", http://www.cartage.org.lb/en/themes/Sciences/Physics/SolidStatePhysics/AtomicBonding/XRAY/XrayDiffraction/XrayDiffraction.htm.

[85] X. Huang, M. Dudley, and R. S. Okojie, "Characterization of SiC epilayers using high-resolution X-ray diffraction and synchrotron topography imaging", *Materials Research Society Symposium Proceedings* 815 (2004) J7.3.1-J7.3.6.

[86] P. F. Fewster, *X-ray Scattering from Semiconductors*, Imperial College Press, River Edge, 2000.

[87] Phillips Analytical, "X'Pert Pro User's Guide," (2002).

[88] P. A. Heiney, "Instrumentation for XRD: Diffractometers and Detectors", http://www.physics.upenn.edu/~heiney/talks/hires/instrument.html#SECTION00033000000000000000, 1996.

[89] S. Perkowitz, *Optical Characterization of Semiconductors: Infrared, Raman, and Photoluminescence Spectroscopy*, Academic Press, London, 1993.

[90] F. Walder and R. Boyle, "FT-IR Measurement of Epitaxial Film Thickness Applications," Report No. Application Note: 0015 (2004).

[91] R. P. Devaty and W. J. Choyke, "Optical Characterization of Silicon Carbide Polytypes", *Physica Status Solidi(a)* 162 (1997) 5-38.

[92] M. Ahoujja, H. C. Crocket, M. B. Scott, Y. K. Yeo, and R. L. Hengehold, "Photoluminescence Characterization of Defects Introduced in 4H-SiC During High Energy Proton Irradiation and Their Annealing Behavior", *Materials Research Society Symposium Proceedings* 815 (2004) J5.21-J5.26.

APPENDICES

Appendix A: NASA-Lewis Chemical Equilibrium Computations and Applications (CEA)

The following instructions were used to determine the equilibrium composition of chemical species within the CVD reactor using the NASA-Lewis Chemical Equilibrium and Applications (CEA) program. The program was written by B. McBride and S. Gordon in ANSI standard Fortran [41]. As stated in Chapter 2, Section 2.2.3, the program calculates chemical compositions by minimizing the Gibbs free energy of the system. In order to run the program, two sets of inputs must be provided. The first set of inputs is the thermodynamic and thermal transport property data (i.e. enthalpy, entropy, etc.). This data is provided in a library within the program which contains the properties for the chemical species. However, if the specie specified is not available, one must the program. The second input is the thermodynamic state functions, which are temperature and pressure for this case, the reactants used, and the reactants flow rates. The input files that are generated from the input data must be saved as "*.inp*" files. After executing the program, an output file is generated as a "*.out*" file and a plot file is generated as a "*.plot*" file. The output file will provide the information from the input file, the results of the computations and the species which were included in the calculations. The plot file generates the data into columns which may be easily plotted within a graphical software program.

The CEA executable file name is "CEAexecute-win.bat," which is used to open the program. When the program is first opened, the screen shown in Figure A.1 is first displayed, with the "Problem" tab already highlighted. The thermodynamic state

functions which will be provided needs to be chosen next. In this case, that would be the "Assigned Temperature and Pressure – tp" problem. Double click on this problem.

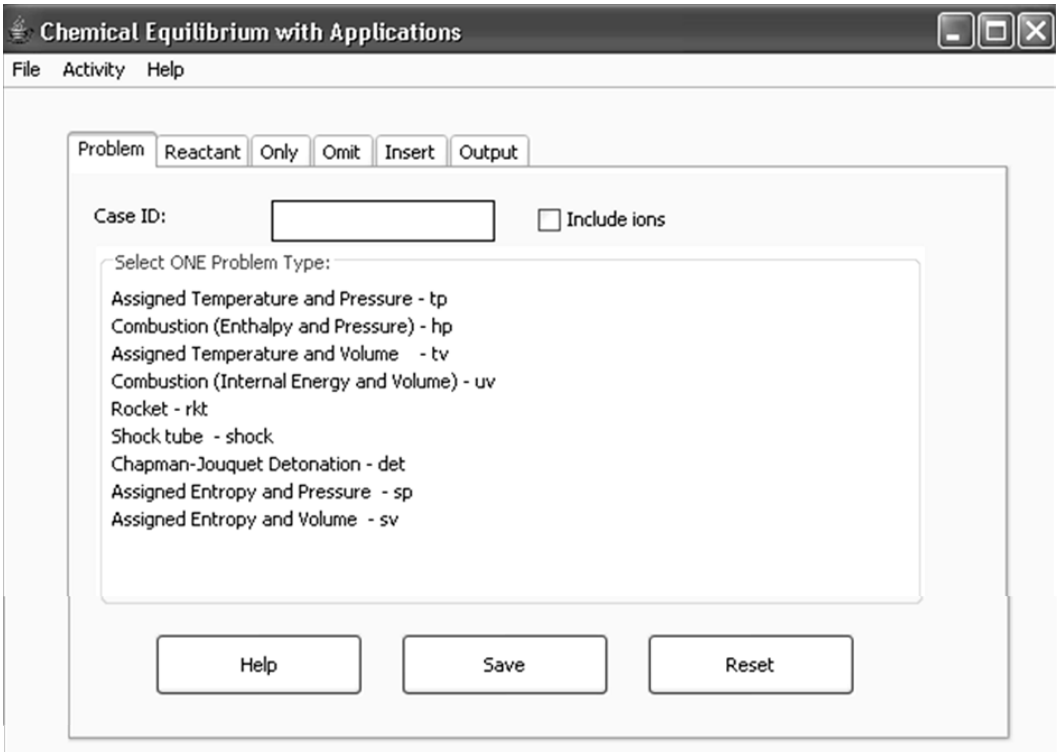

Figure A.1 Screen image of the CEA program display. The problem is specified by chosing which thermodynamic state functions will be used as the input values.

After selecting the problem (thermodynamic state functions), a screen will appear which directs the user to input the temperature and pressure, which is shown in Figure A.2. There are drop down fields which one can specify the units of the thermodynamic state functions of the input values. The choices for the temperature unit are Kelvin, Rankine, Celsius, and Fahrenheit, while those of the pressure are bar, atm, psia, and mmHg. The units specified for this example are Kelvin and mmHg for temperature and pressure, respectively. The input values for the temperature and pressure are then

specified under each column. The total number of input values allowed are 16. For this example, which is the 4H-SiC epitaxial growth baseline process in the 200 mm reactor, the temperature ranged between 1500 and 2000 K in increments of 50K. The process pressure was specified to be 150 mmHg which corresponds to the process pressure of 150 Torr.

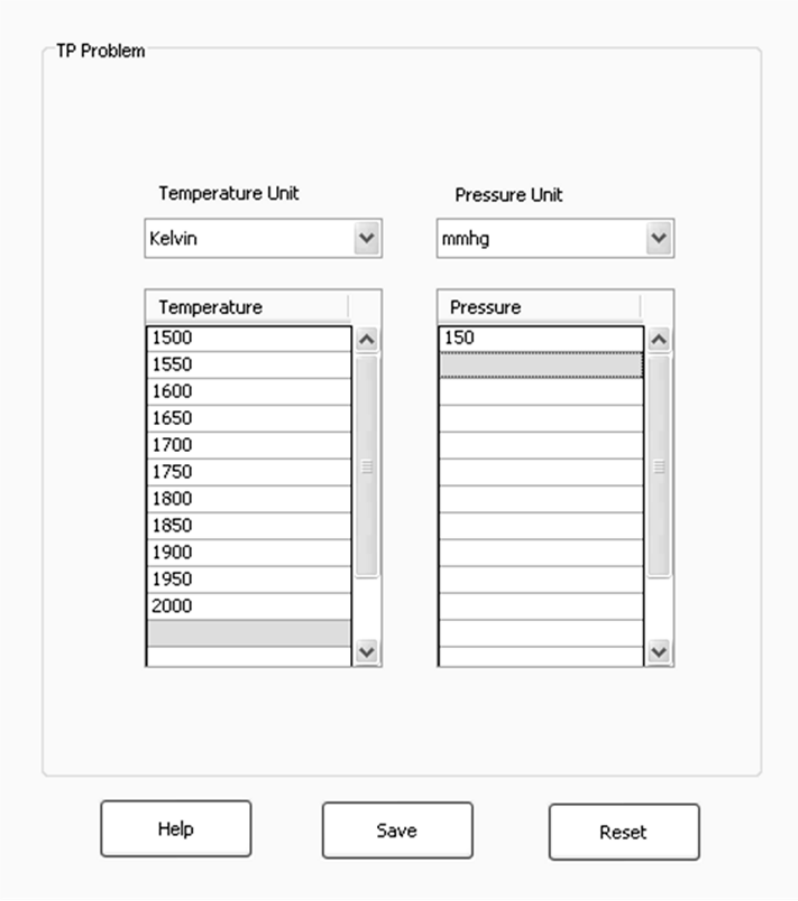

Figure A.2 CEA display screen for the "TP problem." Under the "Temperature" heading, the desired temperature range is input. Under the "Pressure" heading, the desired pressure is specified.

Once the input values have been specified, the "Save" button is pressed to save the input data. The "Reactant" tab is then chosen, which will bring up the screen shown

in Figure A.3. In the "Ident" column, there are three choices to identify the reactant which are name, fuel, and oxide. Choose the "name" identity. In the "Name" column, enter the appropriate reactants which are flown during growth in the CVD system. For this example, H_2, C_3H_8, and SiH_4 from the standard process. In the "Amount" field, input the flow rates used for the growth process. The "Amount" may be specified in moles or in relative weight. Since the temperature and pressure are the same, the flow rates are equal to the number of moles for each species. In this case, the H_2 was set to 30,000 moles (representing 30,000 sccm), the C_3H_8 was set to 10 moles (representing 10 sccm), and the SiH_4 was set to 30 moles (representing 30 sccm). The temperature and energy units may also be specified in the "Reactant" field. Kelvin and kJ/mol were chosen for this problem. The "Save" button is then pressed after specifying all fields.

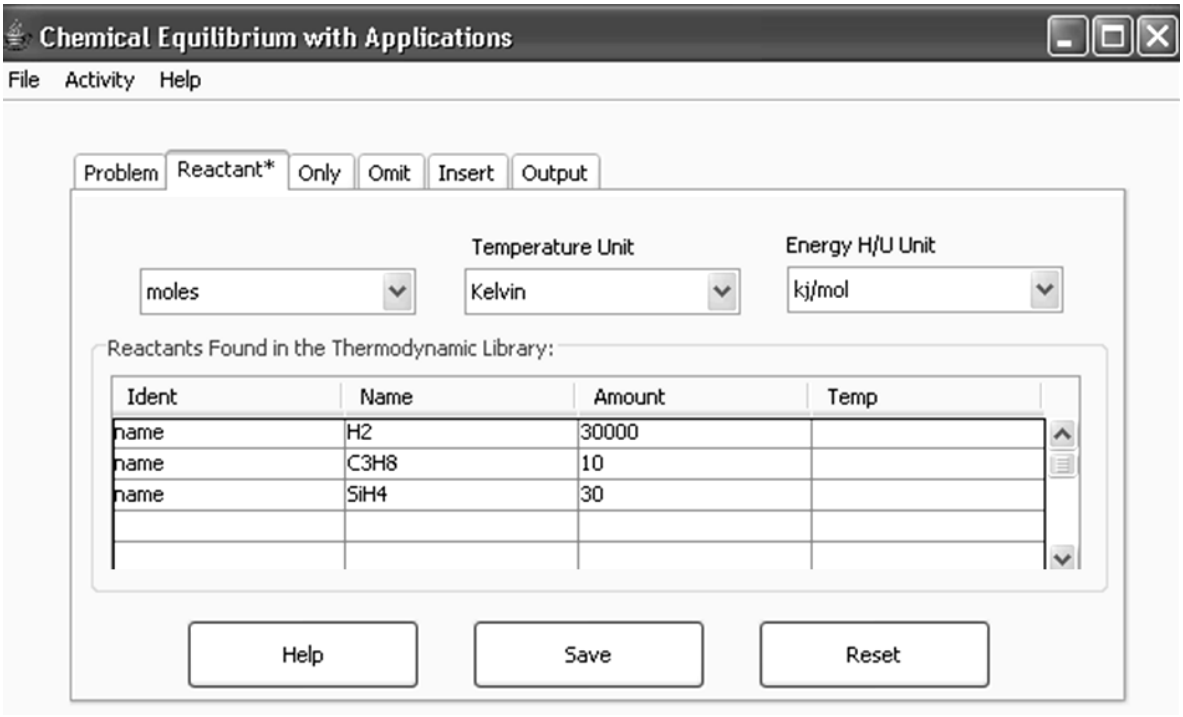

Figure A.3 Display window for the "Reactant" tab. This is where the reactant information is input into the CEA program.

The "Only" tab may be chosen if one wants to consider specified species only for the problem. The display window for this tab is shown in Figure A.4. All possible gaseous and condensed species possible from the input reactants are displayed on the left top and bottom columns in Figure A.4. For this example problem, no species were specified for the "Only" tab. If one does want to enter a specie, it is done by selecting the specie from the left hand columns and clicking the "Add" button. If a mistake was made, a specie may be removed from the "Selected List" by selecting the specie and clicking "Remove". The file is then saved by pressing "Save".

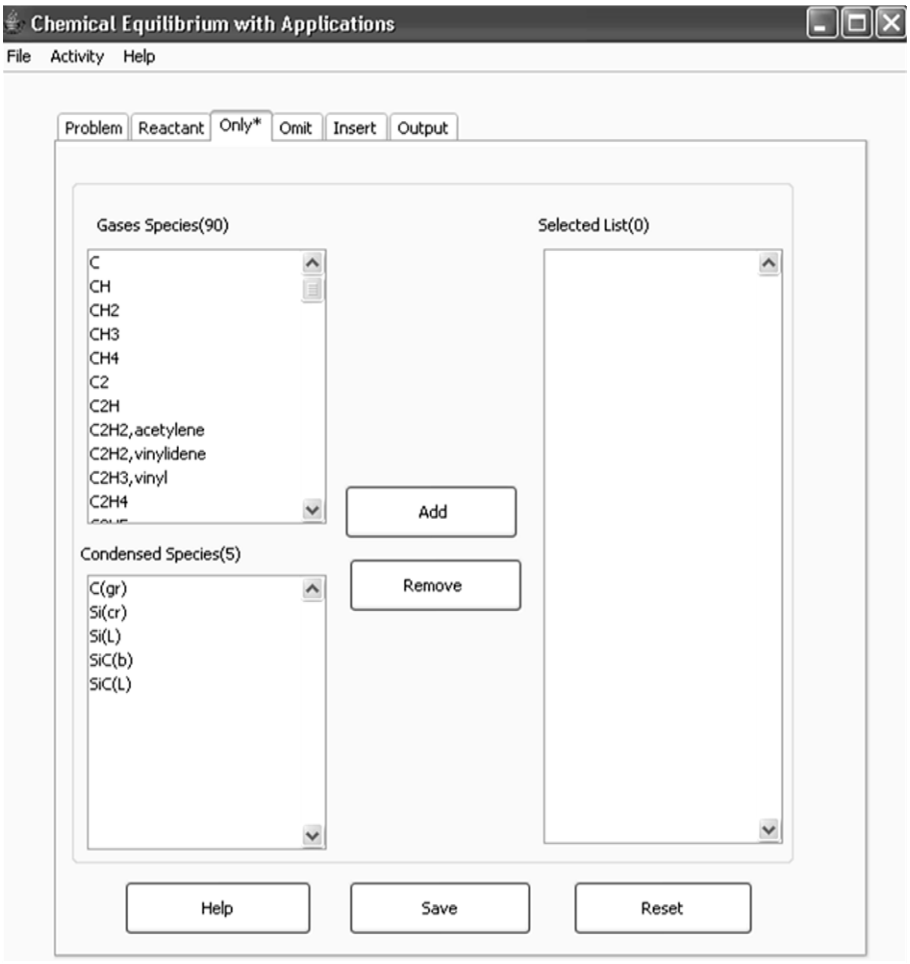

Figure A.4 Display window for the "Only" tab which allows a specified species list to be created. This will allow one to choose which species only are to be included in the calculation.

Another option is the "Omit" tab, which is shown in Figure A.5. If one wishes to omit certain species from the simulation, this tab is the place to choose the specie that is to be omitted. The tab specified as "Insert" is used to insert certain condensed species to be tried in the initial iteration. There may be some cases where no condensed species were entered, and a convergence problem occurred. This may indicate that a condensed species must be entered into the "Insert" tab. For the baseline process example problem,

no species have been selected for either the “Only”, “Omit”, or “Insert” tab. When this occurs, the program will consider all possible species from the reactant species input list, which is on the left hand column in the display screen shown in Figure A.5.

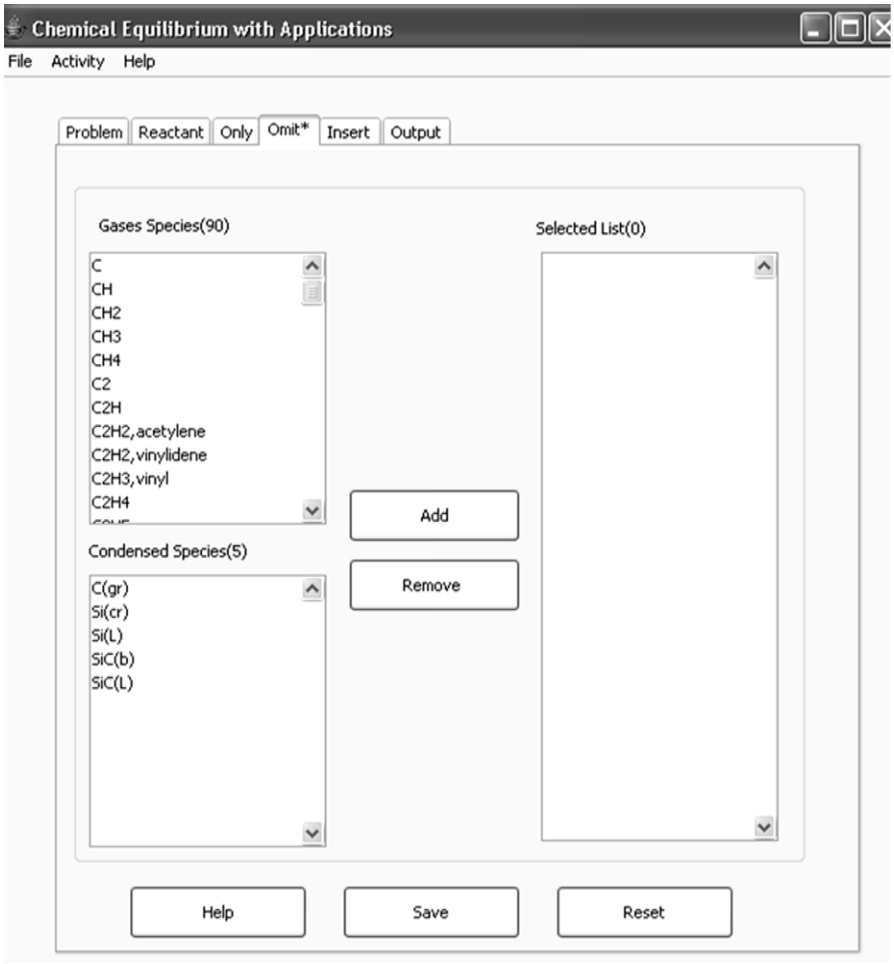

Figure A.5 Display screen for the “Omit” tab in the CEA program. This allows the user to omit certain species that one specifies.

The last set of information that needs to be input into the CEA program is under the “Output” tab. The display screen for this is shown in Figure A.6. The species composition unit may be chosen as mole fractions or mass fractions. For this example,

the unit was chosen to be mole fraction. One may also specify the trace species value, which is set for 10^{-10} for this problem. By putting in the trace species value, species below this value will not be written to the plot file. The chemical species and thermodynamic properties which are to be presented in the plot file must be specified in the box above the "Reset" button and the in the "Selected Plot List" column, respectively. For this case, the temperature and pressure were selected to be displayed in the plot file, along with the relevant chemical species. The plot file is a file which is generated from the calculations which only displays what has been chosen in the "Selected Plot List" and the species list which is the box above the "Reset" button.

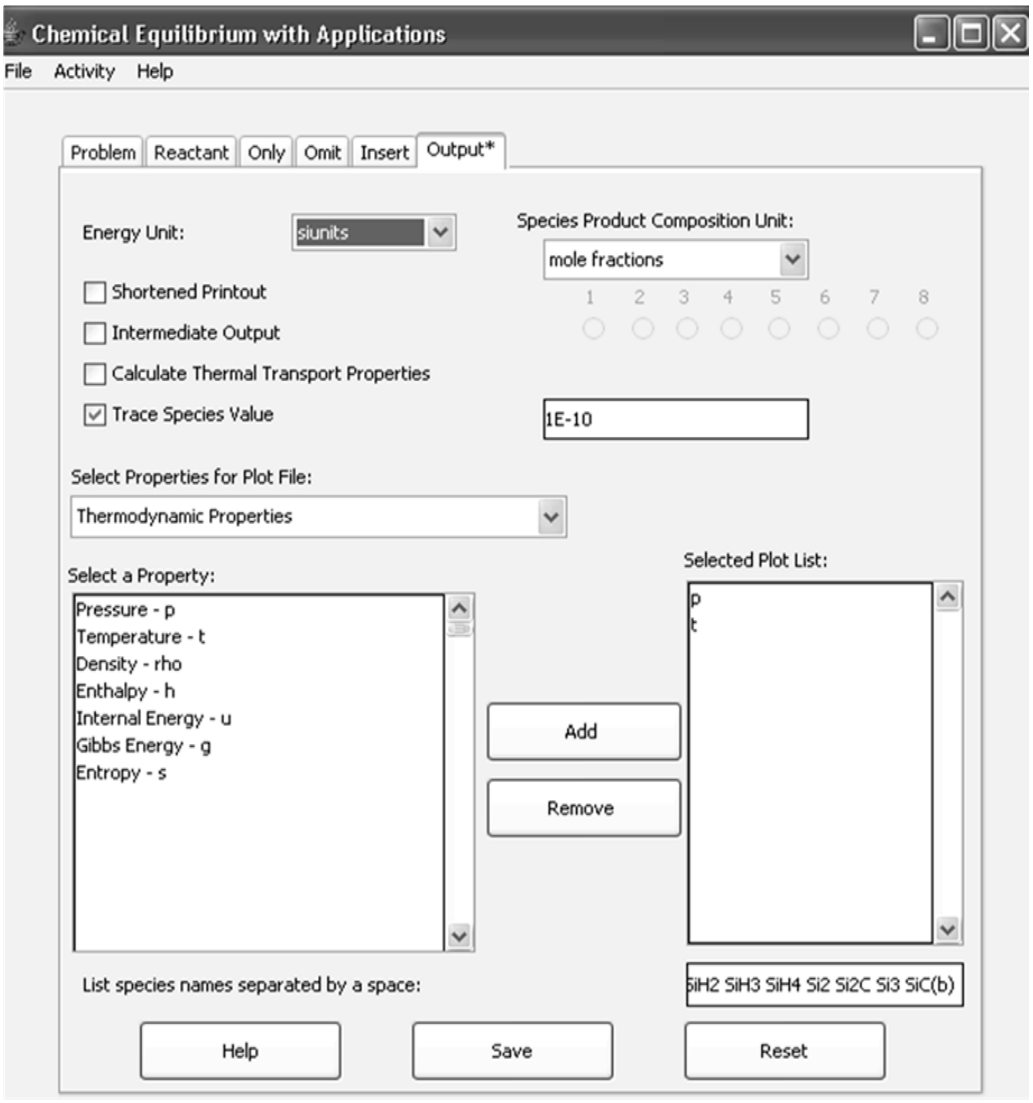

Figure A.6 Display window for the "Output" tab. The thermodynamic properties which are to be put into the output file are specified in this tab, which for this case is temperature and pressure.

Once all of the information has been put into the program, the data is saved as a "*.inp*" file. To execute the program, the user goes to the "Activity" tab at the top of the screen and selects "Execute CEA". To view the plot file or the output file, select "View PLOT File" or "View OUTPUT File" from the "Activity" tab. The plot file may be

Appendix A: (Continued)

imported into another program to plot the results. An example of the data generated by the CEA program is shown next.

Output file:

```
*******************************************************************************

      NASA-GLENN CHEMICAL EQUILIBRIUM PROGRAM CEA2, MAY 21, 2004
            BY  BONNIE MCBRIDE AND SANFORD GORDON
    REFS: NASA RP-1311, PART I, 1994 AND NASA RP-1311, PART II, 1996

*******************************************************************************

 problem
    tp   t,k=1500,1550,1600,1650,1700,1750,1800,1850,1900,1950,2000,  p,mmhg=150
 ,
 react
  name=H2 moles=30000
  name=C3H8 moles=10
  name=SiH4 moles=30
 output    trace=1E-10
    plot p t CH2 CH3 CH4 C2H2,acetylene C2H4 H H2 Si SiC2 SiH SiH2 SiH3 SiH4 Si2
  Si2C Si3 SiC(b)
  end

 OPTIONS: TP=T  HP=F  SP=F  TV=F  UV=F  SV=F  DETN=F  SHOCK=F  REFL=F  INCD=F
 RKT=F  FROZ=F  EQL=F  IONS=F  SIUNIT=T  DEBUGF=F  SHKDBG=F  DETDBG=F  TRNSPT=F

 T,K =  1500.0000  1550.0000  1600.0000  1650.0000  1700.0000  1750.0000  1800.0000
 T,K =  1850.0000  1900.0000  1950.0000  2000.0000

 TRACE= 1.00E-10  S/R= 0.000000E+00  H/R= 0.000000E+00  U/R= 0.000000E+00
 P,BAR =     0.199984

    REACTANT          MOLES    (ENERGY/R),K   TEMP,K  DENSITY
       EXPLODED FORMULA
 N: H2            **********   0.000000E+00     0.00  0.0000
         H  2.00000
 N: C3H8           10.000000   0.000000E+00     0.00  0.0000
         C  3.00000  H  8.00000
 N: SiH4           30.000000   0.000000E+00     0.00  0.0000
         SI 1.00000  H  4.00000

  SPECIES BEING CONSIDERED IN THIS SYSTEM
 (CONDENSED PHASE MAY HAVE NAME LISTED SEVERAL TIMES)
  LAST thermo.inp UPDATE:    9/09/04
```

Appendix A: (Continued)

```
g 7/97  *C              tpis79  *CH             g 4/02  CH2
 g 4/02  CH3             g 8/99  CH4             tpis91  *C2
 g 6/01  C2H             g 1/91  C2H2,acetylene   g 5/01  C2H2,vinylidene
 g 7/01  C2H3,vinyl      g 1/00  C2H4            g 7/00  C2H5
 g 7/00  C2H6            tpis79  *C3             n 4/98  C3H3,1-propynl
 n 4/98  C3H3,2-propynl   g 2/00  C3H4,allene     g 1/00  C3H4,propyne
 g 5/90  C3H4,cyclo-      g 3/01  C3H5,allyl      g 2/00  C3H6,propylene
 g 1/00  C3H6,cyclo-      g 7/01  C3H7,n-propyl   g 9/85  C3H7,i-propyl
 g 2/00  C3H8            g tpis  *C4             g 7/01  C4H2,butadiyne
 g 8/00  C4H4,1,3-cyclo-  n10/92  C4H6,butadiene   n10/93  C4H6,1butyne
 n10/93  C4H6,2butyne     g 8/00  C4H6,cyclo-      n 4/88  C4H8,1-butene
 n 4/88  C4H8,cis2-buten  n 4/88  C4H8,tr2-butene  n 4/88  C4H8,isobutene
 g 8/00  C4H8,cyclo-      n10/84  C4H9,n-butyl     n10/84  C4H9,i-butyl
 g 1/93  C4H9,s-butyl     g 1/93  C4H9,t-butyl     g12/00  C4H10,n-butane
 g 8/00  C4H10,isobutane  g 8/00  *C5             g 5/90  C5H6,1,3cyclo-
 g 1/93  C5H8,cyclo-      n 4/87  C5H10,1-pentene  g 2/01  C5H10,cyclo-
 n10/84  C5H11,pentyl     g 1/93  C5H11,t-pentyl   n10/85  C5H12,n-pentane
 n10/85  C5H12,i-pentane  n10/85  CH3C(CH3)2CH3    g 2/93  C6H2
 g11/00  C6H5,phenyl      g 8/00  C6H6            g 1/93  C6H10,cyclo-
 n 4/87  C6H12,1-hexene   g 6/90  C6H12,cyclo-     n10/83  C6H13,n-hexyl
 g 6/01  C6H14,n-hexane   g 7/01  C7H7,benzyl      g 1/93  C7H8
 n 4/87  C7H14,1-heptene  n10/83  C7H15,n-heptyl   n10/85  C7H16,n-heptane
 n10/85  C7H16,2-methylh  n 4/89  C8H8,styrene     n10/86  C8H10,ethylbenz
 n 4/87  C8H16,1-octene   n10/83  C8H17,n-octyl    n 4/85  C8H18,n-octane
 n 4/85  C8H18,isooctane  n10/83  C9H19,n-nonyl    g 3/01  C10H8,naphthale
 n10/83  C10H21,n-decyl   g 8/00  C12H9,o-bipheny  g 8/00  C12H10,biphenyl
 g 6/97  *H              tpis78  *H2             g 8/97  *Si
 tpis91  SiC             tpis91  SiC2            tpis91  SiH
 g 3/01  SiH2            g 3/99  SiH3            tpis91  SiH4
 tpis91  Si2             tpis91  Si2C            g 7/95  Si3
 n 4/83  C(gr)           n 4/83  C(gr)           n 4/83  C(gr)
 tpis91  Si(cr)          tpis91  Si(cr)          tpis91  Si(L)
 tpis91  SiC(b)          tpis91  SiC(b)          tpis91  SiC(L)

O/F =   0.000000

                  EFFECTIVE FUEL     EFFECTIVE OXIDANT        MIXTURE
ENTHALPY                h(2)/R            h(1)/R             h0/R
(KG-MOL)(K)/KG       0.00000000E+00     0.00000000E+00     0.00000000E+00

KG-FORM.WT./KG           bi(2)             bi(1)             b0i
 *H                  0.97283694E+00     0.00000000E+00     0.97283694E+00
 *C                  0.48480246E-03     0.00000000E+00     0.48480246E-03
 *Si                 0.48480246E-03     0.00000000E+00     0.48480246E-03

POINT ITN      T          H          C          SI
  1   19    1500.000    -10.106     -1.967      0.113
ADD  SiC(b)
  1    5    1500.000    -10.105     -8.102     -3.553
ADD  Si(cr)
  1    2    1500.000    -10.105     -7.069     -4.586
```

```
 1   2   1500.000   -10.105    -7.069    -4.586
 2   3   1550.000   -10.153    -6.941    -4.668
 3   4   1600.000   -10.200    -6.823    -4.748
 4   3   1650.000   -10.246    -6.715    -4.826
REMOVE  Si(cr)
 4   2   1650.000   -10.246    -6.613    -4.928
 5   4   1700.000   -10.291    -6.119    -5.400
 6   4   1750.000   -10.335    -5.652    -5.852
 7   4   1800.000   -10.379    -5.233    -6.261
 8   4   1850.000   -10.421    -4.885    -6.605
          THERMODYNAMIC EQUILIBRIUM PROPERTIES AT ASSIGNED
                TEMPERATURE AND PRESSURE


CASE =   REACTANT            MOLES       ENERGY      TEMP
                                         KJ/KG-MOL     K
NAME      H2              ************     0.000     0.000
NAME      C3H8             10.0000000      0.000     0.000
NAME      SiH4             30.0000000      0.000     0.000

O/F=   0.00000  %FUEL=  0.000000  R,EQ.RATIO= 0.000000  PHI,EQ.RATIO= 0.000000

THERMODYNAMIC PROPERTIES

P, BAR          0.19998  0.19998  0.19998  0.19998  0.19998  0.19998  0.19998  0.19998
T, K          1500.00  1550.00  1600.00  1650.00  1700.00  1750.00  1800.00  1850.00
RHO, KG/CU M   3.2965-3 3.1901-3 3.0903-3 2.9965-3 2.9082-3 2.8249-3 2.7460-3 2.6712-3
H, KJ/KG       17645.8  18438.8  19239.4  20048.6  20867.7  21699.0  22545.5  23411.2
U, KJ/KG       11579.2  12169.9  12768.1  13374.8  13991.2  14619.6  15262.8  15924.6
G, KJ/KG      -122674.2-127364.6-132080.7-136821.9-141587.8-146378.0-151192.1-156030.0
S, KJ/(KG)(K)   93.5466  94.0667  94.5750  95.0730  95.5621  96.0440  96.5209  96.9952

M, (1/n)         2.056    2.056    2.056    2.056    2.056    2.055    2.055    2.055
MW, MOL WT       2.054    2.054    2.054    2.054    2.053    2.053    2.053    2.053
(dLV/dLP)t     -1.00001 -1.00002 -1.00003 -1.00005 -1.00008 -1.00013 -1.00020 -1.00031
(dLV/dLT)p       1.0004   1.0006   1.0011   1.0017   1.0026   1.0040   1.0061   1.0090
Cp, KJ/(KG)(K)   15.7913  15.9327  16.0933  16.2760  16.4965  16.7667  17.1055  17.5382
GAMMAs           1.3446   1.3407   1.3366   1.3321   1.3270   1.3212   1.3144   1.3065
SON VEL,M/SEC    2856.1   2899.1   2941.0   2981.6   3020.8   3058.3   3094.0   3127.5

MOLE FRACTIONS

CH2           1.216-13 3.961-13 1.198-12 3.750-12 1.479-11 5.414-11 1.807-10 5.389-10
CH3           3.1889-9 5.4734-9 9.0795-9 1.6171-8 3.7532-8 8.3289-8 1.7332-7 3.3068-7
CH4           3.9492-6 3.7820-6 3.6334-6 3.8772-6 5.5610-6 7.8455-6 1.0652-5 1.3580-5
C2H2,acetylene  5.229-10 1.360 -9 3.329 -9 9.470 -9 4.606 -8 2.061 -7 8.156 -7 2.728 -6
C2H2,vinylidene 1.299-15 5.398-15 2.051-14 8.808-14 6.310-13 4.065-12 2.269-11 1.050-10
C2H4          3.011-11 4.826-11 7.511-11 1.396-10 4.548-10 1.396 -9 3.867 -9 9.237 -9
*H            3.9368-5 7.0440-5 1.2160-4 2.0319-4 3.2956-4 5.2017-4 8.0073-4 1.2046-3
*H2           9.9896-1 9.9893-1 9.9888-1 9.9880-1 9.9867-1 9.9848-1 9.9819-1 9.9778-1
*Si           5.2591-8 1.6599-7 4.8717-7 1.2085-6 2.1056-6 3.5388-6 5.8893-6 9.9851-6
```

SiC2	8.518-15	6.194-14	3.972-13	2.516-12	1.926-11	1.315-10	7.899-10	4.106 -9
SiH	1.4405-7	3.6484-7	8.7101-7	1.7795-6	2.5826-6	3.6528-6	5.1648-6	7.5042-6
SiH2	1.0237-7	2.0225-7	3.8279-7	6.2919-7	7.4464-7	8.6947-7	1.0263-6	1.2579-6
SiH3	9.2489-9	1.5276-8	2.4447-8	3.4323-8	3.5020-8	3.5551-8	3.6766-8	3.9755-8
SiH4	1.8879-7	2.0073-7	2.1267-7	2.0277-7	1.4380-7	1.0364-7	7.7590-8	6.1827-8
Si2	3.331-10	1.431 -9	5.599 -9	1.641 -8	2.479 -8	3.623 -8	5.386 -8	8.590 -8
Si2C	1.603-10	7.704-10	3.347 -9	1.198 -8	2.943 -8	6.825 -8	1.537 -7	3.466 -7
Si3	7.502-11	3.598-10	1.560 -9	4.543 -9	5.052 -9	5.510 -9	6.331 -9	8.289 -9
Si(cr)	3.4556-6	2.8329-6	1.6553-6	0.0000 0	0.0000 0	0.0000 0	0.0000 0	0.0000 0
SiC(b)	9.9172-4	9.9187-4	9.9200-4	9.9167-4	9.8981-4	9.8703-4	9.8269-4	9.7539-4

* THERMODYNAMIC PROPERTIES FITTED TO 20000.K
PRODUCTS WHICH WERE CONSIDERED BUT WHOSE MOLE FRACTIONS
WERE LESS THAN 1.000000E-10 FOR ALL ASSIGNED CONDITIONS

*C *CH *C2 C2H C2H3,vinyl C2H5 C2H6 *C3 C3H3,1-propynl C3H3,2-propynl C3H4,allene C3H4,propyne C3H4,cyclo- C3H5,allyl C3H6,propylene C3H6,cyclo- C3H7,n-propyl C3H7,i-propyl C3H8 *C4 C4H2,butadiyne C4H4,1,3-cyclo- C4H6,butadiene C4H6,1butyne C4H6,2butyne C4H6,cyclo- C4H8,1-butene C4H8,cis2-buten C4H8,tr2-butene C4H8,isobutene C4H8,cyclo- C4H9,n-butyl C4H9,i-butyl C4H9,s-butyl C4H9,t-butyl C4H10,n-butane C4H10,isobutane *C5 C5H6,1,3cyclo- C5H8,cyclo- C5H10,1-pentene C5H10,cyclo- C5H11,pentyl C5H11,t-pentyl C5H12,n-pentane C5H12,i-pentane CH3C(CH3)2CH3 C6H2 C6H5,phenyl C6H6 C6H10,cyclo- C6H12,1-hexene C6H12,cyclo- C6H13,n-hexyl C6H14,n-hexane C7H7,benzyl C7H8 C7H14,1-heptene C7H15,n-heptyl C7H16,n-heptane C7H16,2-methylh C8H8,styrene C8H10,ethylbenz C8H16,1-octene C8H17,n-octyl C8H18,n-octane C8H18,isooctane C9H19,n-nonyl C10H8,naphthale C10H21,n-decyl C12H9,o-bipheny C12H10,biphenyl SiC C(gr) Si(L) SiC(L)

POINT	ITN	T	H	C	SI
1	4	1900.000	-10.463	-4.621	-6.869
2	4	1950.000	-10.505	-4.428	-7.066
3	4	2000.000	-10.545	-4.284	-7.219

THERMODYNAMIC EQUILIBRIUM PROPERTIES AT ASSIGNED
TEMPERATURE AND PRESSURE

CASE =	REACTANT	MOLES	ENERGY KJ/KG-MOL	TEMP K
NAME	H2	**********	0.000	0.000
NAME	C3H8	10.0000000	0.000	0.000
NAME	SiH4	30.0000000	0.000	0.000

O/F= 0.00000 %FUEL= 0.000000 R,EQ.RATIO= 0.000000 PHI,EQ.RATIO= 0.000000

THERMODYNAMIC PROPERTIES

P, BAR	0.19998	0.19998	0.19998
T, K	1900.00	1950.00	2000.00
RHO, KG/CU M	2.6002-3	2.5325-3	2.4678-3
H, KJ/KG	24301.4	25223.5	26187.0
U, KJ/KG	16610.3	17326.8	18083.1
G, KJ/KG	-160891.7	-165777.1	-170686.7
S, KJ/(KG)(K)	97.4700	97.9490	98.4368

Appendix A: (Continued)

M, (1/n)	2.054	2.053	2.052
MW, MOL WT	2.052	2.051	2.050
(dLV/dLP)t	-1.00046	-1.00067	-1.00096
(dLV/dLT)p	1.0132	1.0188	1.0266
Cp, KJ/(KG)(K)	18.0963	18.8194	19.7601
GAMMAs	1.2973	1.2865	1.2741
SON VEL,M/SEC	3158.7	3187.3	3213.3
MOLE FRACTIONS			
CH2	1.4236-9	3.3818-9	7.4073-9
CH3	5.7223-7	9.0987-7	1.3610-6
CH4	1.6051-5	1.7788-5	1.8895-5
C2H	1.761-10	7.185-10	2.535 -9
C2H2,acetylene	7.5457-6	1.7705-5	3.6933-5
C2H2,vinylidene	3.948-10	1.239 -9	3.407 -9
C2H3,vinyl	2.035-10	5.281-10	1.212 -9
C2H4	1.8567-8	3.2185-8	5.0352-8
C3H3,2-propynl	5.440-11	1.921-10	5.690-10
C3H4,propyne	1.661-11	4.587-11	1.076-10
C4H2,butadiyne	2.261-11	1.251-10	5.471-10
*H	1.7740-3	2.5616-3	3.6322-3
*H2	9.9721-1	9.9641-1	9.9532-1
*Si	1.7529-5	3.1602-5	5.7389-
SiC	1.386-11	5.018-11	1.702-10
SiC2	1.8345-8	7.1694-8	2.5188-7
SiH	1.1380-5	1.7852-5	2.8400-5
SiH2	1.6244-6	2.1889-6	3.0153-6
SiH3	4.5585-8	5.4863-8	6.7863-8
SiH4	5.3105-8	4.8604-8	4.6359-8
Si2	1.5149-7	2.8984-7	5.7767-7
Si2C	7.9586-7	1.8485-6	4.2651-6
Si3	1.2906-8	2.3190-8	4.5172-8
SiC(b)	9.6224-4	9.3828-4	8.9493-4

* THERMODYNAMIC PROPERTIES FITTED TO 20000.K

PRODUCTS WHICH WERE CONSIDERED BUT WHOSE MOLE FRACTIONS
WERE LESS THAN 1.000000E-10 FOR ALL ASSIGNED CONDITIONS

*C *CH *C2 C2H5 C2H6 *C3 C3H3,1-propynl C3H4,allene C3H4,cyclo- C3H5,allyl C3H6,propylene C3H6,cyclo- C3H7,n-propyl C3H7,i-propyl C3H8 *C4 C4H4,1,3-cyclo- C4H6,butadiene C4H6,1butyne C4H6,2butyne C4H6,cyclo- C4H8,1-butene C4H8,cis2-buten C4H8,tr2-butene C4H8,isobutene C4H8,cyclo- C4H9,n-butyl C4H9,i-butyl C4H9,s-butyl C4H9,t-butyl C4H10,n-butane C4H10,isobutane *C5 C5H6,1,3cyclo- C5H8,cyclo- C5H10,1-pentene C5H10,cyclo- C5H11,pentyl C5H11,t-pentyl C5H12,n-pentane C5H12,i-pentane CH3C(CH3)2CH3 C6H2 C6H5,phenyl C6H6 C6H10,cyclo- C6H12,1-hexene C6H12,cyclo- C6H13,n-hexyl C6H14,n-hexane C7H7,benzyl C7H8 C7H14,1-heptene C7H15,n-heptyl C7H16,n-heptane C7H16,2-methylh C8H8,styrene C8H10,ethylbenz C8H16,1-octene C8H17,n-octyl C8H18,n-octane C8H18,isooctane C9H19,n-nonyl C10H8,naphthale C10H21,n-decyl C12H9,o-bipheny C12H10,biphenyl C(gr) Si(cr) Si(L) SiC(L)

Appendix A: (Continued)

Plot File:

P	T	CH2	CH3	CH4	C2H2,acetyle	C2H4	H
2.00E-01	1.50E+03	1.22E-13	3.19E-09	3.95E-06	5.23E-10	3.01E-11	3.94E-05
2.00E-01	1.55E+03	3.96E-13	5.47E-09	3.78E-06	1.36E-09	4.83E-11	7.04E-05
2.00E-01	1.60E+03	1.20E-12	9.08E-09	3.63E-06	3.33E-09	7.51E-11	1.22E-04
2.00E-01	1.65E+03	3.75E-12	1.62E-08	3.88E-06	9.47E-09	1.40E-10	2.03E-04
2.00E-01	1.70E+03	1.48E-11	3.75E-08	5.56E-06	4.61E-08	4.55E-10	3.30E-04
2.00E-01	1.75E+03	5.41E-11	8.33E-08	7.85E-06	2.06E-07	1.40E-09	5.20E-04
2.00E-01	1.80E+03	1.81E-10	1.73E-07	1.07E-05	8.16E-07	3.87E-09	8.01E-04
2.00E-01	1.85E+03	5.39E-10	3.31E-07	1.36E-05	2.73E-06	9.24E-09	1.20E-03
2.00E-01	1.90E+03	1.42E-09	5.72E-07	1.61E-05	7.55E-06	1.86E-08	1.77E-03
2.00E-01	1.95E+03	3.38E-09	9.10E-07	1.78E-05	1.77E-05	3.22E-08	2.56E-03
2.00E-01	2.00E+03	7.41E-09	1.36E-06	1.89E-05	3.69E-05	5.04E-08	3.63E-03
P	T	CH2	CH3	CH4	C2H2,acetyle	C2H4	H

Appendix B: Characterization Techniques

The films grown during this research have been characterized by many different techniques. The film surfaces were analyzed using both scanning electron microscopy (SEM) and atomic force microscopy (AFM). The thickness of the films was determined by cross-section SEM imaging, while a select few were determined by Fourier transform infrared (FTIR) analysis. The electrical characteristics of the films were investigated using the capacitance-voltage (C-V) technique. The structural and optical quality was determined by X-ray diffraction (XRD) and low temperature photoluminescence (LTPL), respectively. The characterization techniques performed on the 4H-SiC grown epitaxial layers are discussed below.

(1) Secondary Electron Microscopy (SEM):

The surface morphology and thickness of 4H-SiC epitaxial films grown during this research were analyzed using a Hitachi S-800 field emission SEM. Magnifications as high as 300,000X are achievable with this Hitachi SEM, however, for the use of the samples grown during this research, a magnification range of 100 - 30,000X was typically used. The image resolution for the Hitachi is ~ 20 Å. The following is a description of how the SEM is used to analyze the surface of the films.

The Hitachi SEM employed in this work uses a field emission electron source to produce an electron beam which is focused onto the sample surface. Secondary electrons are then collected and a magnified image of the secondary electron distribution is

displayed on a cathode ray tube (CRT) [79]. The electron beam is produced by applying a voltage (extraction voltage across a cathode and anode) in which electrons are emitted from the cathode. The typical extraction voltage used to analyze the samples was 2 kV. The electrons were then accelerated by an applied voltage called the acceleration voltage, which was typically set between 15– 20 kV to analyze the 4H-SiC samples in this research. The electron beam is focused by a condensing lens, which reduces the diameter of the electron beam. A scan coil is used to electromagnetically scan the electron beam across the sample surface. An objective lens is also used to focus the electron beam. The SEM is operated under vacuum to prevent atmospheric interactions with the emitted secondary electrons.

The incident electron beam on the sample surface stimulates the emission of secondary electrons from the sample surface. There are three types of electrons emitted: secondary electrons, auger electrons, and backscattered electrons. Figure B.1 shows a sketch of the emitted electrons from the sample created by the incident electron beam. The resolution of images using the SEM is very high because the secondary electrons emerge from the first 50 – 500 Å of the sample surface. The secondary electrons emitted from the sample are then collected by a detector. The main component of the detector is a scintillation material, which emits light when struck by electrons. The light is then amplified and displayed on a CRT. With a CCD camera, the images may also be captured electronically and viewed on a computer monitor.

Appendix B: (Continued)

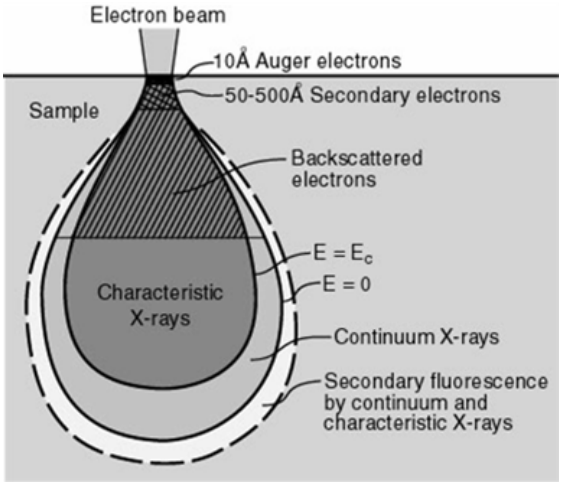

Figure B.1 Sketch of electron distribution from an electron beam bombardment onto a sample surface [80].

An example of the surface morphology evaluated using the Hitachi SEM as a characterization tool is shown in Figure B.2. The film in Figure B.2(a) displays step-bunching, which is created when atomic steps combine. The result is a film with lines on the surface as seen in the micrograph. The surface of a good quality film should be smooth. Therefore, the growth process that resulted in the film in Figure B.2(a) was changed to produce a higher quality surface. Figure B.2(b) displays a film with no surface structure, indicating a smooth morphology. The SEM therefore is a useful tool to help characterize the surface of the grown films and to improve the 4H-SiC epitaxial films.

Appendix B: (Continued)

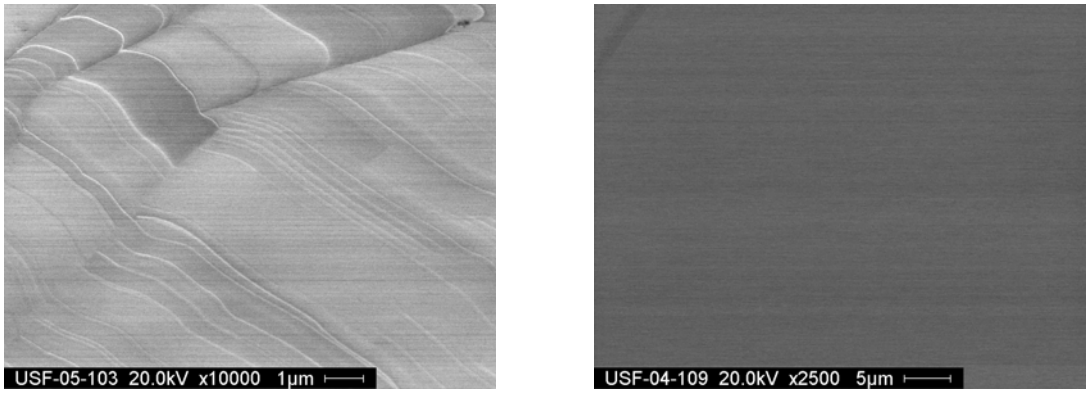

(a) (b)

Figure B.2 Plan-view SEM images of (a) a sample with step bunching and (b) a sample with smooth morphology.

The thickness of the epitaxial layers was estimated by cleaving the samples and looking at the cross-section of the film using the SEM. Contrast between the epitaxial layer and the substrate can be seen with the SEM, provided there is a difference in the doping densities of the two regions (which is typically the case). An n-type material requires a higher energy for secondary electron emission compared to a p-type material [81]. Therefore, the SEM image for p-type material will be brighter compared to that of n-type material for the same voltage applied.

The thickness of each epitaxial film was typically measured in three different positions along the sample edge and the values averaged. Based on the estimated film thickness and known growth time, the growth rate (defined as the average thickness divided by growth time and denoted by V_g in µm/h) was estimated. Figure B.3 shows an example of three cross-section SEM micrographs taken on one sample at different positions. The sample was mounted vertically so that the sample edge could be studied. The measurements were taken on the "top," "middle," and "bottom" of the cleaved edge.

Appendix B: (Continued)

Occasionally, difficulties were experienced in viewing the epitaxial film due to the lack of contrast in the images caused by cleavage lines on the crystal edge. Therefore, the thickness was based on only two positions instead of the typical three. For the sample shown in Figure B.3, the average thickness was approximately 4.2 μm and the growth time was 15 minutes. The calculated average growth rate was therefore 17 μm/h.

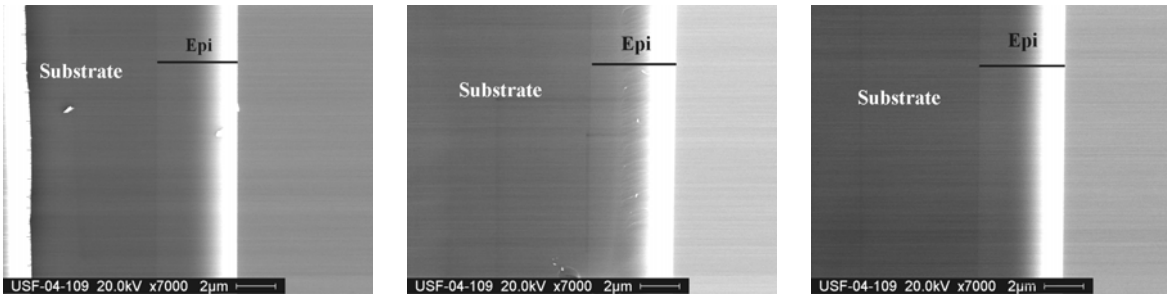

(a) (b) (c)

Figure B.3 Cross-section SEM micrographs of a 4H-SiC cleaved sample edge showing the epitaxial layer and substrate for (a) "top," (b) "middle," and (c) "bottom" positions of the sample. The measured thicknesses were 4.1 μm, 4.3 μm and 4.3 μm, respectively, yielding an average V_g of 17 μm/h (t = 15 minutes).

(2) Atomic Force Microscopy (AFM)

A Digital Instruments Nanoscope Dimension 300 AFM was used to analyze the surface morphology of the 4H-SiC epitaxial films. The AFM provides information of surface topography with angstrom scale resolution. The AFM produces images in 3-dimensions by continuous XY raster scans across a selected area of the sample. Surface features such as step bunching may be investigated with this tool. The RMS surface roughness may be obtained from AFM scans, which is an indication of the vertical

deviation of the AFM tip from a horizontal reference surface. This information is beneficial in characterizing the morphology of the epitaxial layers. For a smooth, specular film morphology, the RMS surface roughness will be lower than that for a surface that contains surface defects or a rough morphology.

A probe, which has an atomically sharp tip at the end of a cantilever (usually Si), is scanned over the surface of a sample using a piezoelectric scanner [82]. When the tip is within an interatomic distance to the sample, van der Waals forces either repel or attract the tip to the sample surface. A laser is focused on the backside of the cantilever tip and is reflected into a position sensitive detector, which is shown in Figure B.4. When the cantilever changes position due to the attractive and repulsive forces between the tip and the sample, the laser position changes and is detected by the detector. This change in height determines the topography of the sample. The AFM images are produced through a feedback loop between the detection system and the scanner [82].

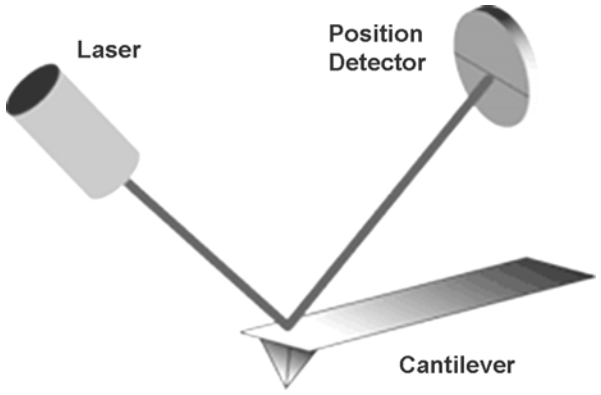

Figure B.4 AFM beam sample detection system [83]. The laser is directed on the backend of the cantilever and is reflected to a position sensitive detector. This is how the height information is detected from the sample surface.

Appendix B: (Continued)

The mode used for the AFM analysis was non-contact tapping mode. In this mode, the cantilever is positioned over the sample and taps the surface for a small portion of the oscillation time, instead of being in continuous contact with the sample. This mode helps to eliminate damaging forces that may occur in contact-mode. The amplitude is maintained constant at the operating frequency [82]. The typical scan area for the 4H-SiC samples was 10 μm x 10 μm. The scan rate depends on the scan size, in that a smaller scan rate is needed for larger scan areas to reduce damage to the surface. The typical scan rate used, for scan areas of 10 μm x 10 μm, was 0.5 Hz. An AFM scan of a sample grown during this research is shown in Figure B.5.

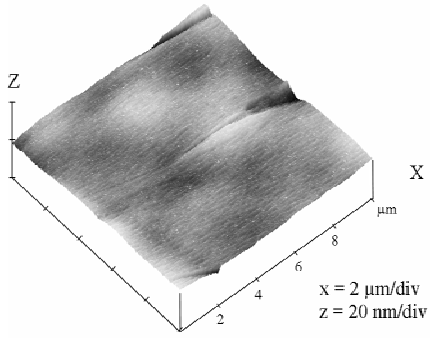

Figure B.5 AFM surface scans of 4H-SiC epitaxial films grown in the 200 mm LP hot-wall CVD reactor. The resulting surface roughness values was 0.9 nm RMS.

The AFM scan shown in Figure B.5 was used to determine the surface morphology of a 4H-SiC film grown during this research. The scan displays a defect on the surface of the film in the top right corner which may have been extended from the substrate. The surface roughness was determined to be 0.9 nm RMS, which is a representative of a relatively smooth film. As seen from the image in Figure B.5, the surface morphology of films may be determined by using the AFM tool.

(3) X-ray Diffraction (XRD)

X-ray diffraction was used to characterize the structural quality of the 4H-SiC epitaxial films grown. This is a non-destructive technique in which the epitaxial film is subjected to an X-ray beam. The X-rays are generated within an X-ray tube where a current is passed through a filament and electrons are thermally produced. The electrons are accelerated from a cathode towards an anode due to an applied potential, in which the electrons within the anode are bombarded out of their valence shell from the collision, creating vacancies. When electrons from a higher shell fill the vacancies of the lower shell, energy is released and is given off as an X-ray. These released X-rays are guided through a window within the X-ray tube and create an X-ray beam. The X-ray beam is then guided toward the sample where diffraction may take place. The X-rays that are diffracted from the film surface are detected by a detector. The amount of X-rays collected are converted into intensity and plotted against the angle position of the detector (or sample stage, depending upon the type of scan performed).

Diffraction is only possible when the waves of the X-rays are in phase with each other. When the waves are out of phase (or destructive interference), they cancel each other out, in which diffraction cannot occur. However, when the waves are in-phase(constructive interference), the waves reinforce each other, creating diffracted X-rays. For diffraction to occur, the Bragg's law must be satisfied (shown in Figure B.6), which is:

$$n\lambda = 2d\sin\theta \tag{B.1}$$

where n = order of diffraction, λ = wavelength of X-rays, d = distance between atomic, and θ = angle of incidence.

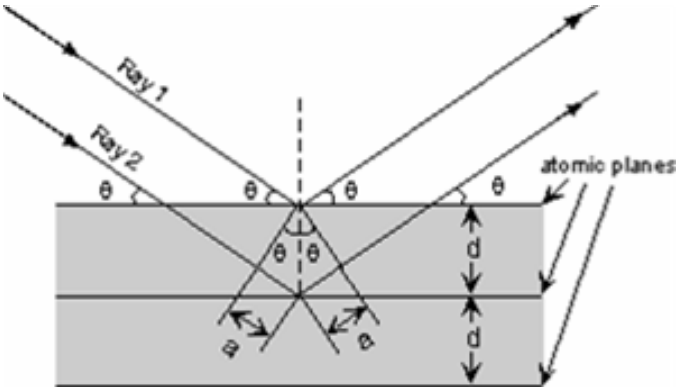

Figure B.6 Demonstration of Bragg's law, showing the angle of incidence, the atomic plane spacing, and two X-rays being diffracted [84].

High-resolution XRD (HRXRD) may be used to investigate epitaxial layer's lattice constants, dopant concentration, lattice mismatch, epitaxial thickness, and crystal perfection [85]. One concentration for characterization of the epitaxial films grown during this research was the determination of crystalline quality. Within the epitaxial film, defects such as dislocations and point defects may be present, which may significantly influence the diffraction of X-rays [86]. The defects may contribute to complicated X-ray diffraction patterns.

The typical scan performed for the 4H-SiC epitaxial structural characterization was an X-ray rocking curve (ω-scan). To obtain a rocking curve, the sample is slowly rotated or rocked about an axis relative the sample normal [79]. The diffraction peak is then collected as intensity versus the angle of diffraction. This type of scan was used to determine the structural quality of the film by measuring the FWHM value of the (0004)

diffraction peak. The (0004) reflection plane was measured because the epitaxial layers were 4H-SiC. The higher quality (less crystal defects) films produce a lower FWHM value. Peak broadening may be contributed to curvature of the crystal or imperfect epilayers created by defects [86]. If double diffraction peaks are observed, it may indicate that the epitaxial film is tilted against the substrate [85].

The high-resolution X-ray diffraction measurements were performed using a Phillips X'Pert Pro XRD system. Figure B.7 shows a schematic drawing of the diffractometer arrangement. The Cu $K\alpha_1$ source (at 45kV and 40 mA) was selected using a 4-bounce Ge (440) high resolution monochromator, which was placed on the incident beam side between the X-ray tube and the sample. The Ge (440) monochromator, used for high quality semiconductor material, is capable of resolving closely spaced peaks [87]. The beam size displaced on the sample was approximately 5mm x 5mm, which was controlled by adjustment knobs on the monochromator. The diffracted beam optics utilized during the XRD measurements was a triple axis attachment, which may be used for rocking curve measurements. This attachment was placed between the sample and the detector. The triple axis optics uses a Ge crystal analyzer which allows an angle of acceptance for the incoming beam of less than 12 arcsec [87]. The combined incident and diffracted beam optics were employed to perform the rocking curve measurements.

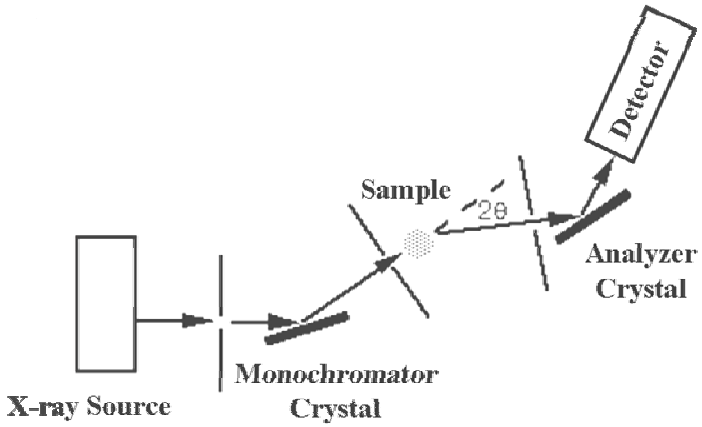

Figure B.7 X-ray diffractometer schematic for rocking curve measurements. The schematic contains the X-ray source, monochromator, sample, analyzer crystal, and detector [88].

Figure B.8 shows XRD rocking curves of the (0004) peak of 4H-SiC samples. The diffraction peak shown in Figure B.8(a) is a single peak with a FWHM of 36 arcsec, indicating a decent quality film. The (0004) diffraction peak of the 4H-SiC sample shown in Figure B.8(b) has two peaks. This may be caused from the epitaxial layer being so thin. When the film is thin, diffraction from the substrate may also be displayed. The FWHM of the peak is approximately 22 arcsec, also indicating decent quality film. As shown from Figure B.8, the film quality of the epitaxial layers may be found by using XRD as a characterization technique.

Appendix B: (Continued)

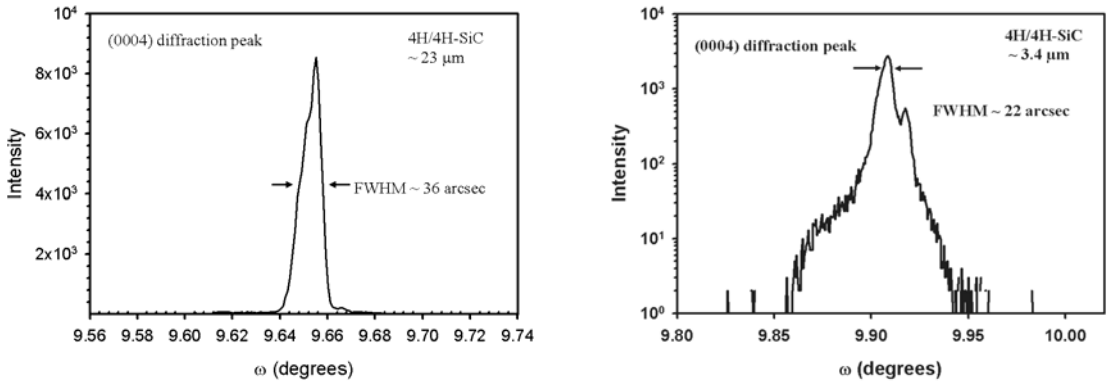

Figure B.8 X-ray diffraction rocking curves for 4H-SiC films of (a) 23 μm thickness and (b) ~ 3.4 μm thickness.

(4) Current-Voltage/ Capacitance-Voltage (CV/IV)

The net carrier concentration of the 4H-SiC samples was determined by performing capacitance-voltage measurements using a HP 4280A C-V meter. The grown samples were deposited with a backside contact of Ni-Ti-Au and a front side contact of Ni-Au. Before capacitance-voltage measurements were performed, current-voltage measurements were taken, using a HP 4145B Semiconductor Parameter Analyzer, to verify the device was a diode. Once determining the device was a schottky diode (this was the type of diode used for the CV-IV measurements during this research), C-V measurements were then be performed. The C-V measurements were based on the depletion approximation. The width of the space charge region, a region where there are no mobile carriers, depends on the applied voltage. The relationship between the space charge region and the doping density is found in the following equations.

$$W = \frac{K_s \varepsilon_0 A}{C} \tag{B.2}$$

where W is the space charge region, K_s is the semiconductor dielectric constant , ε_0 is the permittivity, A is the area of the diode, and C is the capacitance.

and
$$N_A(W) = \frac{2}{qK_s\varepsilon_0 A^2 d\left(1/C^2\right)/dV} \tag{B.3}$$

where N_A is the p-type doping density, q is the electron charge, and V is the voltage. Note that equation (B.3) has assumed that $N_A >> N_D$.

A reverse-bias is applied to the metal/semiconductor junction (schottky diode) and the capacitance is measured as the width of the space charge region is increased. The typical voltage range that was applied to an n-type epitaxial layer was -5V to 0V with a step size of 0.05V. The doping density can be found either by the slope (dC/dV) of the plot, C versus V or by taking the slope ($d(1/C^2)/dV$) of the plot $1/C^2$ versus V [79]. An example of the I-V and C-V plots used to obtain the doping concentration of an n-type, 4H-SiC epitaxial layer are shown in Figure B.9. Note the C-V method measures the net carrier concentration. For an n-type material, Nd-Na is found, while for a p-type film, the carrier concentration is determined as Na-Nd.

Appendix B: (Continued)

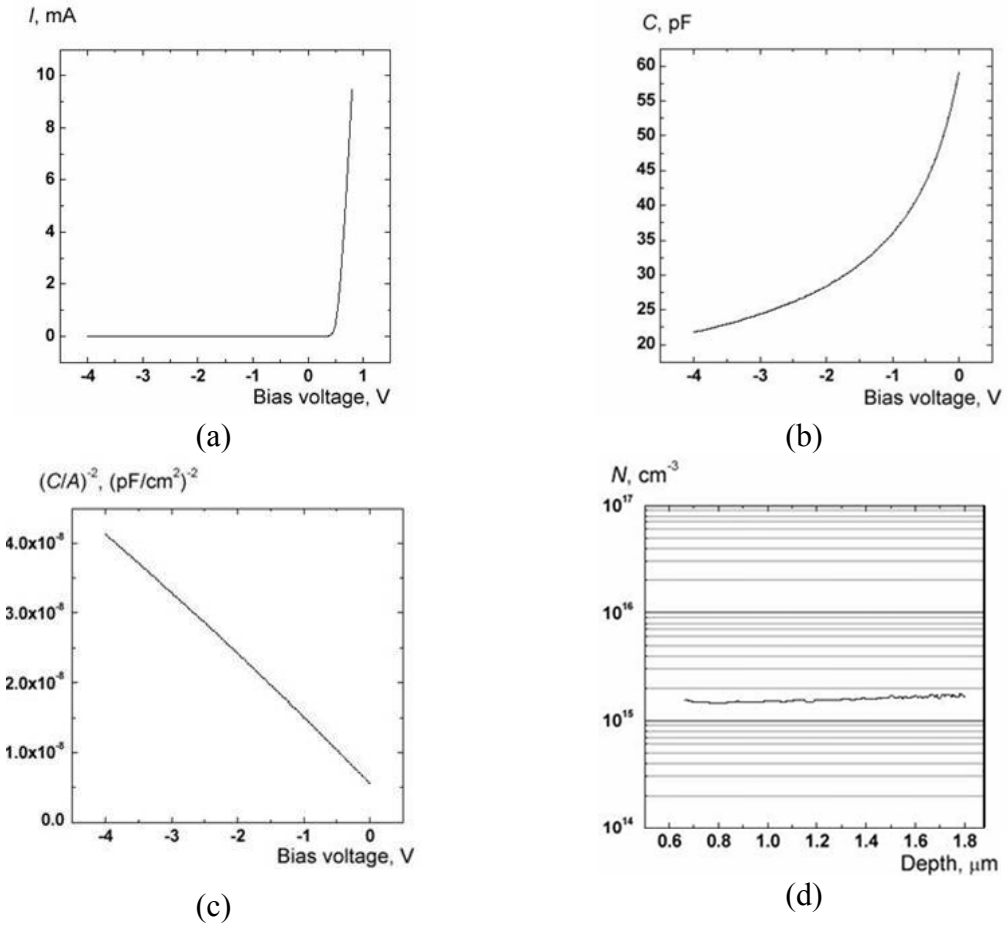

Figure B.9 Data plots of I-V and C-V curves used to extract the doping concentration of an n-type 4H-SiC epitaxial layer. (a) Current-voltage curve, (b) capacitance-voltage curve, (c) inverse of capacitance squared-voltage curve, and (d) net carrier concentration vs. depth curve. Data taken by J. Walker, University of South Florida.

A characteristic I-V curve for an n-type, 4H-SiC epitaxial layer (not grown during this dissertation research), is shown in Figure B.9(a). At approximately 0.5 V, the diode turns on. The capacitance measured as a function of voltage is shown in FigureB.9(b). The data is entered into a plotting program which then plots ($1/C^2$) vs. V, shown in Figure B.9(c), using the equation (B.3). Finally, the doping concentration is extracted (Nd-Na ~1.5×10^{15} cm^{-3}) and an example is shown in Figure B.9(d).

Appendix B: (Continued)

(5) Fourier Transform Infrared Spectroscopy (FTIR)

Selected epitaxial films thicknesses were determined using FTIR analysis, as discussed in Chapter 4, Section 4.3.2. An Accent QS 1200 by Accent Optical Technologies, Inc FTIR spectrometer was used for the measurements. This thickness measurement method is non-destructive and has the added benefit of quick processing results, while that of SEM analysis is destructive due to sample cleavage. The SEM analysis method is quite time consuming.

The basic principle of FTIR spectroscopy is that an optical intensity is determined versus wavelength [89]. With this technique, there is an interference of light waves which is measured. A schematic of an FTIR spectrometer is shown in Figure B.10. An infrared beam is directed to a beam splitter, where part of the beam passes through the splitter and is reflected from a fixed mirror (M1). The other portion is reflected off the beam splitter, and then is directed to a movable mirror (M2), in which the beam is reflected back.

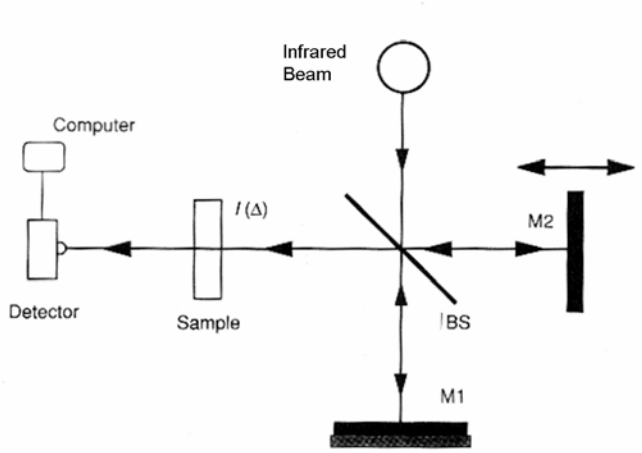

Figure B.10 Diagram of the FTIR spectroscopy set-up. $I(\Delta)$ is the interference signal, *BS* is the beam splitter, M1 is the fixed mirror, and M2 is the movable mirror [89].

As M2 moves, the interference signal varies due to the recombining of the waves from M1 and M2. When M2 changes positions, the length of travel (Δ) changes for the wave from M2, thus changing intensity of the combined wave. The detector measures the interference signal $I(\Delta)$ and an interferogram is developed, which is the intensity versus wavelength. A sample is placed before the detector in order to measure the reflectance from the epitaxial sample. Software is then used to convert the wavelength to the epitaxial thickness.

The data from the FTIR spectrometer is called an interferogram, which is a summation of cosine waves [90]. The configuration of the FTIR to perform epitaxial thickness measurements is reflectance. In this mode, a light is observed by the detector after being displaced by the sample surface. Figure B.11 schematically demonstrates the reflectance of incident radiation upon an epitaxial layer.

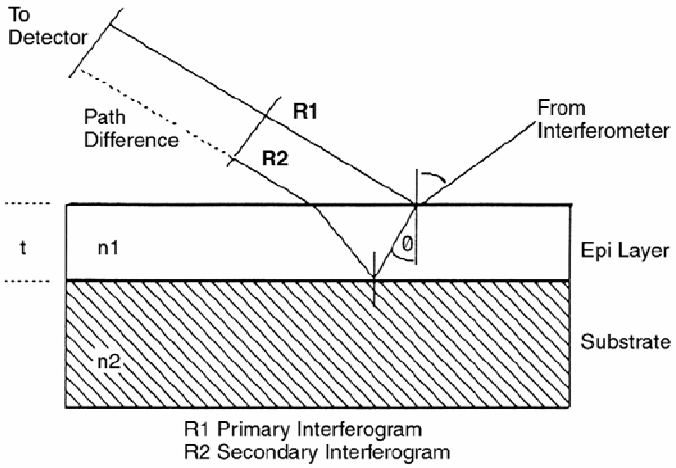

Figure B.11 Schematic drawing of the radiation reflections during epitaxial thickness measurements using FTIR. The radiation exits the interferometer and reflects from the surface of the epitaxial layer (R1) and the remaining radiation penetrates through the epilayer and reflects from the epi/substrate interface (R2) [90].

A portion of the infrared radiation from the interferometer (which consists of the stationary and movable mirrors, M1 and M2, respectively (shown in Figure B.10)) is reflected from the top surface of the epitaxial layer. This is the primary reflection (or primary interferogram), indicated as R1 in Figure B.11. The remaining radiation penetrates through the layer to the epi/substrate interface and is reflected. This is the secondary reflection (or secondary interferogram) and is indicated as R2 in Figure B.11. The difference between the primary and secondary reflections produces an interference pattern. The interference pattern depends on the doping concentration of the epitaxial film, the cosine of the angle shown in Figure B.11, and the thickness of the layer. The doping concentration difference between the epilayer and substrate determines the strength of the thickness measurement signal. In order to obtain the data in a desired format, a Fourier transform is applied. [90]

The process steps used to determine the film thickness using FTIR spectroscopy is shown in Figure B.12. Prior to evaluating the sample, a reference is assessed to eliminate any signal that may not come from the difference between R1 and R2 [90]. Once the interferogram of the reference has been obtained, an interferogram of the epitaxial sample is taken. An example of the interferogram is shown in Figure B.12(a). The spectra are then transformed into single-beam spectra by Fourier transforms (Figure B.12(b)). The sample and reference signals are then subtracted from each other (Figure B.12(c)). A second Fourier transform is applied to the signal, at which time a phase correction is taken of the spectrum. The results are then reported as thickness versus intensity

Appendix B: (Continued)

(Figure B.12(d)). A software package, FilmZ by Accent Optical Technologies, automatically performs these steps for each film thickness measurement. The epitaxial film thickness is displayed as the peak with the strongest signal in Figure B.12(d).

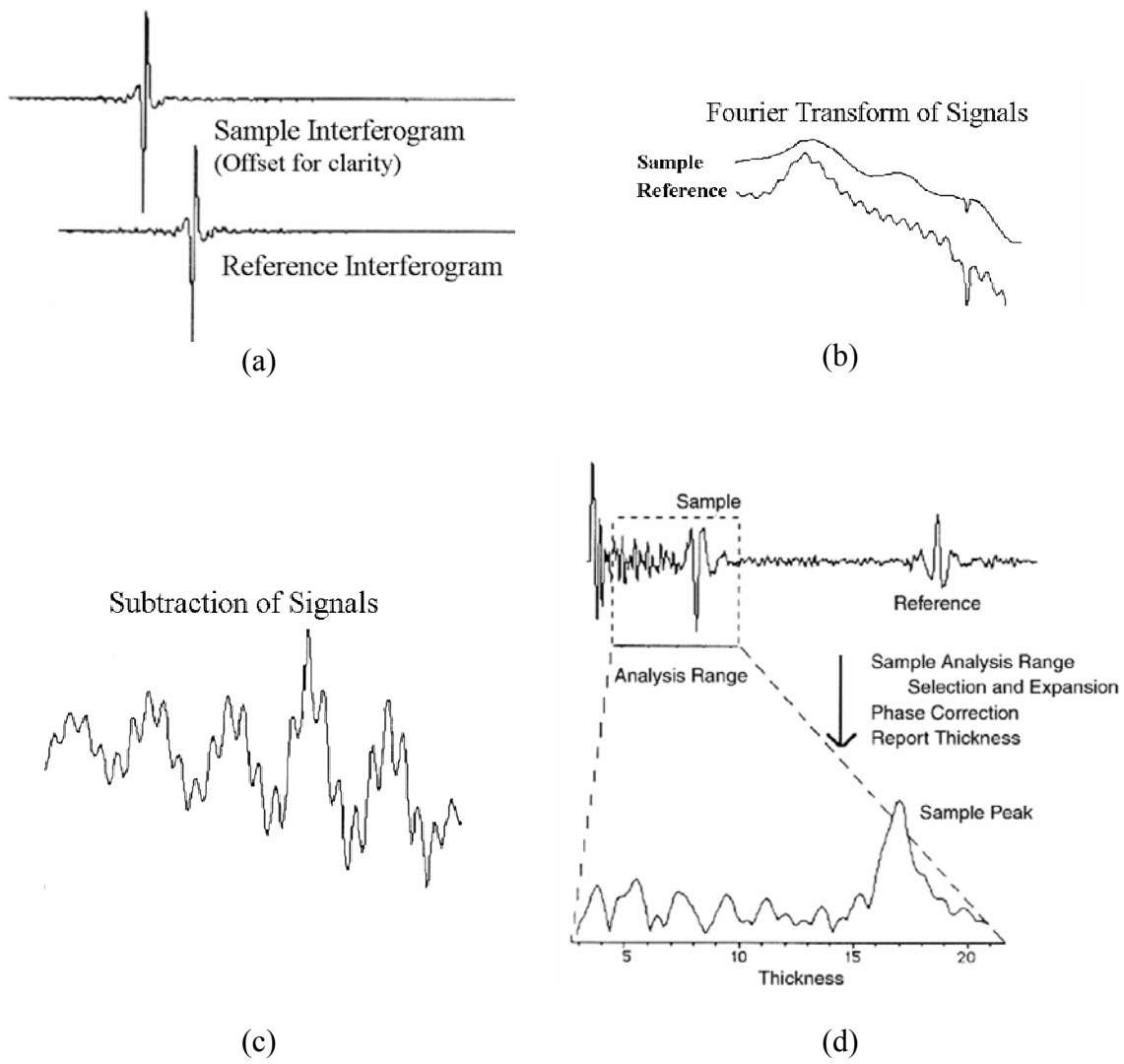

Figure B.12 Flow diagram for epitaxial film thickness determination using FTIR spectroscopy. (a) Reflectance interferograms from the epitaxial layer and epi/substrate interface, (b) single-beam spectra created by Fourier transform of the reflectance interferograms, (c) subtraction of the single-beam spectra, and (d) second Fourier transform of the spectra (top spectra) followed by a report of thickness value determined by phase correction [90].

Appendix B: (Continued)

Figure B.13 shows a representative of a film characterized by FTIR. The film thickness was estimated to be ~ 8 μm as determined from the Fourier transform of the reflectance spectrum. The vertical line in the figure indicates the thickness of the film.

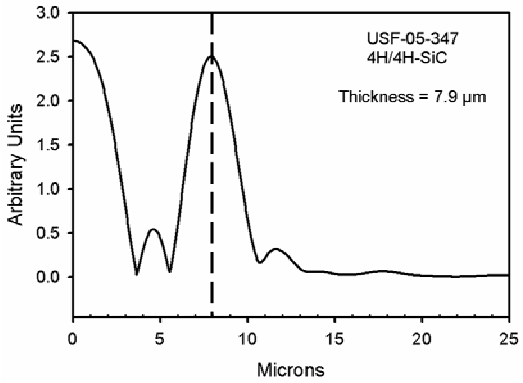

Figure B. 13 Fourier transform of the reflectance spectrum showing a thickness of ~ 8μm.

(6) Low-temperature Photoluminescence (LTPL)

LTPL was performed on the grown 4H-SiC films to determine their optical quality. The analysis was performed at the University of Pittsburgh, by Professor W. J. Choyke's group. PL is a non-destructive method which can determine donor and acceptor impurities within the grown film. The impurities which can be detected are those that produce radiative recombination processes [79].

In LTPL experiments, the sample is typically placed in a cryostat because low temperatures are needed to reduce thermal broadening of excited carriers and reduce non-radiative recombination processes [79,89]. For the LTPL analysis performed by Professor Choyke's group, the measurements were taken at 2K. A laser (with a wavelength ~

4000Å for the measurements performed during this dissertation) is used to excite electrons to create electron-hole pairs, which then recombine and give off photons. For LTPL, the photons should mostly be radiative. The laser must have a higher energy than the band-gap of the material to create the electron-hole pairs. A diagram of the PL arrangement is shown in Figure B.14. The emitted photoluminescence from the sample passes through a monochromator, which provides one wavelength to the detector. The data is collected as photoluminescence intensity versus photon energy or wavelength.

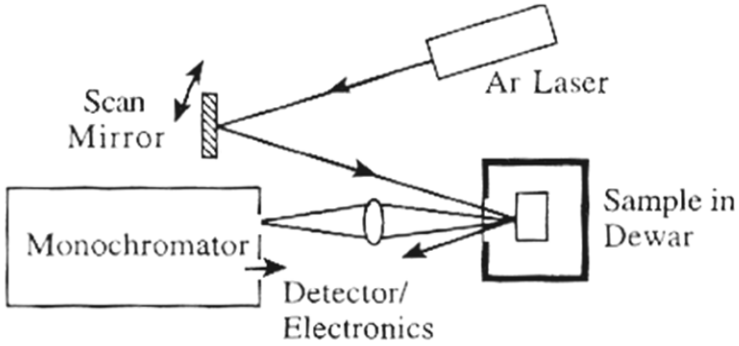

Figure B.14 Diagram of photoluminescence arrangement which includes a source laser, a mirror, a monochromator, a detector, and a sample placed inside a cryostat [79].

The energy of the photons depends on the type of recombination process. There are five main radiative recombination processes which are shown in Figure B.15. Band-to-band recombination is shown in Figure B.15(a), however, it is not typically seen in LTPL. Figure B.15(b) shows a free-exciton recombination,. A free-exciton is an electron-hole pair loosely bound to each other. The free-exciton is free to move throughout the crystal.

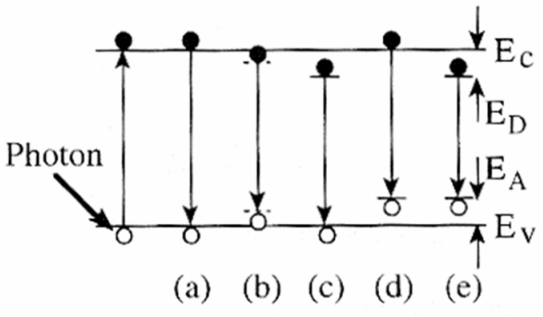

Figure B.15 Recombination processes that may create radiative photons which can be detected for PL analysis. (a) Band-to-band recombination, (b) free-exciton recombination, (c) bound-exciton recombination by a neutral acceptor, (d) bound-exciton recombination by a neutral donor, and (e) donor-acceptor (D-A) recombination. EV is the valence band energy, EC is the conduction band energy, EA is the acceptor energy and ED is the donor energy. [79]

The bound-exciton recombination is shown in Figure B.15(c) and (d). A bound-exciton is where a free exciton (or electron hole pair) is captured by a shallow donor. There are two types of bound excitons; the neutral bound exciton and the ionized bound exciton. The most common is the neutral bound exciton where the free exciton forms a four particle complex together with the donors electron (or acceptors hole) and with the defect core. The ionized bound exciton is a free exciton bound to an ionized donor or acceptor. In Figure B.15(c), the donor is trapped in the shallow site, while in Figure B.15(d), the acceptor is trapped in the shallow site. Note that for less pure films, the bound-exciton recombination dominates that of the free-exciton recombination. Finally, Figure B.15(e) demonstrates an acceptor-donor recombination (also referred to as a donor-acceptor pair recombination) [79]. For heavily doped samples which contain both acceptors and donors, the exciton luminescence may not be strong enough for detection [43]. For this type of material, the most dominant luminescence is that from the donor

acceptor pair (DAP) recombination. The intensity of the DAP recombination typically appears in the no-phonon distant pairs peak along with the phonon replicas [91]. The distance between the donor and acceptor determines the DAP spectrum.

In low temperature photoluminescence, the recombination of neutral bound-excitons (neutral four-particle donor (nitrogen) or acceptor (aluminum) complexes) is measured to determine the photon energies [91]. In a donor complex, the four particles consist of the donor ion, two electrons, and a hole for donors. The presence of nitrogen within the epitaxial film can be determined using photoluminescence, in which the 4N (four-particle nitrogen donor complex) spectrum is associated with the radiative recombination of the neutral nitrogen donor four-particle bound-exciton complex [91]. A neutral four-particle aluminum acceptor bound complex may be observed in 4H- and 6H-SiC polytypes using LTPL as well. The four particles consist of the negatively charged acceptor ion, its hole, and the electron-hole pair which is attached to the exciton. The number of no-phonon lines present within the LTPL spectra is corresponds to the inequivalent sites on the C sub-lattice [91]. There are approximately 15 no-phonon lines present in the 4Al LTPL spectrum for the 6H-SiC polytype. However, for the 4H-SiC, there are only a few no-phonon lines in the 4Al LTPL spectrum.

High-quality material results in the recombination of free excitons during photoluminescence measurements [91]. An example of a near bandedge LTPL spectrum of a 4H-SiC epitaxial film is shown in Figure B.16. The free exciton peak is labeled I_{75} on the spectrum. For higher quality films, the free exciton related line becomes stronger in the spectrum [43]. The $4Al_0$ line indicates the no-phonon line of the neutral four-

particle aluminum acceptor complex. In the 4H-SiC polytype, the P and Q lines are representative of the neutral four-particle nitrogen donor complexes at different lattice sites. While that in the 6H-SiC polytype are indicated at P, R and S. The subscript for each line comprises of the phonon replica energy in meV [91]. The strongest phonon replicas are those with the weakest no-phonon line [43]. The no-phonon lines are indicated with the subscript 0. The P_0 peak is characteristic of the neutral nitrogen bound-exciton at the hexagonal site, while the Q_0 peak is that from the cubic site [92]. The no-phonon lines are due to the loss of constant translation related to the binding of the exciton [91]. There is not a no-phonon line for the free-exciton because it is not bound.

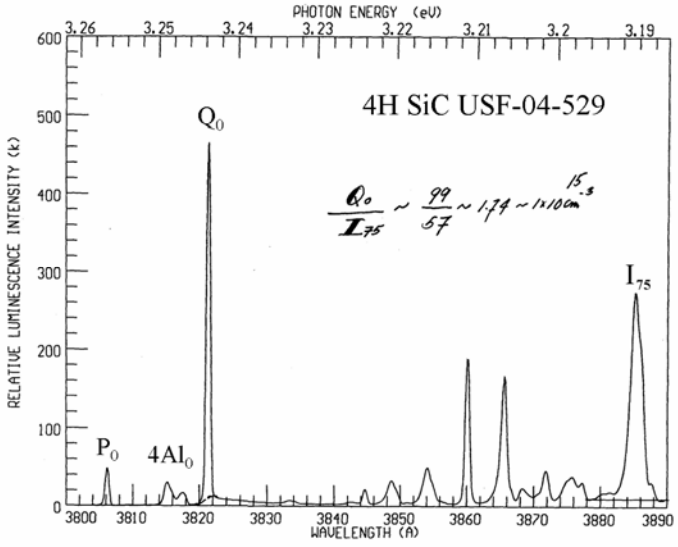

Figure B.16 Near bandedge LTPL spectrum of a 23 μm thick 4H-SiC film. Strong free exciton line is labeled I_{75}. P_0 and Q_0 lines are the neutral four-particle nitrogen donor complexes, while the $4Al_0$ peak indicates the no-phonon line of the neutral four-particle aluminum acceptor complex.

LTPL may also be used to determine the presence of nitrogen, as well as evaluating the epitaxial film quality. The concentration of the dopant may be assessed by

comparing the intrinsic component, i.e. free exciton line, to that of the extrinsic component, i.e. the bound-exciton line [62]. The nitrogen concentration within 6H-SiC may be found by the ratio of the intensity of the no-phonon line, P_0, to the free exciton replica, I_{77}. The I_{77} peak is the strongest free exciton line. The concentration of nitrogen within a 4H-SiC epitaxial layer may be found by the ratio of Q_0 to I_{75}. For films with low nitrogen doping concentrations, the free exciton line will become stronger [43].

Appendix C: Operating Procedure for 4H-SIC Epitaxial Growth in the USF 200 mm Reactor

The development of the 4H-SiC baseline growth process was presented in Chapter 3, Section 3.4. A process has been developed where high, repeatable growth rates are achieved. The process procedure which will be detailed next may be used to grow 4H-SiC in the 200 mm USF hot-wall CVD reactor. Parameters may need to be changed slightly from time to time, such as the temperature due to slight drifts in the apparatus. A sketch of the process schedule was shown in Figure 3.14. The step-by-step procedure for the epitaxial growth is detailed next.

Sample Loading:

1. Verify that the reactor hot-zone is free of debris by vacuuming out the hot-zone.
2. Load SiC substrate onto the polyplate and load the plate into the hot-zone.
3. Close reactor door with uniform pressure - (inspect o-ring seals prior to closing).

Appendix C: (Continued)

Reactor Seal Verification:

Purge Ar for ~ 2 min by pressing the "PURGE" button and the "Ar" button on the reactor control panel. This will purge moisture, air, and contaminants from the reactor.

1. Evacuate the reaction tube via manual pumping: press "H_2 LEAK" and press "MANUAL PUMPING". (The "H_2 LEAK" flows hydrogen through the reaction tube. By pressing the "H_2 LEAK", the H_2 will not flow, which will allow pumping to occur.)
2. Verify "PURGE" button is pressed and switch from "Ar" purge to "H_2" purge.
3. Once reactor pressure is below 500 mTorr, de-press "H_2 LEAK" to allow H_2 to start to pressurize the reaction tube.
4. After approximately 1 min (or when the pressure gauge reads atmospheric pressure), de-press "MANUAL PUMPING". This will begin H_2 purge.
5. Allow H_2 to purge for ~ 2 minutes.
6. Open labview program from reactor computer.
7. Set a flow of 10 slm of H_2 in the labview program.
8. Press "PROCESS MONITOR" and "PROCESS H_2" to enable a H_2 flow for ~ 2 minutes. This will allow the H_2 in the gas line to be purged from the manifold box through the reaction tube.

Appendix C: (Continued)

Growth Process:

1. Make sure all process gases are ready for growth (by having each line purged with the process gases), cooling water is on, and RF generator is on.
2. Set the desired flows for H_2, Ar, C_3H_8 and SiH_4 within the labview program.
3. Set the desired growth temperature, which is the set point temperature based on the Si melt test, in the labview program.
4. Start foam and view port argon purge by pressing “TOP Ar”.
5. Set the desired process pressure in the pressure controller and press “POPPET VALVE”. Make sure process pressure is achieved.
6. Check and clear interlocks by pressing “IRRESET”. If no sensors go off, then proceed to next step. If a sensor is activated, check and fix problem before continuing.
7. Turn off interlock override by pressing “SHUT”. This will enable all sensors so that if they are activated. In the event of a sensor trip, the system will shut down and go into an Ar purge.
8. Turn on RF power by enabling the inverter on the RF generator. This is done by flipping the switch up on the panel of the RF generator.
9. Set the board voltage to 5V in the Labview program.
10. Once the pyrometer is reading temperature from the susceptor, increase the board voltage as needed to continue a steady increase in temperature. Do not set board voltage above 7V.

Appendix C: (Continued)

11. Flow Ar, SiH_4 and C_3H_8 within the vent line to establish a steady flow for each gas approximately 10 minutes before growth by pressing "VENT Ar" first. Wait ~ 1 minute and then press "VENT SiH_4" and "VENT C_3H_8". This allows the gases to go directly to vent.
12. Once temperature is ~ 20 °C before set point temperature, go into automatic temperature control by pressing "Go AUTO" in labview program.
13. 15 °C before set point temperature, increase H_2 flow from 10 to 30 slm.
14. Once at growth temperature, introduce propane into process by de-pressing "VENT C_3H_8" and press "PROCESS C_3H_8".
15. After 30 seconds, introduce SiH_4 into the process by pressing "PROCESS SiH_4" and de-pressing "VENT SiH_4". The growth time starts from the time SiH_4 is added into the process.
16. Shut off "PURGE Ar" 30 seconds after "VENT SiH_4" has been de-pressed.
17. Maintain these flows and temperature throughout the growth run.
18. After the growth run is over, turn off RF power by setting the set point temperature and board voltage to zero. Shut SiH_4 and C_3H_8 off by de-pressing "PROCESS SiH_4" and then "PROCESS C_3H_8".
19. Disable the inverter on the RF generator by flipping the switch down and reset alarm on the RF generator.
20. Switch the H_2 flow from 30 slm to 10 slm.
21. When temperature drops below 1000 °C under these conditions, press and hold "PURGE" until the light on the button flashes.

Appendix C: (Continued)

Note: This step is an auto purge which initially flows H_2 for 30 seconds, and then is followed by an Ar purge for 30 minutes.

22. De-press “POPPET VALVE”.

23. After ~ 30 seconds, de-press “TOP Ar”.

24. Press “SHUT” to turn off interlocks.

Unload sample:

1. After auto purge is complete and the susceptor is no longer glowing, press “SAFE” button to de-activate the safety locks.

2. Open reactor door, pull out the polyplate and remove sample from polyplate.

Appendix D: HCl Purge Panel Operating Procedure

As described in Chapter 4, it is imperative to purge all HCl process lines with Ar at the end of use to prevent corrosion within the gas lines. If water vapor enters the HCl gas line, hydrochloric acid forms which is not only corrosive but also highly toxic. An HCl purge panel was implemented into the gas delivery system at the beginning of the HCl gas line to reduce corrosion. The step-by-step procedure for evacuating the HCl gas line is described next. A photograph of the HCl purge panel was shown in Figure 4.4 and is duplicated here for easy reference.

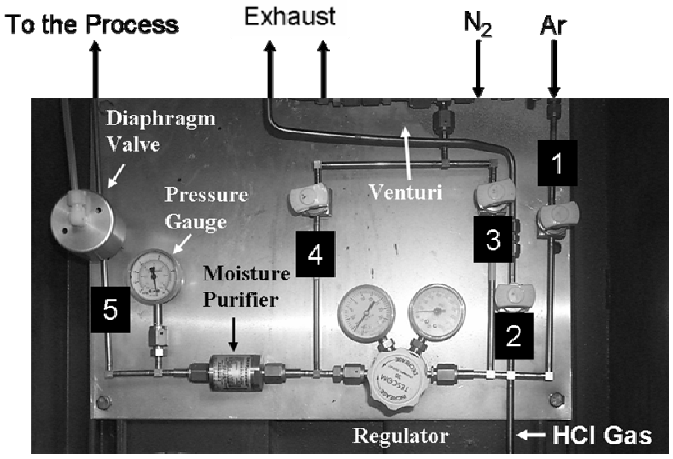

Figure D.1 HCl purge panel near the HCl gas bottle which was used to replace HCl with Ar in the gas lines to help prevent corrosion. Numbers in the picture represent valve numbers.

Appendix D: (Continued)

To purge the HCl gas out of the line, the HCl gas tank is closed and the following steps followed:

(1) Close valves 1-4.

(2) Open valve 5 (safety valve).

(3) Open valve 6.

This allows N_2 to flow through the venturi (shown in Figure 4.4(b)). The N_2 gas goes through the venturi at a high flow rate and to the exhaust. The N_2 creates a vacuum, where the gases from the "gas line" are vacuumed out of the gas lines through valves 3 and 4 from Figure 4.4(a).

(4) Open valve 4 until low pressure (~ 20 mmHg) is read on the low pressure side of the regulator.

By opening this valve first, the pressure will not exceed that which is set on the low pressure side of the regulator.

(5) Open valve 3.

This allows the HCl gas to be purged from the gas lines.

(6) Close valves 3 and 4.

(7) Open valve 1 to back-fill Ar into the gas lines. Note the Ar tank should always be open to prevent HCl from backfilling into the Ar line.

(8) Once the maximum pressure has been reached (~ 10 – 15 psi), which is set by the regulator, close valve 1.

(9) Repeat steps 4 - 8 approximately 10 – 15.

(10) At the last backfill of Ar, leave valve 1 open and close valve 6.

Appendix D: (Continued)

(11) Purge Ar through the gas line for 10 minutes by setting a maximum flow (20 sccm) in the labview program [49] and press "VENT Ar" on the control panel.

(12) Turn off gas flow by closing the HCl MFC and close valves 1-6.

It should be noted that Valve '2' is a secondary exhaust valve and is opened only when necessary. This may occur when the venturi has been damaged and the line needs to be purged with argon to the exhaust.

To introduce HCl back into the gas lines, the following steps are followed:

(1) Follow steps 2 – 11 above, which entailed purging of the gas lines with Ar. This is performed to ensure that no air is in the gas line after not being operational for a long period of time.

(2) Close valve1.

(3) Open the HCl tank slowly.

(4) Set a flow of 20 sccm in the labview program. Flow HCl gas to vent by pressing "HCl VENT" for 15 minutes. Simultaneously flow Ar through the "vent" to dilute the exhaust line.

Appendix E: Thickness Determination via Cross-Section SEM and FTIR Analysis

The thickness of the films grown in the 200 mm hot-wall reactor with the addition of HCl was presented in Chapter 4. The film thickness was initially determined by cross-section SEM analysis of the cleaved edge of the samples, which was the method employed for all the epi film thickness measurements reported in this dissertation. Results from LTPL analysis of the films displayed in Figure 4.22, performed by Professor Choyke's group at the University of Pittsburgh, were not in agreement with the HCl additive 4H-SiC epitaxial thickness values that were measured using this method at USF. That is to say the Pittsburgh group noted substrate luminescence from epi samples which should not have been present given that the epi thickness was greater than the optical absorption depth. Therefore, a study was performed to verify the thickness of the films grown (Figure 4.22) with the addition of HCl, as determined by cross-section SEM analysis. Fourier Transform Infrared Spectroscopy (FTIR) analysis was used to verify the thickness of the films as a new FTIR system (Accent Model QS 1200) was recently acquired by the SiC research group.

Before addressing the specific goal of validating the growth rate of 4H-SiC using HCl as a growth additive (growth rates displayed in Figure 4.22), a comparison of both the SEM and FTIR methods was made. A comparison of the estimated film thickness determined by both FTIR and cross-section SEM was performed on a sample grown using the standard growth process (no HCl additive, see Chapter 3) in the 200 mm hot-wall reactor. The epilayer was subjected first to thickness measurement by FTIR. The measurement was performed three times for accuracy purposes. The sample was then

cleaved and the cross-section studied under the SEM where the thickness was taken at three positions along the film edge. The average value of the three measurements was then computed and tabulated. The sample was then again analyzed by FTIR to compare both measurements (note that only a single point on the sample can be measured with the FTIR due to the small sample size of ~5 mm x 8 mm and concerns that the optical beam impinges on the sample edge which would reduce the accuracy of the measurement). Table E.1 gives the average thicknesses from these three experiments.

Table E.1 Epi layer thickness as determined by FTIR and cross-section SEM analysis.

Sample ID	Thickness (μm), 1st FTIR measurement	Thickness (μm) by cross-section SEM*	Thickness (μm), 2nd FTIR measurement
USF-04-060A	8.2	7.2	8.2

*value shown is average value of 3 measurements made along the film edge.

The FTIR spectra (reflectance spectra of the epi and the reference substrate ratioed and shown in μm units) from measurements of sample USF-05-060A prior to and after cleavage are shown in Figure E.1. As seen in the figure, there is a dominant peak which indicates the thickness of the epitaxial layer. The peak centered at 0 μm in this figure (as well as in all other figures in this Appendix) represents low frequency noise and should be disregarded.

Appendix E: (Continued)

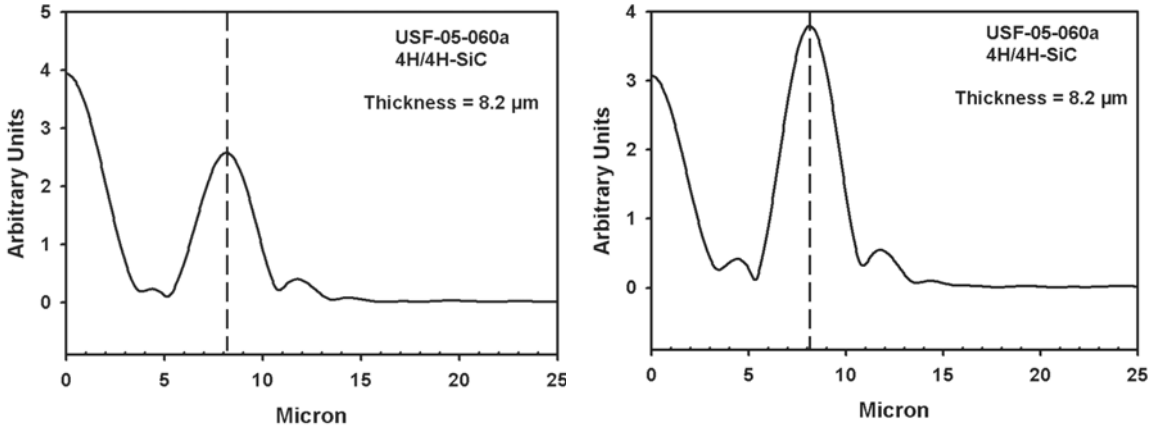

(a) (b)

Figure E.1 FTIR spectra of sample USF-05-060A (a) before sample was cleaved and (b) after sample was cleaved. In both cases the FTIR estimated thickness is 8.2 µm.

A cross-section SEM micrograph for the same sample (USF-05-060A) is shown in Figure E.2(a). Although the thickness seen in Figure E.2(a) is 7.39 µm, the average thickness from three positions along the sample edge was calculated to be 7.2 µm. Along with the epi thickness measurement, a 10 µm calibration sample was used to determine how accurately the SEM was calibrated. The plan-view image of the calibration sample is shown in Figure E.2(b). The distance from one etched line to another is known to be 10 µm, however, as seen in Figure E.2(b), it is only 9.33 µm. Therefore, the thickness was underestimated using the Hitachi S-800 SEM with an error of ~ 7.5 %. The thickness measurements were adjusted to give the correct values of the epitaxial thickness via cross-section SEM. The corrected average value is 7.7 µm for sample USF-06-060A in Figure E.2(a).

Appendix E: (Continued)

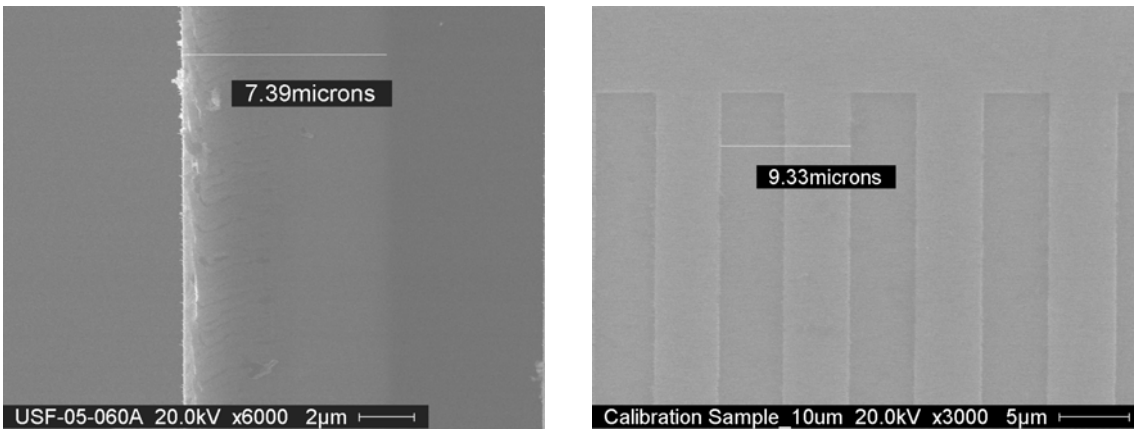

(a) (b)

Figure E.2 (a) Cross-section SEM micrograph of USF-05-060A cleaved edge and (b) plan-view SEM micrograph of 10 µm calibration sample. An error in the measurement of ~7.5% was observed. Note the error resulted in an underestimate of the film thickness and, therefore, growth rate.

The thickness values from the FTIR analysis and the cross-section SEM analysis are similar with approximately a 6.5% difference between the two methods for this example. With the results of the comparison between the two thickness measurements in reasonable agreement, the thickness of the 4H-SiC epitaxial films grown with HCl additive were determined using FTIR analysis. This was performed to compare the FTIR results with those of cross-section SEM analysis applied earlier.

The thickness of the grown films using HCl as a growth additive were first determined by cross-section SEM analysis (results presented in the graph of Figure 4.22). The samples were cleaved and thickness measurements taken at different positions. The average thickness was then calculated from these three values. The sample thicknesses were then evaluated using the FTIR. The thickness of each sample was measured three

times for accuracy purposes. The results of the average thickness using cross-section SEM and FTIR analysis are presented in the Table E.2 below.

Table E.2 HCl growth additive epi layer thickness summary from Chapter 4.

Sample ID	Thickness (μm) via cross-section SEM	Thickness (μm), via FTIR	% Error
USF-05-347	7.67	7.9	3.0
USF-05-348	9.06	9.8	8.2
USF-05-350	10.15	10.4	2.5
USF-05-360	12.4	12.2	1.6

Representative spectra from the FTIR measurements and cross-section SEM micrographs are shown below. Figure E.3 displays the spectrum for sample USF-05-347 and an SEM micrograph in which the film has an average thickness of 7.9 μm. The average thickness of sample USF-05-348 is 9.8 μm and a representative FTIR spectrum along with a cross-section SEM image is shown in Figure E.4. The representative spectrum and SEM micrograph for sample USF-05-350 is shown in Figure E.5. The mean thickness measured is 10.4 μm. Finally, sample USF-05-360 has an average thickness of 12.2 μm. A representative FTIR spectrum and SEM image is shown in Figure E.6.

Appendix E: (Continued)

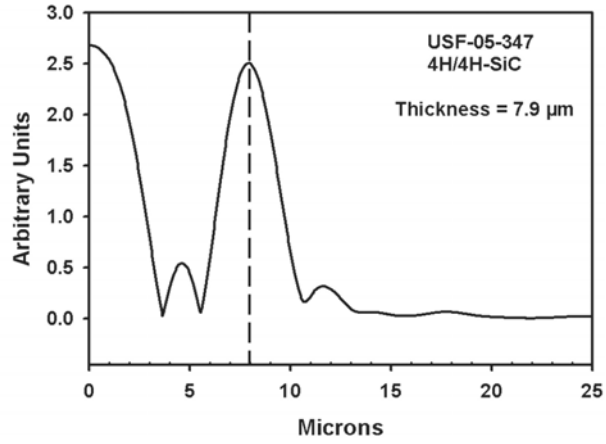

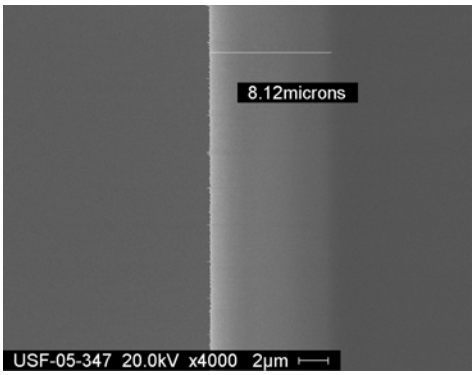

(a) (b)

Figure E.3 Sample ID USF-05-347 (a) FTIR spectrum and (b) cross-section SEM micrograph of bottom edge showing thickness of 8.12 µm.

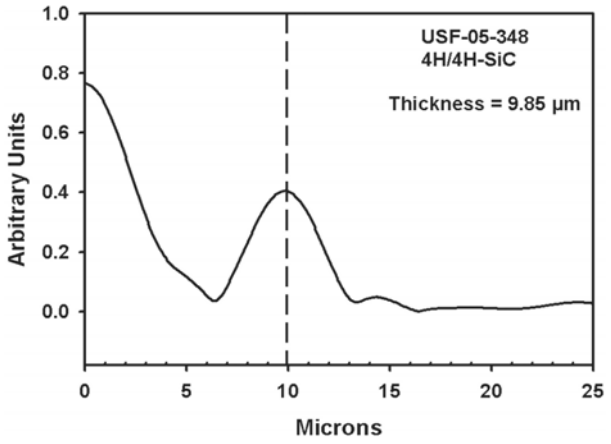

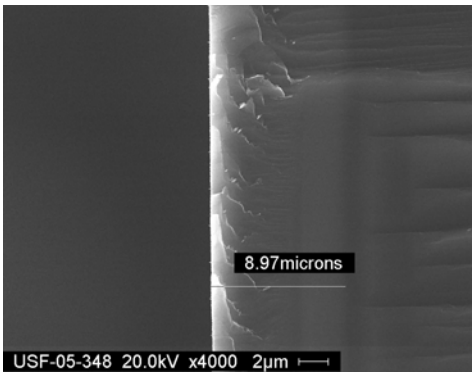

(a) (b)

Figure E.4 Sample ID USF-05-348 (a) FTIR spectrum and (b) cross-section SEM micrograph of bottom edge showing thickness of 8.97 µm.

Appendix E: (Continued)

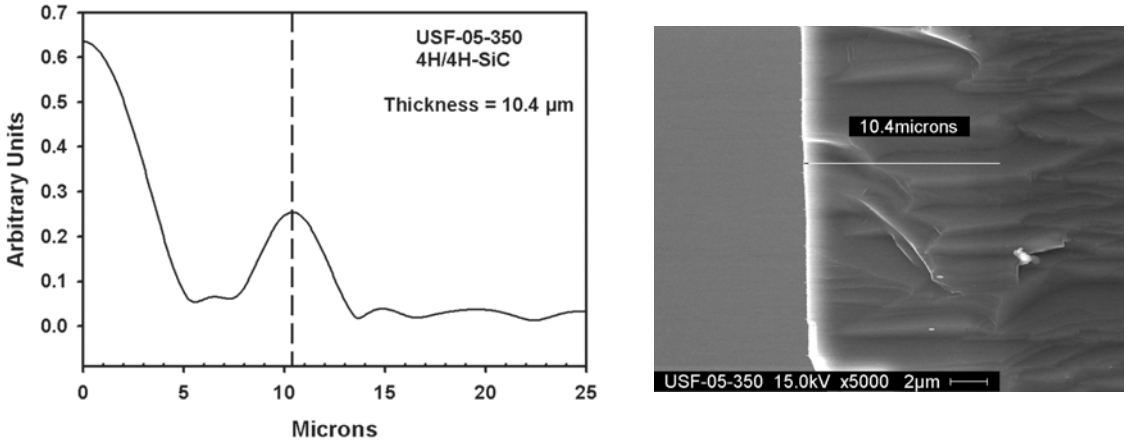

(a) (b)

Figure E.5 Sample ID USF-05-350 (a) FTIR spectrum and (b) cross-section SEM micrograph of bottom edge showing thickness of 10.4 µm.

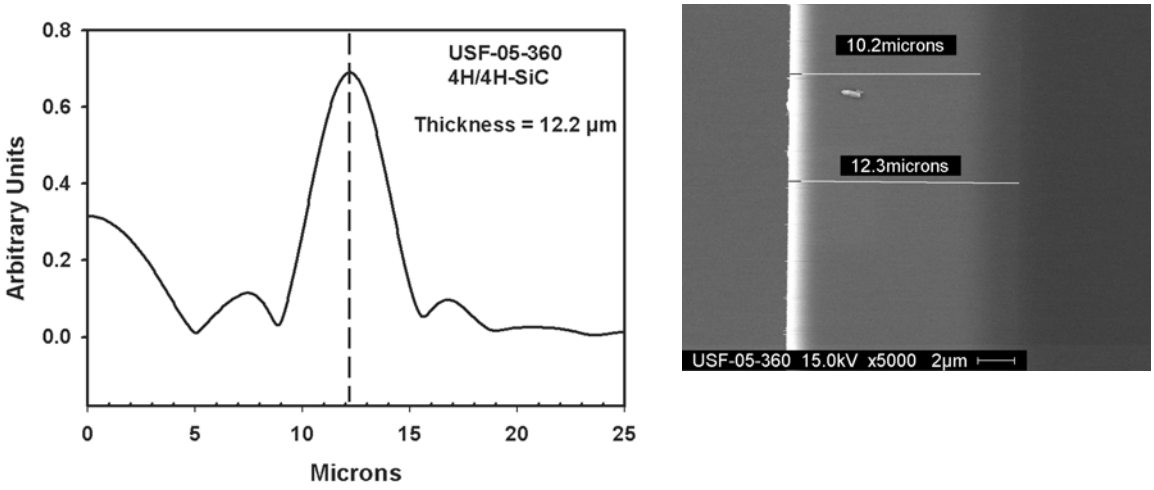

(a) (b)

Figure E.6 Sample ID USF-05-360 (a) FTIR spectrum and (b) cross-section SEM micrograph of middle edge showing thickness of 12.3 µm.

Cross-section SEM analysis was initially used to determine the thickness of the samples. However, LTPL measurements performed at the University of Pittsburgh cast doubt on these measurements. The samples thicknesses were therefore measured

independently using an FTIR to corroborate the thickness measurements that had been made previously using cross-section SEM analysis. For each sample, there is less than a 5 % difference between the two measurements except for sample USF-05-350, which has an error of ~8%. Therefore, when comparing the FTIR thickness measurements to the cross-section SEM measurements, there is evidence that the thickness of the samples grown using the HCl additive were indeed what was presented in Chapter 4, Figure 4.22.

ABOUT THE AUTHOR

Rachael L. Myers-Ward obtained a Master of Science degree in Chemical Engineering from the University of South Florida in 2003. The focus of the research was 3C-SiC growth on novel Si substrates. She received her Bachelor of Science degree in Chemical Engineering from the same university. Her Doctor of Philosophy degree will be in Electrical Engineering. The research work performed during both her Master's and Ph.D. has been supported by federal as well as industrial sponsors. She had studied abroad for six weeks at the Max-Planck Institute in Stuttgart, Germany under Dr. U. Starke during her dissertation work and has presented her research at the 2003 International Conference on Silicon Carbide and Related Materials (ICSCRM) (Lyon, France), 2004 Spring Materials Research Society (MRS) meeting (San Francisco, CA), 2004 European Conference on Silicon Carbide and Related Materials (ECSCRM) (Bologna, Italy), and lastly at the 2005 ICSCRM (Pittsburgh, PA).